

Examination of the influences of additives on the crystallization of CaCO_3



Max Planck **Graduate Center** 
mit der Johannes Gutenberg-Universität

Dissertation zur Erlangung des Grades eines
`Doktor rerum naturalium (Dr. rer. nat.)´ der Fachbereiche:

08 - Physik, Mathematik und Informatik • 09 – Chemie, Pharmazie und Geowissenschaften • 10 – Biologie • Universitätsmedizin

der Johannes Gutenberg-Universität Mainz

vorgelegt von Mirko Montigny

geb. am 01.08.1990 in Bad Kreuznach

Die vorgelegte Arbeit wurde in der Zeit von Februar 2015 bis Juni 2018 am Institut für Anorganische Chemie und Analytische Chemie der Johannes Gutenberg-Universität Mainz in der Arbeitsgruppe von **Prof. Dr. Wolfgang Tremel** angefertigt.

1. Gutachter: Prof. Dr. Wolfgang Tremel
2. Gutachter: Prof. Dr. Hans-Jürgen Butt

vorgelegt am: XX.YY.2019
Datum der Prüfung: YY/2019

I hereby declare that I wrote the dissertation submitted without any unauthorized external assistance and used only sources acknowledged in the work. All textual passages which are appropriated verbatim or paraphrased from published and unpublished texts as well as all information obtained from oral sources are duly indicated and listed in accordance with bibliographical rules. In carrying out this research, I complied with the rules of standard scientific practice as formulated in the statutes of Johannes Gutenberg-University Mainz to ensure standard scientific practice.

Traunstein, August 2019

A handwritten signature in black ink, appearing to read "André Metzger". The signature is written in a cursive style with a prominent flourish at the end.

Danksagung

Zu allererst möchte ich mich bei meiner Frau **Miriam Montigny** und meinen Kindern **Max** und **Mira** bedanken, die mich während der Zeit der Entstehung dieser Arbeit immer wieder aufgebaut und für einen Ausgleich zum Labor- und Schreiballtag in den vergangenen gut drei Jahren gesorgt haben.

Ebenso danke ich meinen **Freunden**, die mich während stressigen Zeiten immer wieder abgelenkt haben.

Mein besonderer Dank gilt meinem Doktorvater **Prof. Dr. Wolfgang Tremel** der mir mit größtem Vertrauen dieses überaus interessante und vielfältige Forschungsthema anvertraut hat und während der gesamten Zeit der Promotion stets mit guter Betreuung den Fortschritt dieser Arbeit unterstützt hat.

Dr. Martin Panthöfer und **Dr. Ruben Ragg** danke ich für hilfreiche Anregungen und Kommentare zu meinen Ergebnissen sowie das Korrekturlesen.

Besonders bedanken möchte ich mich bei **Dr. Moritz Susewind** für die kollegiale und sehr gewinnbringende Zusammenarbeit über den gesamten Zeitraum sowie der Knüpfung weitreichender Kontakte zu anderen Arbeitskreisen.

Dr. Nawaz Muhammad Tahir möchte ich vor allem für die guten Tipps zur Nanopartikel-Synthese und die hilfreichen Diskussionen danken.

Weiterer Dank gebührt **Herrn Prof. Dr. Hans-Jürgen Butt**, der durch das Angebot analytischer Methoden einen Großteil der analytischen Arbeit überhaupt erst ermöglichte. Dazu danke ich vor allem **Maren Müller**; **Katrin Kirchhoff** und **Gunnar Glaser** für die großartige Zusammenarbeit zur Kompositanalytik.

Ich danke weiterhin all meinen Kooperationspartnern, die entweder durch die Bereitstellung von Messmethoden oder durch den wissenschaftlichen Austausch die Bearbeitung des Themas vorangebracht haben. Vor allem danke ich hierbei **Hao Lu** und **Domenik Prozeller** sowie **Dr. Svenja Morsbach** für die großartige Zusammenarbeit.

Ebenfalls danke ich **Dr. Ralf Bienert** und **Dr. Franziska Emmerling** für die großartige Gastfreundschaft bei der SAXS-Messreise und den tollen wissenschaftlichen Austausch.

Weiterhin gebührt **Dr. Daniela Treiber** sowie ihrem Chef **Prof. Dr. Jürgen Markl** besonderer Dank für die unkomplizierte Kooperation im Rahmen des **Max Planck Graduate Centers**, welchem ich für die Finanzierung meiner Doktorarbeit, Auslandsreisen und Soft-Skill Kursen danke.

Ebenso danke ich **Dr. Eva-Marie Langhammer (geb. Christ)** und ihrem Chef **Prof. Dr. Holger Frey** für die gute, fruchtbare Zusammenarbeit im Bereich der PolyTHF Copolymere für die Biomineralisation.

Außerdem danke ich dem **AK Kühnle**, im Speziellen **Dr. Martin Nalbach** sowie **Stefanie Klassen** für die AFM Messungen und hilfreichen Diskussionen zum Thema.

Ebenso gebührt mein Dank der **IMB Microscopy Core Facility** und im Speziellen **Dr. Sandra Ritz**, die mir an den konfokalen Mikroskopen stets hilfreich beratend zur Seite stand.

Weiterhin danke ich **Prof. Dr. Wolfgang Hofmeister** und im Speziellen **Dr. Tobias Häger** für die gute Zusammenarbeit im Bereich der Raman-Spektroskopie.

Außerdem gebührt mein Dank dem **AK Kläui** im Speziellen **Prof. Dr. Gerhard Jakob** für die zur Verfügung gestellte Messzeit am Bruker D8 Discover.

Ebenso danke ich der **Biomineralisations-Kleingruppe** und allen Kollegen für ihre konstruktive Kritik an meiner Forschung und die lehrreichen Diskussionen.

Außerdem danke ich meinen Modulanten: **Christian Ulrich**, **Rene Dören**, Bacheloranden: **Marcel Maslyk**, **Steven Nothhelfer**, meiner Masterandin: **Melanie Viel** und meinem Auszubildenden **Jonas Junginger** für die großartige Arbeit unter meiner Anleitung und mit mir zusammen im Labor in guten und schlechten Zeiten. Ich hoffe, dass es zu keiner Zeit langweilig war und ich viel Wissen und Durchhaltevermögen generieren konnte.

Zu guter Letzt möchte ich mich vor allem bei meinen Eltern **Gabriele Montigny** und **Peter Montigny** für die immerwährende Unterstützung in allen Lebenslagen, der Ermöglichung dieses Studiums und der Promotion sowie den Ausgleich zum Studienalltag bedanken.

Abstract

CaCO_3 is the most common biomineral on earth and building block of many endo- and exoskeletons of snails, sea urchins, and mussels. In these natural examples CaCO_3 is often assembled as hydrated amorphous calcium carbonate (ACC) transported to the preferred area of transformation and crystallized to aragonite or calcite as kinetic and thermodynamic stable polymorphs. Thereby the stabilization and polymorph-controlled transformation is often managed by ions, small molecules or even proteins. After a CaCO_3 nucleation occurred, the crystallization in such systems is mostly a heterogeneous growth, controlled by additives that are finally either pushed out of the crystal lattice or incorporated within the crystal. Crystals that contain foreign material under keeping their overall crystal orientation over long distances are called mesocrystals. To learn from nature how it is controlling crystallization and which exclusion criterion rules whether an additive is included or pushed out by fusion during transformation is still not well understood. Only with this knowledge mesocrystalline structures as new composite materials of extraordinary properties become synthesizable in the future. How to control the morphology and polymorphism of CaCO_3 in mesocrystal synthesis is a complex area of research one needs to investigate for future perspectives.

This work gives an overview of existing literature on calcium carbonate crystallization with additives and the discussion of effects of mostly acidic additives on CaCO_3 crystallization. The thesis research deals with soft natural as well as soft and rigid synthetic additives containing different functional groups as studying objects to learn how additives and their chemical nature control crystallization and which criteria additives need to fulfill to be incorporated to tune mesocrystal properties.

1. Rigid synthetic additives:

Functionalized Au and Au@ Fe_3O_4 nanoparticles are studied for the effect of functionalization of either domains and the effect of amphiphilic and anisotropic additive structure on calcium carbonate crystallization. For the Au nanoparticles the need of carboxylic acids bound on gold surface to trigger interaction with CaCO_3 is identified. This moiety induces epitaxy of CaCO_3 on gold nanoparticles surface which

results in dumbbell shaped mesocrystals of Au@CaCO₃. Au@Fe₃O₄ surface functionalization is conducted on particle batches synthesized via a new simplified synthesis route. The functionalization is driven out by using the HSAB concept to either get isotropic anionic or anisotropic amphiphilic Au@Fe₃O₄ particles to study their influence on CaCO₃ crystallization and investigate them for the purpose of inclusion for different functionalization patterns. The colloidal stability is hereby identified as a central need for good integration of nanoparticles within CaCO₃ crystals.

2. Flexible synthetic additives:

PolyTHF copolymers as new class of non-polar polymers have been post-functionalized with carboxylic acids to study their effect on CaCO₃ crystallization. The polymers of either linear or hyper-branched structure have been synthesized by Dr. Eva-Maria Langhammer (born Christ) as former member of the AK Frey and used as received to study the effects on calcium carbonate crystallization. For better comparison similar carboxylic acid loading of the non-polar polymers of similar molecular weight was ensured to study only their structural effects on the morphology and phase of CaCO₃ crystals. While the linear copolymer induced formation of scale inhibited calcites with inclusions of polymer and high degree of nano-crystallinity, the addition of hyper-branched copolymer results in scale inhibited dumbbell shaped calcite crystals. So the structural motif of the additive was shown to be a factor for the final morphology of the crystallization product.

3. Flexible “natural” additives:

As flexible “natural” additives a study on recombinantly expressed *Bg*-AChBP proteins effect on calcium carbonate crystallization is presented in the last part of the thesis. The proteins influence on CaCO₃ crystallization is a still discussed property of the AChBP class, which has a strong sequential similarity to the amorphous calcium carbonate stabilizing protein family (ACCBP). In the studied *Biomphalaria glabrata* snail two different isoforms of the proteins are expressed that are called *Bg*-AChBP1 and *Bg*-AChBP2. The discussed functions are signal transduction, detoxification and crystallization of CaCO₃. For both protein isoforms no assignment to a specific property was conducted until yet because their exact localization within the tissue is still unknown. The first study on the localization of the isoforms was conducted recently by Daniela Treiber a PhD students of the group of Prof. Markl,

who are the cooperation partners of this study and provider of the recombinant protein.

The mechanism of binding to calcium and magnesium ions is studied for both existing isoforms and the influence on CaCO_3 precipitation in ammonia diffusion method is also facilitated in this project. *Bg-AChBP2* is identified to form calcium and carbonate complexes, while *Bg-AChBP1* shows only weak complexation behavior. With the knowledge of localization of the isoforms of the protein – *Bg-AChBP1* is expressed close to CaCO_3 formation while *Bg-AChBP2* can only be found in the neuronal cells of the snail brain – one can understand the role each isoform has. *Bg-AChBP1* with the good aragonite stabilizing properties and its co-localization with CaCO_3 within the snail stabilizes CaCO_3 and ensures aragonite selective crystallization of CaCO_3 . In contrast *Bg-AChBP2* works as crystallization inhibitor to circumvent urgent calcification of the snail's neuronal tissue. By *in vitro* crystallizations of CaCO_3 under simultaneous presence of magnesium ions and recombinant protein (synthesized by Daniela Treiber, AG Markl) we were able to identify *Bg-AChBP1* to be responsible for phase selectivity of the CaCO_3 crystallization within the snail.

Zusammenfassung

CaCO_3 ist das meist verbreitete Biomineral auf der Erde und Baustein vieler Endo- und Exoskelette von z.B. Schnecken, Seeigel und Muscheln. In diesen Beispielen wird CaCO_3 oft als hydratisiertes amorphes Calciumcarbonat (ACC) in den bevorzugten Umwandlungsbereich transportiert und zu Aragonit oder Calcit als kinetisch beziehungsweise thermodynamisch stabiler Polymorph kristallisiert. Dabei werden die Stabilisierung und Kontrolle der Polymorphie während der Transformation oft durch Ionen, kleine Moleküle oder sogar Proteine gesteuert. Nach der ersten Keimbildung ist die Kristallisation in solchen Systemen meist ein heterogenes Wachstum, das durch Additive beeinflusst wird, die schließlich entweder aus dem Kristallgitter herausgedrückt oder durch Überwachsen in den Kristall eingebaut werden. Diese Art von Kristallen, die unter Beibehaltung ihrer gesamten Kristallorientierung über große Entfernungen Fremdstoffe enthalten, wird als Mesokristalle bezeichnet. Um von der Natur zu lernen, wie diese die Kristallisation über Additive steuert und welches Ausschlusskriterium bestimmt, ob ein Additiv während der Transformierung durch Fusion eingeschlossen oder herausgedrängt wird, ist nicht vollständig verstanden. Einen Zugang können Untersuchungen von natürlichen oder synthetischen Additiven in Kristallisationsprozessen bieten. Denn nur mit diesem Wissen können in Zukunft neue Verbundwerkstoffe auf Basis des umweltfreundlichen CaCO_3 hergestellt werden, die außergewöhnliche Eigenschaften bieten. Wie man die Morphologie und den Polymorphismus von CaCO_3 kontrollieren kann, ist dabei von enormer Wichtigkeit für diese Werkstoffe.

Diese Arbeit soll hierfür einen Überblick über bestehendes Wissen zur Rolle von Additiven in der Calciumcarbonat-Kristallisation geben. Die Dissertation beschäftigt sich inhaltlich sowohl mit weichen natürlichen als auch weichen und starren synthetischen Additiven verschiedener Funktionsgruppen als Studienobjekte, um zu verstehen, wie Additive die Kristallisation steuern können und welche Kriterien für Additive erfüllt sein müssen, um Mesokristalle auf Basis von CaCO_3 mit integrierten Additiven zu erhalten.

1) Starre synthetische Additive:

Funktionalisierte Au- und Au@Fe₃O₄-Nanopartikel werden in dieser Arbeit herangezogen um den Effekt der äquipolaren Funktionalisierung beider Domänen und den Effekt der amphiphilen und anisotropen Additivstruktur auf die Calciumcarbonat-Kristallisation zu untersuchen. Für die Au-Nanopartikel wird die Notwendigkeit von an der Goldoberfläche gebundenen Carbonsäuren zur Wechselwirkung mit CaCO₃ identifiziert. Diese funktionelle Gruppe induziert die Epitaxie von CaCO₃ auf der Oberfläche der Goldnanopartikel, was zu hantelförmigen Mesokristallen von Au@CaCO₃ führt. Au@Fe₃O₄-Funktionalisierung mit Molekülen wie z.B. 11-MUA, 4-TBC und 1-DT wird auf gleichen Nanopartikelchargen durchgeführt, die mit einer neuen vereinfachten Synthese synthetisiert werden. Zur selektiven Funktionalisierung wird das HSAB-Konzepts zur Synthese isotroper anionischer oder anisotroper amphiphiler Au@Fe₃O₄-Partikel herangezogen. Die kolloidale Stabilität der Proben kann dabei als zentrale Voraussetzung für eine gute Integration von Nanopartikeln in CaCO₃-Kristalle identifiziert werden.

2) Flexible synthetische Additive:

PolyTHF-Copolymere als neue Klasse unpolarer Polymere wurden ebenfalls mit Carbonsäuren postfunktionalisiert, um ihre Wirkung auf die CaCO₃-Kristallisation zu untersuchen. Die Polymere mit linearer und hyperverzweigter Struktur wurden von Dr. Eva-Maria Langhammer (geb. Christ) im AK Frey synthetisiert und zur Untersuchung der Auswirkungen auf die Calciumcarbonat-Kristallisation verwendet. Zur besseren Vergleichbarkeit wurde die gleiche Menge an Carbonsäuregruppen am unpolaren Polymergerüsts gleicher Molmasse sichergestellt, um vor allem die strukturellen Effekte auf die Endmorphologie von Calcit Kristallen zu untersuchen. Während das lineare Copolymer die Bildung von stark größeninhibierten Calciten mit Einschlüssen von Polymeren und einem hohen Grad an Nanokristallinität induzierte, bildeten sich unter Zugabe des hyperverzweigten Copolymers hantelförmige Calcit-Kristalle. Daraus ergibt sich, eine Beziehung zwischen dem strukturellen Motiv und der finalen Morphologie der CaCO₃ Kristalle.

3) Flexible "natürliche" Additive:

Als flexible "natürliche" Additive wird im letzten Teil der Arbeit eine Studie zur Wirkung rekombinant hergestellter *Bg*-AChBP-Proteine auf die Calciumcarbonat-Kristallisation vorgestellt. Der Einfluss der Proteine auf die CaCO_3 -Kristallisation ist eine noch immer diskutierte Eigenschaft der Acetylcholin Binde Protein (AChBP)-Klasse, die eine starke sequentielle Beziehung zur amorphen Calciumcarbonat-stabilisierenden Proteinfamilie (ACCBP) aufweist. In der untersuchten *Biomphalaria glabrata* Schnecke werden zwei verschiedene Isoformen der Proteine exprimiert, die *Bg*-AChBP1 und *Bg*-AChBP2 genannt werden. Die diskutierten Funktionen der Proteine reichen von neuronaler Signal-Transduktion über Entgiftung bis hin zur Beeinflussung der CaCO_3 Kristallisation bei der Schalenbildung der Schnecke. Eine Zuordnung der Eigenschaften zur jeweiligen Isoform der Proteinklasse ist jedoch bis heute nicht möglich gewesen, da die histologische Verteilung bisher nicht untersucht war. Durch die Arbeiten von Dr. Daniela Treiber in der AG Markl (Zoologie, Universität Mainz) wird diese Zuordnung erstmals möglich.

Mit dem Wissen zur Lokalisation der Isoformen des Proteins - *Bg*-AChBP1 wird nahe der CaCO_3 -Bildung exprimiert, während *Bg*-AChBP2 primär in den neuronalen Zellen des Schneckenengehirns zu finden ist – können die Rollen der Proteine der entsprechenden Isoform zugeordnet werden. *Bg*-AChBP1 mit den guten Aragonit-stabilisierenden Eigenschaften und seiner Co-Lokalisation mit CaCO_3 in der Schnecke stabilisiert CaCO_3 und sorgt für selektive Aragonit Kristallisation von CaCO_3 . Im Gegensatz dazu wirkt *Bg*-AChBP2 als Kristallisationsinhibitor zur Umgehung von unkontrollierter Verkalkung des neuronalen Gewebes der Schnecke. Dabei konnte sowohl der Bindungs-Mechanismus Calcium- und Magnesium-Ionen, wie auch der Einfluss der einzelnen Isoformen auf die CaCO_3 -Ausfällung in der Ammoniakdiffusionsmethode konnte untersucht werden. *Bg*-AChBP2 wurde hierbei als stark komplexierendes Protein identifiziert, während *Bg*-AChBP1 nur schwache komplexierende Eigenschaften aufweist. Um die Rolle der Proteine in der CaCO_3 Kristallisation noch genauer nachvollziehen zu können wurden *in vitro*

Kristallisationsexperimenten mittels Fällung und Ammoniakdiffusionsmethode unter gleichzeitiger Anwesenheit von Magnesium-Ionen und rekombinanten Proteinen beider Isoformen durchgeführt.

List of Abbreviations

ACC	Amorphous Calcium Carbonate
HSAB	Hard and Soft Acid Base
PAA	Polyacrylic acid
SAM	Self-Assembled Monolayer
PolyTHF	Polytetrahydrofuran
<i>Bg</i>	<i>Biomphalaria Glabrata</i>
AChBP	Acetylcholine Binding Protein
ACCBP	Amorphous Calcium Carbonate Binding Protein
CNT	Classical Nucleation Theory
BCF	Burton, Cabrera, Frank
PDF	Pair Distribution Function
XRD	X-Ray Diffraction
PILP	Polymer Induced Liquid Phase
DOLLOP	Dynamically Ordered Liquid-Like Oxyanion Polymer
ADT	Automated Diffraction Tomography
IR	Infra-red
UV-Vis	Ultraviolet-visible
Oam	Oleylamine
Oac	Oleic acid
PEG	Polyethylene glycol
PP	Polypropylene

PE	Polyethylene
PAMPS	Poly-2-Acrylamido-2-methylpropanesulfonic acid
TMAH	Tetramethylammoniumhydroxid
11-MUA	11-Mercaptoundecanoic acid
1-DT	1-Dodecanethiol
4-SBA	4-Sulfobenzoic acid
4-TBC	4- <i>Tert</i> -butyl-chatecol
DNA	Deoxyribonucleic acid
PSPMA-PDPA	Poly-2-(sulfobenzoic)propylmethacrylate-Poly(2-diisopropylamino)ethyl methacrylate
HR-TEM	High Resolution – Transmission Electron Microscopy
CLSM	Confocal Laser Scanning Microscopy
AFM	Atomic Force Microscopy
TMA	N,N,N,N-Trimethyl(11-mercaptoundecyl) ammonium chloride
NIR	Near Infra-red
SEM	Scanning Electron Microscopy
STEM	Scanning Tunnel-Electron Microscopy
TEM	Transmission Electron Microscopy
SAXS	Small-Angle X-Ray Scattering
ODE	1-Octadecene
MRT	Magnet Resonance Tomography
EDX	Electron Dispersive X-Ray
SAED	Selected Area Electron Diffraction

FFT	Fast Fourier Transformation
BHMO	Bis-hydroxymethyloxetane
CEO	Cyano-ethylene oxide
CROP	Cationic Ring Opening Polymerization
pH	Potentio Hydrogenii
DOSY	Diffusion-ordered Nucleus Magnetic Resonance Spectroscopy
NMR	Nucleus Magnetic Resonance
ISE	Ion-selective Electrode
AAS	Atomic Absorption Spectroscopy
XPS	X-Ray Photo-electron Spectroscopy
ITC	Isothermal Titration Calorimetry
DAPI	4', 6-Diamidin-2-phenylindol (Fluoreszenzfarbstoff)

List of tables

Table 2.1: Crystallographic data of vaterite.....	28
Table 2.2: Crystallographic data of aragonite.	29
Table 2.3: Crystallographic data of calcite.	31
Table 3.1: Polymorph-selective protein pulldown assay.	195

List of tables of supporting information

Table S 3.1: Calculations for 2θ scans of reference example and calcite precipitated with 0.2 g/L of differently functionalized Au-NPs.	85
Table S 3.2: Calculations from Gaussian fits for Rocking curve data.....	87
Table S 3.3: Calculations for 2θ scans of reference sample and calcite precipitated if 0.2 g/L of different Au@Fe ₃ O ₄ Janus particles of various functionalization patterns is added.	134
Table S 3.4: Calculations from fits of rocking curve data.	136
Table S 3.5: Calculations for 2θ scans of Reference example and calcite precipitated with μ M concentration of linear PTHF polymer added.	164
Table S 3.6: Calculations from Gaussian fits for Rocking curve data. Reference shows a single mode of crystals only slightly tilted and of very small mosaicity.	165
Table S 3.7: Summary of XPS determined elemental composition for the regions outside and inside snail shells.	198
Table S 3.8: XPS elemental composition (%) of direct precipitation of CaCO ₃ from Ca:Mg 94:6% with and without addition of no protein, <i>Bg</i> -AChBP1 or <i>Bg</i> -AChBP2 protein, respectively.	202
Table S 3.9: XPS elemental composition (%) of direct precipitation of CaCO ₃ from Ca/Mg 89:11 % with and without addition of no protein, <i>Bg</i> -AChBP1 or <i>Bg</i> -AChBP2 protein, respectively.	203
Table S 3.10: Calculations for 2θ scans of Reference example and calcite precipitated with μ M concentrations of different protein fractions and structures.....	232
Table S 3.11: Calculations from Gaussian fits for Rocking curve data. All samples show a single reflex of different FWHM.	234

List of figures

Figure 1.1: Literature analysis: (A) Number of publications on the topics “Composites” and (B) “ Mesocrystals”.....	1
Figure 2.1: LaMer-model of seed nucleation and growth.	6
Figure 2.2: Correlation of Gibbs free energy and seed radius.....	7
Figure 2.3: Relationship of Gibbs free energy and critical seed radius for different supersaturations.	8
Figure 2.4: Heterogeneous nucleation of a spherical droplet on a flat surface...	9
Figure 2.5: Transition from homogenous (red line fit) to heterogeneous nucleation (blue line fit) regime for CaCO_3	11
Figure 2.6: Scheme to describe the relationship of driving force, here supersaturation against the resulting crystal morphology, rate determination and overall crystal structure is shown.	13
Figure 2.7: AFM image series of calcite (104) surface under time lapse without additive (a-c) and with Kongo red as additive (d-f).....	13
Figure 2.8: Scheme for oriented growth along a specific direction under thermodynamic control.....	14
Figure 2.9 Various possibilities for crystal unit attachment on a growing surface of a crystal.	15
Figure 2.10: AFM image series of BaSO_4 (001)-surface under spiral growth around step displacement from very low supersaturation	16
Figure 2.11: Illustration of the Bliznakov-Chernov mechanism (A) and the Cabrera-Vermilyea mechanism (B).....	17
Figure 2.12: Scheme of classical and non-classical crystallization to (A) single crystals (B) oriented crystals of nano-building-blocks (C) polycrystals and (D) mesocrystals.....	18
Figure 2.13: Orientation along organic skeleton	20
Figure 2.14: Alignment by physical forces.....	20
Figure 2.15: Epitactic growth by assembly of organic bridges.....	21
Figure 2.16: Assembly within confinement	22
Figure 2.17: Oriented attachment.....	23
Figure 2.18: Orientation by face selective binding of additives.....	24
Figure 2.19: Thermodynamic stability of CaCO_3 polymorphs.....	25
Figure 2.20: Vaterite.....	27
Figure 2.21: Aragonite.....	30
Figure 2.22: Coordination sphere of a calcium ion within calcite lattice with sixfold geometry caused by carbonate ion coordination.	31
Figure 2.23: Calcite	32

Figure 2.24: Graphic of relationship between reaction temperature and nanoparticle diameter.	34
Figure 2.25: Plasmon absorption shift of Au nanoparticles f.l.t.r. up to 20 nm diameter.	35
Figure 2.26: Au@Fe ₃ O ₄ Janus particles	37
Figure 2.27: Functionalization of nanoparticles of this thesis	39
Figure 2.28: PAA-PAMPS as additive for scale inhibition	40
Figure 2.29: Influence of polyglycerol polymers on CaCO ₃	41
Figure 2.30: Influence of linear Poly(THF) polyacids on CaCO ₃ crystallization.	42
Figure 2.31: Proteins as additives.....	44
Figure 3.1: Studied system of 11-MUA@Au and PEG2000/11-MUA@Au.....	54
Figure 3.2: Schematic presentation of the effects of functionalization (A), agglomeration by calcium ion addition (B) and interaction with CaCO ₃ during ADM desiccator experiments (C) on 11-MUA@Au NPs and PEG2000/11-MUA@Au NPs.	62
Figure 3.3: AFM images of freshly cleaved (104) calcites under addition of a solution of 0.2 g/L 11-MUA@Au-NPs (A) and dialyzed PEG2000/11-MUA@Au-NPs	64
Figure 3.4: Microscopy images of precursors and final crystals of CaCO ₃	66
Figure 3.5: HR-TEM analysis of final CaCO ₃ crystals	68
Figure 3.6: Scheme of simplification step for synthesis of Au@Fe ₃ O ₄ Janus particles.	91
Figure 3.7: (A) Comparison of a conventional reaction and a one pot seed-mediated synthesis of Au@Fe ₃ O ₄ JPs.	97
Figure 3.8: Size evolution of Au domains during the growth phase.	98
Figure 3.9: (a) HR-TEM images of Au@Fe ₃ O ₄ JPs obtained from a one-pot reaction (I, left column) and a conventional two-step synthesis (II).	100
Figure 3.10: Powder X-ray diffraction patterns of Au@Fe ₃ O ₄ JPs (black lines) synthesized via novel one-step synthesis (A) and the conventional two-step approach (B).....	101
Figure 3.11: Scheme of functionalization patterns of Au@Fe ₃ O ₄ Janus particles.	107
Figure 3.12: Sketch of Au@Fe ₃ O ₄ functionalization and agglomeration of Janus Particles (black boxes) and the resulting CaCO ₃ crystals.....	114
Figure 3.13: (A) Scheme of a type (a) functionalized Au@Fe ₃ O ₄ Janus particles (B) TEM image after 8 h desiccator CaCO ₃ precipitation.	117
Figure 3.14: (A) Scheme of type (b) functionalized Au@Fe ₃ O ₄ Janus particle (B) TEM image after 8 h desiccator CaCO ₃ precipitation.	119
Figure 3.15: (A) Scheme of type (c) functionalized Au@Fe ₃ O ₄ Janus particles.....	121
Figure 3.16: Relationships between linear and hyper-branched polymer and the related influences on CaCO ₃ precipitates caused by the polymers structure.	141

Figure 3.17: Functionalization of PolyTHF polyols to polyacids and degradation to polyols and succinic acid by hydrolysis at basic pH.	148
Figure 3.18: Apparent diffusion coefficient D_{app} plotted versus the squared scattering vector q^2 for P(THF ₈ -co-BHMO ₃₈ -(C ₄ H ₆ O ₄) ₈₁) dispersed in water at pH 10 after filtration (100 nm filter).	149
Figure 3.19: (I) Product of free polymer concentration and detected free $c(\text{Ca}^{2+})$ plotted against concentration of bound $c(\text{Ca}^{2+})$ what can be defined as Polymer- Ca^{2+} complex concentration.	150
Figure 3.20: (I) Calcium ISE signal of CaCO_3 nucleation titrations in 10 mM carbonate buffer at pH 9,75 in a teflon vial with black no addition of polymer, green addition of 3 $\mu\text{mol/L}$ and red addition of 6 $\mu\text{mol/L}$ P(THF ₈ -co-BHMO ₃₈ -(C ₄ H ₆ O ₄) ₈₁).	151
Figure 3.21: A: SEM of three calcite mesocrystals cut by FIB-SEM technique	153
Figure 3.22: AFM on freshly cleaved (10.4)-calcite with pH 10 solutions of 0.166 μM hyper-branched PolyTHF (I, II, III, height profile of II plotted in IIp) and 0.3 mM linear PolyTHF (IV, V, VI, height profile of V plotted in Va)	155
Figure 3.23: (A) SEM image of elongated calcite crystal precipitated from 5 mM CaCl_2 solution with 20 $\mu\text{mol/L}$ P(THF ₈ -co-BHMO ₃₇ -(C ₄ H ₆ O ₄) ₇₈) added..	157
Figure 3.24: A, B: STEM images of two different sections of a TEM lamella showing a nano-structuring caused by occlusions that can be identified by HR-TEM images C and D.	158
Figure 3.25: Scheme of central question how shell growth gets effected by both structures of Isoform 1 of <i>Bg</i> -AChBP protein class at distinct ratios of calcium and magnesium.	177
Figure 3.26: Shell structure and <i>Bg</i> -AChBP1 presence in the shell material..	184
Figure 3.27: TEM and STEM-EDX analysis of the shell.	186
Figure 3.28: Whole mount immunofluorescence microscopy of <i>B. glabrata</i> larvae	189
Figure 3.29: Immunofluorescence microscopy of a tissue section from <i>B. glabrata</i>	190
Figure 3.30: Calculations for relative polymorph contributions	193
Figure 3.31: Scheme on CaCO_3 protein crystallizations in the desiccator presented in this paragraph.	208
Figure 3.32: (A) Titrations of calcium chloride into a pH 7.5 TRIS buffered solution of pentamer proteins.	217
Figure 3.33: The nano-structure of a typical CaCO_3 crystal (104) surface after addition of 0.2 g/L pH 7.5 TRIS buffered pentameric <i>Bg</i> -AChBP1 protein solution is added	219
Figure 3.34: CaCO_3 crystals precipitated via desiccator ADM CaCO_3 precipitation experiment for 15 h with dodecahedral <i>Bg</i> -AChBP1.	220
Figure 3.35: CaCO_3 crystals precipitated via desiccator experiment for 15 h.	222

List of figures of supporting information

Figure S 3.1: TGA data of 11-MUA@Au-NP samples (A) and PEG2000/11-MUA@Au (B).....	71
Figure S 3.2: IR spectra of (A) 11-MUA (black) and 11-MUA@Au (red)	72
Figure S 3.3: (A, B) Titration of 0.05 g/L TRIS buffered solutions of non-dialyzed PEG2000/11-MUA@Au-NPs (magenta), dialyzed PEG2000/11-MUA@Au-NPs (blue) and 11-MUA@Au NPs (red) with calcium chloride solution at pH 9.75.	73
Figure S 3.4: SAXS patterns of (A) 11-MUA@Au-NPs (red) and PEG2000/11-MUA@Au-NPs (green) in TRIS buffer.....	74
Figure S 3.5: AFM of PEG2000/11-MUA@Au-NPs on (104) calcite shows small amounts of nanoparticles and free ligand attached to surface (A).....	75
Figure S 3.6: SEM images of CaCO ₃ crystals from ammonia diffusion method CaCO ₃ precipitation with addition of (A-C) 0.05 g/L (D-F) 0.1 g/L and (G-I) 0.2 g/L of 11-MUA@Au-NPs.	76
Figure S 3.7: SEM images of CaCO ₃ crystals from ammonia diffusion method CaCO ₃ precipitation with addition of (A-C) 0.05 g/L (D-F) 0.1 g/L and (G-I) 0.2 g/L of dialyzed PEG2000/11-MUA@Au-NPs.....	77
Figure S 3.8: SEM images of CaCO ₃ crystals from ammonia diffusion method CaCO ₃ precipitation with addition of (A-C) 0.05 g/L (D-F) 0.1 g/L and (G-I) 0.2 g/L of non-dialyzed PEG2000/11-MUA@Au-NPs.....	78
Figure S 3.9: SEM images of CaCO ₃ crystals from desiccator experiments with addition of (A-C) 0.05 g/L (D-F) 0.1 g/L and (G-I) 0.2 g/L of PEG2000/11-MUA ligand and increasing zoom-in on kinks from left to right.	79
Figure S 3.10: HR-TEM images of (A) agglomerated ACC around non-dialyzed PEG2000/11-MUA@Au-NPs after 8 h of desiccator crystallization (ADM).80	
Figure S 3.11: Raman spectra of CaCO ₃ crystals.....	81
Figure S 3.12: SEM-EDX of surface of final mesocrystal from precipitation of 11-MUA@Au-NPs	82
Figure S 3.13: TEM-EDX of surface of core area of cross-section of mesocrystal from precipitation of 11-MUA@Au-NPs in the desiccator experiment of 15h duration.	83
Figure S 3.14: TEM-EDX of occluded nanoparticles crystal from precipitation of CaCO ₃ with PEG2000/11-MUA@Au-NPs in the desiccator experiment of 15h duration.	84
Figure S 3.15: XRD 2 θ scan of calcites (104) reflex for different crystal samples with as labeled additives added to the crystallizations.....	85
Figure S 3.16: Rocking curve analysis in the range of 4° and 24° ω angle.....	86

Figure S 3.17: DLS data plot of Diffusion coefficient against q^2 for five different points (t_1 - t_5 from top to bottom) shown in Figure 3.8 of the main paragraph.	102
Figure S 3.18: IR-Spectra of Janus particles functionalized with (a) 1-DT/Au@Fe ₃ O ₄ /4-SBA, (b) 11-MUA/Au@Fe ₃ O ₄ /TBC and (c) 11-MUA/Au@Fe ₃ O ₄ /4-SBA.....	123
Figure S 3.19: UV-Vis spectra of aqueous Janus particle dispersions at basic pH value and of a hexane dispersion for reference sample.	124
Figure S 3.20: TGA data of Janus particles of functionalization pattern shown in Figure S 3.18.	125
Figure S 3.21: Optical microscopy images of (A) reference without additive and with 4-SBA as additive	126
Figure S 3.22: SEM images of CaCO ₃ crystals precipitated under presence of various concentrations of 1-DT/Au@Fe ₃ O ₄ /4-SBA NPs	127
Figure S 3.23: SEM images of CaCO ₃ crystals precipitated under presence of various concentrations of 11-MUA/Au@Fe ₃ O ₄ /4-TBC NPs	128
Figure S 3.24: SEM images of CaCO ₃ crystals precipitated under presence of various concentrations of 11-MUA/Au@Fe ₃ O ₄ /4-SBA NPs	129
Figure S 3.25: STEM image of a cross-section of an exemplary CaCO ₃ crystal precipitated after 15 h duration under presence of 0.2 g/L of (a) 1-DT/Au@Fe ₃ O ₄ /4-SBA NPs	130
Figure S 3.26: STEM image of cross-section of an exemplary CaCO ₃ crystal precipitated after 15 h duration under presence of 0.2 g/L of (b)11-MUA/Au@Fe ₃ O ₄ /4-TBC NPs	131
Figure S 3.27: Raman spectra of CaCO ₃ precipitated under addition of (A) 11-MUA/Au@Fe ₃ O ₄ /4-SBA (black: reference, red: 0.05 g/L, blue: 0,1 g/L, magenta: 0,2 g/L).....	132
Figure S 3.28: XRD 2 θ scan of calcites (104) reflex for different additives added to the crystallization.	133
Figure S 3.29: Rocking curve analysis from 5° to 24° ω angle under constant 2 θ angle of 29.42° analyzing the (104) truncated CaCO ₃ mesocrystals	135
Figure S 3.30: A series of ¹ H NMR (300 MHz, pyridine-d ₅) spectra of P(THF ₈ -co-BHMO ₃₈ -(C ₄ H ₆ O ₄) ₈₁) at varied pH values, from pH 10 to 14, as well as a spectrum at pH 10 with a delay of two weeks.	160
Figure S 3.31: Diffusion ordered spectroscopy (400 MHz, pyridine-d ₅) of P(THF ₈ -co-BHMO ₃₈ -(C ₄ H ₆ O ₄) ₈₁) at pH 10 after a delay of two weeks.....	161
Figure S 3.32: FTIR spectra of P(THF ₈ -co-BHMO ₃₈ -(C ₄ H ₆ O ₄) ₈₁) in black and the same polymer after overnight incubation at pH 12 (red) and pH 13 (green).	162
Figure S 3.33: A,B: SEM images of classically obtained calcite rhombohedra. C: CLSM image of calcite rhombohedra not showing any fluorescence activity.	163

Figure S 3.34: XRD 2θ scan of characteristic (104) reflex of calcite. FWHM is determined by Gaussian fits of both curves. Data is presented in Table S 3.5.	164
Figure S 3.35: Rocking curve analysis between 9,5 and 19 ° ω angle under constant 2θ angle of 29.42° analyzing the (104) truncated nano-crystals of the mesocrystal.	165
Figure S 3.36: SEM images of crystals in the presence of 10 $\mu\text{mol/L}$ (A/B) , 20 $\mu\text{mol/L}$ (C/D), and 40 $\mu\text{mol/L}$ (E/F) of P(THF ₈ -co-BHMO ₃₇ -(C ₄ H ₆ O ₄) ₇₈ after 15 h crystallization time.	166
Figure S 3.37: TEM time course of the crystallization of calcium carbonate in the presence of P(THF ₈ -co-BHMO ₃₇ -(C ₄ H ₆ O ₄) ₇₈ (40 $\mu\text{mol/L}$).	167
Figure S 3.38: CLSM z-stack of a mesocrystal formed by addition of 20 $\mu\text{mol/L}$ of Rhodamine B tagged P(THF ₈ -co-BHMO ₃₈ -(C ₄ H ₆ O ₄) ₈₁	168
Figure S 3.39: Raman spectra of calcite reference (magenta), final calcite mesocrystals with 10 $\mu\text{mol/L}$ (red), 20 $\mu\text{mol/L}$ (black) and 40 $\mu\text{mol/L}$ (blue) polymer added.	169
Figure S 3.40: (A) STEM HAADF image of IM of snail shell, light colored areas contain elements of high Z.	197
Figure S 3.41: (A) IR-spectra of ACC precipitated without addition and (B) with addition of dodecahedra of <i>Bg</i> -AChBP1 by Faatz-Wegner method.	199
Figure S 3.42: IR Spectra of CaCO ₃ precipitated for 72 h with (red) and without (black) pentamers of <i>Bg</i> -AChBP1 from a 89:11 % Ca/Mg solution (A), a 94:6 % Ca/Mg solution (B) and pure CaCl ₂ solution (C).	200
Figure S 3.43: XRD pattern of CaCO ₃ precipitated for 72 h.	201
Figure S 3.44: Optical microscopy images from PE vial precipitations of CaCO ₃ with and without Mg ²⁺	204
Figure S 3.45: TEM images of proteins prepared with negative staining with uranyl acetate.	224
Figure S 3.46: CaCO ₃ crystals precipitated without additive in a desiccator crystallization for 15 h.	225
Figure S 3.47: Exemplary Raman spectrum of vaterite crystals precipitated if 0.8 μM of dodecahedral <i>Bg</i> -AChBP1 was added.	226
Figure S 3.48: A-I: SEM images of CaCO ₃ crystals from desiccator experiment after 15 h.	227
Figure S 3.49: A-I: SEM images of CaCO ₃ crystals from desiccator experiment after 15 h.	228
Figure S 3.50: Optical microscopy images of glass-slides covered with CaCO ₃ crystals	229
Figure S 3.51: Raman spectroscopy of CaCO ₃ crystals on glass slides precipitated with presence of (A) pentamers of <i>Bg</i> -AChBP1 and (B) pentamers of <i>Bg</i> -AChBP2 protein	230

Figure S 3.52: Light microscopy image of CaCO ₃ crystals after 1 year of aging (Rocking curve sample).	231
Figure S 3.53: XRD 2 θ scan of calcites (104) reflex for different additives added to the crystallizations.....	231
Figure S 3.54: Rocking curve analysis between 10° and 20° ω angle under constant 2 θ angle of 29.42° analyzing the (104) truncated nano-crystals of the mesocrystal.....	233

Table of content

1	Introduction	1
2	Theoretical background	5
2.1	Crystallization	5
2.1.1	Classical Nucleation Theory (CNT)	5
2.1.2	Heterogeneous Nucleation	9
2.1.3	Crystal Growth	12
2.1.3.1	Classical Crystal Growth	12
2.1.3.2	Non-classical Crystal Growth – Mesocrystals	18
2.2	Calcium carbonate.....	25
2.2.1	Amorphous CaCO ₃	26
2.2.2	Vaterite	27
2.2.3	Aragonite	29
2.2.4	Calcite	30
2.3	Additives for Crystallization.....	33
2.3.1	Nanoparticle	33
2.3.1.1	Au-Nanoparticles	34
2.3.1.2	Au@Fe ₃ O ₄ Janus Particles	36
2.3.1.3	Functionalization of Nanoparticles	38
2.3.2	Polymers	39
2.3.3	Proteins	43
2.4	References	46
3	Results and Discussion	53
3.1	Functionalized nanoparticles as additives in CaCO ₃ crystallization	53
3.1.1	Inclusion mechanism of 11-MUA and PEG/11-MUA functionalized gold nanoparticles within CaCO ₃	54
3.1.1.1	Introduction	55
3.1.1.2	Experimental	57
3.1.1.3	Results & Discussion	62

3.1.1.4	Conclusion	69
3.1.1.5	Supporting Information	71
3.1.1.6	References	88
3.1.2	Seed-mediated one-pot synthesis of Au@Fe ₃ O ₄ Janus Particles	91
3.1.2.1	Introduction	93
3.1.2.2	Experimental	95
3.1.2.3	Result & Discussion	97
3.1.2.4	Conclusion	101
3.1.2.5	Supporting Information	102
3.1.2.6	References	103
3.1.3	Au@Fe ₃ O ₄ Janus type nanoparticles as non-isotropic additives – CaCO ₃ mesocrystal formation with nanoparticle inclusion	107
3.1.3.1	Introduction	108
3.1.3.2	Experimental	110
3.1.3.3	Results & Discussion	114
3.1.3.4	Conclusion	122
3.1.3.5	Supporting Information	123
3.1.3.6	References	137
3.2	Novel THF based (co-)polymers for mineralization	141
3.2.1	Polymer structure influence on calcium carbonate morphology	141
3.2.1.1	Introduction	142
3.2.1.2	Experimental	144
3.2.1.3	Result & Discussion	148
3.2.1.4	Conclusion	158
3.2.1.5	Supporting Information	160
3.2.1.6	References	170
3.3	<i>Bg</i> -AChBP protein isoforms effect on CaCO ₃	176
3.3.1	Effects of <i>Biomphalaria glabrata</i> Acetylcholine-Binding Proteins on CaCO ₃ polymorph selective crystallization	176
3.3.1.1	Introduction	177
3.3.1.2	Experimental	180
3.3.1.3	Results & Discussion	184
3.3.1.4	Conclusion	196

3.3.1.5	Supporting Information	197
3.3.1.6	References	205
3.3.2	<i>Bg</i> -AChBP proteins calcium ion complexation and their effects on CaCO ₃ crystallization	208
3.3.2.1	Introduction	209
3.3.2.2	Experimental	212
3.3.2.3	Results & Discussion	216
3.3.2.4	Conclusion	223
3.3.2.5	Supporting Information	224
3.3.2.6	References	235
4	Conclusion and Outlook	238
5	Declaration for Scientific Contributions	242
5	Authorship Statements	244
5.1	Functionalized nanoparticles as additives in CaCO ₃ crystallization	244
5.2	Novel THF based (co-)polymers for mineralization.....	248
5.3	<i>Bg</i> -AChBP protein effect on CaCO ₃	250
6	Curriculum Vitae	252

1 Introduction

In the recent century the research on composite materials underwent a renaissance due to the development and perspectives of mesocrystals as underlined by the number of publications on the topic composites and mesocrystals shown in Figure 1.1.

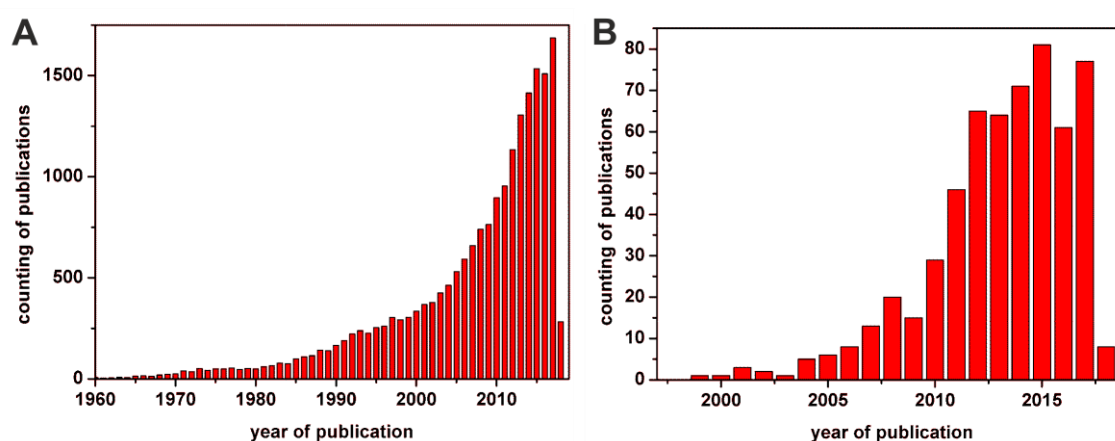


Figure 1.1: Literature analysis: (A) Number of publications on the topics “Composites” and (B) “ Mesocrystals”. Numbers were extracted from searches on www.scifinder.cas.org on 01.07.2018.

But why are these research fields pushed in recent years?

Besides the description of mesocrystal formation in natural materials it is the diversity of possible composites one can formulate via mesocrystal assemblies. As nature genetically controls such assemblies, human beings need to learn from nature's mechanisms to achieve new so called "bio-inspired" composites such as artificial trees, nacre, bone or other extremely tough, flexible materials. Furthermore, mesocrystals can be powerful materials by their possibility of multi-functionality. These materials can be used as novel filler or carrier materials for industrial purposes.

For mineralization studies CaCO_3 is known as the best researched model system. Hence still a lot of unsolved questions especially on interactions of CaCO_3 with

additives need to be answered. This thesis tries to solve a few of these key questions by studying the effects of additives with various functional groups, optical, mechanical properties as well as different polarity. The theoretical background on crystallization and especially non-classical growth is presented in Chapter 2. The results and discussion paragraph 3 is splitted into three main topics of research that have been studied during the last three years.

First the thesis gives an insight to the requirement of carboxylic acid groups mobilized on gold nanoparticles as interacting and stabilizing site to occlude them in mineralizing CaCO_3 . The formed mesocrystals are identified as new composite material with interesting optical properties (see Chapter 2.3.1.1). Besides the well-known gold nanoparticles synthesis a new synthesis approach for the formation of monodisperse dumbbell $\text{Au@Fe}_3\text{O}_4$ Janus particles is presented in Chapter 3.1.1. The synthesis aims to improve the bad reproducibility and dispersity of $\text{Au@Fe}_3\text{O}_4$ nanoparticles to yield larger amounts than usual. The effects of anisotropy of such Janus particles is used to study the formation of mesocrystals with CaCO_3 . In this second part of the work, shown in Chapter 3.1.2, we demonstrate the need of good colloidal stability to be the central challenge for studying. Furthermore, another identification of the epitaxy of CaCO_3 on Au surfaces is conducted.

Besides these rigid inflexible inorganic additives, PolyTHF polyacid copolymers of linear and hyper-branched structural motive are studied for the role of structural effects of non-polar carboxylic acid groups containing copolymers in comparison to previously reported studies (see Chapter 3.2).

As third part of this thesis the function of the isoforms of proteins called Acetylcholine binding proteins (*Bg-AChBP* – claimed to be responsible for controlled shell growth of *Biomphalaria glabrata* snail) are studied. One of the isoforms is identified to have large impact together with magnesium ions on the polymorph that is forming during precipitation (see Chapter 3.3) while the other isoform is identified to have large mineralization scaling effects that might play a role in keeping the "oversaturated" snail body stable against random mineralization of CaCO_3 (compare Chapter 3.3.1.1 for details).

The thesis only presents a shortcut of the large and variable topic of mesocrystal or even composite formation, the work is concluded at the end and the findings are compared to existing literature and interesting ideas and suggestions for future work on CaCO₃ biomineralization are provided.

2 Theoretical background

2.1 Crystallization

According to Ehrenfest, a crystallization is a first order phase transition of a solid material from a supersaturated solution, melt or gas of its building components. ^[1] In general crystallization is split in two main events first the nucleation and second the crystal growth. For both events several classical and non-classical approaches have been conducted during the last two centuries.

2.1.1 Classical Nucleation Theory (CNT)

Each classical crystallization event is induced by a classical nucleation that only occurs if the system overcomes its activation energy barrier (see Figure 2.19 in Chapter 0). It prevents that the system even nucleates at low or zero supersaturation. Interestingly the classical nucleation itself induces heterogeneity into the system by the formation of a second phase. This phase is separated by a new surface which permanently gains surface energy due to its growth. Simultaneously the package density of the formed material gets higher than the density of the surrounding material. This fact causes a loss in bulk free enthalpy due to an increased number of attractive interactions. As shown in Equation 1 CNT phrases homogeneous nucleation by a surface and volume term. The system nucleates if the sum gets negative and the system wins energy by nucleation.

$$\Delta G_{total} = \Delta G_{surface} - \Delta G_{volume} \quad (1)$$

Herein a central need for nucleation is an oversaturated solution of ions (S stands for supersaturation of the solution), which is defined as the fraction of diluted material a and the final equilibrium concentrations of the material in solution a_e .

$$S = \frac{a}{a_e} \quad (2)$$

For a binary system this equation complexifies slightly to a quotient of the activities of the diluted components a and the solubility product K_{SP} of the material.

$$S = \frac{a_{A^+} \cdot a_{B^-}}{K_{SP}} \quad (3)$$

On basis of this simple definition LaMer [2] published its calculations of concentration versus time as observed on the crystallization of sulfur from an oversaturated ethanol solution. From these observations the theory of seed nucleation and growth has been conducted as shown in Figure 2.1.

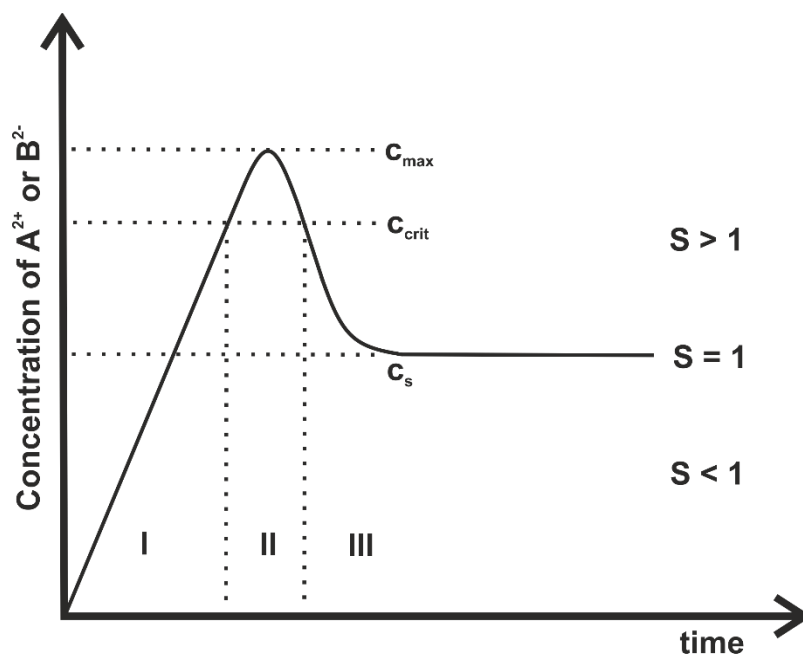


Figure 2.1: LaMer-model of seed nucleation and growth.

During phase (I) the concentration of building blocks in solution increases until the critical concentration is reached. The first saturated solution is correctly already called oversaturated, but nucleation does still not occur. Only if the maximal concentration c_{\max} is reached during phase (II) nucleation from the meta-stable growth solution occurs due to spinodal demixing. The ion concentration starts to sink continuously, due to growth of nuclei. In the following phase (III) c_{crit} is reached again and the saturation of the solution still sinks until it reaches the equilibrium concentration $S = 1$, which is well known as the solubility product of the precipitated solid

phase. During this phase only growth continues and no further nucleation takes place. Over time only Ostwald ripening occurs and smaller crystals dilute for growth of the larger ones. The rate of nucleation during the describe process is defined as the following.

$$R_N = \rho \cdot j \cdot Z \cdot \exp\left(\frac{-\Delta G_c^*}{k_B \cdot T}\right) \quad (4)$$

Herein ρ is the mass density of ions, ΔG_c^* the critical barrier of free Gibbs enthalpy in crystal growth. [3] j is the speed of absorption of building units of the crystal and Z is the so called Zeldovich factor, a correction factor that calculates the ion interactions caused by Brownian motion. In Figure 2.2 the relationship between free Gibbs energy and maximal seed radius is shown.

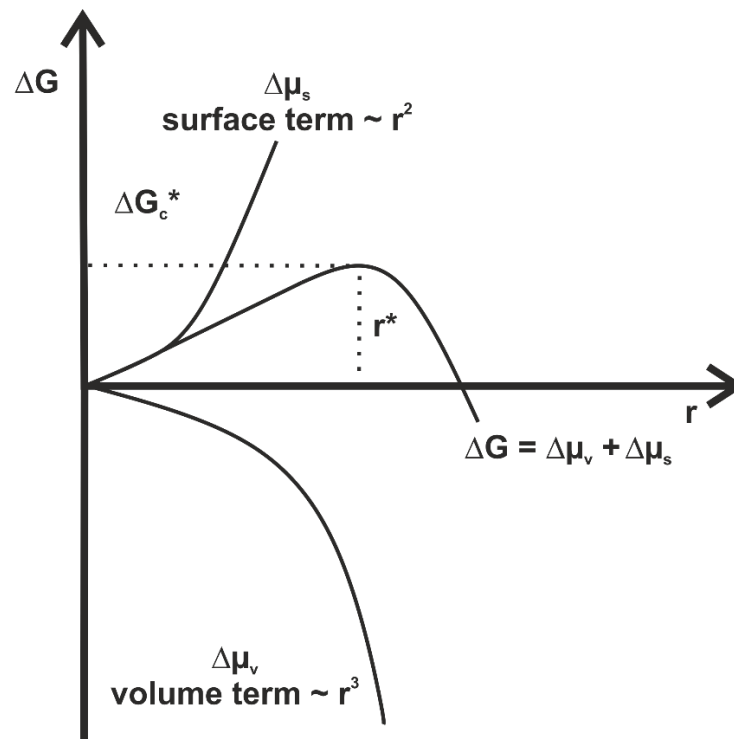


Figure 2.2: Correlation of Gibbs free energy and seed radius.

The maximum of energy for a certain critical radius at a given supersaturation results from the scaling factor difference of the volume term, which scales with r^3 , while the surface term only scales with the square of the radius of the seed. Thus

the radius of the maximum seed size is related to type of system and the saturation of the system shown in Figure 2.3.

$$\Delta G = \Delta\mu_v + \Delta\mu_s = \frac{4}{3}\pi r^3 \Delta G_v + 4\pi r^2 \quad (5)$$

In Equation 5 the origin the sphere typical scaling with surface and volume is calculated. The constant μ_s herein corresponds to the available free energy of a given system surface and μ_v of the same systems volume. For example this value is extremely different in the case of calcite for polar and non-polar facets which gives proof of why calcite is truncated by (104)-facets.

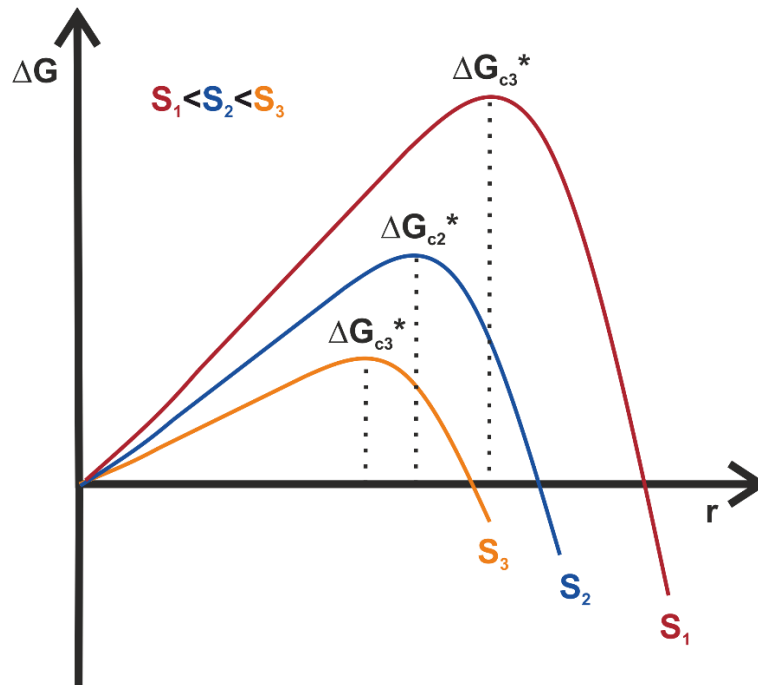


Figure 2.3: Relationship of Gibbs free energy and critical seed radius for different supersaturations.

The maximum of the nuclei radius results from differentiation of Equation 5 (see Equation 6).

$$r^* = \frac{-2\gamma}{\Delta G_v} = \frac{2\gamma V_m}{RT \ln S} \quad (6)$$

The resulting free Gibbs energy of the critical sized nuclei can be calculated by using Equations 5 and 6 as:

$$\Delta G_c^* = \frac{16\gamma^3 V_m^2}{3(RT \ln S)^2} \quad (7)$$

LaMer curves have a maximum at c_{\max} and the growth of the crystals (phase III) starts after the c_{crit} is passed as described above. After the concentration falls beneath the supersaturation, the concentration strives to the equilibrium concentration of growth and dissolution of the crystals, which is called solubility product of the crystal.

2.1.2 Heterogeneous Nucleation

In contrast to homogenous nucleation the heterogeneous case needs a template to proceed. Templates can either be vessel walls, phase boundaries or mobile templates such as polymers, proteins or functionalized nanoparticles. For all these mobile types of additives this thesis describes an example for a rather heterogeneous than homogenous nucleation.

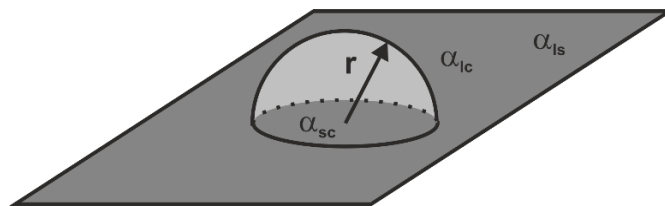


Figure 2.4: Heterogeneous nucleation of a spherical droplet on a flat surface: α_{xy} describes the corresponding surface energy of a boundary of any type. ls = liquid, surface; lc = liquid, crystal; sc = surface, crystal.^[4]

In most cases of a standard lab system one of the above mentioned conditions is present e.g. glass walls or bubbles function as nucleating surfaces. The nucleation of a half sphere on a flat surface can be described as shown in Figure 2.4. This model system can be developed in analogy to the relationship of Gibbs energy for the homogenous case (compare Equations 1-7). The central relation of homogenous and heterogeneous nucleation is implemented by a slight change, compared to Equation 5, in Equation 8.

$$\Delta G = \Delta G_V + \Delta G_S = \frac{1}{2} \cdot \left(\frac{4\pi r^3}{\Sigma} \cdot \Delta G_V \right) + \frac{1}{2} \cdot (4\pi r^2 \alpha_{lc}) + \pi r^2 \alpha_{sc} - \pi r^2 \alpha_{ls} \quad (8)$$

From this equation we get in analogy to the homogenous case the radius r^* of the critical nucleus from heterogeneous nucleation to be:

$$r^* = -\frac{2\Omega\alpha'}{\Delta G_V} \quad (9)$$

Herein Ω is the volume of a seed and α' the respective surface energy.

In Equation 9 slight changes regarding optimized surface energy according to the homogenous case are made.

$$\alpha' = \alpha_{lc} \cdot \left(1 - \frac{\alpha_{ls} - \alpha_{sc}}{2\alpha_{lc}} \right) \quad (10)$$

From Equation 10 one can conduct that, if α_{sc} , the energy between substrate and seed, gets large compared to the surface energy between the nucleating crystal and the surrounding solution (α_{lc}) as well as the energy of the boundary of the substrate and the solution (α_{ls}) the nucleation energy α' reaches its maximum value. This circumstance is especially given if a good structural equality of lattice parameter of the seed and substrate, called "lattice match", is present. The growth process of one substrate on the other caused by a good lattice congruence is called "epitaxial growth". Besides the small lattice mismatch strong coulomb interactions of substrate and seed trigger the epitaxy case as well as contrary charges and weak surface roughness of the substrate. Heterogeneous is favored against homogenous nucleation, if the seed building blocks are tightly binding to the surface of the substrate. Thus the heterogeneous growth of CaCO_3 is likely on carboxylate group carrying surfaces. Nature also uses heterogeneous nucleation by membrane proteins working as nucleation sites for mineral material like bone.

Another typical heterogeneous nucleation is the nucleation and oriented growth of Magnetite on Au. $\text{Au@Fe}_3\text{O}_4$ Janus particles are synthesized by thermal decomposition of an iron oxide precursor under presence of Au nanoparticles. For such an epitaxy a low-energy interface that has a reduced energy compared to homogeneous nucleation is the domain for heterogeneous growth. The central need

therefore is a maximum tolerated lattice misfit of both materials a that is lower than 10 % for ϵ in Equation 11.

$$\epsilon = \frac{a_{\text{phase}} - a_{\text{substrate}}}{a_{\text{substrate}}} \quad (11)$$

Epitaxy is the central effect on templated nucleation of CaCO_3 with additives in Chapters 3.1.1, 3.1.2 and 3.1.3.

The most important point to determine whether a nucleation and growth is either dominated by homogenous or heterogeneous mechanisms is hard to answer. While strong supersaturations compared to the additive concentration favors homogenous nucleation it can also be heterogeneous at some point of supersaturation (importance highlighted with red S in Equation 12), because the rate of heterogeneous growth overtakes the rate for the homogenous case as shown in Equation 12 and illustrated by Figure 2.5 for CaCO_3 .

$$\Delta t_1 \sim \frac{1}{J_{\text{hetero}}} \sim \exp\left(\frac{16\pi\gamma^3\omega^2 S}{3RT(\Delta\mu)^2}\right) \quad (12)$$

But one can doubtless claim that nucleation is never strictly homogenous or heterogeneous due to the large number of influences on the crystallization. Thus a mixtures of morphologies or even polymorphs of CaCO_3 are an example for a typical additive influence.

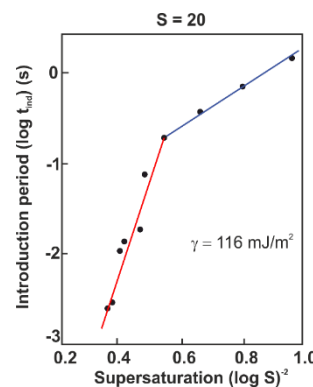


Figure 2.5: Transition from homogenous (red line fit) to heterogeneous nucleation (blue line fit) regime for CaCO_3 at supersaturation $S = 20$ depending both on fraction of final supersaturation and the resulting induction period (both logarithmic scale). Redrawn from data printed in “Crystallization” from J.W. Mullin (ISBN: 978-0-7506-4833-2). [5]

Crystal Growth

Classical growth theories describe the formation of final crystals from nuclei. From the LaMer model this is basically described by phase (III) in Figure 2.1. If the equilibrium concentration, called solubility product of the growing crystal, is reached, growth results from the solution of smaller particles for growth of larger ones (known as Ostwald-ripening). Alongside with the classical approach that is described as an ion by ion attachment non-classical approaches, that are mainly based on pre-clustering and particle mediated attachment of building units are discussed in the following paragraphs.

2.1.3.1 Classical Crystal Growth

The classical approach describes growth as a layer-wise attachment of single ions/molecules as non-dividable building units under ideal conditions to form a crystal surface. In general a mass transfer from the surrounding medium to the crystal is needed for growth. Near the equilibrium the rate of this process is proportional to its driving force. The driving force is described by a gain in chemical potential, which can be influenced by temperature, pressure, concentration, electric or magnetic fields as well as gravity or surface tension. Three different transfer processes are involved in the crystal growth. First the mass transfer in the medium toward a crystal, second the heat transfer caused by crystallization from the crystal surface into the medium and last the mass transfer through the crystal/medium interface. This mass transfer can be described in general as a combined diffusion and interface limited growth from solution.

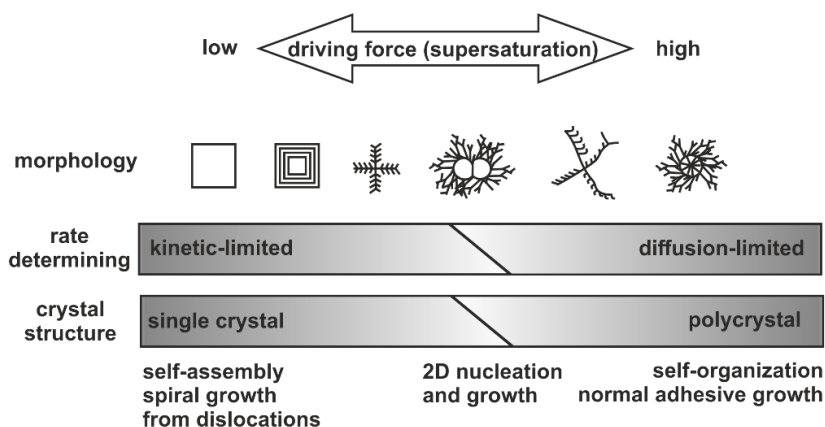


Figure 2.6: Scheme to describe the relationship of driving force, here supersaturation against the resulting crystal morphology, rate determination and overall crystal structure is shown.

A strictly diffusion-controlled process hereby is very rare. The growth regime determines whether single-crystal (kinetic limit) or polycrystals (diffusion limit) are formed. By increasing the supersaturation as driving force the process can become diffusion controlled rather than interface controlled (resulting morphologies are shown Figure 2.6). From this fact one can predict structures for etch pits formation on CaCO_3 as shown in Figure 2.7 a-c.



Figure 2.7: AFM image series of calcite (104) surface under time lapse without additive (a-c) and with Kongo red as additive (d-f). (a-c) Show classical etch pit formation over time while Kongo red terminates the polar step edges and inhibits dissolution of CaCO_3 for growth of etch pits from a supersaturated solution. The figure is reprinted with permission from Langmuir. ^[6]

Thereby thermodynamic control comes into play at very low supersaturation so that the above described rate of crystallization is very low. The surface energy of the facets of a crystal determines the facets growth rate as shown in Figure 2.7 for calcite facets. The lower the surface energy, the faster their growth and thus the lowest energy surfaces are finally the facets that truncate the crystal. As energy correlates with speed of growth the high energy facets are growing slower than the low energy facets and thus in the state of thermodynamic equilibrium the crystals are truncated by slow growing facets. Crystals grown under classical conditions are described by the Wulff construction shown in Figure 2.8 ^[7] which is the graphic construction of the Bravais-Friedel law $V_{hkl} \sim 1/d_{hkl}$. The law states: The larger the inner-planar distance d_{hkl} the smaller the growth rate V_{hkl} or the more pronounced the crystal face.

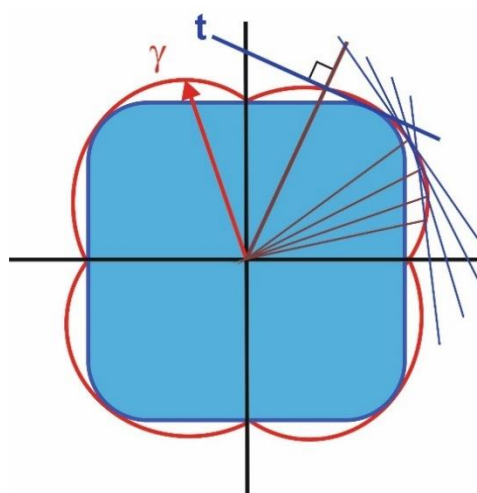


Figure 2.8: Scheme for oriented growth along a specific direction under thermodynamic control (Wulff construction, redrawn from original by Michael Schmid, google.de, image search).

The most prominent approach for a layer-by-layer growth is the Frank-van-der-Merwe growth, or also called normal growth. ^[8] Thereby the formation of a new monolayer occurs from building blocks. Their critical size can be calculated as a heterogeneous nucleation event from ion by ion agglomeration on a surface. So finally the formation is equal to a flat surface adhesion. The more prominent example is shown in Figure 2.9.

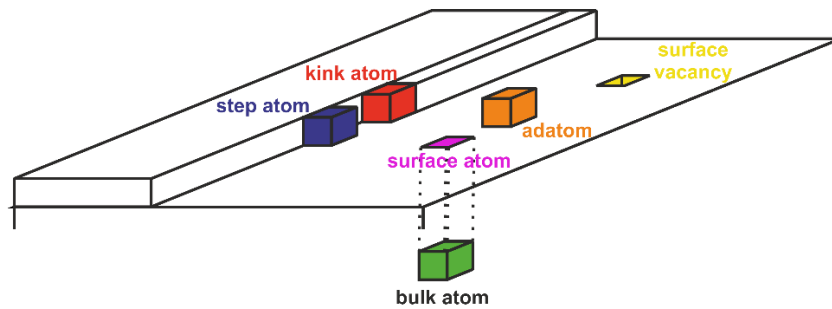


Figure 2.9 Various possibilities for crystal unit attachment on a growing surface of a crystal. Different numbers of next neighbors result from different positions and have a different binding enthalpy.

Especially at elevated temperatures the thermal motion induces surface roughness through formation of kinks to which step atoms can attach by overcoming a lower energy barrier than in the case of adatom attachment. The adatom formation is favored at higher supersaturation as the energy barrier is too high at low supersaturation and can only be reached by additional driving force as high supersaturation. This can induce a two-dimensional nucleation to form etch pits as shown for CaCO_3 in Figure 2.7 (a-c).

Another possible origin of growth is the permanent source of growth steps from screw dislocations as described by the BCF theory (Burton, Cabrera, Frank) shown in Figure 2.10. It basically describes screw dislocations to be favored as growth locations against all other possible growth mechanism.

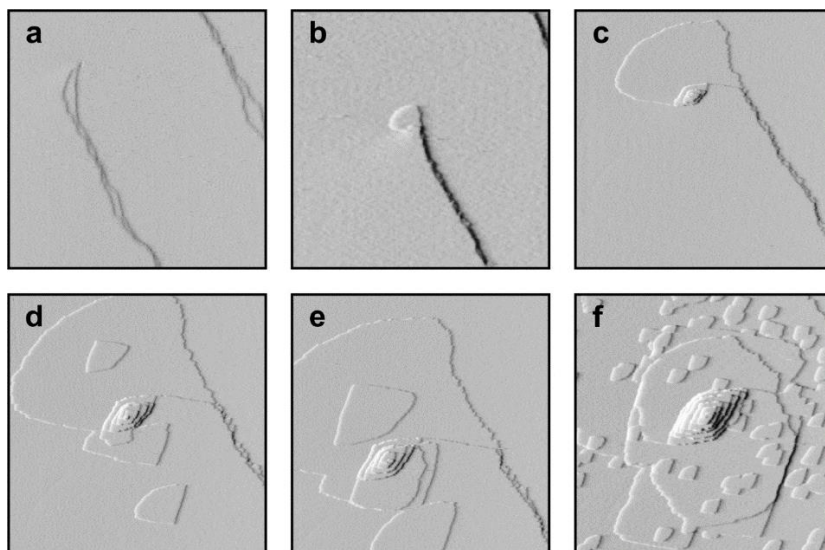


Figure 2.10: AFM image series of BaSO₄ (001)-surface under spiral growth around step displacement from very low supersaturation (a-e) and with fresh injection of extreme supersaturated solution (f) which results in a high rate of island growth. The figure is reprinted with permission from Macmillan Publishers Ltd: Nature copyright 1998. ^[9]

Defects as vacancies or adatoms can also become step sources. Furthermore the formation of twin boundaries, absorption of impurities or even crystal edges can be fast growing areas. Biological environments bear a plethora of crystallization influencing additives. Thus the crystallization is often kinetically controlled in these cases. Classical strictly thermodynamically controlled crystallizations are thus very rare. In the kinetically controlled case the growth rate of the whole crystal is often faster than the growth rate of specific facets. Thus kinetic control hinders the crystal to reach perfect truncation with facets such as the (104) facet of calcite. Sometimes also polymorphism of a given composition comes into play. For example aragonite is the favored stable polymorph in the case of calcium carbonate instead of calcite for kinetically controlled crystallizations. But in general also a plethora of possible morphologies of polymorphs are observed in nature for kinetically controlled crystal growth. The truncation of specific facets for example with polycarboxylates as it occurs in nature is another path to influence morphology of crystals. Ca²⁺ double layer formation, complex formation with additives or addition of foreign ions for influence of lattice parameters are also key influencing factors of the work presented in the following chapters of this thesis.

Effect of impurities on classical growth

First the additive can absorb on a growing kink and block it. This is called Bliznakov-Chernov mechanism and shown in Figure 2.11 (A). The consequences of such absorptions can be morphology changes while kinetics of growth and surface micro-morphology are unaffected. Nonetheless a face selective absorption can totally inhibit growth of facets.

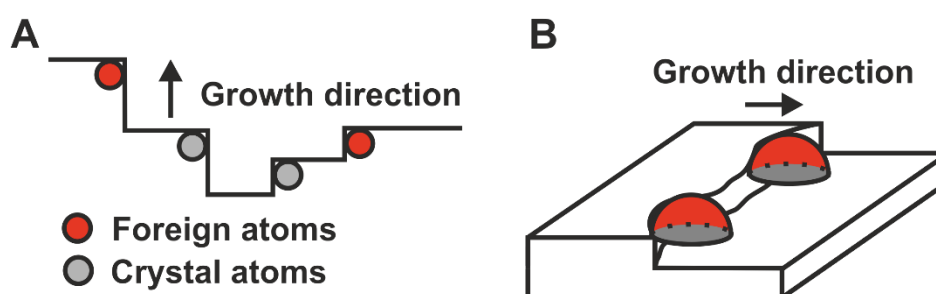


Figure 2.11: Illustration of the Bliznakov-Chernov mechanism (A) and the Cabrera-Vermilyea mechanism (B) for the effect of impurities of kink absorbed foreign atoms (A) and step pinning (B).

The second effect can be a step pinning, the so-called Cabrera-Vermilyea mechanism, that describes binding of an impurity as an inducer of a dead zone and triggers tapering and formation of curved surfaces as shown in Figure 2.11 (B). Additives can be occluded by overgrowth as shown for PAA by de Yoreo *et al.* ^[10]

As already mentioned, occlusion of additives can result in a zoning, sector-zoning or concentrating of additives in twin boundaries or dislocations. This can change the crystals morphology as well as its properties as demonstrated in the results and discussion part of this thesis and by many examples in literature. ^[11–15]

2.1.3.2 Non-classical Crystal Growth – Mesocrystals

Currently the non-classical nucleation approaches are under controversial discussion in literature as findings could also be describable by the classical approach. Although non-classical nucleation is still a discussed field of research the non-classical crystal growth is a central and widely accepted approach that describes findings from natural and synthetic composites. Non-classical growth is based on the formation theory of crystals build of pre-formed complexes, agglomerates or particles. If the final crystal lattice is disturbed by the occlusion of additives or defects (e.g. holes, multiple twinning, nano-crystallinity) under keeping an overall ordered orientation of the crystal building blocks the crystal is called a mesocrystal. If the crystal does no longer have a common axis of orientation of its building blocks it is called a polycrystal as described by Schenk *et al.* (see Figure 2.12 (C)). [16]

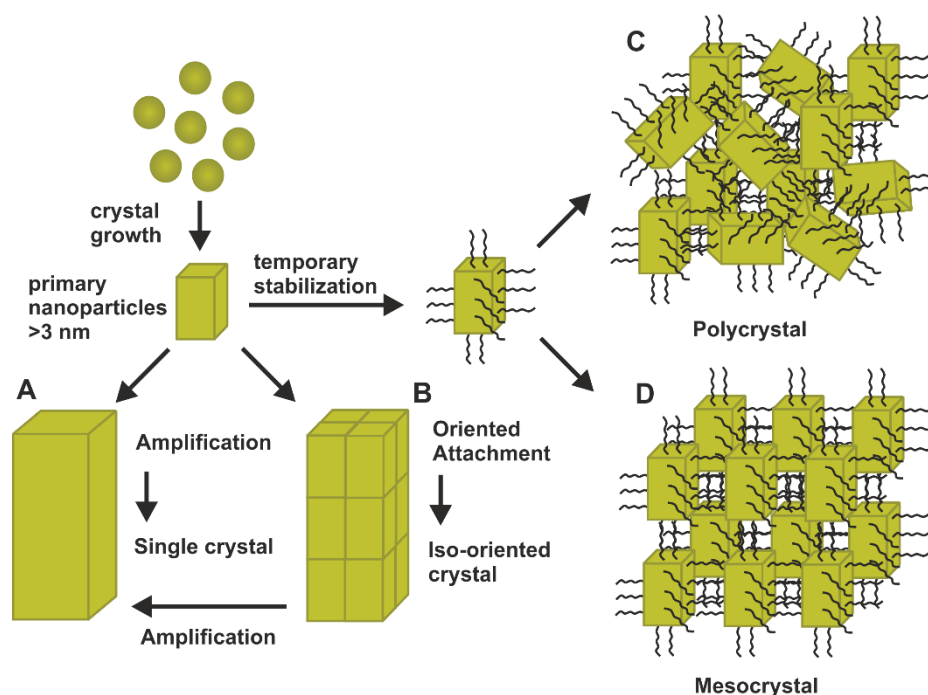


Figure 2.12: Scheme of classical and non-classical crystallization to (A) single crystals (B) oriented crystals of nano-building-blocks (C) polycrystals and (D) mesocrystals. Scheme is adapted from literature. [17]

In the above shown graphic pathway (A) describes the classical way of crystallization starting from small primary nanoparticles as building blocks for ordering and

classical growth which reaches to the formation of a single crystal. If non-classical growth comes into play, two different cases can be distinguished as (B) oriented attachment of primary nanoparticles with a subsequent oriented fusion to an iso-oriented crystal with subdomains which can undergo amplification to become a single crystal over time or temporary stabilization of such building blocks for example by stabilizing molecules. The stabilized nanocrystals can subsequently agglomerate either misoriented to become a polycrystal (C) or oriented along the crystal lattices axis to form a mesocrystal (D).

Another important way to form a crystal is via amorphous, liquid like pre-phases as already discussed in Chapter 2.1.3.1 for CaCO_3 . The Ostwald rule of stages ^[18] gives an explanation why the formation of this phase especially for large supersaturation (easily soluble material) is favored compared to others. That this amorphous species can adapt many different internal and external structures is another way of explanation of mesocrystal formation of complex morphologies as given by Cölfen *et al.* ^[19] The most important point to distinguish between polycrystals and mesocrystals is the common crystallographic orientation of nano-crystal building blocks within mesocrystals which is not the case for polycrystals. There is a plethora of mechanisms that can result in mesocrystal formation. Doubtless there are molecule and substance classes that favor mesocrystals against single or polycrystals assemblies. The most common mechanisms and systems are discussed in the following subparagraphs.

Orientation along organic skeleton

In this mechanism an organic structure defines the space for crystallization. The organic matrix is pre-assembled and thus this mechanism is dynamic in inorganic material transport than the other mechanisms (see Figure 2.13 (A)) The most prominent example is the hierarchical growth of bones nano-sized mineral building blocks of hydroxyapatite as shown in Figure 2.13 (B). Especially for this system the role of collagen fibrils is commonly accepted but still partially bad understood. Wang *et al.* ^[20] have shown that collagen is initiating the crystallization on the one hand but on the other it is also able to orient the precipitated platelets by control of the atomic assembly of hydroxyl apatite nanomaterial.

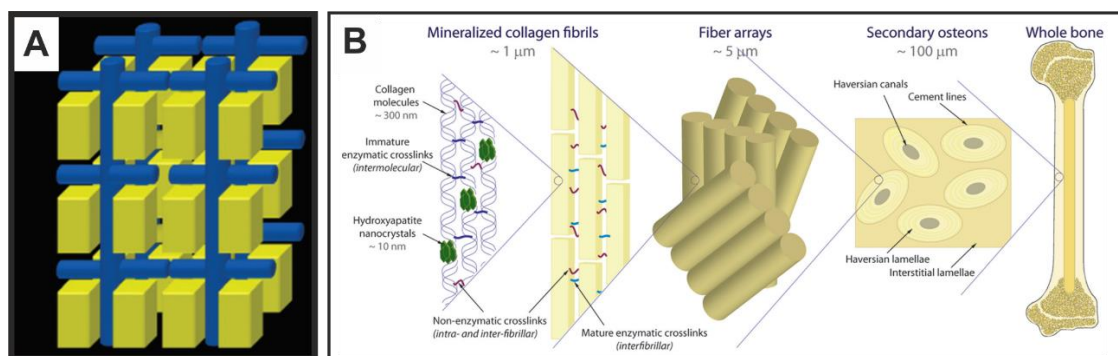


Figure 2.13: Orientation along organic skeleton: (A) Scheme for alignment on organic skeleton. Reprinted with permission. ^[21] Copyright 2016 Wiley-VCH. (B) Scheme on its most prominent example: The hierarchical structure of bone with the oriented alignment of hydroxylapatite nanocrystals. Reprinted with permission. ^[22] Copyright 2017 American Chemical Society.

Alignment by physical forces

An example for the assembly by physical forces is the electrical field assisted alignment of CdSe nanoparticles on a TEM grid is shown in Figure 2.14 (B). The second possible technique to assemble magnetic material is shown in Figure 2.14 (C). By evaporation of solvent on a QCM mesocrystal formation can be monitored by physical parameters.

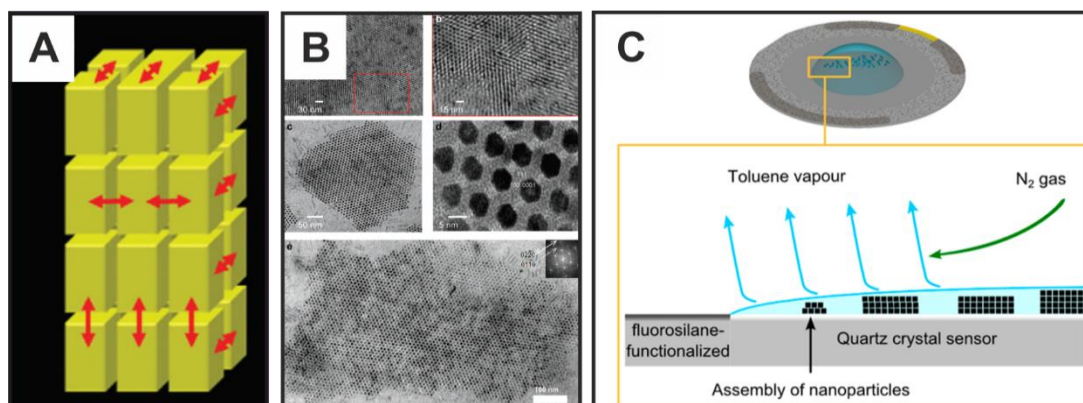


Figure 2.14: Alignment by physical forces: (A) Scheme of physical forces between building blocks of a mesocrystal. Reprinted with permission. ^[21] Copyright 2016 Wiley-VCH. (B) CdSe nanocrystals assembled under application of an electric field perpendicular to the paper plane. Reprinted with permission. ^[23] Copyright 2016 American Chemical Society. (C) Scheme on the assembly of superparamagnetic iron oxide nano-cubes by evaporation with monitored dissipation with a quartz microbalance. Reprinted with permission. ^[24] Copyright 2017 American Chemical Society.

Besides these mechanisms the application of dipole or even within the earth gravitation field can lead the crystal assembly to the wanted pathway to assemble unusual structures under keeping the nanoscale level unchanged. Another not negligible force is the capillary force which can push CaCO_3 into unusual shape to form speculi as published elsewhere. [25]

Epitactic growth by assembly of mineral bridges

Another way of mesocrystal formation is the interaction of nano-sized building-blocks via mineral bridges. This concept first has been found for mother pearl nacre platelets shown in Figure 2.21 (D) in Chapter 0, and furthermore described for the mineral skeleton of sea urchins as shown in Figure 2.15 (B a) and the during egg-shell formation see (B b,c). The description shown in Figure 2.15 (C) explains formation of mineral bridges by a mineralization through a defect within an additive cover of nano-building-blocks wherefrom it penetrates the next additive layer to grow together with a second building block. [26] This mechanism can continue until the polymer layer is either occluded within a mesocrystal or pushed out by further fusion.

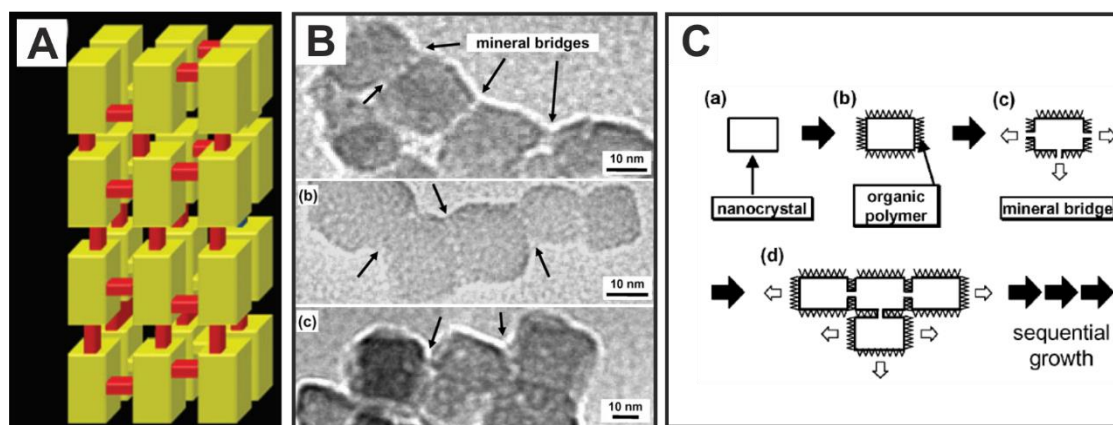


Figure 2.15: Epitactic growth by assembly of organic bridges: (A) Scheme of interaction via mineral bridges (red). Reprinted with permission. [21] Copyright 2016 Wiley-VCH. (B) Example of mineral bridges in a sea urchin (a) and during egg shell formation (b, c). (C) Theoretical mechanism of mineral bridge formation. Both (B) and (C) are reprinted with permission. [26] Copyright 2016 Wiley-VCH.

Assembly within confinement

This theory is based on the central finding that crystalline spherical nanoparticles perform oriented growth within confinement for entropy reasons. Precursor particles are assembled loosely at the beginning of growth but further precipitation within the confinement results in mechanical stress and thus in a constrained orientation as shown with the green crystallite in Figure 2.16.

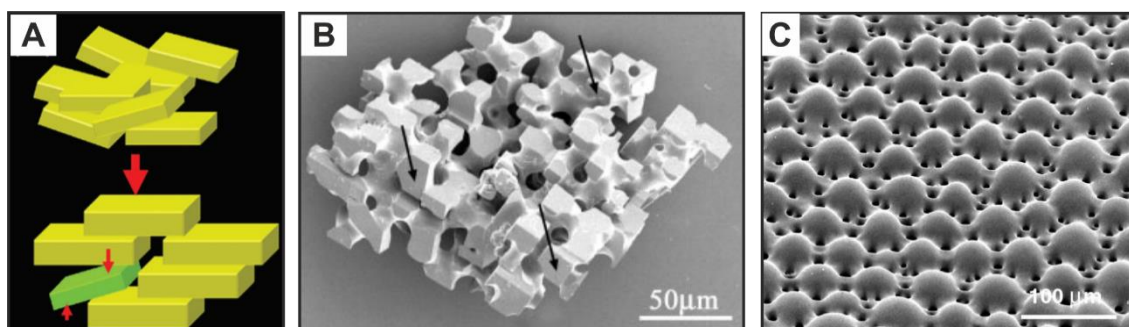


Figure 2.16: Assembly within confinement: (A) Scheme of assembly of a mesocrystal with external constraint. Reprinted with permission. ^[21] Copyright 2016 Wiley-VCH. (B) CaCO₃ precipitated within a polymer membrane. Reprinted with permission. ^[27] Copyright 2016 American Chemical Society. (C) SEM of an microlens array of the dorsal arm plate of the brittlestar *O. wendtii* using calcites birefringance for focusing objects, which is described in Chapter 2.2.4 ^[28] Copyright 2004 RSC Publishing.

Oriented attachment

The basis of this theory has already been described above and is often called Ostwald-ripening. [18] This theory assumes that the growth of larger crystallites from small subunits is accelerated by the gain in surface energy. By lowering distinct surface energies unusual orientations of attachment can be observed.

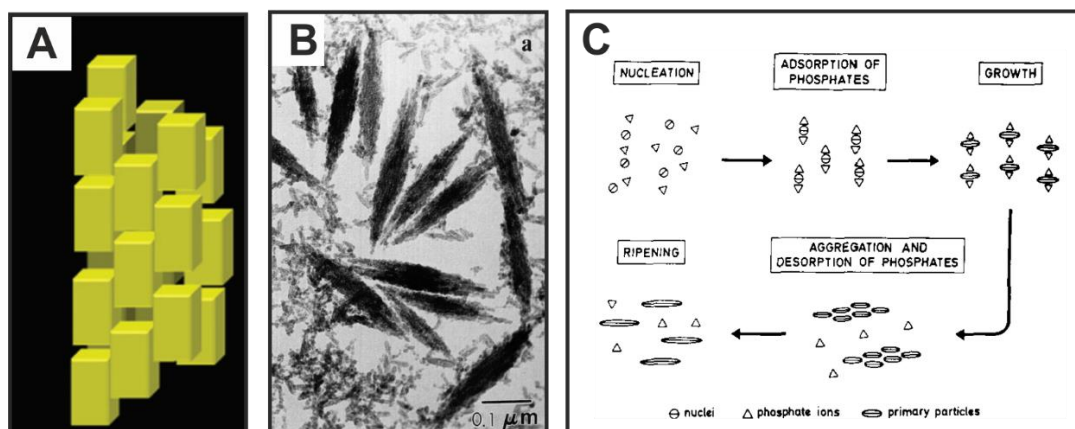


Figure 2.17: Oriented attachment: (A) Scheme of assembly of a crystal building blocks to form a mesocrystal under oriented attachment. Reprinted with permission.[21] Copyright 2016 Wiley-VCH. (B) TEM image of α -Fe₂O₃ nanoparticles that assemble to nano-rice of sub-micrometer size. (C) Mechanism of assembly that describes oriented growth by absorption of phosphate anions on building blocks for truncation of growth facet perpendicular to the growing direction. Both (B) and (C) are reprinted by permission from Macmillan Publishers Ltd: Nature, [29] copyright 1995.

Also assemblies of nano-sized building blocks to mesocrystal structures can be a result thereof and are furthermore driven by a gain in entropy of the solution of particles due to particle attachment. A nice example for such a process is the assembly of α -Fe₂O₃ nanoparticles triggered by phosphate addition to assemble sub-micrometer sized mesocrystal structures, so-called nano-rice (see Figure 2.17).

Orientation by face selective binding of additives

Another method to describe mesocrystal formation is the truncation of specific facets by selectively binding additives. For example the binding of Silicatein- α on nano-size CaCO₃ building blocks and subsequent maturation of about 100 μ m long spicules occurs in a distinct orientation ((100)-direction, see Figure 2.18 (B)). The final spicule waveguides light and is highly flexible for bending. Even relaxation after bending 360° does not break the spicule and it relaxes back to 180° after

bending. The origin of the flexibility is the weak coordination of the silica specialized protein on CaCO_3 building blocks within this brick-mortar structure.

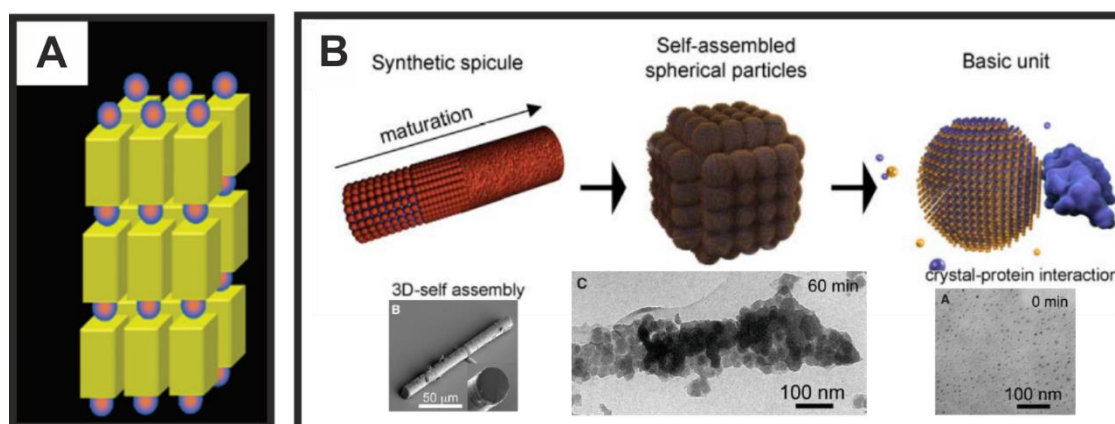


Figure 2.18: Orientation by face selective binding of additives: (A) Scheme for mesocrystal assembly due to molecules face selective binding. Reprinted with permission. ^[21] Copyright 2016 Wiley-VCH. (B) Mechanism of assembly of mesocrystalline calcitic spicule grown along (100)-direction via precipitation of CaCO_3 by desiccator ammonia diffusion method under presence of Silicatein- α Reprinted with permission. ^[15] Copyright 2013 American Association for the Advancement of Science.

For instance crystallization from solution can also have further influencing pathways not shown here, for example magnesium ions are famous to trigger aragonite precipitation by lattice distortion due to incorporation of smaller ions with larger water association and strip-off energy. This also shows the complexity of crystallization with additives, one needs exact knowledge about the added substances such as charge, mass, volume, reactivity and other physical and chemical properties. Hence the coexistence of two or more of the above shown pathways of influence can trigger crystallization into complex assembly cascades with abstract structural results that are challenging to describe. Chapter 3.3.1 describes such a dual mechanism that plays an important role for the formation of the shell of the pondsnail *Biomphalaria glabrata*. Another example for additives with complex influence pathway are nanoparticles added into the CaCO_3 precipitations.

2.2 Calcium carbonate

Three hydrated (monohydrocalcite, ikaite and ACC) and three non-hydrated polymorphs (vaterite, aragonite and calcite) of calcium carbonate are known.

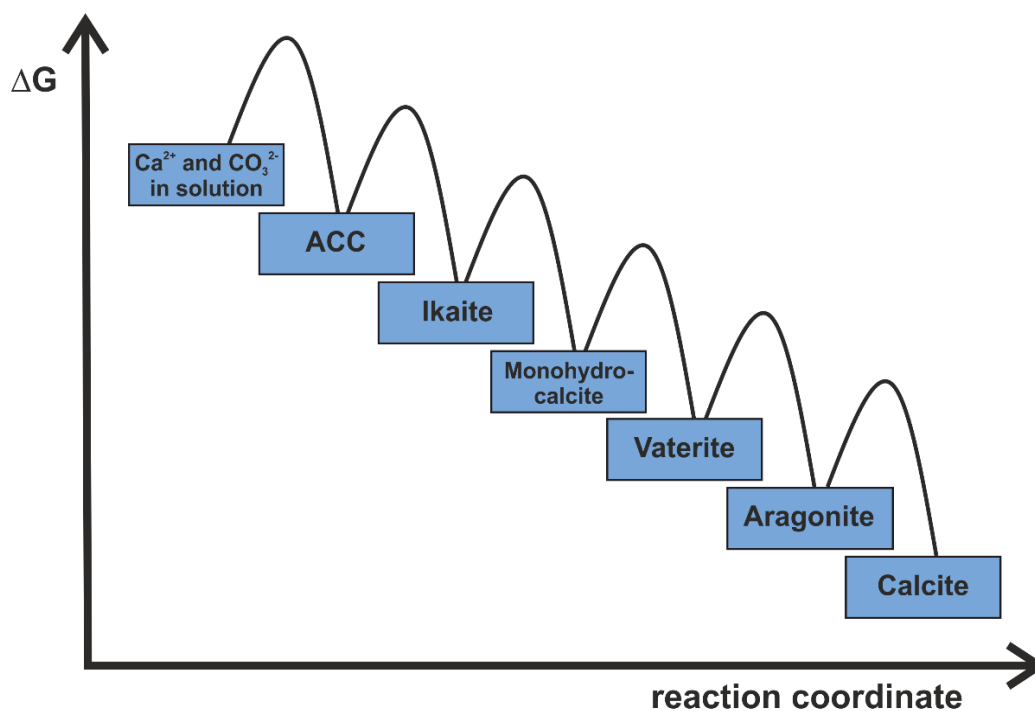


Figure 2.19: Thermodynamic stability of CaCO_3 polymorphs.

Two of the three hydrated phases called monohydrocalcite $^{[30]} \text{CaCO}_3 \cdot \text{H}_2\text{O}$, that crystallizes in symmetry group $P3_121$ in a trigonal unit cell with eightfold coordination of calcium $^{[31,32]}$ and ikaite $\text{CaCO}_3 \cdot 6 \text{H}_2\text{O}$, that crystallizes in space group $C2/c$ in a monoclinic unit cell with eightfold coordination of calcium $^{[33,34]}$ are very rare in nature. As for the structure of ikaite $^{[35-37]}$, monohydrocalcite shows an eightfold coordination of calcium ions, of which some oxygen coordination are direct carbonate oxygen coordination and some to oxygen of water molecules. In monohydrocalcite the eightfold Ca coordination consists of bonding to four neighboring carbonate groups and two water molecules. Two of the carbonate groups are involved in two bonds from Ca to two separate oxygen atoms, and two others are involved in one bond from calcium. The reason for their rarity is that both polymorphs only form under non-ambient conditions (high pressure, low temperatures

or very high supersaturation respectively) and have an extremely good solubility what makes them unstable at ambient conditions. [38–41] Thus these polymorphs are not discussed in closer detail. The relative energy level order of each named species shown in Figure 2.19. Calcite is the thermodynamic stable phase while Aragonite is the kinetic stable phase. Besides these phases also metastable vaterite, ACC or the mentioned phases ikaite and monohydrocalcite can form. [18] But still the main product under thermodynamic optimal conditions is Calcite and mainly the phase shown in the discussion paragraphs of this thesis.

2.2.1 Amorphous CaCO₃

Amorphous CaCO₃ (ACC) is of high interest as metastable precursor phase which is often observed in nature and in laboratory precipitations of CaCO₃. The most relevant precipitation process has been published by Faatz-Wegner in 2004. [42] They report on an industrial relevant process to form synthetic spherical ACC particles from hydrolysis of carbonic esters at extreme basic aqueous conditions. It has been shown in the range of biological relevant temperatures that ACCs has very high solubility and crystallization to vaterite is induced within minutes and subsequent transformation to calcite within hours due to a solution-reassembling process. [43] Thus the key point for investigations on ACC is to keep ACC stable within the time of measurement to study its structure. This is mostly facilitated by additives or precipitation routes in anhydrous environment as published by Cölfen *et al.* [44] They used ammonia diffusion method into a solution of CaCl₂ in ethanol to enrich CaCO₃ and separate it from a faded solution of about 50 nm large particles. Another route is the addition of polymer additives that hinder dissolution and recrystallization and restrict ion mobility in the ACC that is needed for transformation to crystalline phase. The phase one precipitates with this process is formerly known as PILP phase of calcium carbonate. [45] Besides this phase that stands in strong conformational relationship to ACC another name was called for the structure. DOLLOPs, written dynamically ordered liquid-like oxyanion polymer, were investigated by calculations of Gale *et al.* in 2012 and popped up the question about the number of existing amorphous species. [46] As long as non-classical nucleation

pathways are still under controversial discussion in literature [47,48] to be also describable with classical approaches this chapter stops discussing in to close detail because there is no need of discussion for the goals of this thesis.

2.2.2 Vaterite

Vaterite as thermodynamically metastable non-hydrated form is very rare as biomineral in sediments because of its thermodynamic instability against reordering and phase transformation.

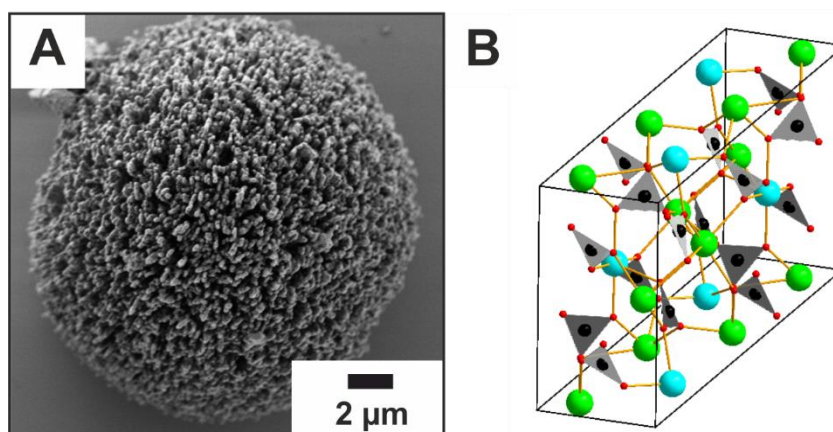


Figure 2.20: Vaterite: (A) SEM snapshot of a classical vaterite crystal. (B) Unit cell of Kolb *et al.* TEM reconstructed structure with two different coordination environments for calcium ions. Black: Carbon, Red: Oxygen, Green: Calcium position 1, Blue: Calcium position 2. [49]

According to the beforehand described Ostwald rule for transformation processes, vaterite is formed as intermediate phase and plays an important role as inorganic/organic hybrid material as it will be described in the discussion part. Vaterite usually forms spherical flower like structures as shown in Figure 2.20 (A). The complexity of coordination environments results in the huge number of nano-domains such a crystal usually forms, which makes structural research on this biomineral highly complex. Nowadays two general structural solutions from electron diffraction are published by Kolb *et al.* [49] and Pokroy *et al.* [50] Kolb *et al.* overcame the problem of nano-crystallinity by ADT of a 50 nm crystal. The resulting crystal structure is shown in Figure 2.20 (B) and the calculated parameters for the unit cell, solubility, and density are shown in Table 2.1.

Table 2.1: Crystallographic data of vaterite. [49,51]

<i>Space group</i>	<i>C2/c (15), monoclinic, Z = 12</i>
Lattice parameters	$a = 12.41 \text{ \AA}, b = 7.14 \text{ \AA}, c = 9.41 \text{ \AA}, \beta = 115.85^\circ$
ρ	2.66 g/cm^{-3}
$K_L^{25^\circ\text{C}}$	$3.31 \cdot 10^{-9} \text{ mol}^2/\text{L}^2$

A hexagonal coordination of calcium ions by bridging carbonate ions results in total coordination number eight for each calcium atom. In contrast to the more stable Calcite and Aragonite modifications the vaterite lattice has higher calcium atom coordination numbers and two different coordination environments of carbonate sub-lattices which result in split modes in Raman- and IR-spectroscopy.

2.2.3 Aragonite

The coordination of calcium ions in aragonite is a ninefold coordination of carbonate oxygen atoms to form an orthorhombic crystal as shown in Figure 2.21 (A) with in Table 2.2 shown physical parameters.

Table 2.2: Crystallographic data of aragonite. [49,51]

Space group	<i>Pmcn</i> (62) orthorhombic, $Z = 4$
Lattice parameters	$a = 4.96 \text{ \AA}$, $b = 7.97 \text{ \AA}$, $c = 5.74 \text{ \AA}$
ρ	2.93 g/cm^{-3}
$K_L^{25^\circ\text{C}}$	$4.57 \cdot 10^{-9} \text{ mol}^2/\text{L}^2$

Synthetically aragonite can form under increased temperature [52] or under presence of foreign bivalent ions as Fe^{2+} or Mg^{2+} ions which is one central aspect in the discussion on the precipitation of described bundles of aragonite in *Biomphalaria glabrata* as shown in Figure 2.21 (C) and discussed in paragraph 3.3.1.

This polymorph of CaCO_3 is mostly precipitating in bundles as shown in Figure 2.21 (B) in the lab which differs from the most relevant biomineral structure of this modification, nacre, wherein it forms dense platelets of 500 nm thickness that are stacked over edge and glued with a biopolymer mixture to one another which gives extreme fracture toughness (see Figure 2.21 (D)). [53]

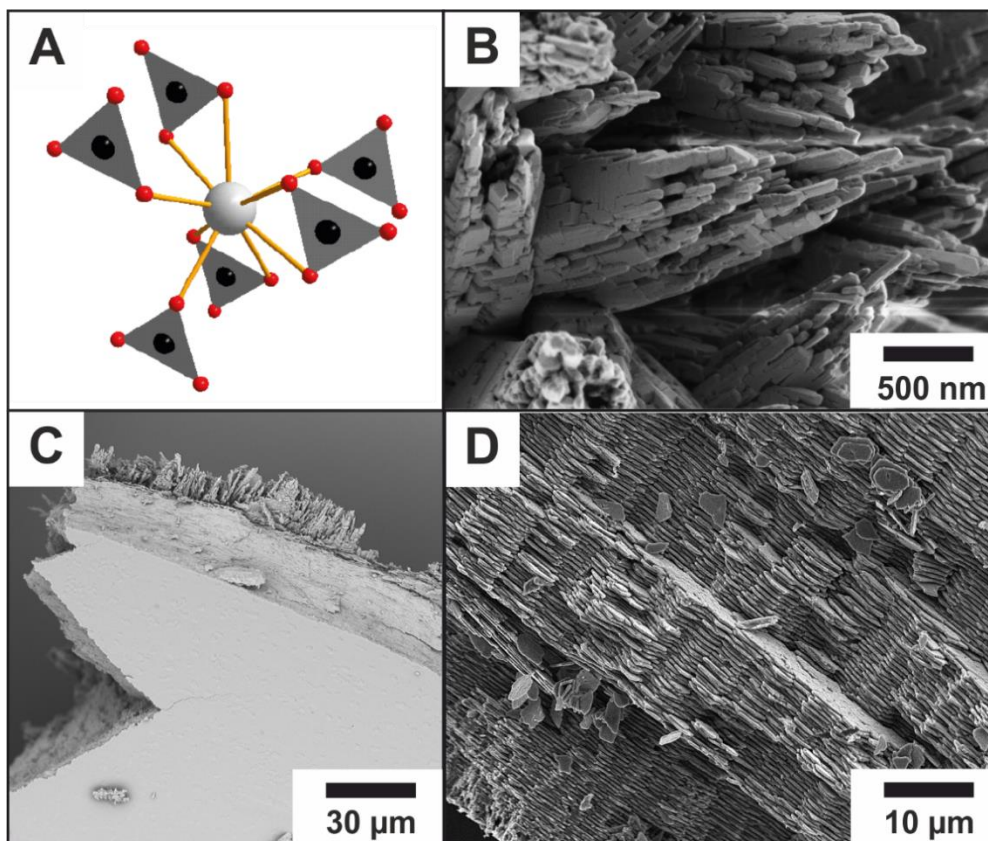


Figure 2.21: Aragonite: (A) Coordination sphere of a single calcium atom in aragonite structure Black: Carbon, Red: Oxygen, Grey: Calcium. (B) Aragonite bundle as usual structure of crystalline material from synthesis. (C) SEM image from snail shell of *Biomphalaria glabrata* showing 90° crossed bundles of aragonite as building units (D) SEM micrograph of a part of the nacre layer of *Leymeriella*, a Lower Cretaceous (Albian) ammonite, showing the typical stacks of tabular hexagonal crystals (Image taken by Dr. René Hoffmann).

2.2.4 Calcite

Calcite is the thermodynamically stable polymorph of calcium carbonate and crystallizes in the diagonal-scalenohedric crystal class $\bar{3}2/m$ with a sixfold coordination of each calcium ion by oxygen atoms as shown in Figure 2.22 and has the following properties (see Table 2.3).

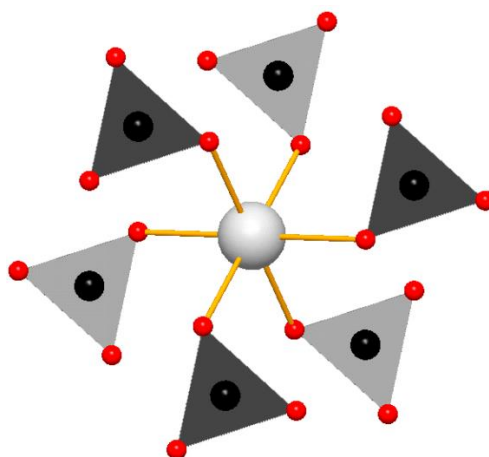


Figure 2.22: Coordination sphere of a calcium ion within calcite lattice with sixfold geometry caused by carbonate ion coordination. Black: Carbon, Red: Oxygen, Grey: Calcium

Table 2.3: Crystallographic data of calcite. ^[51,54]

<i>Space group</i>	<i>R3-c (167), trigonal, Z = 6</i>
Lattice parameters	$a, b = 4.99 \text{ \AA}, c = 17.06 \text{ \AA}, \beta = 102^\circ$
ρ	2.72 g/cm^{-3}
$K_L^{25^\circ\text{C}}$	$3.31 \cdot 10^{-9} \text{ mol}^2/\text{L}^2$

These usually rhombohedral shaped crystals shown in Figure 2.23 (A) are truncated by the (104)-lattice plane which is over all neutral and thus lowest in surface energy and thus slowest growth layer. In Figure 2.23 (C) the (010)-lattice plane is shown as an example for a polar lattice plane within the calcite lattice due to its truncation with calcium and carbon atoms of carbonate groups pointing out of plane. Figure 2.23 (D) shows the most relevant polar facet for binding of negative charged additives, the (001)-lattice plane. Its high polarity results in strong interactions with anionic additives which often results in elongation along the c-axis which is perpendicular to the (001)-layer.

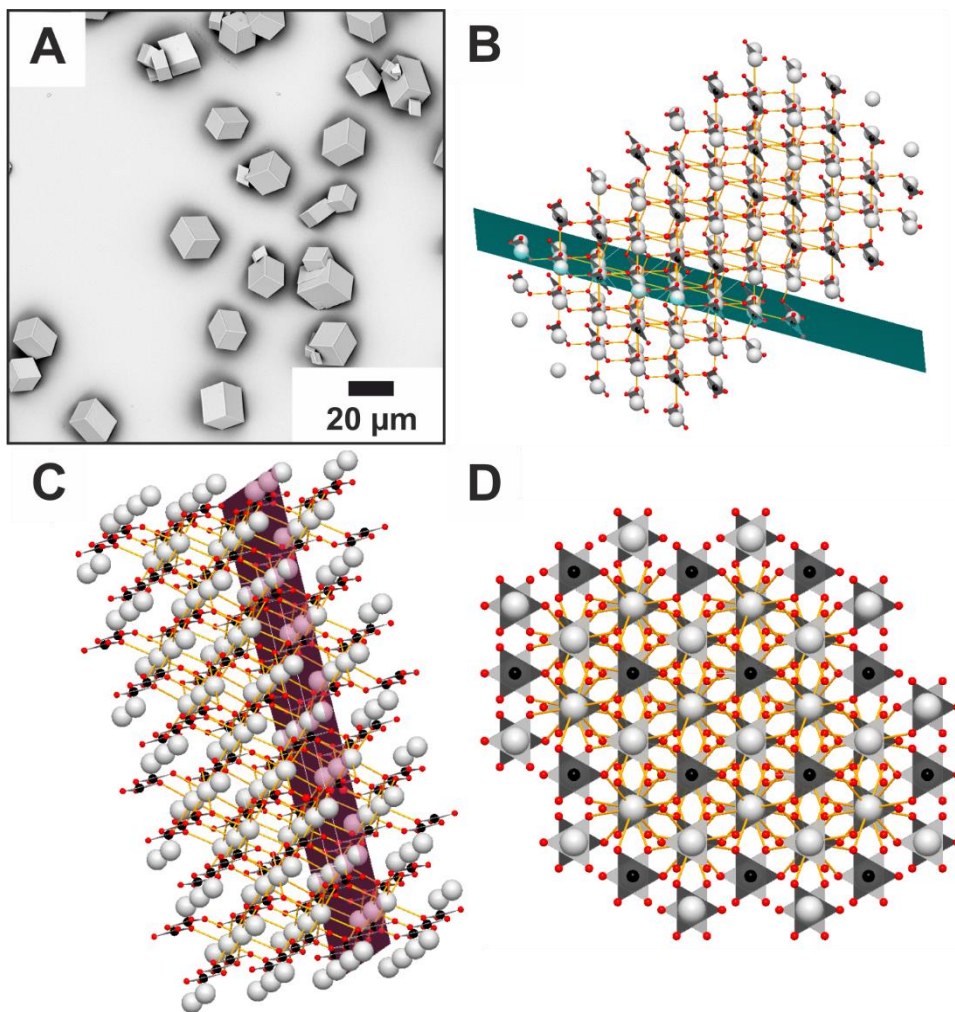


Figure 2.23: Calcite: (A) SEM image of classical rhombohedra of calcite. (B) Calcite lattice with an exemplary $\{104\}$ facet in green. Black: Carbon, Red: Oxygen, Grey: Calcium for all structures (C) $\{010\}$ facet colored in magenta showing calcium and carbon atoms of carbonate groups on their surface. (D) Assembly of atoms on $\{001\}$ -layer of calcite with the view along c -axis (plane is not colored) showing undersaturated calcium ions on its surface.

Another important property of calcite is its birefringence that is caused by two different refractive indices one perpendicular to the mentioned c -axis and one parallel to this axis. ^[55] Calcite has the lowest solubility in aqueous media and also the highest density of all polymorphs. Thus it can happen that during transformation from amorphous to crystalline material holes form inside the crystal. This, so-called Kirkendall effect, forms holes due to densification for example by crystallization of amorphous to crystalline phase of a crystal of constant volume. ^[56]

2.3 Additives for Crystallization

2.3.1 Nanoparticle

In general nanoparticles are defined as all particles within the size range from 1 to 100 nm. ^[57] The truncation of this definition is basically due to the extraordinary properties of many materials in comparison to bulk material, which is also called size quantification effect (e.g. optical properties of conducting metal particles). Nanoparticles show often more pronounced heterogenic catalytic activity compared to bulk material due to their much larger relative surface. ^[58] Furthermore nanoparticles can be synthesized as a custom toolbox for drug delivery and tumor therapy ^[59,60] as well as environmental chemistry purposes. ^[61] For synthesis of such materials there are two general mechanisms possible: First bottom-up from the basis of a precursor and second the top-down method from bulk material to nanometer sized particles by physical treatment such as grinding. Either solvo-thermal, micro-emulsion, direct precipitation or sol-gel-synthesis as bottom-up approaches are methods of choice for good particle monodispersity and distinct morphology. Hence a basic disadvantage of the bottom-up approaches is the relatively small yield of each synthesis. To reach satisfying yields continuous synthesis approaches (e.g. microfluidic) are needed to overcome polydispersity issues due to bad reproducibility in batchwise synthesis. In the following paragraphs basically the non-continuous decomposition method starting from a precursor solution is presented.

2.3.1.1 Au-Nanoparticles

Already the Romans have used colloidal gold particles for coloring of cups during the fourth century after Christ. Sure it was unclear which great potential colloidal gold particles will have nowadays. So as the beginning of scientific research on synthetic and physical chemistry of Au nanoparticles the work of Michael Faraday in 1856 can be seen. [62,63] besides this work also Mie described the origin of plasmonic activity and its significance for research. The smart approaches within the last centuries are that plasmon resonance can be tuned by surface functionalization [63] for example with small molecules [64] as well as size [64–69], shape [64,70–72] and assembly to [73–76] resonance relationships demonstrated for gold nanoparticles. The synthesis and growth of Au nanoparticles can be described by the LaMer model for homogenous nucleation as described in Chapter 2.1.1. Caused by different timing due to different nucleation temperature one can control the size of the final nanoparticles in organic solution as described by Peng *et al.* and shown in Figure 2.24. [77]

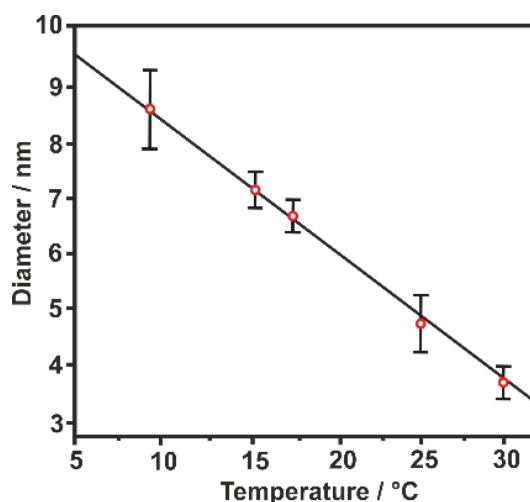


Figure 2.24: Graphic of relationship between reaction temperature and nanoparticle diameter. Redrawn from literature. [77]

The size depended properties caused by the size-quantification effect as for example shown for the plasmonic activity of Au nanoparticles in the wavelength range

of visible light which results in the reddish to purple color of the particle dispersions in Figure 2.25. [78]



Figure 2.25: Plasmon absorption shift of Au nanoparticles f.l.t.r. up to 20 nm diameter. Image Source: Sigma Aldrich Webpage February 2015.

Gold nanoparticles are still *en vogue* systems due to their extraordinary surface chemistry [58] easy signal transduction due to electrical conductivity and cooperative behavior of conduction electrons with other (semi-)conductors [79–81] and their large polarizability of optical frequencies caused by the excitation of the surface plasmon. [82] Especially the knowledge of HSAB concept for functionalization with small and described influences on the particles optical properties make gold nanoparticles an often used optical and spectroscopic sensor in science. [83–86] Thus the easy optical detectability via dark field and UV-Vis spectroscopy so either using Au nanoparticles emission or absorption properties is an often used Au nanoparticle property [87–92] Furthermore X-ray diffraction and scattering (XRD, SAXS, WAXS) can easily facilitated with these particles due to their large X-Ray scattering cross-section. The synthesis of spherical gold nanoparticles usually starts from auric acid that is either reduced in aqueous medium by the famous citrate route [93–95] or via using strong reducing borane complexes in organic solvents. [77] Instead of the mentioned temperature control during nucleation of gold nanoparticles, which often results in polydispersity, an increase in diameter of such small gold nanoparticles is managed by further thermal decomposition of HAuCl_4 under presence of oleylamine as capping and reducing agent. [96] This approach yields nice monodisperse particles but small overall reaction yields which is a key capability for the following Chapter on $\text{Au}@\text{Fe}_3\text{O}_4$ Janus particles.

2.3.1.2 Au@Fe₃O₄ Janus Particles

The synthesis of Janus particles with a single Au and Fe₃O₄ domain can be described as a preliminary heterogeneous overgrowth of (111)-truncated gold seeds with more gold to increase the gold domain size and a subsequent heterogeneous growth of a single Fe₃O₄ (magnetite) domain. The counting of domains of Fe₃O₄ is mainly influenced by the solvent polarity and the amounts of oleic acid and oleylamine during the thermal decomposition of an iron oxide precursor as iron oleate, iron pentacarbonyl or iron acetylacetonate.

Generally the single domain growth occurs between magnetite (220) and the gold (111) lattice-plane by heteroepitactic growth. In recent years such heterodimer particles gain increasing attention due to their extraordinary combination of optical and magnetic properties under simultaneous existence of different surfacial properties due to the different oxyphilicity of the particles domains. Thus a plethora of possible structure-property relationships that even can be used for complicating functionalization combinations have been explored in history.^[96–101] But the synthesis of such particles needed a lot of synthesis development research to control the reaction which is facilitated between kinetic and thermodynamic control. Thus heterodimers^[97,101,102] can be synthesized by right mixing and temperature control as well as solution polarity and precursor supersaturation instead of tri- or tetramers or even flower like particles with multiple Fe₃O₄ domains.^[101] Therefore atomic diffusion and interactions as well as surface reactivity are mainly controlled by the addition of the right amount of oleylamine and oleic acid as key parameters of synthesis control.

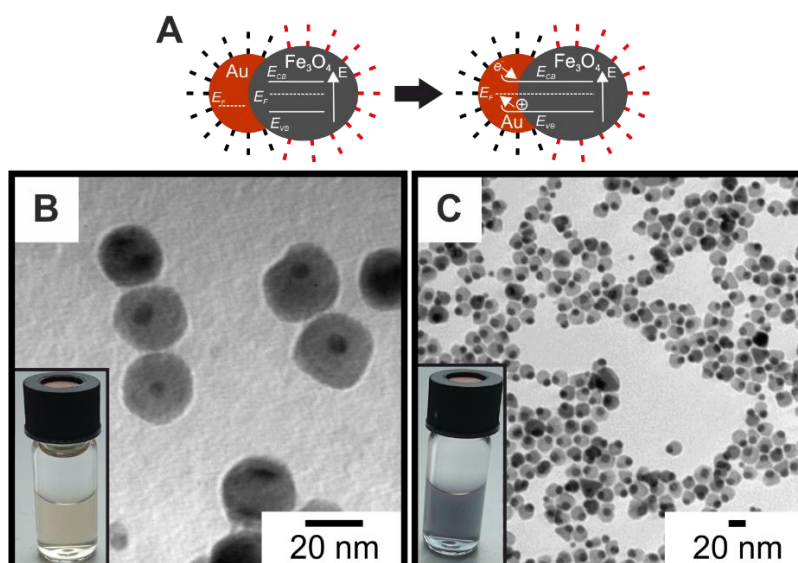


Figure 2.26: Au@Fe₃O₄ Janus particles: (A) Electronic influence of the contact of Fe₃O₄ and Au domain within Au@Fe₃O₄ Janus particles. Fermi level gets equalized due to charge carrier transport between Au as metal and Fe₃O₄ as semiconductor with a 0.14 eV band gap. Resulting color of Janus particles with small gold domain (B) and large gold domain (C).

One can simply use small Au nanoparticles as seeds to synthesize brownish non-plasmon-active Au@Fe₃O₄ Janus particles shown in Figure 2.26 (B). The reason of missing plasmon activity is the charge carrier flux of almost all free oscillating electrons from the metal Au domain to the semi-conducting Fe₃O₄ domain through the heteroepitactic contact plane. This effect, called Schottky barrier as schematically presented in Figure 2.26 (A) and reported in literature ^[103], is much weaker in the case of using large (above 8 nm in diameter) Au nanoparticles to grow Fe₃O₄ on as a large number of charge carriers remains on the gold domain where they oscillate and cause the greyish color of the nanoparticles (see Figure 2.26 (C)). Particle and their functionalization and inter-particle interaction detection gets much easier for this case due to the plasmon activity these particles still show. The synthesis of reproducible large amounts of equally sized Janus particles is essential for the use of such particles as additives for the formation of composites with extraordinary optical and magnetic properties or to study the surface functionalization effects on CaCO₃ crystallization as they will be studied in Chapter 3.1.3. This motivated the development of a seed mediated one pot synthesis with small waste

of particles due to intermediate cleaning steps and good reproducible monodispersity.

2.3.1.3 Functionalization of Nanoparticles

As already mentioned the Au as well as the Au@Fe₃O₄ Janus particles need to be functionalized with so called self-assembled monolayers (SAM) of CaCO₃ interacting molecules or even molecules that ensure good solubility in water. From organic synthesis the particles both bear a self-assembled mono- or even multilayer of Oam and/or Oac respectively. ^[104] This needs to be retarded and the blank surfaces need to be functionalized with the liked molecules mostly thiol containing ones for Au and catechol or carboxylic acid containing ones for the Fe₃O₄ domain. The total detachment of ligand and surface is unfortunately impossible due to immediate Ostwald ripening occurring especially for Au particles causing unwanted shape and size changes. The surface chemistry in general is based on the famous HSAB concept and the oxyphilia or oxophobia of the domains ensures orthogonal functionalization to become possible. ^[105] To get good water solubility, often silica in combination with silano-PEG coverage is used to make oxides water soluble. As long as this results in no direct contact of the precipitating CaCO₃ and the magnetite domain, which is liked to be studied, in this thesis simple carboxylic acids and catechol chemistry is used to functionalize the Fe₃O₄ domain to get water solubility. ^[59,106] The gold domain has also been functionalized by using the described thiophily of the Au domain with different functional molecules to study the need of carboxyl termination of gold particles and Janus particles for interaction with CaCO₃. This step has been facilitated first for the Janus particle Au@Fe₃O₄ and second the Fe₃O₄ domain has been functionalized. The toolbox of particles that are studied in Chapters 3.1.1 and 3.1.3 for Au and Janus particles respectively, are shown in Figure 2.27.

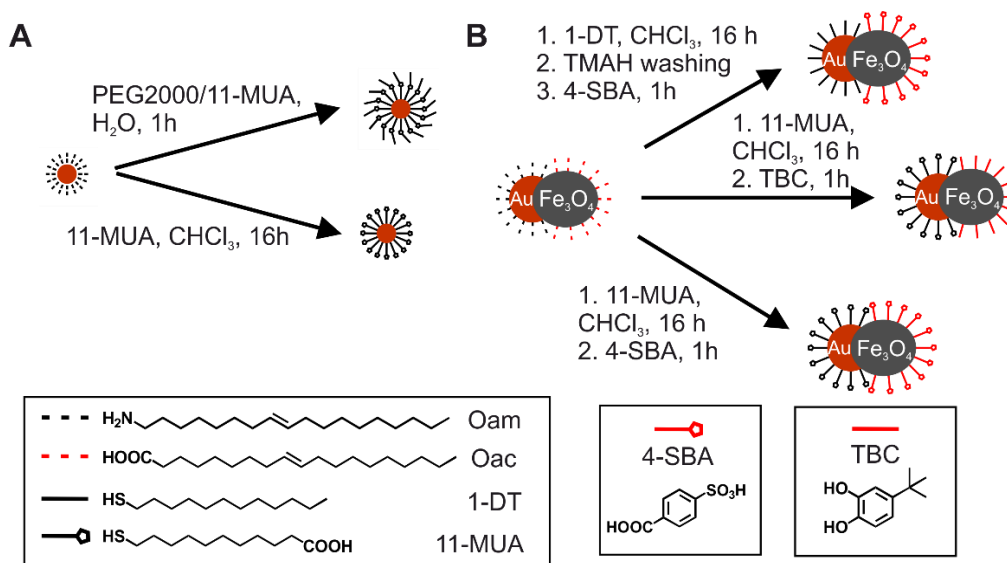


Figure 2.27: Functionalization of nanoparticles of this thesis: (A) Representation of gold nanoparticles functionalized with 11-MUA or PEG2000/11-MUA to study effect of carboxylic acid group on the interaction with CaCO_3 and (B) Tool box of $\text{Au}@Fe_3O_4$ Janus particles to study for the effects of anisotropy and general functionalization pattern on different domains of the integration of particles into CaCO_3 .

2.3.2 Polymers

Polymers as large molecules synthesized from monomer units with a plethora of different possible solubility, functional groups and physical properties are a good toolbox to study their structural as well as functional effects on CaCO_3 crystallization. For sure all these examples show an effect of adding a polymer during precipitation, but the mostly used interaction of polymer and CaCO_3 is the fabrication of blends with non-polar polymers without functional groups such as PP, PE or PVC. Therein CaCO_3 works as filler material to stiff the polymer framework by enlarging the shear viscosity of the plastic material. For example PE and PP filled with CaCO_3 is used as packing plastic and PVC filled with CaCO_3 is used to fabricate tough window frames by superposition of expensive polymer by cheap mineral filler. ^[107]

Polymers are such prominent additive because of their scale inhibition properties on CaCO_3 crystal growth by strong calcium binding and lowering of supersaturation in aqueous solutions. In combination with other anionic additives in an acidic pH

moeity anionic polymers such as PAA have been used as detergents for cleaning solutions. [108] Even block-copolymers such as PAA-PAMPS have recently been identified by the group of Tremel *et al.* to have more efficient scale inhibiting properties than neat PAA polymers due to effective calcium ion complexation as shown by DLS and crystallization experiments in Figure 2.28. [41]

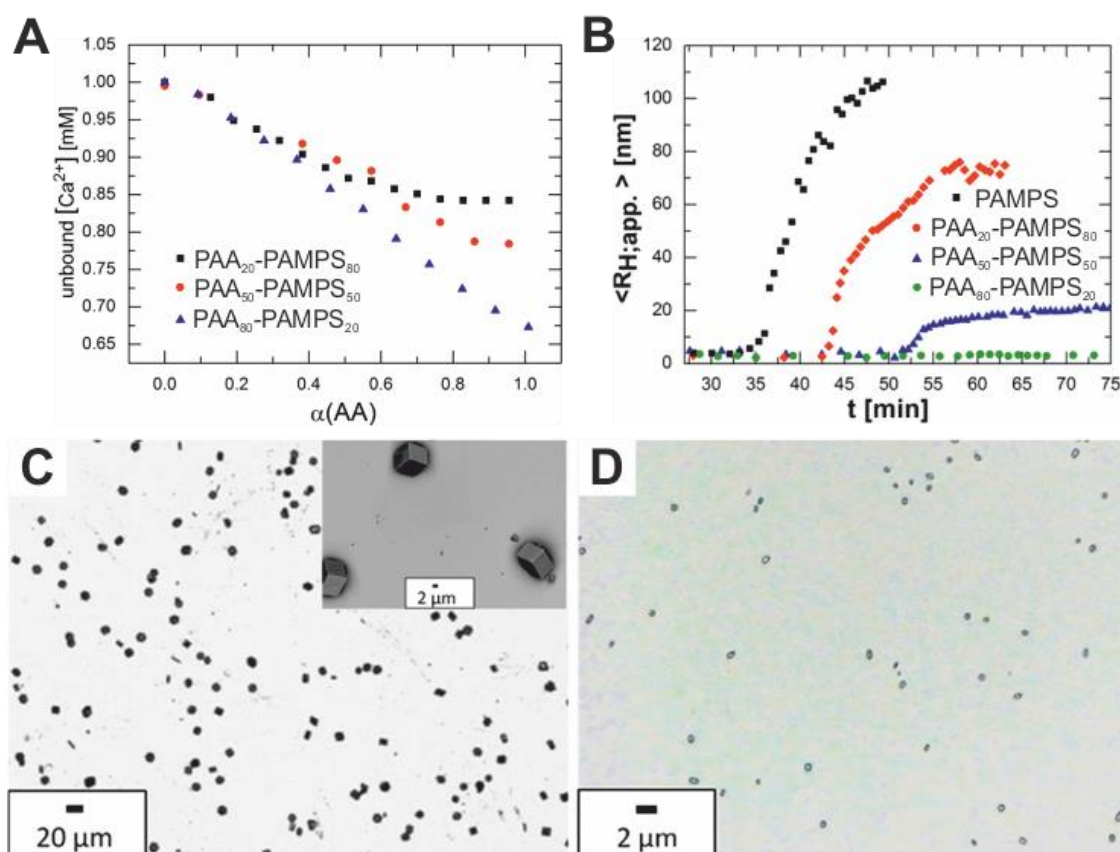


Figure 2.28: PAA-PAMPS as additive for scale inhibition: (A) Degree of complexation of acidic groups of PAA-PAMPS polymers of various relative amounts of AA and AMPS monomers in relation to the degree of dissociation. (B) The apparent hydrodynamic radius evolution of precipitating CaCO₃ in a desiccator experiment from PAA-PAMPS polymer of various relative PAA and PAMPS amounts. (C) Light microscopy image of CaCO₃ precipitated without polymer addition and (D) with addition of 5 mM PAA₈₀PAMPS₂₀ to 10 mM CaCl₂ solution in ammonia carbonate method precipitation. Both samples were taken after 1 h. Reprinted with permission. [41] Copyright 2013 American Chemical Society.

While these examples show the variety of possible influences on CaCO₃ precipitation, the effect of linear PEG has only been studied by the addition of PEG 6000 on the thermal decomposition of Ca(HCO₃)₂. The resulting polymorphs from this method usually are a diverse mixture of small amounts of aragonite and large

amounts of both vaterite and calcite. By addition of the PEG polymer the polymorph aragonite was found to be favored against calcite. ^[109] Hence the main reason for Aragonite formation in this work is the increased synthesis temperature.

Besides the research on these linear polymers, which is still not completed, the effect of hyper-branched polyglycerol polyacids has given surprising results both in solution and immobilized as a SAM on a gold surface. As polyglycerol is less good in binding calcium and thus less effective in scale inhibition, it shows pronounced face selective binding affinity from solution, which results in dumbbell shaped crystals of fluorapatite reported by Kniep *et al.* Besides the unusual shaped CaCO₃ crystals from solution the same polymer class allows control of polymorphism to precipitate aragonite phase of CaCO₃ on polyglycerol polyacid functionalized SAM. Both results are shown in Figure 2.29. ^[110]

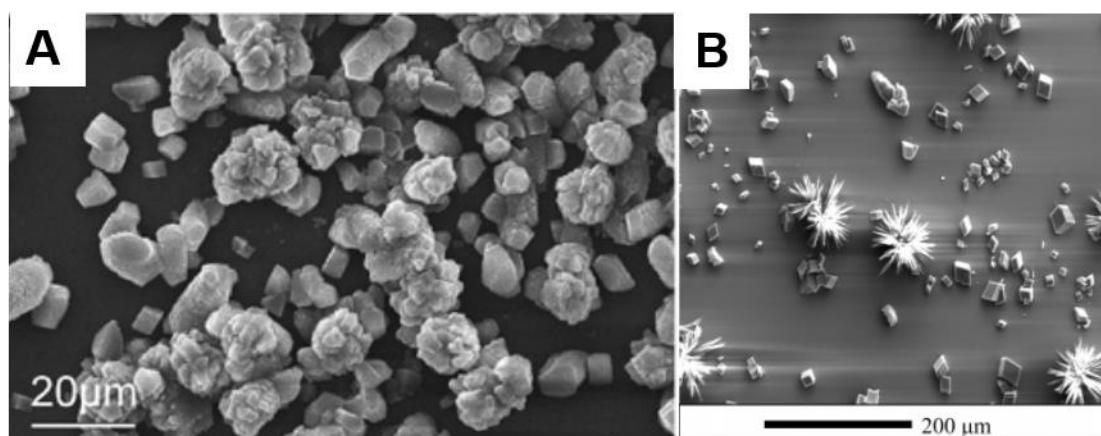


Figure 2.29: Influence of polyglycerol polymers on CaCO₃: (A) SEM images of calcium carbonate crystals precipitated from a solution containing COOH terminated *hb*-polyglycerol (5 g/L) and 25 mM CaCl₂. ^[111] Reprinted with permission. Copyright 2004 RSC Publishing. (B) Crystals formed on a COOH-terminated SAM with adsorbed *hb*-polyglycerol ($M_n = 5000$ g/mol). Both samples were taken after overnight ammonia diffusion method precipitation. Reprinted with permission. ^[110] Copyright 2005 American Chemical Society.

The introduction of two additional methylene groups, so the use of tetrahydrofurane (THF) instead of ethylene oxide (EO), as main monomer for the formation of a linear statistical block-copolymer with cyano ethylene oxide (CEO) arises a new class of copolymers to study for effects on scale inhibition of CaCO₃. The CEO

subunits are post-oxidized to carboxylic acid groups, which are known to strongly interact with CaCO_3 during its precipitation.

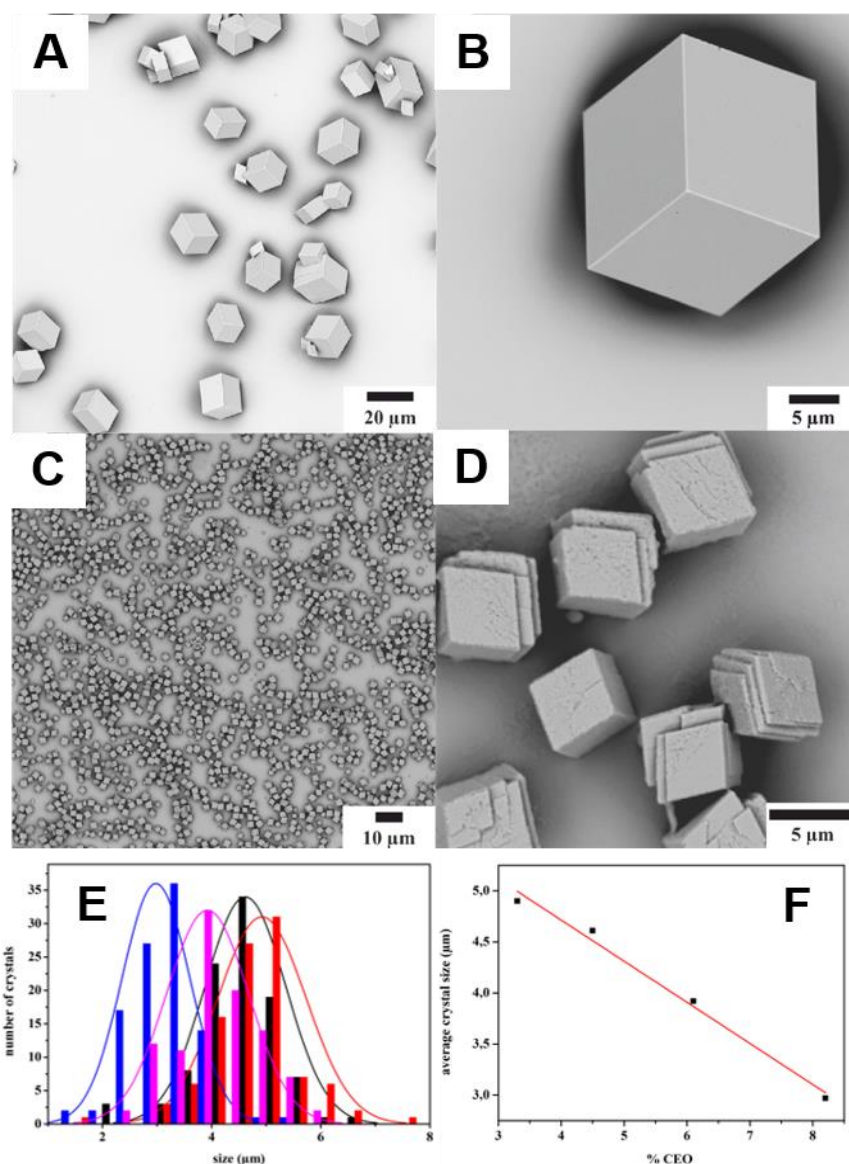


Figure 2.30: Influence of linear Poly(THF) polyacids on CaCO_3 crystallization: (A, B) SEM images of calcium carbonate crystals precipitated from a solution via ADM containing no additive at 5 mM Ca^{2+} giving about 15 μm edge length calcite rhombohedra. (C, D) Crystals formed after 15 h and the addition of linear PTHF-CEO polyacid copolymer ($M_n = 10900$ g/mol, 3.3 % acid groups) resulting in maximum 5 μm edge length multi step edged rhombohedra with micro-structured surfaces. (E, F) Relationship between amount of acid groups and average crystal size showing a linear relationship of scale inhibition. Reprinted with permission. ^[112] Copyright 2016 American Chemical Society.

In Figure 2.30 the relationship of amount of carboxylic groups to scale inhibition of these copolymers is demonstrated. The linear relationship is an evidence for the strong interaction of the polymer with CaCO_3 during precipitation. We started to ask ourselves after our study if the polarity of the backbone is changed, we see analogous difference in crystal shape resulting from the addition of a hyper-branched analogue during CaCO_3 synthesis as reported for the polyacids PAA and the PEG/polyglycerol system.

2.3.3 Proteins

Proteins are natural polymers formed from a pool of amino acids as monomers by the formation of peptide bonds. The protein synthesis code of a living animal or human body is saved in its DNA and thus high genetic controlled reproducibility is ensured. The tertiary structure of the amino acid sequence of proteins is the key to understand its function within an organism. Thus especially the interaction with ions and small molecules for catalysis (enzymes) or signal transduction needs to be understood. Especially acidic amino acids like glutamic, aspartic acid or even asparagine or serine have been identified as key needs for the complexation of ions such as Ca^{2+} . Sequence alignment raised the question of binding motives to predict functions of proteins and predict their effects on calcium binding and CaCO_3 precipitation. By comparison of many obviously calcium binding sites the identification of the so-called EF-Hand model for calcium binding has been conducted. (see Figure 2.31 (A) for the exemplary p11 protein).^[113,114] Such proteins have often been found bound to membranes wherein they often fulfill the equilibration of ion gradients. But also soluble EF-Hand bearing proteins have been identified and especially their influence on CaCO_3 precipitation has been studied extensively for mollusk shells of *Pnicata funcata* to understand the Aragonite platelet formation process (see Figure 2.21).^[115] Besides these effects the agglomeration of proteins with addition of calcium ions and formation of calcium carbonate is an extensively studied field during recent years.

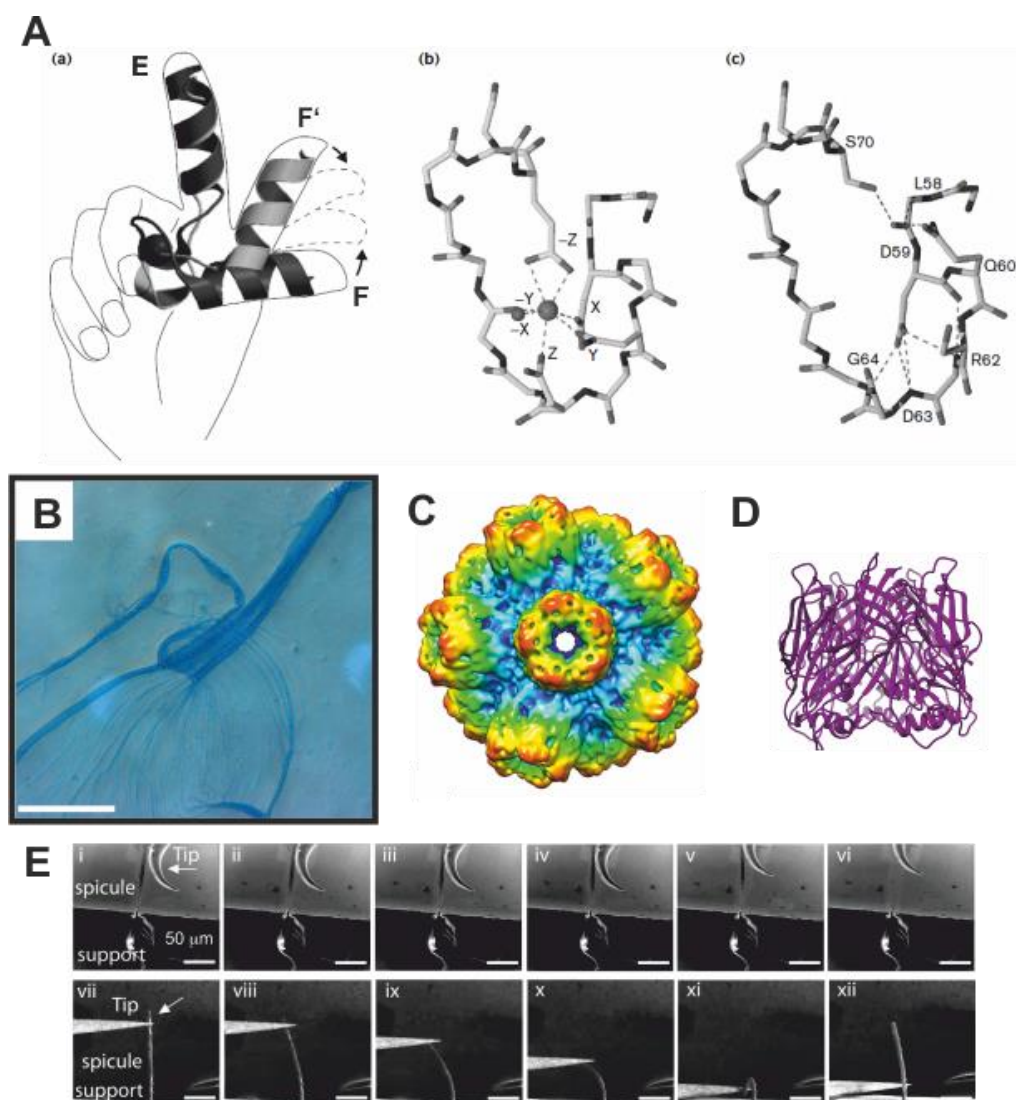


Figure 2.31: Proteins as additives: (A) The EF-hand motif (a) as symbolic representation. Helix E and Helix F wind together and Helix F moves from the closed (F' , apoprotein, light grey) to the open (F , holoprotein, dark grey) conformation if calcium ion binds. (b) Geometry of calcium ligand amino acid side groups. Positions X and Y represent aspartic acid or asparagine while Z position corresponds to either aspartic acid, asparagine or serine. -Y position represents peptide carbonyl oxygen and -Y usually corresponds to a water molecule and -Z to a conserved bidentate ligand as glutamic acid or aspartic acid. (c) The modified EF-Hand loop of p11 (S100A10) with stabilizing hydrogen bonds (dashed lines). Reprinted with permission. ^[114] Copyright 2000 Elsevier. (B) Light microscopy image of fibrous structured Ovalbumin after aggregation induced by calcium ion interaction. Protein is stained with comassie brilliant blue dye. Reprinted with permission. ^[116] Copyright 2008 American Chemical Society. (C) 6 Å TEM reconstruction of Isoform 1 of *Bg*-AChBP protein showing twelfold geometry of the centro-symmetric 20 nm large protein subunit assembly. (D) Predicted structure by TEM reconstruction of SEM images of Isoform 2 of *Bg*-AChBP showing protein pentamer as final quaternary assembly. Both are reprinted from open access from PLOS One. ^[119] (E) (i-vi) Bending of natural siliceous speculi by micromanipulator showing fragile material and fracture between image (v) and (vi). (vii-xii) show micromanipulation of synthetic CaCO_3 -Silicatein- α speculi which does not break even after bending by 270° and relaxes to original shape. Reprinted with permission. ^[15] Copyright 2013 American Association for the Advancement of Science.

The structural changes of the egg-white protein ovalbumin during precipitation of the egg shell has been found to be a calcium ion mediated polymerization mechanism for the formation of up to millimeter long fibrils of a protein CaCO_3 composite as shown in Figure 2.31 (B).^[116,117] Besides this calcium specialized protein, the interaction of Silicatein- α with CaCO_3 was found to form an interesting brick-mortar structure spicule composite. Silicatein- α has been identified as enzymatic catalyst for the hydrolysis of silica subunits to silicate structures as building units for the exoskeleton of *Demospongiae domuncula*^[118]. The found spicules from CaCO_3 precipitation with protein added were able to be bend to almost 180° with relaxation to its original shape without fracture which has been observed for the natural silica species formed with Silicatein- α (for the experiment see Figure 2.31 (E)).^[15] Besides the binding to bivalent (e.g. calcium and magnesium) ions by known amino acid motives as the EF-Hand motif a lot of other structures especially found in CaCO_3 precipitating animals as mollusks, shells and snails have been studied in literature for centuries. The role of ACCBP analogue protein sequences in snails such as *Biomphalaria glabrata* is interesting to study to find new CaCO_3 polymorph controlling amino acid motifs in the structures, for example in *Bg*-AChBP1 and *Bg*-AChBP2.

2.4 References

- [1] P. Ehrenfest, *Z. Physik* **1927**, *45*, 455–457.
- [2] V. K. LaMer, R. H. Dinegar, *J. AM. CHEM. SOC.* **1950**, *72*, 4847–4854.
- [3] J. W. Gibbs, *Collected Works*, Longman, New York, **1928**.
- [4] J. J. de Yoreo, P. G. Vekilov, *Rev. Mineral. Geochem.* **2003**, *57*–93.
- [5] J.W. Mullin, *Crystallization*, Butterworth-Heinemann, Oxford, USA, **2001**.
- [6] R. Momper, M. Nalbach, K. Lichtenstein, R. Bechstein, A. Kühnle, *Langmuir* **2015**, *31*, 7283–7287.
- [7] G. Wulff, *Zeitschrift für Kristallographie* **1901**, 449–530.
- [8] W. K. Burton, N. Cabrera, F. C. Frank, *Phil. Trans. Royal Society London* **1950**, *Series A*, 299–358.
- [9] C. M. Pina, U. Becker, P. Risthaus, D. Bosbach, A. Putnis, *Nature* **1998**, *395*, 483–486.
- [10] R. C. Kang, Y.-Y. Kim, P. Yang, W. Cai, H. Pan, A. N. Kulak, J. L. Jau, J. DeYoreo, *Nat Commun* **2016**, *7*, 10187–10194.
- [11] B. Kahr, R. W. Gurney, *Chem. Rev.* **2001**, *101*, 893–952.
- [12] A. Thomas, E. Rosseeva, O. Hochrein, W. Carrillo-Cabrera, P. Simon, P. Duchstein, D. Zahn, R. Kniep, *Chemistry* **2012**, *18*, 4000–4009.
- [13] H. Tlatlik, P. Simon, A. Kawska, D. Zahn, R. Kniep, *Angew. Chem.* **2006**, *118*, 1939–1944.
- [14] J. Küther, R. Seshadri, G. Nelles, W. Assenmacher, H.-J. Butt, W. Mader, W. Tremel, *Chem. Mater.* **1999**, *11*, 1317–1325.
- [15] F. Natalio, T. P. Corrales, M. Panthfer, D. Schollmeyer, I. Lieberwirth, W. E. G. Mller, M. Kappl, H.-J. Butt, W. Tremel, *Science* **2013**, *339*, 1298–1302.
- [16] Y.-Y. Kim, A. S. Schenk, D. Walsh, A. N. Kulak, O. Cespedes, F. C. Meldrum, *Nanoscale* **2014**, *6*, 852–859.
- [17] M. Niederberger, H. Cölfen, *Phys. Chem. Chem. Phys.* **2006**, *8*, 3271–3287.
- [18] W. Ostwald, *Grundriss der allgemeinen Chemie*, Verlag von Wilhelm Engelmann, Leipzig, **1890**.
- [19] H. Cölfen, M. Antonietti, *Mesocrystals and Nonclassical Crystallization*, John Wiley & Sons, Ltd, Chichester, UK, **2008**.

-
- [20] Y. Wang, T. Azaïs, M. Robin, A. Vallée, C. Catania, P. Legriel, G. Pehau-Arnaudet, F. Babonneau, M.-M. Giraud-Guille, N. Nassif, *Nat Mater* **2012**, *11*, 724–733.
- [21] E. V. Sturm Née Rosseeva, H. Cölfen, *Chem. Soc. Rev.* **2016**, *45*, 5821–5833.
- [22] E. A. Zimmermann, R. O. Ritchie, *Adv. Health. Mater.* **2015**, *4*, 1287–1304.
- [23] K. M. Ryan, A. Mastroianni, K. A. Stancil, H. Liu, A. P. Alivisatos, *Nano Lett.* **2006**, *6*, 1479–1482.
- [24] M. Agthe, E. Wetterskog, L. Bergström, *Langmuir* **2017**, *33*, 303–310.
- [25] A. Verch, A. S. Côté, R. Darkins, Y.-Y. Kim, R. van de Locht, F. C. Meldrum, D. M. Duffy, R. Kröger, *Small* **2014**, *10*, 2697–2702.
- [26] Y. Oaki, A. Kotachi, T. Miura, H. Imai, *Adv. Funct. Mater.* **2006**, *16*, 1633–1639.
- [27] R. J. Park, F. C. Meldrum, *Adv. Mater.* **2002**, *14*, 1167–1169.
- [28] J. Aizenberg, G. Hendler, *J. Mater. Chem.* **2004**, *14*, 2066–2072.
- [29] M. Ocaña, M. P. Morales, C. J. Serna, *J. Colloid Interface Sci.* **1995**, *171*, 85–91.
- [30] H. Hull, A. Turnbull, *Geochim. Cosmochim. Acta* **1973**, 682–694.
- [31] H. Effenberger, *Monatshefte für Chemie* **1981**, *112*, 899–909.
- [32] M. Neumann, M. Epple, *J. Inorg. Chem.* **2007**, 1953–1957.
- [33] K.-F. Hesse, H. Küppers, E. Suess, *Zeitschr. Kristall.* **1983**, 227–231.
- [34] S. Papadimitriou, H. Kennedy, P. Kennedy, D. N. Thomas, *Geochim. Cosmochim. Acta* **2013**, *109*, 241–253.
- [35] I. P. Swainson, R. P. Hammond, *American Mineral.* **2001**, *86*, 1530–1533.
- [36] I. P. Swainson, R. P. Hammond, *Mineral. Mag.* **2003**, *67*, 555–562.
- [37] A. R. Lennie, *Mineral. Mag.* **2005**, *69*, 325–336.
- [38] L. Addadi, S. Weiner, *PNAS* **1985**, *82*, 4110–4114.
- [39] L. Addadi, J. Moradian, E. Shay, N. G. Maroudas, S. Weiner, *PNAS* **1987**, *84*, 2732–2736.
- [40] C. Beato, M. S. Fernández, S. Fermani, M. Reggi, A. Neira-Carrillo, A. Rao, G. Falini, J. L. Arias, *Cryst. Eng. Comm.* **2015**, *17*, 5953–5961.

-
- [41] M. Dietzsch, M. Barz, T. Schüler, S. Klassen, M. Schreiber, M. Susewind, N. Loges, M. Lang, N. Hellmann, M. Fritz, K. Fischer, P. Theato, A. Kühnle, M. Schmidt, R. Zentel, W. Tremel, *Langmuir* **2013**, *29*, 3080–3088.
- [42] M. Faatz, F. Gröhn, G. Wegner, *Adv. Mater.* **2004**, *16*, 996–1000.
- [43] J. D. Rodriguez-Blanco, S. Shaw, L. G. Benning, *Nanoscale* **2011**, *3*, 265–271.
- [44] S.-F. Chen, H. Cölfen, M. Antonietti, S.-H. Yu, *Chem. Commun* **2013**, 1-3.
- [45] A. S. Schenk, H. Zope, Y.-Y. Kim, A. Kros, N. A. J. M. Sommerdijk, F. C. Meldrum, *Faraday Discuss.* **2012**, *159*, 327–344.
- [46] J. H. E. Cartwright, A. G. Checa, J. D. Gale, D. Gebauer, C. I. Sainz-Díaz, *Angew. Chem. Int. Ed. Engl.* **2012**, *51*, 11960–11970.
- [47] D. Gebauer, M. Kellermeier, J. D. Gale, L. Bergström, H. Cölfen, *Chem. Soc. Rev.* **2014**, *43*, 2348–2371.
- [48] Y.-Y. Kim, M. Semsarilar, J. D. Carloni, K. R. Cho, A. N. Kulak, I. Polishchuk, C. T. Hendley, P. J. M. Smeets, L. A. Fielding, B. Pokroy, C. C. Tang, L. A. Estroff, S. P. Baker, S. P. Armes, F. C. Meldrum, *Adv. Funct. Mater.* **2016**, *26*, 1382–1392.
- [49] E. Mugnaioli, I. Andrusenko, T. Schüler, N. Loges, R. E. Dinnebier, M. Panthöfer, W. Tremel, U. Kolb, *Angew. Chem. Int. Ed.* **2012**, *51*, 7041–7045.
- [50] B. Pokroy, A. N. Fitch, L. Bloch, *Science* **2013**, 454–456.
- [51] L. Plummer, E. Busenberg, *Geochim. Cosmochim. Acta* **1982**, *46*, 1011–1040.
- [52] Z. Hu, Y. Deng, *J. Colloid Interface Sci.* **2003**, *266*, 359–365.
- [53] X. Li, W.-C. Chang, Y. J. Chao, R. Wang, M. Chang, *Nano Lett.* **2004**, *4*, 613–617.
- [54] E. N. Maslen, V. A. Streltsov, N. R. Streltsova, *Acta Cryst.* **1993**, *B49*, 636–641.
- [55] G. Ghosh, *Optics Comm.* **1999**, *163*, 95–102.
- [56] A. G. Guy, *Zeitschr. Metall.* **1967**, *58*, 164–168.
- [57] N. Marmé, A. Aupperle-Pauls, F. Pauls, J.-P. Knemeyer, *Chemie konkret* **2014**, *21*, 181–187.
- [58] C. Wang, H. Yin, S. Dai, S. Sun, *Chem. Mater.* **2010**, *22*, 3277–3282.

-
- [59] T. D. Schladt, K. Schneider, H. Schild, W. Tremel, *Dalton Trans.* **2011**, 40, 6315–6343.
- [60] T. Zhang, R. Yuan, Y. Chai, K. Liu, S. Ling, *Microchim. Acta* **2009**, 165, 53–58.
- [61] S. R. Kanel, J.-M. Greneche, H. Choi, *Environ. Sci. Technol.* **2006**, 40, 2045–2050.
- [62] M. Faraday, F.-V. v. Hahn, *Experimentelle Untersuchungen über das Verhalten von Gold (und anderen Metallen) zum Licht*, Akad. Verl.-Ges, Leipzig, **1925**.
- [63] J. M. Abad, S. F. L. Mertens, M. Pita, V. M. Fernández, D. J. Schiffrin, *J. Am. Chem. Soc.* **2005**, 127, 5689–5694.
- [64] J. Katyal, R. Soni, *J. Mod. Opt.* **2013**, 60, 1717–1728.
- [65] M. Barisik, S. Atalay, A. Beskok, S. Qian, *J. Phys. Chem. A* **2014**, 118, 1836–1842.
- [66] Ö. Çelik, M. M. Can, T. Firat, *J. Nano. Res.* **2014**, 16, 1–7.
- [67] A. Lak, M. Kraken, F. Ludwig, A. Kornowski, D. Eberbeck, S. Sievers, F. J. Litterst, H. Weller, M. Schilling, *Nanoscale* **2013**, 5, 12286–12295.
- [68] K. Nishad, R. Pandey, *Mater. Sci. Eng.* **2013**, 178, 1380–1389.
- [69] A. Shanmugavani, R. Kalai Selvan, S. Layek, C. Sanjeeviraja, *J. Magn. Mater.* **2014**, 354, 363–371.
- [70] M. Grzelczak, J. Pérez-Juste, P. Mulvaney, L. M. Liz-Marzán, *Chem. Soc. Rev.* **2008**, 37, 1783–1791.
- [71] A. R. Tao, S. Habas, P. Yang, *Small* **2008**, 4, 310–325.
- [72] Y. Wei, R. Klajn, A. O. Pinchuk, B. A. Grzybowski, *Small* **2008**, 4, 1635–1639.
- [73] S. Han, L. Hu, N. Gao, A. A. Al-Ghamdi, X. Fang, *Adv. Func. Mater.* **2014**, 24, 3725–3733.
- [74] F. Amin, *Disputation*, Universität Marburg, Marburg, **2012**.
- [75] R. Schreiber, J. Do, E.-M. Roller, T. Zhang, V. J. Schüller, P. C. Nickels, J. Feldmann, T. Liedl, *Nature Nano.* **2014**, 9, 74–78.
- [76] T. Hanafusa, Y. Mino, S. Watanabe, M. T. Miyahara, *Adv. Powder Tech.* **2014**, 25, 811–815.

-
- [77] S. Peng, Y. Lee, C. Wang, H. Yin, S. Dai, S. Sun, *Nano Res.* **2008**, *1*, 229–234.
- [78] X. Liu, M. Atwater, J. Wang, Q. Huo, *Coll. Surf. B* **2007**, *58*, 3–7.
- [79] X. Ben, H. S. Park, *Appl. Phys. Lett.* **2013**, *102*, 41909–41914.
- [80] K. Yu, M. S. Devadas, T. A. Major, S. S. Lo, G. V. Hartland, *J. Phys. Chem.* **2014**, *118*, 8603–8609.
- [81] L. Anghinolfi, *Self-Organized Arrays of Gold Nanoparticles. Morphology and Plasmonic Properties*, Imprint: Springer, Berlin Heidelberg, **2012**.
- [82] C. E. Talley, J. B. Jackson, C. Oubre, N. K. Grady, C. W. Hollars, S. M. Lane, T. R. Huser, P. Nordlander, N. J. Halas, *Nano Lett.* **2005**, *5*, 1569–1574.
- [83] J. D. Driskell, C. G. Larrick, C. Trunell, *Langmuir* **2014**, *30*, 6309–6313.
- [84] T. Ghodselahi, S. Hoornam, M. Vesaghi, B. Ranjbar, A. Azizi, H. Mobasheri, *Appl. Surf. Sci.* **2014**, *314* (2014), 138–144.
- [85] S. Rastegarzadeh, Z. Barkat Rezaei, *Environ. Monitor. Assess.* **2013**, *185*, 9037–9042.
- [86] J. Sittiwong, F. Unob, *Spectrochim. Acta A* **2015**, *138*, 381–386.
- [87] T. Bu, T. Zako, M. Fujita, M. Maeda, *Chem. Commun.* **2013**, *49*, 7531–7533.
- [88] S. Findlay, N. Shibata, Y. Ikuhara, *Ultramicroscopy* **2009**, *109*, 1435–1446.
- [89] Y. Huang, D.-H. Kim, *Nanoscale* **2011**, *3*, 3228–3232.
- [90] T. Kobori, J. Watanabe, H. Nakao, *Anal Sci* **2012**, *28*, 61–64.
- [91] H. Liu, C. Dong, J. Ren, *J. Am. Chem. Soc.* **2014**, *136*, 2775–2785.
- [92] F. Verpillat, F. Joud, P. Desbiolles, M. Gross, *Opt. Express.* **2011**, *19*, 26044–26055.
- [93] X. Ji, X. Song, J. Li, Y. Bai, W. Yang, X. Peng, *J. Am. Chem. Soc.* **2007**, *129*, 13939–13948.
- [94] N. R. Jana, L. Gearheart, C. J. Murphy, *J. Phys. Chem. B* **2001**, *105*, 4065–4067.
- [95] J. Huang, H. Wang, Y. Cui, G. Zhang, G. Zheng, S. Liu, L. Xie, R. Zhang, *Mar Biotechnol* **2009**, *11*, 596–607.
- [96] H. Yu, M. Chen, P. M. Rice, S. X. Wang, R. L. White, S. Sun, *Nano Lett.* **2005**, *5*, 379–382.

-
- [97] A. Walther, A. H. E. Müller, *Chem. Rev.* **2013**, *113*, 5194–5261.
- [98] C. Xu, J. Xie, D. Ho, C. Wang, N. Kohler, E. G. Walsh, J. R. Morgan, Y. E. Chin, S. Sun, *Angew. Chem. Int. Ed.* **2008**, *47*, 173–176.
- [99] L. Landgraf, P. Ernst, I. Schick, O. Köhler, H. Oehring, W. Tremel, I. Hilger, *Biomater.* **2014**, *35*, 6986–6997.
- [100] B. Wu, S. Tang, M. Chen, N. Zheng, *Chem. Commun.* **2013**, *50*, 174–176.
- [101] Z. Wang, L. Wu, F. Wang, Z. Jiang, B. Shen, *J. Mater. Chem. A* **2013**, *1*, 9746–9751.
- [102] M. Kuang, D. Wang, H. Möhwald, *Chem. Mater.* **2006**, *18*, 1073–1075.
- [103] I. Schick, D. Gehrig, M. Montigny, B. Balke, M. Panthöfer, A. Henkel, F. Laquai, W. Tremel, *Chem. Mater.* **2015**, *27*, 4877–4884.
- [104] A.-H. Lu, E. L. Salabas, F. Schüth, *Angew. Chem. Int. Ed.* **2007**, *46*, 1222–1244.
- [105] R. Hong, N. Fischer, T. Emrick, V. Rotello, *Chem. Mater.* **2005**, *17*, 4617–4621.
- [106] W. S. Seo, J. H. Lee, X. Sun, Y. Suzuki, D. Mann, Z. Liu, M. Terashima, P. C. Yang, M. V. McConnell, D. G. Nishimura, H. Dai, *Nat. Mater.* **2006**, *5*, 971–976.
- [107] S. N. Maiti, P. K. Mahapatro, *J. Appl. Poly. Sci.* **1991**, *42*, 3101–3110.
- [108] C. M. Seok, O. Young-Kee, C. Kee-Heon, Hyun-Chang, K., Sang-Woon, K., US Patent 0137185.
- [109] J. Jiang, J. Ye, G. Zhang, X. Gong, L. Nie, J. Liu, T. Vaimakis, *J. Am. Ceram. Soc.* **2012**, *95*, 3735–3738.
- [110] M. Balz, E. Barriau, V. Istratov, H. Frey, W. Tremel, *Langmuir* **2005**, *21*, 3987–3991.
- [111] G. Wang, L. Li, J. Lan, L. Chen, J. You, *J. Mater. Chem.* **2008**, *18*, 2789–2797.
- [112] E.-M. Christ, J. Herzberger, M. Montigny, W. Tremel, H. Frey, *Macromolecules* **2016**, *49*, 3681–3695.
- [113] M. Ikura, *Trends Biochem. Sci.* **1996**, *21*, 14–17.
- [114] A. Lewit-Bentley, S. Réty, *Curr. Opin. Struct. Bio.* **2000**, *10*, 637–643.
- [115] Z. Ma, J. Huang, J. Sun, G. Wang, C. Li, L. Xie, R. Zhang, *J. Bio. Chem.* **2007**, *282*, 23253–23263.

- [116] V. Pipich, M. Balz, S. E. Wolf, W. Tremel, D. Schwahn, *J. Am. Chem. Soc.* **2008**, *130*, 6879–6892.
- [117] D. Schwahn, M. Balz, W. Tremel, *Physica B*: **2004**, *350*, 947-949.
- [118] X. Wang, H. C. Schröder, W. E. Müller, *Trends Biotech.* **2014**, *32*, 441–447.
- [119] M. Saur, V. Moeller, K. Kapetanopoulos, S. Braukmann, W. Gebauer, S. Tenzer, J. Markl, E. A. Permyakov, *PLoS ONE* **2012**, *7*, e43685.

3 Results and Discussion

3.1 Functionalized nanoparticles as additives in CaCO₃ crystallization

The idea to use nanoparticles as additives has its origin in a publication of Küther *et al.* about the effect of Au nanoparticles functionalized with a SAM of *p*-Mercapto-phenol on the crystallization of CaCO₃ published by our group in 1999.^[27] The authors unfortunately did not have the equipment available to monitor the assembly and occlusion of the nanoparticles during the process of crystallization. In this work the extraordinary optical and spectroscopic properties of plasmonic gold nanoparticles are used to track the interaction of calcium ions and the CaCO₃ mineral. The need of the carboxyl function for good interaction with CaCO₃ and thus good occlusion of the particles to form a new composite material with extraordinary properties is underlined by grafting a PEG 2000 polymer on the 11-MUA to get water soluble but loosely CaCO₃ interacting particles. To study the effect of anisotropy of nanoparticles as well as to give another example for the need of anionic stabilized nanoparticles to produce a well interacting additive Au@Fe₃O₄ Janus particles are synthesized via an alternative route combining two separate steps within a single step of better yield and monodispersity. For both the amphiphilic non-isotropic Au@Fe₃O₄ and anionic isotropic Au nanoparticles epitaxy between the Au and CaCO₃ lattices are also demonstrated in the following chapters.

3.1.1 Inclusion mechanism of 11-MUA and PEG/11-MUA functionalized gold nanoparticles within CaCO_3

The article “Inclusion mechanism of 11-MUA and PEG/11-MUA functionalized gold nanoparticles within CaCO_3 ” will be submitted to *Crystal Growth & Design* by the *American Chemical Society*. The following chapter is based on the most recent draft of this main manuscript and the supporting information.

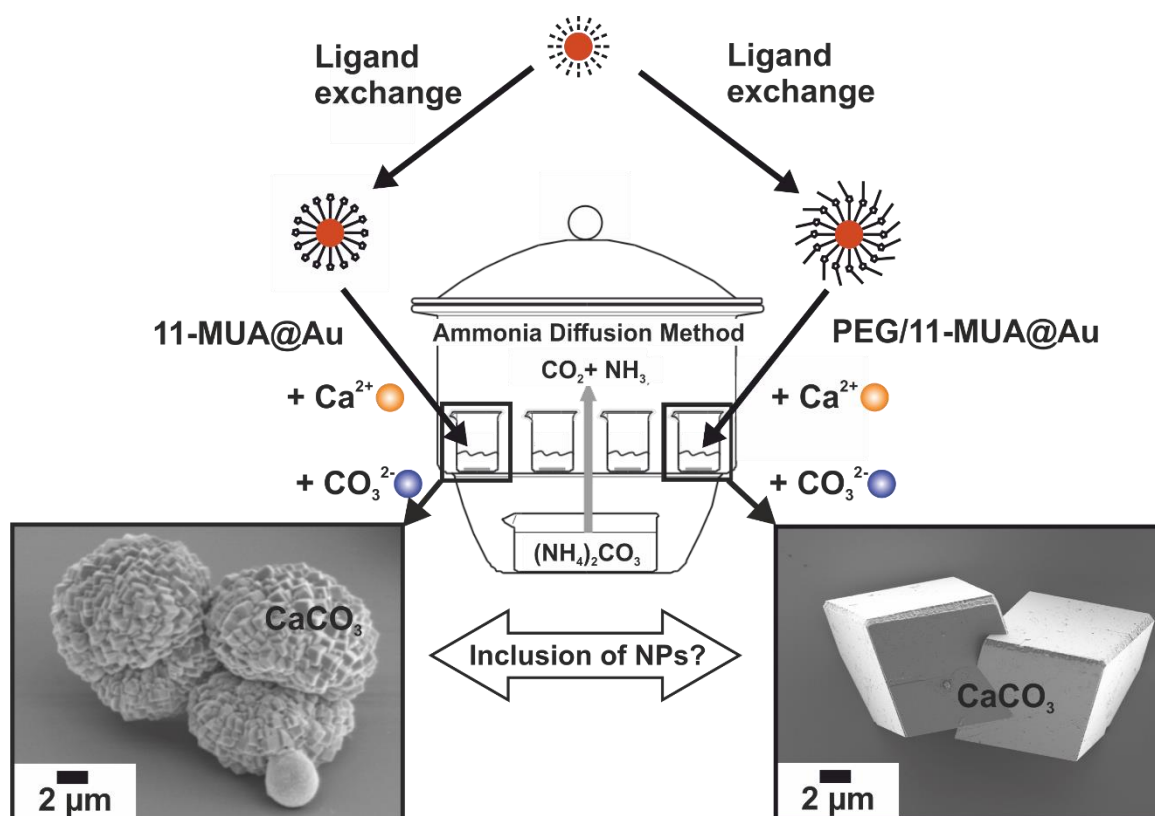


Figure 3.1: Studied system of 11-MUA@Au and PEG2000/11-MUA@Au with addition of calcium ions to observe aggregation and subsequent CaCO_3 precipitation by applying the ammonia diffusion method.

Most work on additive inclusion within CaCO_3 has been conducted through many different integration strategies to tune properties, polymorph (calcite, vaterite, aragonite) and shape of the CaCO_3 crystals. Most integration mechanisms for additives into CaCO_3 base on postulates from the final crystal morphology of poly- or even

mesocrystalline assemblies. This simplified way might be useful for flexible materials such as small molecules or even polymers as they can easily be incorporated into grain boundaries of the crystal. In contrast the inclusion of inflexible inorganic nanoparticles to introduce the particles properties into the final crystal is very complex. The nanoparticle functionalization, their inflexibility and material type influence the CaCO_3 host material simultaneously. In this chapter the first systematic assembly approach of Au@CaCO_3 mesocrystals via an amorphous core shell precursor material to dumbbell shaped mesocrystals is presented. The need of carboxylic acid groups for this specific interaction is pointed out by giving an insight into the growth mechanism of epitactic metal/biomineral composite mesocrystals and the integration of nano-sized additives into grain boundaries of the CaCO_3 host lattice.

3.1.1.1 Introduction

Inclusion of synthetic additives into biominerals is of high interest for understanding the influence of natural additives like amino acids ^[1], peptides ^[2–4] or even proteins ^[5,6] on the inorganic framework material during composite formation. A plethora of publications on the incorporation of surfactants like polymers and even more complex additives into CaCO_3 have been published in the recent two decades. ^[3,7–12] While foreign bi- or trivalent cations integrate easily into CaCO_3 under unit cell expansion or changing the crystallized polymorph, ^[13–15] Pokroy *et al.* postulated amino acids of a few angstroms size to get integrated into the unit cell of CaCO_3 as well. ^[1] Hence broad XRD reflexes were an evidence for inclusion into grain boundaries but not an expansion of the calcite unit cell size. ^[1] Some publications also discuss integration of nanoparticles (NPs) into the calcite unit cell, with one order of magnitude larger size than the unit cell parameter of CaCO_3 . ^[16,17] Sure the cut-off criteria for size and surface charge of additives is still not well understood for CaCO_3 to provide a reliable statement neither pro nor contra this conclusion. Nonetheless integration of Au-NPs published by Meldrum *et al.* was triggered via a functionalization of Au-nanocrystals with a pH responsive copolymer, which expresses carboxylic acids on its surface at basic pH. ^[17] Hence the HR-TEM analytics in this publication do not show epitaxy of CaCO_3 on Au-NPs. We postulate the

strong interaction of the polymer in which the nanoparticle is embedded is the clue of Au nanocrystal integration within the CaCO_3 nano-crystal grain boundaries. [18–20] This also describes the final red color of the composite as this strong color can only be seen, if the refractive index of the NPs surrounding medium remains the same as in aqueous phase, because the refractive index of solid CaCO_3 next to the oscillating surface plasmon charge of Au would red-shift the plasmon absorption. [21–23] A similar integration strategy has been published to use carboxylic acid containing polymers as surface coverage for Fe_3O_4 nanocrystals by the same group. For this case the inclusion can also be described as an integration of a polymer micelles into CaCO_3 , which contains Fe_3O_4 nanocrystals, to get a magnetic nanocomposite material. [16]

Above mentioned literature on integration of NPs within CaCO_3 crystals can be concluded as integration of nanocrystals fixed in functional polymer matrices to get them included in crystalline CaCO_3 . [24] None of the studies observed a direct CaCO_3 to Au-NP epitaxy. This relationship has already been demonstrated to be possible for flat Au templates functionalized with a self-assembled monolayer (SAM) of 11-Mercaptoundecanoic acid (11-MUA) almost 15 years ago. [25,26] On the topic of using SAM-like functionalization on nanoparticles to study for ligand and substrate influence on crystallizing CaCO_3 the work of Küther *et al.* on Au-NPs functionalized with *p*-Mercaptophenol as hydrophilic additive for CaCO_3 can be called a breakthrough work. [27] The CaCO_3 assembles in dumbbell and spherical shaped mesocrystals if the nanoparticles are added, but no evidence was given for nanoparticle incorporation. Lee *et al.* later used a similar system with *p*-Mercaptophenol functionalized Au-NPs as additive in CaCO_3 precipitations. [28] They showed vaterite phase forms instead of calcite as in reference crystallization for short duration of CaCO_3 formation. This gives a hint for an inhibiting role on the additive in the CaCO_3 crystallization. [29] Grzybowski *et al.* developed the research on functionalized Au-NPs and used 11-MUA and *N,N,N,N*-Trimethyl(11-mercaptopundecyl) ammonium chloride (TMA) functionalized Au-NPs of various molar fractions to study the particles self-assembly. [30] Nevertheless the pure 11-MUA/Au-NPs to CaCO_3 interaction is still almost undiscovered in the concern of crystallization influence by carboxylic nanoparticles. The question on requirements

for the integration of Au-NPs arises. To study the need of the calcium interaction of 11-MUA the water soluble non-calcium interacting ligand PEG2000/11-MUA was used to functionalize the NPs.^[32] First the mentioned functionalized NPs (analyzed by UV-Vis, SAXS, TGA, IR) were used to study the interactions of the ligand with calcium and carbonate ions and second microscopic structure details (FIB-SEM, HR-TEM, rocking curve measurements) on the control of CaCO₃ precipitation and inclusion of Au-NPs to form a functional composite are presented by using the ammonia diffusion method for CaCO₃ precipitation.

3.1.1.2 Experimental

Materials and handling details

Chloroauric acid dihydrate (99.999% trace metals basis abcr GmbH), borane *tert*-butylamine complex, (97%, Sigma Aldrich) oleylamine (80-90%, Acros), sodium hydroxide (98%, Sigma Aldrich), 11-mercaptoundecanoic acid (95%, Sigma Aldrich), PEG2000 monomethylether (99%, flakes, Sigma Aldrich), calcium chloride (0.5M, Fluka), ammonia carbonate (>30%, NH₃ basis, Sigma Aldrich), cyclohexane (p.A., Fisher scientific), ethanol (p.A., Fisher scientific), chloroform (>99%, Sigma Aldrich), hexane (p.A. Fisher scientific) were used as received without further purification.

Synthesis of Au-NPs

The Au-NPs were synthesized using a modified procedure reported by Peng *et al.*^[33] For getting a diameter about 4 nm the whole reaction was conducted at room temperature. The process of washing has been improved by adding 5% Oam to precipitation solution of 1:1 EtOH:MeOH due to aggregation taking place otherwise. The product was precipitated from solution by centrifugation (9000 rpm, 10 min). Washed with the mentioned solution once, redispersed in hexane and refrigerated.

Surface functionalization of Au-NPs

The Au-NPs were functionalized by using either 11-MUA or the 11-MUA/PEG2000 polymer synthesized as reported in literature. [32] For surface functionalization ten-fold excess (in relation to surface Au-atoms) of 11-MUA or PEG2000/11-MUA was solved in 20 mL of CHCl_3 or water respectively and a solution of 10 mg Au-NPs in 10 mL CHCl_3 was added. After 3 hours of stirring or 5 min of intense shaking the functionalized Au-NPs were centrifuged (9000 rpm, 10 min) and washed once with CHCl_3 , once with ethanol and once with MQ water to extract unbound 11-MUA. For the PEG2000/11-MUA ligand on Au-NPs the samples were washed with water and lyophilized to get powdered particles. A part of these NPs than have been solved in a small amount of water and dialyzed over a 3000 kDa cut-off membrane for 72 h to filter out any unbound polymer ligand. This sample is named with the paraphrase “dia” while the non-dialyzed sample with free ligand is paraphrased “no dia”.

Crystallizations of CaCO_3 and titration experiments

All reagents for crystallization and titration experiments were purchased from Sigma Aldrich and were used as received, unless otherwise stated. Quartz glass-slides for crystallization as well as TEM and scanning electron microscopy (SEM) equipment was received from Plano GmbH, Wetzlar, Germany. For water deionization a water purification setup from Millipore (Millipore GmbH) was used. The quartz glass slides were cleaned by subsequent washing with Ethanol, NaOH, MQ water, HCl and threefold MQ water in an ultrasonic bath for 10 minutes each. To finalize cleaning the slides have been dried under nitrogen flow. All calcium ion selective electrode (Ca-ISE) titrations were done with volumetric standard solutions purchased from Fluka. CaCO_3 crystallization experiments were carried out using the standard ammonia diffusion method (ADM). [5,34,8,35,36] The reaction has a short induction time during which desiccator atmosphere was supersaturated with ammonia and carbon dioxide via subsequent thermal decomposition of the ammonium carbonate (7g) placed on the bottom of a desiccator. From the atmosphere the solution starts to (super-)saturate with NH_3 and CO_2 and the hydrogencarbonate-

carbonate equilibrium is generated. Crystallization was performed on quartz-glass slides with a diameter of 13 mm and a thickness of 1 mm placed on the bottom of 5 mL beakers. The beakers were filled with 2 mL of aqueous solutions of 5 mM CaCl_2 and certain amounts of Au-NPs with variable functionalization as mentioned in the TOC graphics. The beakers were covered with perforated Parafilm (Neenah, WI, USA) to prevent external impact by dust or other impurities. The pH of the solution subsequently increased from about 7 to 9.75 during crystallization. After 15 h crystallization time the glass-slides were removed from the solution, washed carefully with saturated CaCO_3 solution on both sides to ensure complete removal of ammonium carbonate crystals and unbound NPs without inducing dissolution / recrystallization processes.

Instrumentation

Optical imaging was performed with a confocal Keyence VK8710 laser light microscope equipped with a $\lambda = 658$ nm diode laser to get height information of the precipitated samples.

For SEM the CaCO_3 crystals were sputtered with 7.5 nm Ag or 4 nm Pt respectively and analyzed using a JEOL-JSM 5610LV (JEOL Ltd., Tokyo, Japan) or FEI Phenom (Hillsboro, OR, USA). Images were acquired with an accelerating voltage of 20 kV or 10 kV respectively.

For FIB cuts, a FEI 600 Nanolab focused ion beam (FIB)/SEM dual beam instrument (FEI, Hillsboro, Oregon) equipped with an Omniprobe micromanipulator (Omniprobe Inc. Dallas, Texas) was used.

TEM images were recorded using a FEI Technai F20, F30 or T12, all equipped with a 4K CCD camera and a LaB_6 or FEG cathode working at 200 kV or 120 kV acceleration voltage respectively. The HR-TEM was furthermore equipped with EDX system by EDAX and a STEM detector by FEI.

Titration experiments were carried out using the Tiamo system (Metrohm AG) with a pH-, a turbidity ($\lambda = 523\text{nm}$) and a calcium ion selective electrode (Ca-ISE). External calibration of the Ca-ISE was done with a four-point calibration with various

concentrations of a CaCl_2 solution in a 0,1 M KCl solution. The influence of carbonate species is not considered in this way of calibration. External pH calibration was carried out with standard solutions of pH 4, 7 and 9 purchased from Metrohm.

Simultaneously to the titration experiments the SAXS measurements have been performed from the same solution. For a simultaneous measurement a distinct probe volume from the sample titration vial was circularly pumped through both instruments by a peristaltic pump with a flow of 6.8 mL/min. SAXS data was collected using the SAXSess (Anton Paar) equipped with a sealed copper X-ray tube ($\lambda = 0.154$ nm) and a 1D X-ray detector (MYTHEN R 1K, Dectris). Data acquisition, reduction, and deconvolution were performed with the SAXSquant program (Anton Paar). All data were corrected for the effect of slit smearing, transmission and background scattering. The corrected scattering curves were fitted using a homogenous sphere as model, and with a structure factor model of a hard sphere using SASFIT.

TGA data has been collected with a Perkin Elmer TGA sampler controlled by the Pyris 8 software. The instrument ran a temperature program with constant 50 °C for 10 min, a slope with 5 °C/min to 650 °C and a plateau at this temperature for another 10 min. For all measurements particle amounts between 2 and 10 mg have been used.

Raman and IR-spectroscopy measurements for phase identification and NP functionalization verification were carried out using a confocal HR800 μ -Raman by Horiba Scientific and a NicoletTM iSTM10 FT-IR spectrometer from Thermo Fischer scientific. Both instruments used a $\lambda = 633,318$ nm He-Ne laser for excitation of vibrational modes fulfilling the Raman- and/or IR-selection rules. Each spectrum was taken with resolution of 1 cm^{-1} at 16 iterations.

CLSM images were recorded using a confocal Leica SP5 system. All images shown were collected by exciting the gold plasmon resonance with a visible Ar-Laser beam and detecting in bandwidth between $\lambda = 629 - 762$ nm. By switching the detection window lower than $\lambda = 629$ nm no emission from the particles has been observed anymore.

UV-Vis-spectra were collected from 1 mL NP solutions in a standard quartz glass cuvette by a Varian Cary 5000 UV Vis/NIR-spectrometer equipped with a tempered stage at constant 25°C.

Calcite crystals for AFM with a sample size of 4 x 4 mm² were purchased from Korth Kristalle GmbH. The crystals were freshly cleaved and cleaned with a nitrogen flow prior to each experiment. We conducted all in-situ AFM measurements in the frequency modulation (FM) mode using a modified ^[37,38] commercial AFM from Bruker Corporation (MultiMode V with Nanoscope V controller) for high-resolution imaging in liquid environment. All AFM images shown were taken at a constant temperature of 28 °C and with a liquid cell from Bruker Nano Surfaces Division. The used cantilevers were gold-coated and p-doped silicon (PPP-NCHAuD, Nanosensors and Tap300GD-G, BudgetSensors) and exhibit a typical eigenfrequency in liquids of 100-150 kHz and a spring constant of ~40 N/m. For all measurements, we kept the oscillation amplitude of the cantilever constant at 1 nm. In all AFM images shown here, we display the slow and fast scan direction and the measured channel in the schematics in the upper right corner.

XRD measurements were conducted with a Bruker D8 Discover equipped with a proportional counter and a vacuum stage on a Eulerian cradle. All measurements were facilitated with Cu-K α radiation and a 0.4 mm slit after the X-Ray source and in front of the detector. Rocking curve measurements were conducted at the 2θ angle of maximum intensity of the calcite (104) reflection within the ω angle range of 5° - 24° at 1s measurement time at increments of 0.02°. To ensure calcite is the measured CaCO₃ phase of all samples, a 2θ scan around the characteristic 29.4° angle was conducted with 0.02° increments at 1s measuring time.

3.1.1.3 Results & Discussion

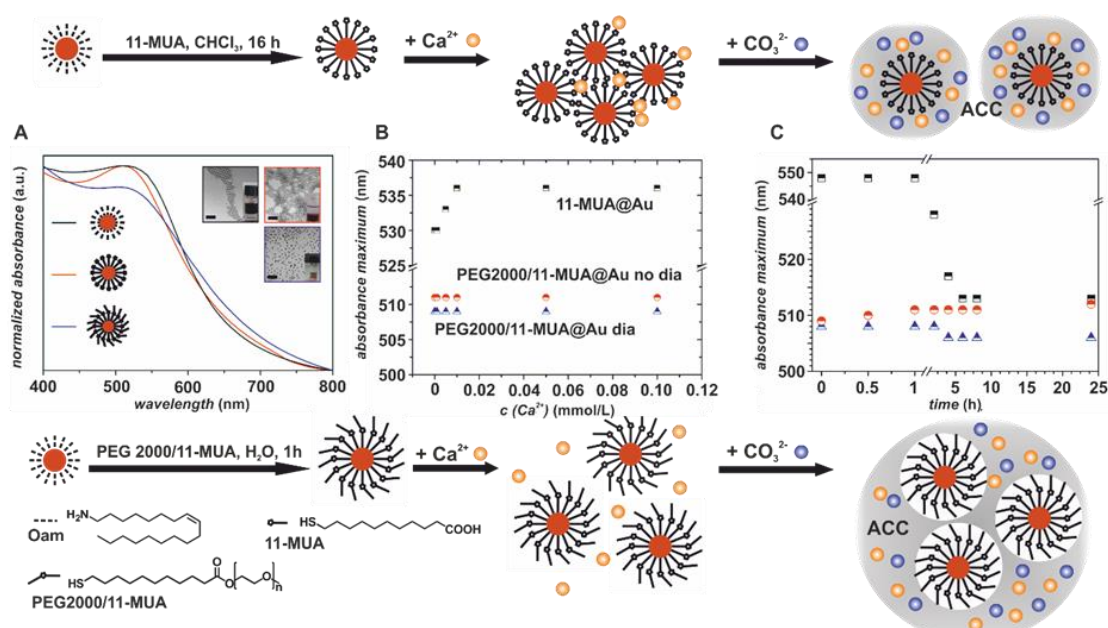


Figure 3.2: Schematic presentation of the effects of functionalization (A), agglomeration by calcium ion addition (B) and interaction with CaCO_3 during ADM desiccator experiments (C) on 11-MUA@Au NPs and PEG2000/11-MUA@Au NPs. UV-Vis, TEM and inlays of solubility tests (upper phase: hexane, bottom phase: water) show successful functionalization without morphological changes of Au-NPs. The UV-Vis data in (B) shows the effect of addition of calcium ions: aggregation in the case of 11-MUA ligand (black) by direct coulomb interactions of calcium cations and anionic NP surface. The plasmon shift is caused by plasmon coupling due to the direct contact of the NPs. PEG2000/11-MUA@Au (red: “no dia” and blue: “dia”) both show no plasmon absorption changes due to missing coulomb interactions with added calcium ions. The effect of addition of carbonate ions over the duration of the ammonia diffusion experiment for CaCO_3 on the functionalized NPs is shown in the plot of UV-Vis absorption maxima against crystallization time ((C), legend similar to (B)). Calcium and carbonate assemble around the anionic 11-MUA@Au NPs (see also Figure 3.4 and Figure S 3.3 and Figure S 3.4 of the Supporting Information). This results in separation of the Au-NPs and interruption of plasmon coupling. None to only a weak shift is observed for PEG2000/11-MUA@Au, which indicates missing interactions of NPs to calcium and carbonate ions.

As first step Au-NPs were functionalized with 11-MUA and PEG2000/11-MUA respectively using the presented reactions (see TGA (Figure S 3.1), IR (Figure S 3.2), UV-Vis (Figure 3.2, A) and solubility tests (Figure 3.2, A)). While only 18 w% ligand coverage was found for 11-MUA on gold nanoparticles, almost 92 w% of PEG2000/11-MUA corresponds to a nice Au particle coverage. By dialysis free unbound ligand was successfully removed for the PEG2000/11-MUA case. For 11-MUA, washing of nanocrystals with ethanol did not change the relative mass of

ligand bound on the surface of Au clusters (see Figure S 3.1, Supporting Information). If a certain amount of calcium ions is added to both particle fractions 11-MUA@Au-NPs and PEG2000/11-MUA@Au-NPs a redshift of the surface plasmon resonance (SPR) can be observed for the 11-MUA ligand sample, while the maximum of the plasmon absorbance keeps constant for the PEG2000/11-MUA ligand carrying particles. This redshift is caused by plasmon coupling of the SPRs due to agglomeration of small Au-NPs. The agglomeration can also be observed in the turbidity and the SAXS measurements of the particles shown in Figure S 3.3 and Figure S 3.4 of the Supporting Information. For both the non-dialyzed and dialyzed samples of PEG2000/11-MUA@Au-NPs no agglomeration of the particles has been observed by UV-Vis plasmon coupling. Hence the SAXS measurement also shows a weak aggregation for PEG2000/11-MUA@Au-NPs which can be caused by the flow technique which has been used. However, this aggregation starts and completes at much higher concentration of Ca^{2+} and is less pronounced compared to the 11-MUA stabilized Au-NPs. If the particle clusters are added to an ammonia diffusion CaCO_3 precipitation experiment the agglomeration of 11-MUA@Au is lost after 4 h duration of the experiment. This can be described by the precipitation of ACC around Au-NPs as shown in UV-Vis and TEM (see Figure 3.2 (C) and Figure 3.4 (A)). In contrast to that the ligand corona of PEG2000/11-MUA@Au suppresses direct contact of early stage precipitating ACC as demonstrated by missing plasmon shift, if CaCO_3 crystallizes after 4 h in the desiccator (Figure 3.2 (C) and Figure 3.4 (C)). If the particles are not dialyzed the distance between gold and ACC increases to several nanometers as shown in Figure S 3.10, Supporting Information. The addition of particles has an influence on faster CaCO_3 precipitating methods such as titrations with millimolar concentrations of calcium and carbonate ions. Hence it is not possible to distinguish between the particles. The titration and SAXS measurements show a shift from mostly homogeneous nucleation and growth without particles to a strictly heterogeneous growth with particles addition (see Figure S 3.3 and Figure S 3.4 C and D, Supporting Information).

The differences of interaction with calcium ions or even a calcium carbonate substrate of both species of functionalized nanoparticles can also be observed by AFM measurements of aqueous particle solutions on (104) calcite surfaces. The 11-

MUA@Au-NPs agglomerate if their solution is flown on a calcium carbonate substrate. The agglomerates mainly attach to polar step edges of the (104) surfaces as shown in Figure 3.3 (A) and (B). In contrast PEG2000/11-MUA@Au-NPs only weakly agglomerate on the CaCO₃ and precipitate non-specifically all over the crystal (see Figure 3.4 (C) and (D)). For the non-dialyzed particles, more than for the dialyzed particles, the absorption of unbound ligand on polar step-edges can also be observed as a 1 nm thick layer of molecules (see Figure S 3.5 A and B). The ligand attachment is also the reason for the surface restructuring observed in Figure S 3.5 (B), Figure S 3.8 and Figure S 3.9 of the Supporting Information.

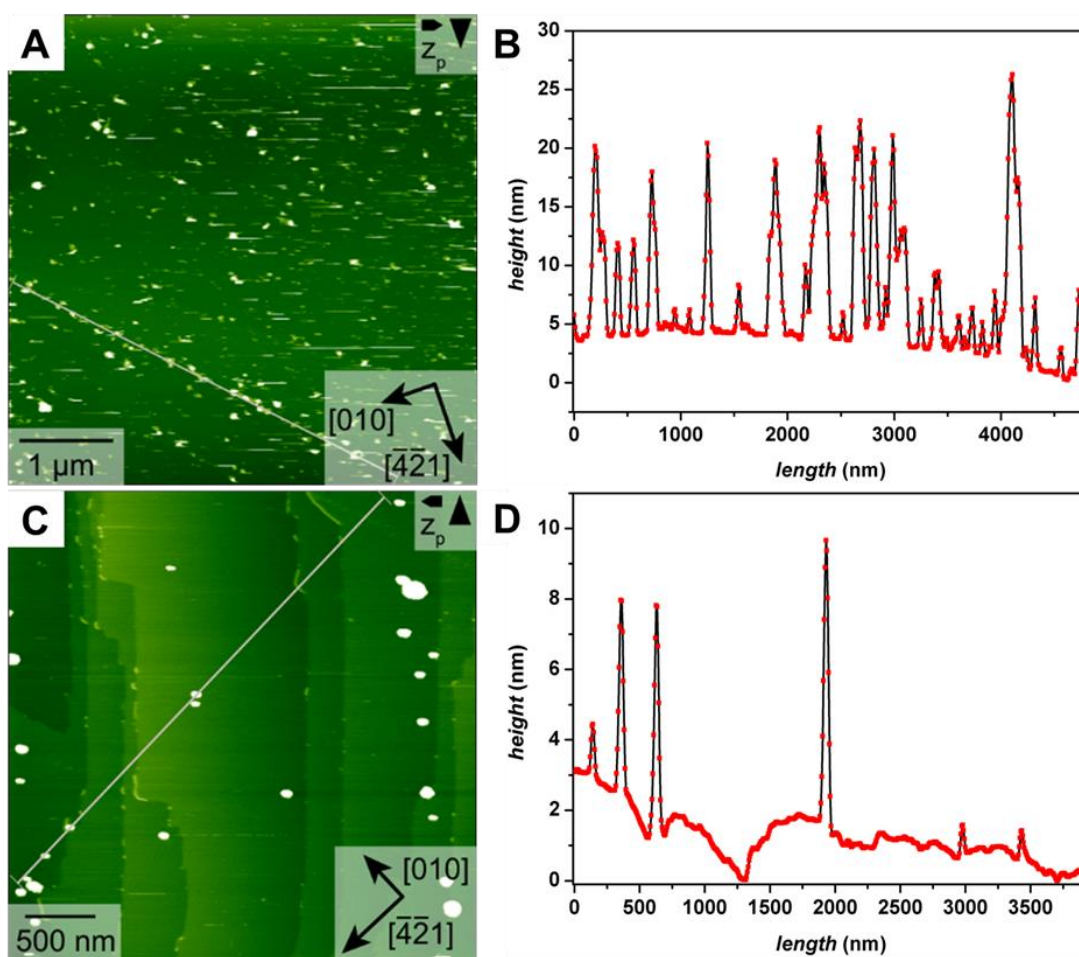


Figure 3.3: AFM images of freshly cleaved (104) calcites under addition of a solution of 0.2 g/L 11-MUA@Au-NPs (A) and dialyzed PEG2000/11-MUA@Au-NPs(C) the profile plots in (B) and (D) showing height of agglomerates lying on the white line. 11-MUA@Au NPs agglomerate to spherical agglomerates of 10-20 nm diameter and height mainly close to polar step edges (B). The dialyzed PEG2000/11-MUA@Au NPs also agglomerate, but much weaker (agglomerates 5-10 nm in height, see (D) and do not interact specifically with step edges. Small amounts of free ligand favor absorption along (010) direction on polar step edges.

To identify the influence of both types of particles on CaCO₃ precipitation crystallizations with the ammonia diffusion method were facilitated. Concentrations between 0.05 and 0.2 g/L of 11-MAU@Au-NPs, dialyzed PEG2000/11-MUA@Au-NPs, non-dialyzed PEG2000/11-MUA@Au-NPs and neat PEG2000/11-MUA ligand in a 5 mM CaCl₂ solution were prepared and used for crystallizations. The neat 11-MUA ligand has not been added to the crystallizations as it is almost insoluble in water at pH 9.75. The 11-MUA@Au-NPs as a solid and rigid polyacid polymer analogue form dumbbell shaped mesocrystals of CaCO₃ with many polar kinks and edges as shown in Figure 3.4 and Figure S 3.6 of the Supporting Information. For the 11-MUA@Au system the increase of nanoparticle concentration increases the degree of inhibition of crystallization significantly. This is due to calcium complexation and nanoparticle absorption on crystalline material as described above. While the composites shown in Figure 3.4 with 0.05 g/L nanoparticle addition give medium sized dumbbell shaped crystals, an increase to 0.1 g/L triggers strong elongation to a cigar shaped crystal morphology. Further increase to 0.2 g/L almost only gives maximum 2 μm edge length rhombohedra with rounded edges of the (12-1) surface (see Figure S 3.6, Supporting Information). For all cases the Raman spectra show Au-NPs binding on the crystal surface and a decrease of crystallinity by the shift and broadening of the 283 cm⁻¹ lattice peak. The nano-crystallinity increases with decrease of nanoparticle concentration, which has also been found in a previous study by Gryzbiowski *et al.* [39] (see Figure S 3.11 (A), Supporting Information).

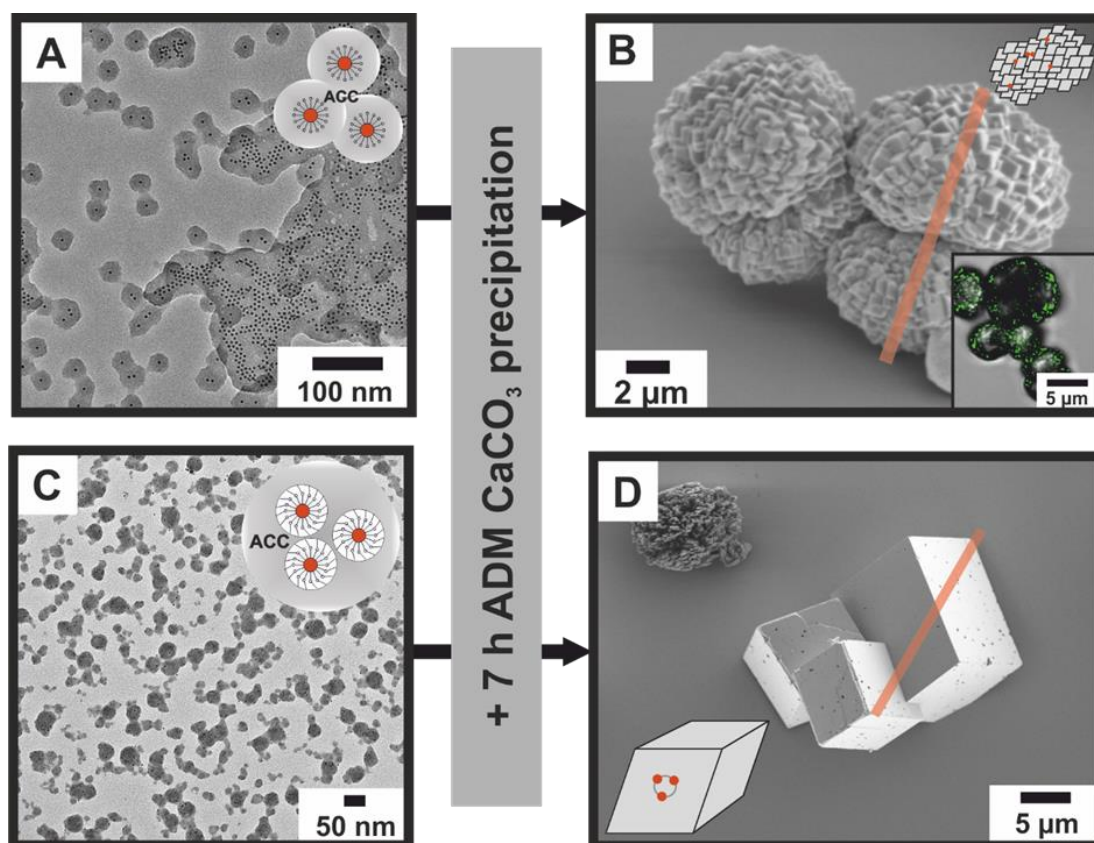


Figure 3.4: Microscopy images of precursors and final crystals of CaCO_3 : (A) Agglomerates of Au-NPs and amorphous CaCO_3 form after 8 h of CaCO_3 crystallization (ADM), that subsequently agglomerate, densify and crystallize under formation of dumbbell shaped mesocrystals of CaCO_3 (B). The inlay locates surficial bound Au-NPs by CLSM of plasmon active particles excited by 532 nm wavelength laser light. Dialyzed PEG2000/11-MUA@Au@ CaCO_3 from amorphous precursor with PEG stabilized NPs showing coronal shielding against direct ACC contact (C) to typical rhombohedral shaped CaCO_3 crystals with slightly rounded step edges and scattered crystal defects (D).

For the dialyzed PEG2000/11-MUA@Au the crystallization result is shown in Figure 3.4 (D) and Figure S 3.7 of the Supporting Information. All samples show only weakly altered rhombohedral calcite crystals. This underlines the effect of binding the PEG2000 on the 11-MUA to have a water soluble but no longer calcium interacting additive. The influence on the crystals turns out to be weak because the solubility of the particles is better in water phase than in solid CaCO_3 , which is totally different in the case of 11-MUA@Au-NPs. This finding is also underlined by the Raman spectra shown in Figure S 3.11 (B), which have much sharper signals than for the 11-MUA@Au-NP@ CaCO_3 composite. The free ligand PEG2000/11-

MUA has a strong influence on the morphology of the calcite as shown by crystallizations before dialysis and with neat ligand without gold particles (see Figure S 3.8 and Figure S 3.9 of the Supporting Information). The microscopic details of the non-dialyzed PEG2000/11-MUA@Au@CaCO₃ composite shown in Figure S 3.10 of the Supporting Information also shows no inclusion of particles. Only small amounts of particles adsorb on the rough surface of the crystals. The influence on the morphology merges with less crystallinity of the CaCO₃ as shown by Raman spectra shown in Figure S 3.11 of the Supporting Information. FIB cut preparation of CaCO₃ crystal from the precipitation with 0.05 g/L 11-MUA@Au-NPs added, gives an insight into the crystalline structure. The core part of the cut crystal contains scattered holes caused by the Kirkendall effect.^[40] Hereby the amorphous to crystalline material transformation that occurred after the outer massive part crystallized results in hole formation due to higher density of crystalline matter. The reason can be visualized by HR-TEM imaging of certain areas of the crystal. The outer, massive part does not contain particles, only surficial bound particles can be found by Raman spectroscopy, CLSM and TEM imaging (see Figure S 3.11 (A), Figure 3.4 (B) and Figure 3.5 (A)). The crystals periphery underwent a fusion process while the core area bears large amounts of Au-NPs. These particles interact through the functionalization with 11-MUA with the crystallizing calcite. A possible structure relationship would be an epitaxial growth of calcites (100) and the expressed Au (111) surfaces of the nanoparticles. This combination is the most favorable combination due to small lattice mismatch of only 0.2%. It can be concluded from Rocking curve XRD measurements that the addition of 11-MUA@Au-NPs causes the large increase of mosaicity. This is due to the oriented growth of nanocrystallites and their interparticular mismatch, caused by the large quantity of included particles (compare Table S 3.1 and Table S 3.2 as well as Figure S 3.12 and Figure S 3.13 of the Supporting Information). For the PEG2000/11-MUA@Au the whole situation is different. After 15 h the final precipitated crystals on the glass slides are not red but transparent. The final crystal morphology is unaffected by the added NPs (see Figure 3.5 B and Figure S 3.7). All concentrations added have weak effects on the crystals size and crystallinity and only show weak absorption of Au-NPs on the crystals surface (see Figure 3.4 and Figure 3.5 as well as Figure S 3.7, Figure S 3.11 (B) of the Supporting Information). The effect on the crystal

size reveals to be much weaker than in the above described 11-MUA case, which is also due to the missing binding of free calcium ions, resulting agglomeration, stabilization of ACC on the NPs surface and epitactic and thus heterogeneous growth of crystalline CaCO_3 . The FIB preparation from the 0.2 g/L PEG2000/11-MUA@Au-NPs CaCO_3 sample gives insight into the crystal cross-section that all over the size looks single crystalline and massive.

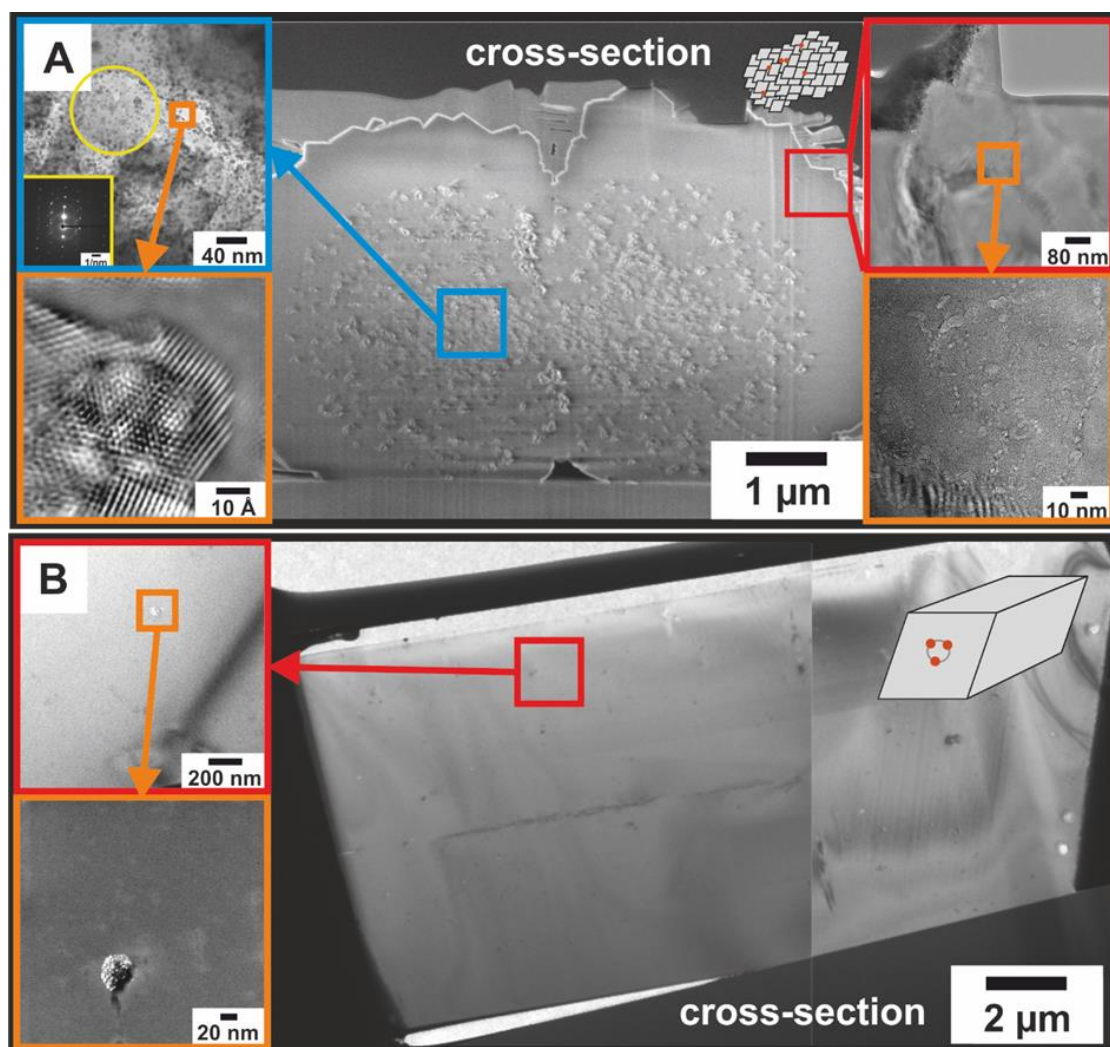


Figure 3.5: HR-TEM analysis of final CaCO_3 crystals : (A) Image assembly on crystallographic details on 11-MUA@Au@ CaCO_3 growth. The cross-section shows two domains inside the crystal of an onion like structure. At the inside widely scattered holes caused by the Kirkendall-effect^[40] from the ACC to calcite transformation (see Figure S 3.11 for Raman spectra) show up. By a closer look (blue and orange box) one can find epitaxy of CaCO_3 (100) on the Au (111) facets (TEM-EDX identification of Au is shown in Figure S 3.13, Supporting Information). This causes nano-crystallin-

ity and formation of a mesocrystal. The outside is built from massive (104) truncated CaCO_3 rhombohedra without inclusions. Agglomerates of Au-NPs are pushed out of the crystal from the outer 1 μm thick area by a fusion process (see the red and orange framed inlay image). SEM-EDX (Figure S 3.12, Supporting Information) also identifies Au-NPs on the polar step edges outside of the crystal. (B) In contrast to the cross-section of 11-MUA@Au@ CaCO_3 almost no holes are observed in the crystallization product for the addition of PEG2000/11-MUA@Au-NPs to the CaCO_3 crystallization. As shown in the red box only around scattered holes a few particles are included as agglomerates (see Figure S 3.14 for STEM-EDX measurements). This causes defects in the rhombohedra of CaCO_3 .

A closer look with HR-TEM shows a much smaller mass of Au-NPs included. Only a few NPs are assembled by unspecific absorption within defects (holes) in the truncating (104) surfaces of the precipitated rhombohedra (Figure 3.5 (B) and inlays). This fact can also be underlined with Rocking curve XRD measurements (compare Figure S 3.14, Table S 3.2 of the Supporting Information). The NPs added have almost no influence on the crystals nano-crystallinity and mosaicity. Instead for free PEG2000/11-MUA ligand and the non-dialyzed particle batch, the Rocking curve measurement shows well pronounced nano-crystallinity and nano-structuring of the samples (compare Table S 3.1 and Table S 3.2 as well as Figure S 3.8, Figure S 3.9 for SEM and for XRD Figure S 3.12 and Figure S 3.16 of the Supporting Information). The dialysis mainly ensures to remove unbound ligand that induces surface restructuring on AFM (104) calcite crystals by face selective absorption (Figure 3.4 and Figure S 3.5 of the Supporting Information). For the non-dialyzed particles as additives also the formation of more vaterite is observed after 15 h precipitation (Figure S 3.6, Supporting Information), which might be caused by free ligand.

3.1.1.4 Conclusion

The integration of Au-NPs covered with 11-MUA as CaCO_3 interacting ligand has been approved in this study. The details on agglomeration of the Au-NPs and microscopic details on CaCO_3 interaction of as functionalized particles have been distinguished for both ligands: 11-MUA and the less Ca^{2+} interacting PEG2000/11-MUA ligand. We have facilitated integration of Au-NPs with a functionalization with ω -thiol carboxylic acids (11-MUA, 18% ligand by mass) into CaCO_3 and clearly

identified integration to be caused by a direct surface interaction of the Au and the CaCO_3 lattices. The presence of a high density of calcium ions and subsequently also carbonate ions induces a close contact precipitation of amorphous CaCO_3 around the 11-MUA@Au-NPs. The material densifies and subsequently crystallizes to dumbbell shaped composite particles with high mechanical brittleness (data not shown). This is caused by nano-crystallinity, misalignment of lattices and the Kirkendall effect, which is due to density increase from ACC to calcite phase. ^[41] Thus integration of nano-sized foreign particles with fitting lattice parameters has been shown to be rather a forming agent for nano-crystalline CaCO_3 composites, than integration of nano-sized objects into a single crystal of CaCO_3 as has been reported for polymer covered NPs. The need of carboxylic acid groups on gold surfaces to trigger epitaxy due to closest contact to ACC has also been proven by secondary functionalization with PEG2000 monomethylether that still ensures Au-NPs to be water soluble. The weaker interactions with calcium ions and polymer layer formation on the Au-NPs make them better soluble in aqueous phase than in densifying ACC, which causes a push-out mechanism. On the non-polar (104) facets an agglomeration of PEG2000/11-MUA@Au-NPs has been found which is in strong contrast to the 11-MUA@Au-NPs. The final crystal is also almost unaffected by the addition of 11-MUA/PEG2000@Au NPs and thus forms single crystalline rhombohedra as shown by AFM, SEM, TEM, titrations and SAXS measurements. We were able to identify carboxylic acid group as a key requirement for surface functionalization of Au-NPs to accomplish the formation process of an Au@ CaCO_3 composite by epitaxy on NP facets. The clue to stabilize ACC, the crystalline materials precursor around the Au-NPs turned out as key achievement and need for inclusion of nanoparticles.

3.1.1.5 Supporting Information

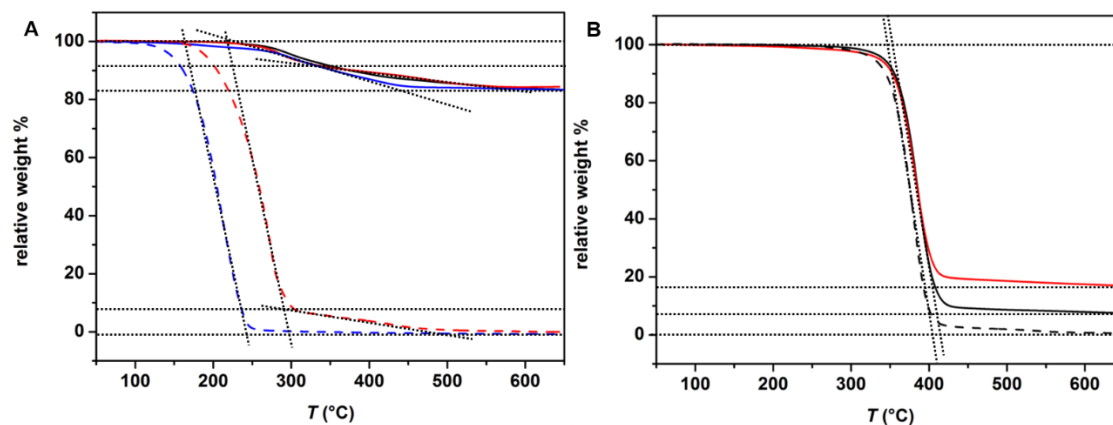


Figure S 3.1: TGA data of 11-MUA@Au-NP samples (A) and PEG2000/11-MUA@Au (B). Dashed lines correspond to ligands Oam (blue) and 11-MUA (red). Solid lines represent NP fractions Oam@Au (blue), 11-MUA@Au-NPs (red directly from synthesis, black washed three times with ethanol). Maximum surface coverage for Oam and thiol ligand 11-MUA is 18 w%. A denser functionalization with the PEG2000/11-MUA ligand (black dashed) on Au-NPs is observed directly after reaction (black solid line) with about 92 w% ligand detected. Hence dialysis of these particles for 72 h in water shows a decrease to 82 w% ligand (red solid line).

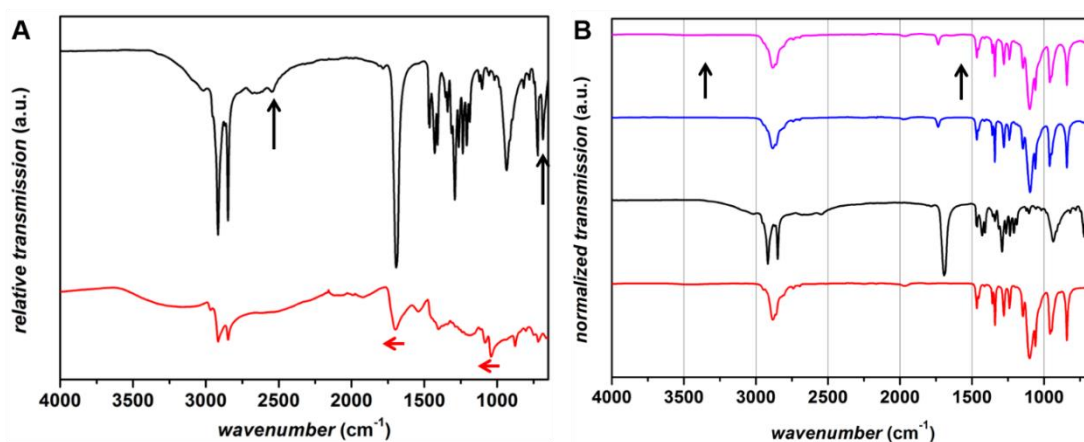


Figure S 3.2: IR spectra of (A) 11-MUA (black) and 11-MUA@Au (red) as raw data in relative transmission. Black arrows highlight symmetrical -S-H and asymmetrical -S-H bending modes at 2550 cm⁻¹ and 655 cm⁻¹ respectively. The shift of -COOH vibrational modes in the red spectrum 11-MUA@Au is due to the strong inter-ligand interactions of the particles. For the PEG-Ligand in (B) the red line shows PEG2000 monomethylether, 11-MUA is shown in black. The mentioned 11-MUA modes can not be any longer observed in IR due to its low concentration (compare blue line for pure PEG2000/11-MUA). Hence the ligand synthesis was identified as successful by adding Au-NPs for functionalization. The particle spectrum in magenta is almost identical with the blue spectrum of the neat ligand. The PEG2000/11-MUA@Au spectrum occurred to be similar even after dialysis and washing, which indicates a successful functionalization by the thiol functionality of the PEG.

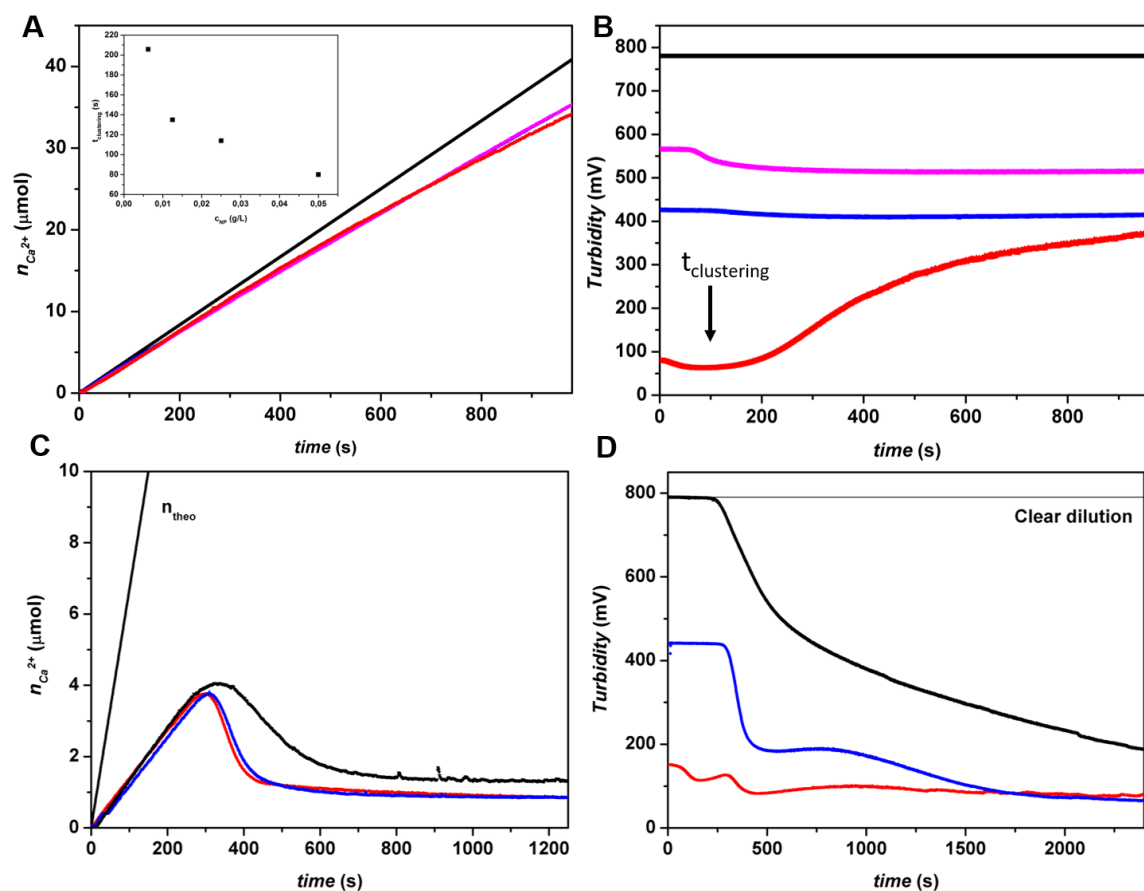


Figure S 3.3: (A, B) Titration of 0.05 g/L TRIS buffered solutions of non-dialyzed PEG2000/11-MUA@Au-NPs (magenta), dialyzed PEG2000/11-MUA@Au-NPs (blue) and 11-MUA@Au NPs (red) with calcium chloride solution at pH 9.75. For all samples lower concentrations were detected than theoretically determined (black line), which can be due to ligand dissociation from surface or conductivity changes of the solution during detection. In plot (B) the turbidity can be used as indicator of absorption and scattering of particles or particle agglomeration in the solutions over the course of time, which corresponds to the amount of added calcium ions. For this sample a continuous increase of the signal can also be observed after clustering which can be addressed to precipitation of particle clusters. Diagrams (C and D) show nucleation titrations of CaCO_3 from carbonate buffer at pH 9.75 by continuous addition of CaCl_2 solution. The color coding is the same as in (A and B). In (C) classical LaMer curves show the nucleation of CaCO_3 . The addition of each functionalized particle batch induces heterogeneous nucleation and early nucleation. Graph (D) shows the corresponding turbidity measurement, which indicates the differences in growth. A smooth decrease in turbidity over a long period of time as in reference (black) identifies nucleation and growth dominated by the homogenous path, while the sharp decrease as in blue indicates heterogeneous nucleation on Au-NPs. For the 11-MUA ligand one can also identify the previous clustering followed by a nucleation event.

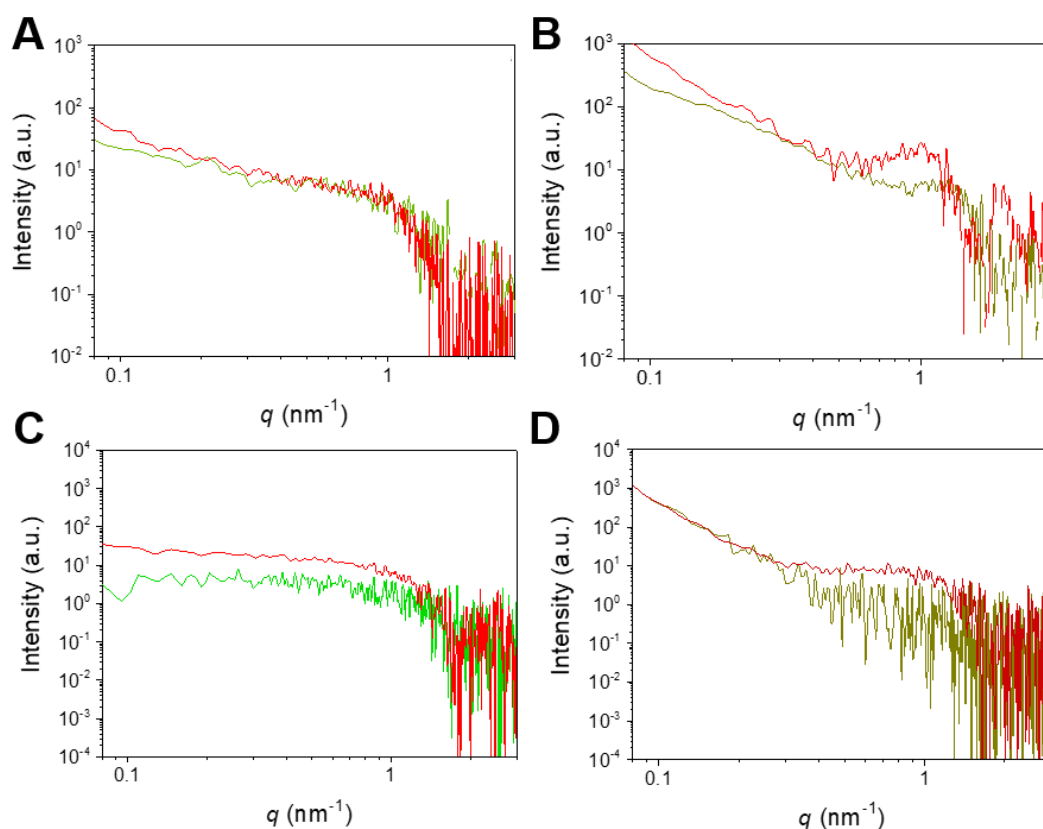


Figure S 3.4: SAXS patterns of (A) 11-MUA@Au-NPs (red) and PEG2000/11-MUA@Au-NPs (green) in TRIS buffer. Graph (B) shows the SAXS pattern if CaCl_2 solution is continuously added to the TRIS buffered particle solution. (C) 11-MUA@Au-NPs (red) and PEG2000/11-MUA@Au-NPs (green) in carbonate buffer at pH 9.75. (D) Pattern if CaCl_2 is added to the solutions. In carbonate buffer the Au-NPs are competing with the bicarbonate ions for Ca^{2+} for complexation or nucleation of CaCO_3 . While for 11-MUA@Au-NPs (red) a structure factor contribution at around 1 nm^{-1} clearly indicates an aggregation of the Au-NPs. This can't be observed for PEG2000/11-MUA@Au-NPs (green) due to small Ca^{2+} concentration compared to the experiments in TRIS buffer (B and D).

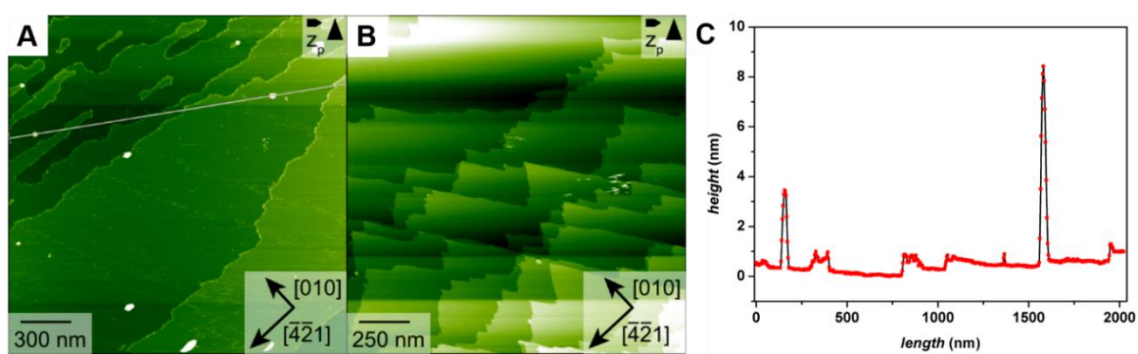


Figure S 3.5: AFM of PEG2000/11-MUA@Au-NPs on (104) calcite shows small amounts of nanoparticles and free ligand attached to surface (A). The free ligand attachment and the functionalized particles differ in height as shown in the profile plot (C). The particles are randomly distributed on the non-polar (104) facet without specific interaction. The ligand is attached to the polar step edges and restructures the surface if neat ligand solution is measured on (104) facet of CaCO_3 (B).

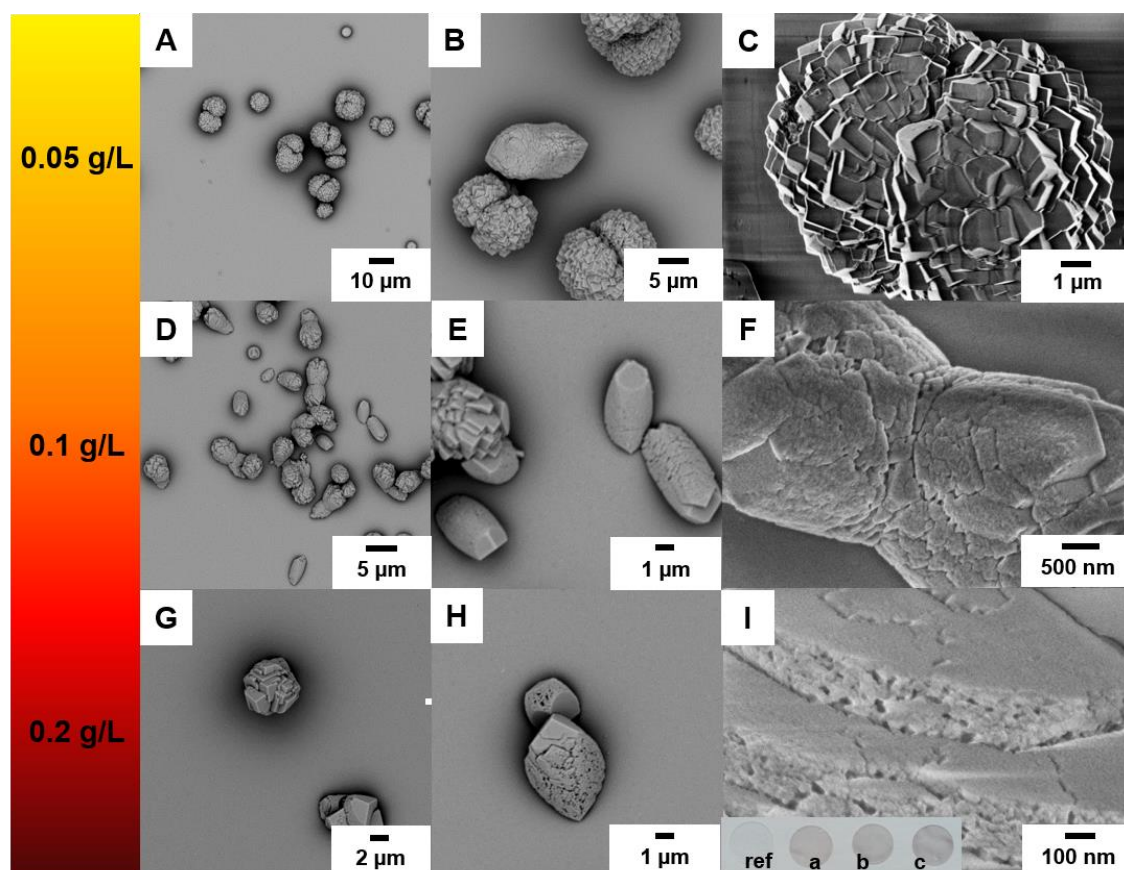


Figure S 3.6: SEM images of CaCO₃ crystals from ammonia diffusion method CaCO₃ precipitation with addition of (A-C) 0.05 g/L (D-F) 0.1 g/L and (G-I) 0.2 g/L of 11-MUA@Au-NPs. Inlay of (I) shows photograph of glass slides with precipitated CaCO₃ crystals shown in SEM images indicating nanoparticle absorption/inclusion by red to violet color of the slides.

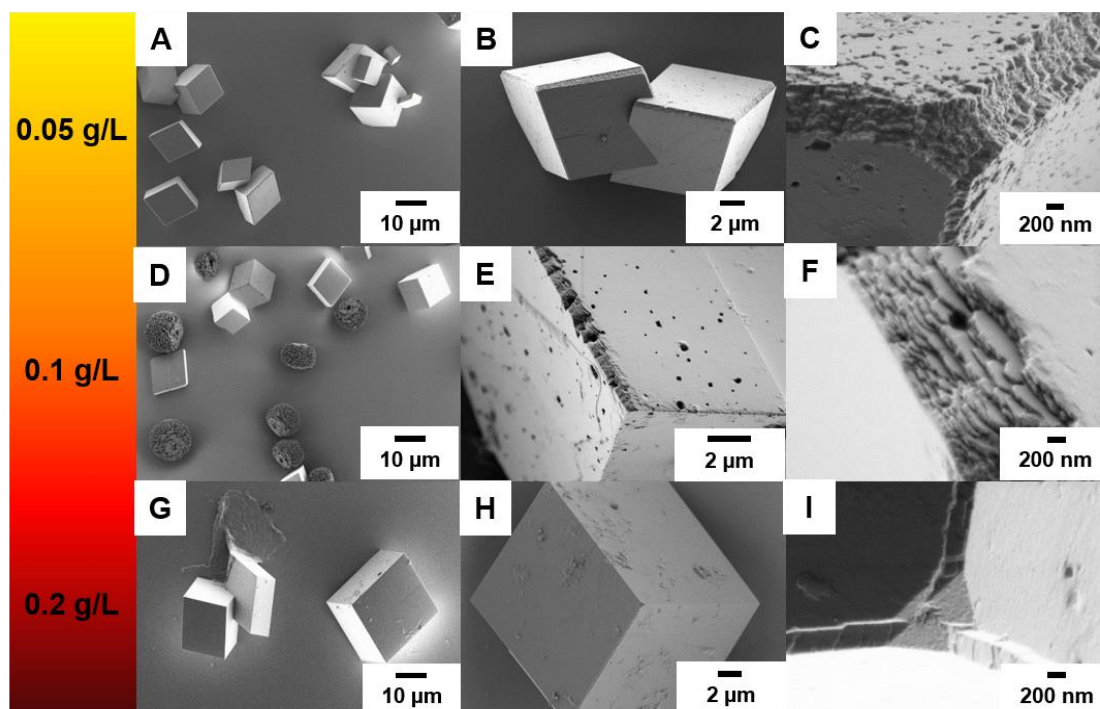


Figure S 3.7: SEM images of CaCO₃ crystals from ammonia diffusion method CaCO₃ precipitation with addition of (A-C) 0.05 g/L (D-F) 0.1 g/L and (G-I) 0.2 g/L of dialyzed PEG2000/11-MUA@Au-NPs.

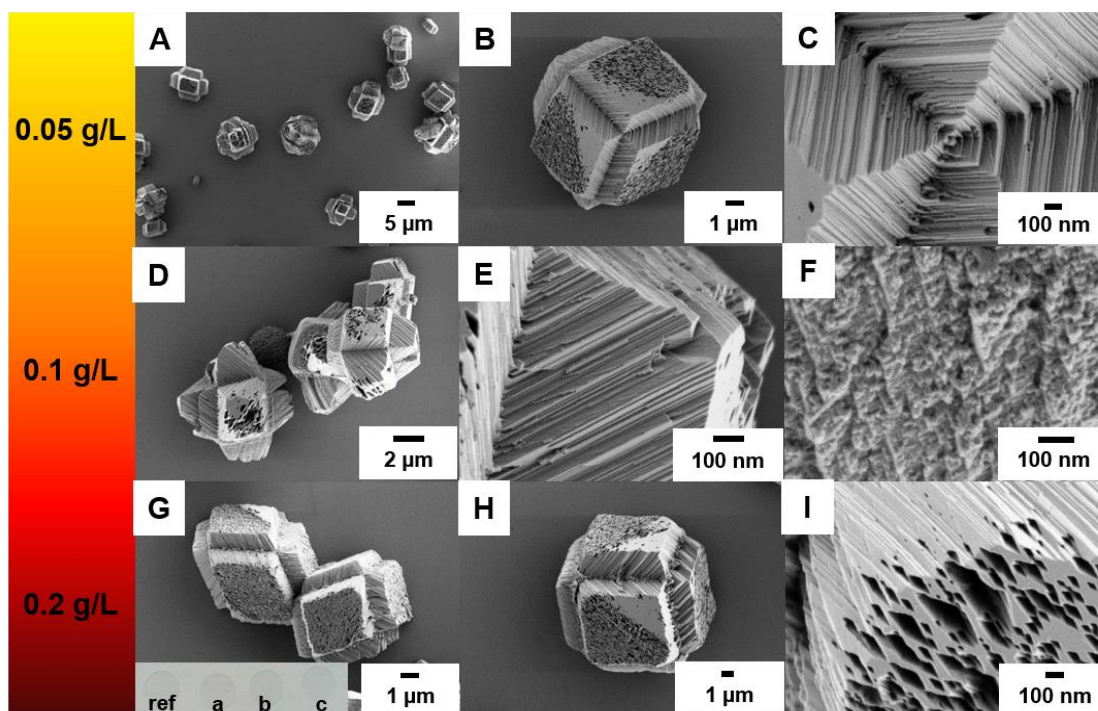


Figure S 3.8: SEM images of CaCO₃ crystals from ammonia diffusion method CaCO₃ precipitation with addition of (A-C) 0.05 g/L (D-F) 0.1 g/L and (G-I) 0.2 g/L of non-dialyzed PEG2000/11-MUA@Au-NPs. Inlay of (G) shows photograph of glass slides with precipitated CaCO₃ crystals shown in SEM images.

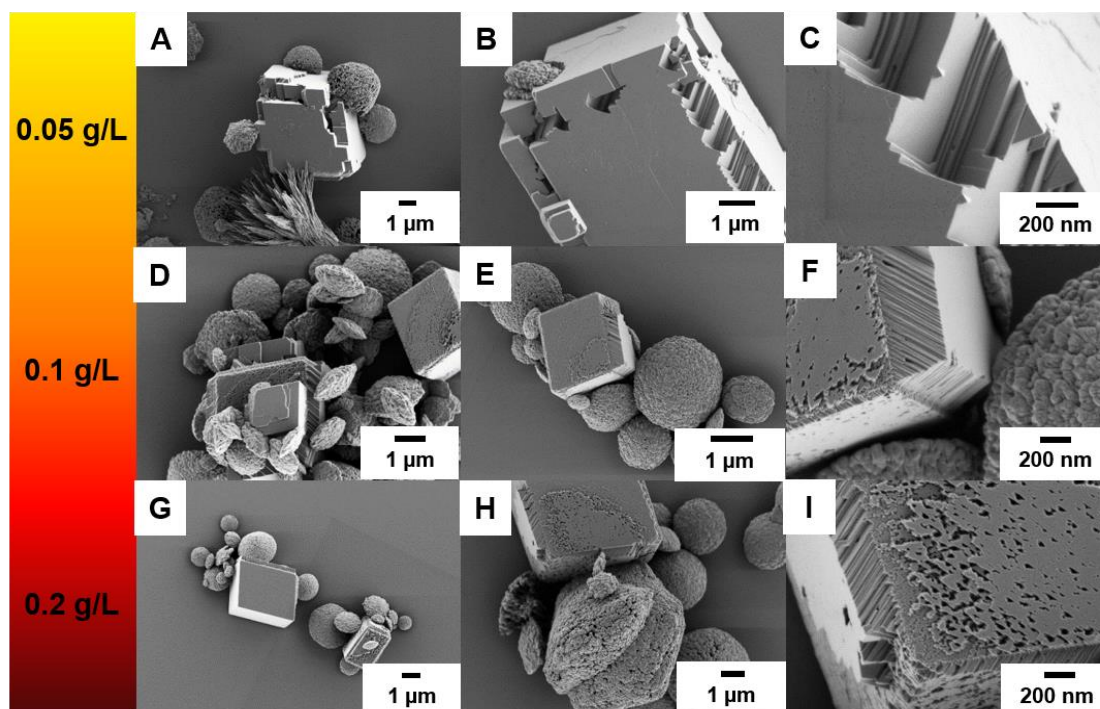


Figure S 3.9: SEM images of CaCO₃ crystals from desiccator experiments with addition of (A-C) 0.05 g/L (D-F) 0.1 g/L and (G-I) 0.2 g/L of PEG2000/11-MUA ligand and increasing zoom-in on kinks from left to right. The main polymorph changes with increasing amount of PEG2000/11-MUA from calcite to vaterite that indicates an inhibition of crystallization.

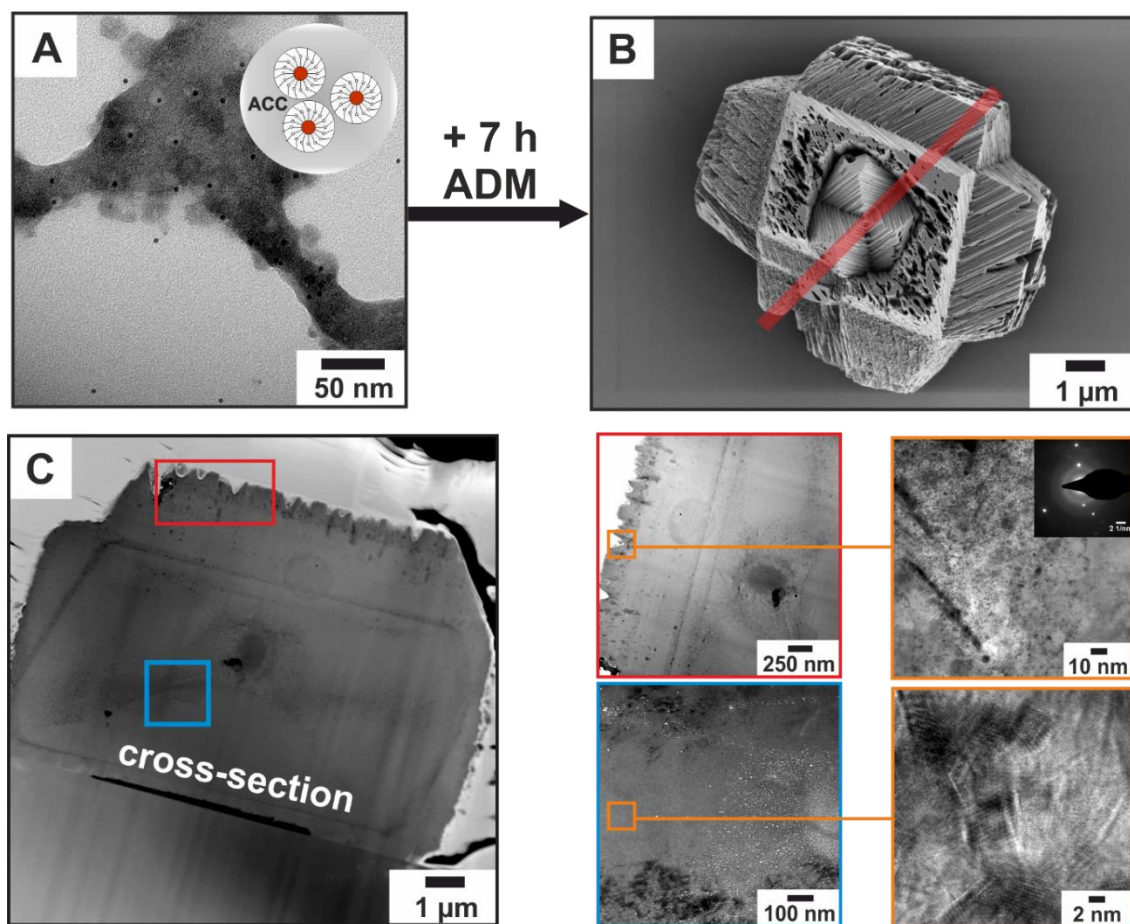


Figure S 3.10: HR-TEM images of (A) agglomerated ACC around non-dialyzed PEG2000/11-MUA@Au-NPs after 8 h of desiccator crystallization (ADM). The polymer corona is larger than for the dialyzed sample shown in the main paper Figure 3.4. (B) Exemplary crystal after 15 h ammonia diffusion method CaCO₃ precipitation with beechnut shape. Note the high amount of surface kinks and holes (red line: cut of cross-section). (C) STEM overview image of the cross-section with areas of interest for detailed lamella analysis. The red box of the crystal surface area shows cross-section of wholes in STEM with absorbed Au-NPs on the surface. The core area shows nano-crystalline CaCO₃ with inclusions of polymer identified in STEM mode (light areas).

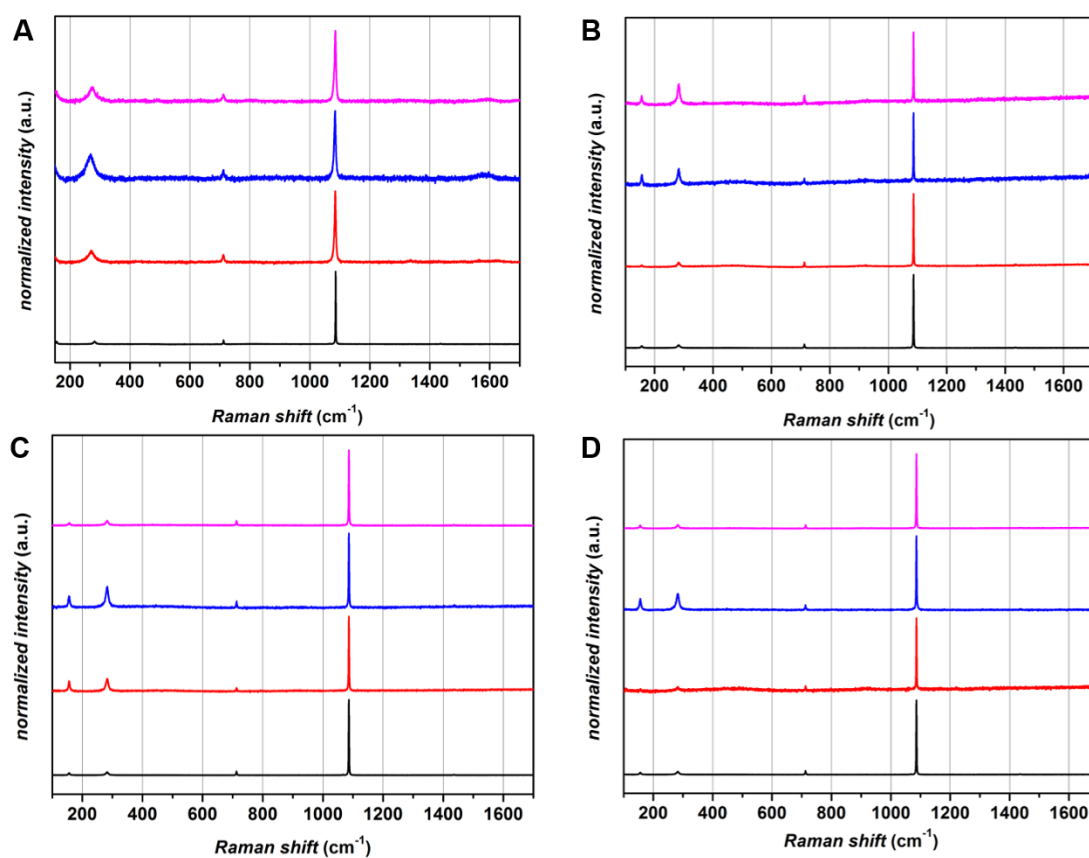


Figure S 3.11: Raman spectra of CaCO₃ crystals (I) 11-MUA@Au-NP, (II) PEG2000/11-MUA@Au-NP dialyzed, (III) PEG2000/11-MUA@Au-NP non-dialyzed and (IV) PEG2000/11-MUA@Au-NP blank with addition of no particles (black), 0.05 g/L (red), 0.1 g/L (blue) and 0.2 g/L (magenta). Au-NP occlusion of 11-MUA@Au-NPs is indicated by bands 1550-1650 cm⁻¹ and peak shift and broadening of the lattice peak at 283 cm⁻¹.

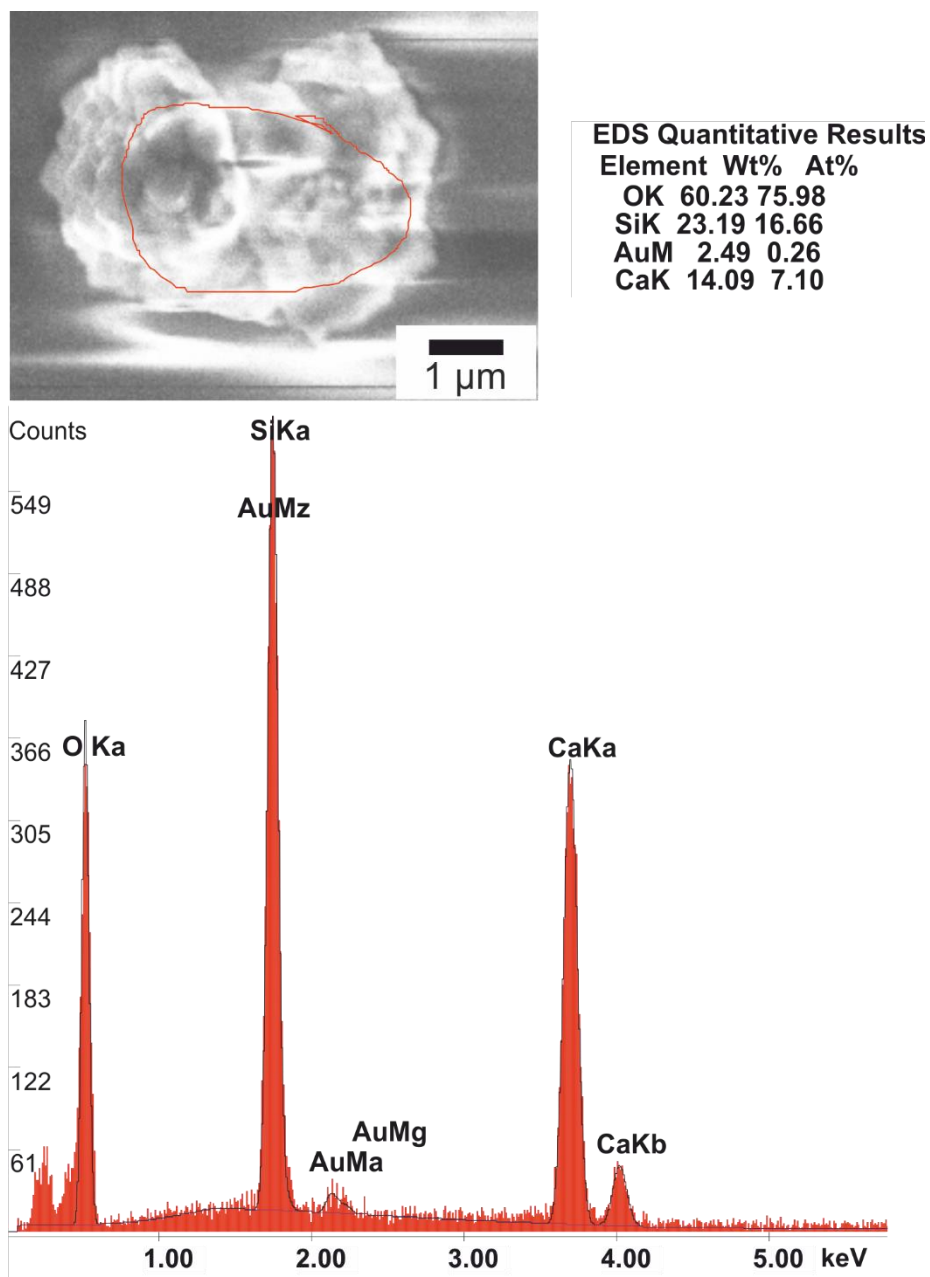


Figure S 3.12: SEM-EDX of surface of final mesocrystal from precipitation of 11-MUA@Au-NPs in the desiccator experiment over 15h. Agglomerates of gold nanoparticles found on the surface.

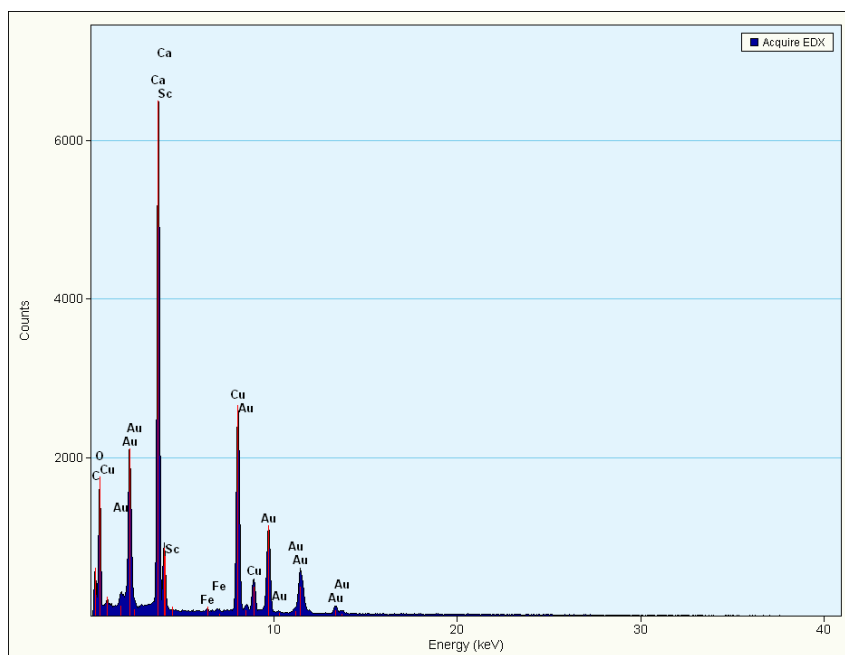


Figure S 3.13: TEM-EDX of surface of core area of cross-section of mesocrystal from precipitation of 11-MUA@Au-NPs in the desiccator experiment of 15h duration.

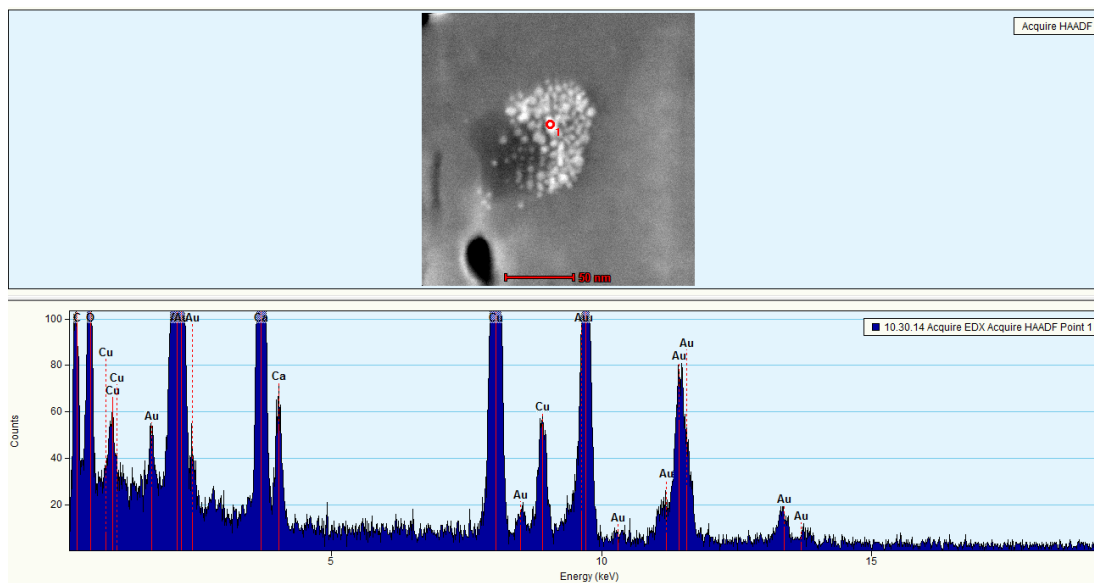


Figure S 3.14: TEM-EDX of occluded nanoparticles crystal from precipitation of CaCO_3 with PEG2000/11-MUA@Au-NPs in the desiccator experiment of 15h duration.

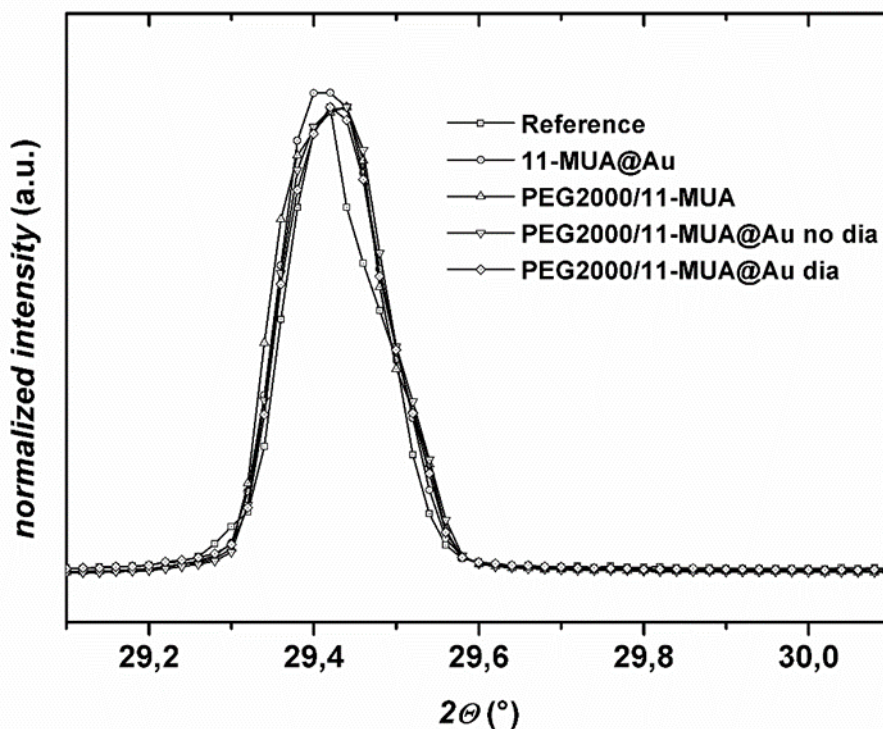


Figure S 3.15: XRD 2θ scan of calcites (104) reflex for different crystal samples with as labeled additives added to the crystallizations. For all samples Gaussian fits were used to find the reflex maximum and FWHM for average crystallite size determination shown in Table S 3.1.

Table S 3.1: Calculations for 2θ scans of reference example and calcite precipitated with 0.2 g/L of differently functionalized Au-NPs. FWHM of the reflex increases if any additive is added. This means a smaller average crystal size within the crystal assemblies is present.

Sample	FWHM (°)	d (nm)	2θ (°)
Reference	0.120	76.1	29.42
11-MUA@Au	0.142	61.3	29.41
PEG2000/11-MUA	0.152	60.1	29.41
PEG2000/11-MUA@Au no dia	0.149	61.3	29.41
PEG2000/11-MUA@Au dia	0.146	62.5	29.41

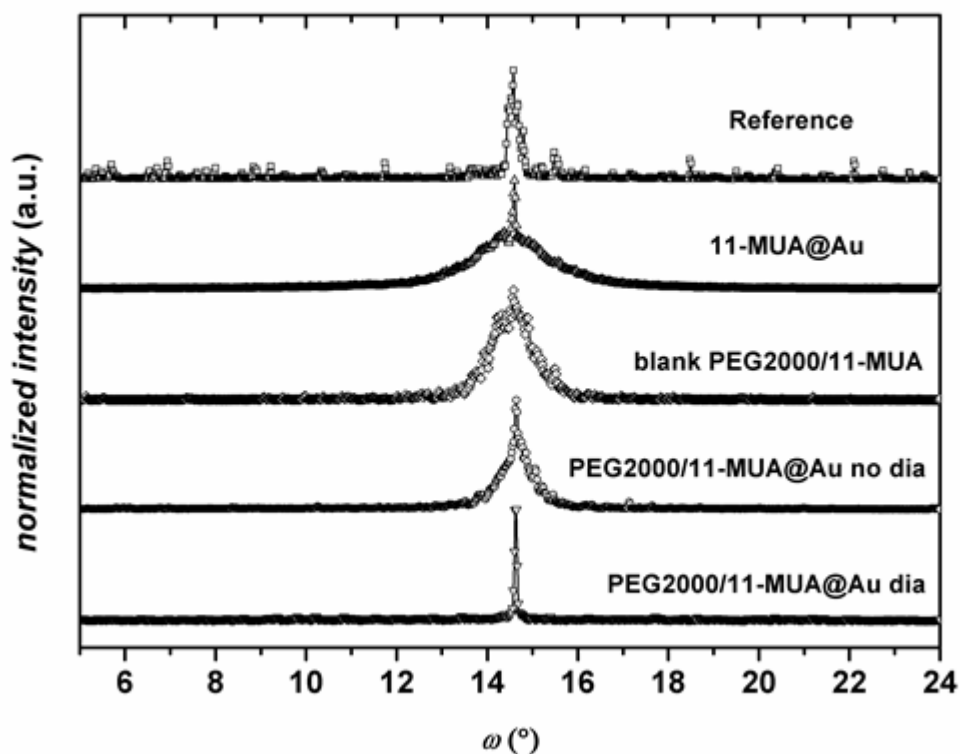


Figure S 3.16: Rocking curve analysis in the range of 4° and 24° ω angle. The 2θ angle was kept constant at of 29.42° to analyze the (104) truncated nano-crystals of the precipitated CaCO_3 crystals. For the reference sample a sharp reflex indicates well oriented crystallites in the sample. The side reflections result from random orientation of crystals on the glass substrate. For addition of 11-MUA@Au-NPs the main reflex is sharper than the reference sample, which indicates low mosaicity of parts of the crystals, which can be assigned to the (104) truncation of the dumbbell structures. The nano-crystalline interior of the CaCO_3 crystals, causes large mosaicity background signal. For the CaCO_3 formed with addition of PEG2000/11-MUA ligand (see Figure S 3.8 and Figure S 3.9 for nano-structuring) also large mosaicity is measured, which might be due to the incooperation of the polymer into grain-boundaries of the mesocrystals. If the polymer is bound to Au-NPs and added to the CaCO_3 crystallization procedure without dialysis, still large mosaicity is observed (see Table S 3.2 for calculations). If this type of NPs is dialyzed and added to the crystallization almost no influence and nice oriented (104) crystals of CaCO_3 can be found. This is due to the small amount of free polymer in the particle batch and also the very weak interaction of the particles with the CaCO_3 substrate (see Figure 3.3, Figure 3.4 and Figure 3.5 of the main paper).

Table S 3.2: Calculations from Gaussian fits for Rocking curve data. All samples show reflections of different FWHM and small variations in the ω angle. Addition of 11-MUA@Au-NPs causes large mosaicity with FWHM = 1.904°. Hence a well oriented sharp reflex with a FWHM value of 0.145° is also observed and assigned to the nicely crystalline (104) rhombohedra truncating the surface. The addition of PEG2000/11-MUA with a FWHM value of 2.036° and 0.859° has large effect on the mosaicity of the mesocrystals. By functionalization of Au-NPs with PEG2000/11-MUA the effect of the additive weakens but is still present if the particles are not dialyzed prior their use. The mosaicity mainly has its origin in free unbound polymer influencing the crystal structure of CaCO₃ as shown in Figure S 3.8 and Figure S 3.9. The dialysis of the particles ensures removing of the unbound polymer from the particles and thus results in an even sharper and more oriented reflex than the reference sample is with FWHM of 0.055°. As shown in the main paragraph, there is almost no structural influence of the CaCO₃ crystals by addition of dialyzed PEG2000/11-MUA@Au particles. For all samples the ω angle difference is almost zero for all samples, which are weakly influenced by the additive. A shift of the reflex to smaller angles is only observed if 11-MUA@Au or if neat PEG2000/11-MUA ligand is added to the crystallization.

Sample	<i>FWHM</i> (°)	ω (°)	ω_{theo} (°)	$\Delta\omega$ (°)
Reference	0.251	14.63	14.7	0.07
11-MUA@Au	0.145	14.59	14.7	0.11
	1.904	14.53	14.7	0.17
PEG2000/11-MUA	0.859	14.55	14.7	0.15
	2.036	14.55	14.7	0.15
PEG2000/11-MUA@Au no dia	0.597	14.66	14.7	0.04
PEG2000/11-MUA@Au dia	0.055	14.63	14.7	0.07

3.1.1.6 References

- [1] S. Borukhin, L. Bloch, T. Radlauer, A. H. Hill, A. N. Fitch, B. Pokroy, *Adv. Funct. Mater.* **2012**, *22*, 4216–4224.
- [2] D. L. Masica, S. B. Schrier, E. A. Specht, J. J. Gray, *J. Am. Chem. Soc.* **2010**, *132*, 12252–12262.
- [3] B. Kowalczyk, K. J. M. Bishop, I. Lagzi, D. Wang, Y. Wei, S. Han, B. A. Grzybowski, *Nat Mater* **2012**, *11*, 227–232.
- [4] T. Schüler, J. Renkel, S. Hobe, M. Susewind, D. E. Jacob, M. Panthöfer, A. Hoffmann-Röder, H. Paulsen, W. Tremel, *J. Mater. Chem. B* **2014**, *2*, 3511–3518.
- [5] L. Addadi, S. Weiner, *PNAS* **1985**, *82*, 4110–4114.
- [6] M. Yáñez, J. Gil-Longo, M. Campos-Toimil, *Adv. Exp. Med. Bio.* **2012**, *740*, 461–482.
- [7] J. Yu, M. Lei, B. Cheng, X. Zhao, *J. Solid State Chem.* **2004**, *177*, 681–689.
- [8] M. Dietzsch, M. Barz, T. Schüler, S. Klassen, M. Schreiber, M. Susewind, N. Loges, M. Lang, N. Hellmann, M. Fritz, K. Fischer, P. Theato, A. Kühnle, M. Schmidt, R. Zentel, W. Tremel, *Langmuir* **2013**, *29*, 3080–3088.
- [9] D. Gebauer, H. Cölfen, A. Verch, M. Antonietti, *Adv. Mater.* **2009**, *21*, 435–439.
- [10] J. Ihli, Y.-Y. Kim, E. H. Noel, F. C. Meldrum, *Adv. Funct. Mater.* **2013**, *23*, 1575–1585.
- [11] D. Ren, Q. Feng, X. Bourrat, *Micron* **2011**, *42*, 228–245.
- [12] R.-Q. Song, H. Cölfen, *Cryst. Eng. Comm.* **2011**, *13*, 1249.
- [13] F. C. Meldrum, S. T. Hyde, *J. Cryst. Growth* **2001**, *231*, 544–558.
- [14] Y. Politi, D. R. Batchelor, P. Zaslansky, B. F. Chmelka, J. C. Weaver, I. Sagi, S. Weiner, L. Addadi, *Chem. Mater.* **2010**, *22*, 161–166.
- [15] W. Mejri, I. Ben Salah, M. M. Tlili, *Cryst. Res. Tech.* **2015**, *50*, 236–243.
- [16] A. N. Kulak, M. Semsarilar, Y.-Y. Kim, J. Ihli, L. A. Fielding, O. Cespedes, S. P. Armes, F. C. Meldrum, *Chem. Sci.* **2013**, *5*, 738–743.
- [17] A. N. Kulak, P. Yang, Y.-Y. Kim, S. P. Armes, F. C. Meldrum, F. C. Meldrum, *Chem. Commun* **2014**, *2014*, 67–69.

-
- [18] D. L. Olgaard, B. Evans, *J. Am. Ceram. Soc.* **1986**, *69*, C-272-C-277.
- [19] W.-J. Shih, Y.-F. Chen, M.-C. Wang, M.-H. Hon, *J. Cryst. Growth* **2004**, *270*, 211–218.
- [20] A. Buob, *Am. Mineral.* **2006**, *91*, 435–440.
- [21] G. Mie, *Ann. Phys.* **1908**, *25*, 377–445.
- [22] A. C. Templeton, J. J. Pietron, R. W. Murray, P. Mulvaney, *J. Phys. Chem. B* **2000**, *104*, 564–570.
- [23] T. Wang, H. Cölfen, M. Antonietti, *J. Am. Chem. Soc.* **2005**, *127*, 3246–3247.
- [24] R. C. Kang, Y.-Y. Kim, P. Yang, W. Cai, H. Pan, A. N. Kulak, J. L. Jau, J. DeYoreo, *Nat. Commun.* **2016**, *7*, 10187–10194.
- [25] J. Stettner, P. Frank, T. Griesser, G. Trimmel, R. Schennach, E. Gilli, A. Winkler, *Langmuir* **2009**, *25*, 1427–1433.
- [26] P. Supaphol, W. Harnsiri, J. Junkasem, *J. Appl. Polym. Sci.* **2004**, *92*, 201–212.
- [27] J. Küther, R. Seshadri, G. Nelles, W. Assenmacher, H.-J. Butt, W. Mader, W. Tremel, *Chem. Mater.* **1999**, *11*, 1317–1325.
- [28] I. Lee, S. W. Han, H. J. Choi, K. Kim, *Adv. Mater.* **2001**, *13*, 1617–1620.
- [29] I. Lee, S. W. Han, S. Lee, H. Choi, K. Kim, *Adv. Mater.* **2002**, *14*, 1640–1642.
- [30] A. M. Kalsin, M. Fialkowski, M. Paszewski, S. K. Smoukov, K. J. M. Bishop, B. A. Grzybowski, *Science* **2006**, *312*, 420–424.
- [31] S. Ristig, D. Kozlova, W. Meyer-Zaika, M. Epple, *J. Mater. Chem. B* **2014**, *2*, 7887–7895.
- [32] S.-S. Wang, A.-W. Xu, *Cryst. Growth Design* **2013**, *13*, 1937–1942.
- [33] S. Peng, Y. Lee, C. Wang, H. Yin, S. Dai, S. Sun, *Nano Res.* **2008**, *1*, 229–234.
- [34] L. Addadi, Moradian, J. , Shay, E., Maroudas, N.G., S. Weiner, *PNAS* **1987**, *84*, 2732–2736.
- [35] C. Beato, M. S. Fernández, S. Fermani, M. Reggi, A. Neira-Carrillo, A. Rao, G. Falini, J. L. Arias, *Cryst. Eng. Comm.* **2015**, *17*, 5953–5961.

- [36] M. Schreiber, M. Eckardt, S. Klassen, H. Adam, M. Nalbach, L. Greifenstein, F. Kling, M. Kittelmann, R. Bechstein, A. Kühnle, *Soft Matter* **2013**, *9*, 7145–7149.
- [37] S. Rode, R. Stark, J. Lübbe, L. Tröger, J. Schütte, K. Umeda, K. Kobayashi, H. Yamada, A. Kühnle, *Rev. Sci. Instr.* **2011**, *82*, 73703–73711.
- [38] H. Adam, S. Rode, M. Schreiber, K. Kobayashi, H. Yamada, A. Kühnle, *Rev. Sci. Instr.* **2014**, *85*, 23703–23711.
- [39] D. Wang, R. J. Nap, I. Lagzi, B. Kowalczyk, S. Han, B. A. Grzybowski, I. Szleifer, *J. Am. Chem. Soc.* **2011**, *133*, 2192–2197.
- [40] A. G. Guy, *Zeitschr. Metall.* **1967**, *58*, 164-168.
- [41] S. K. Ghosh, T. Pal, *Chem. Rev.* **2007**, *107*, 4797–4862.

3.1.2 Seed-mediated one-pot synthesis of Au@Fe₃O₄ Janus Particles

The article “Seed-mediated one-pot synthesis of Au@Fe₃O₄ Janus Particles” will be submitted to *Crystal Engineering Communication* by the Royal Society of Chemistry. The following chapter is based on the latest version of the manuscript and its supporting information.

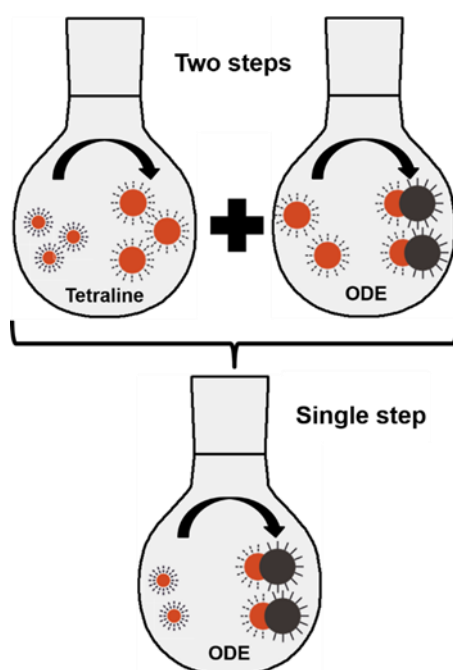


Figure 3.6: Scheme of simplification step for synthesis of Au@Fe₃O₄ Janus particles. A seed growth step for large Au nanoparticle formation in tetraline with a subsequent washing and seed mediated growth of single Fe₃O₄ domains on these gold seeds is conducted in the literature synthesis. The new approach combines both reactions in a single reaction for synthesis with octadecene as solvent to produce a high yield of similar shaped nanoparticles.

The synthesis of Janus-type Au@Fe₃O₄ nanoparticles (NPs) with large gold domains requires two separate reactions with a purification step in between. The large number of reaction variables limits the reproducibility, yield and morphological control of the products. Thus a one-pot synthesis of highly monodisperse Au@Fe₃O₄ Janus particles with large Au domains grown from Au seeds was developed. The Au domains serve as epitaxial templates the formation of the Fe₃O₄ domains during the thermal decomposition of Fe(CO)₅ in the presence of oleic acid.

Phase composition, morphology and optical properties of the Au@Fe₃O₄ Janus particles were characterized by UV-Vis spectroscopy, DLS, HR-TEM and PXRD. This one-step synthesis has a certain potential for being scaled-up by microfluidics.

3.1.2.1 Introduction

Janus-type heteroparticles composed of organic ^[1–3] or inorganic ^[4,5] materials can impart two or more physical properties to a single particle like magnetism, ^[6,7] optical absorption, ^[8,9] electrochemical anisotropy, ^[10] hydrophilicity, hydrophobicity, ^[11,12] or even different catalytic activity ^[13] due to chemical surface anisotropy. ^[14] This makes them versatile nano-tools ^[3] with applications as surfactant, ^[15] drug carrier ^[14,16,17] or diagnosis tool. ^[18,19] The morphology of heteroparticles can range from rod- to disc-like, stars, dumbbell, cubic, spherical or wire-like. ^[20,21] The particles can exhibit motility by virtue of a propulsion force, ^[22] controlling their orientation, ^[23] or they can have them anisotropic optical ^[24] or magnetic properties. ^[6,25] Janus particles (JPs) are not only intriguing for basic science, but also in biochemistry, physics, and colloidal chemistry, because of practical applications in electronic devices ^[26] and for optical ^[24] or magnetic biosensors. ^[27] Their surface chemistry allows to enhance the particle anisotropy, e.g. to study the rheology in the living cell or as a tracer in microfluidics. ^[28,29]

Inorganic heteroparticles can be synthesized e.g. by thermal ^[30] or electrochemical ^[31] decomposition of metal-oxide or metal sulfide precursor on a crystalline metal nucleus with lattice parameters suitable for epitaxial growth. ^[32–34] Many possible combinations of binary or ternary materials ^[35] like Au@Ag, ^[36] Au@Fe₃O₄, ^[37,38] Pt@Fe₃O₄, ^[26] Au@ZnO, ^[39] Pd@Fe₂O₃, ^[40,41] Au@SiO₂, ^[42] Fe₃O₄@SiO₂, ^[43] Ni@Fe₂O₃, ^[44] Cu@Fe₃O₄ ^[45] have been reported. Orthogonal functionalization of the domains relies on thiol chemistry for the metals (especially gold) and carboxylate/catecholate chemistry for metal oxide (often Fe₃O₄) surface, respectively. ^[17,46,47] This allows tailoring their use as MRT diagnosis tool or cancer cell agent with low cytotoxicity for a variety of cell lines. ^[48] The synthesis of Au@Fe₃O₄ JPs bases on a strategy that involves the synthesis of Au NPs in cyclohexane as seeding particles for a sequentially following growth step via reductive decomposition of HAuCl₄ in tetraline and Oam. ^[49] The subsequent epitaxial growth of Fe₃O₄ on the Au domains ^[50] in 1-octadecene (ODE) by thermal decomposition of iron pen-

tacarbonyl in the presence of the capping agents oleic acid (Oac) ^[51] and oleylamine (Oam) ^[52] ensures the formation of a single Fe₃O₄ domain on an Au (111) facet. ^[38,53] The synthesis of JPs is often tedious, and the yields and reproducibility of the synthesis call for improvement. The maximum yield of a batch starting with 20 mg Au seeds was ~ 60 mg of Janus particles. The need of many different reaction agents and solvents as well as temperature programs preclude a high reproducibility of the reaction. Therefore, a simple one-step synthesis with the potential for scale-up (e.g. by microfluidics) is an important goal. This contribution presents a one-step synthesis that allows the formation of large Au nanoparticles from Au seeds that serve subsequently as a template for the epitaxial growth of the Fe₃O₄ domain in a one-pot reaction.

3.1.2.2 Experimental

Materials

Chloroauric acid dihydrate (99.999% trace metals basis, abcr GmbH), borane *tert*-butylamine complex, (97%, Sigma Aldrich), $\text{Fe}(\text{CO})_5$ (>99%, Sigma Aldrich), octadecene (>80% techn., Acros), oleylamine (>50%, TCI), oleic acid (>90% techn., Sigma Aldrich), cyclohexane (p.A., Fisher scientific), ethanol (p.A., Fisher scientific), acetone (>99%, Sigma Aldrich) and isopropanol (>99%, Sigma Aldrich) were used as received without further purification.

Synthesis of Au nanoparticles

All reactions were carried out using standard Schlenk techniques with argon as inert gas. Gold seed nanoparticles (Au NPs) were synthesized using a modified procedure reported by Peng *et al.* [49] Au NPs were synthesized at room temperature (RT). The process of washing has been improved by adding 5% of Oam to a 1:1 mixture of EtOH:MeOH (that was used for Au NP precipitation) in order to prevent aggregation. The product was precipitated from the solution by centrifugation (9000 rpm, 10 min, RT), washed one with EtOH:MeOH (1:1 + 5% Oam) and redispersed in octadecene to obtain a stock solution that was stored at 7 °C.

Synthesis of Au@Fe₃O₄ heterodimer JPs

The Au NPs were diluted in ODE and used as seeds. 1 mg of Oam capped seeds were diluted from the stock solution in 20 mL of ODE and 4 mL of Oam. 23.6 mg (0,07 mmol) of $\text{HAuCl}_4 \cdot 2 \text{H}_2\text{O}$ were added in a three-necked round bottom flask and stirred magnetically while the solution was heated to 100 °C in argon atmosphere for 40 minutes and kept at this temperature for another 120 minutes. Subsequently, 0.05 mL (0.0038 mmol) of $\text{Fe}(\text{CO})_5$ were added simultaneously with 4 mL of Oac before the reaction mixture was heated to 310 °C within 30 min and kept at this temperature for 120 min (see Figure 1 (II) for the temperature program). The Janus particles formed during this reaction were separated by adding isopropanol

and washing three times with acetone/isopropanol mixtures and subsequent centrifugation (9000 rpm, 10 min, RT). The overall yield was about 30 mg of Oam/Oac capped Au@Fe₃O₄ JPs per batch.

Instrumentation

Copper 400 mesh carbon film TEM grids were received from Plano GmbH, Wetzlar, Germany. TEM images were recorded on a FEI Technai F20 or T12, both equipped with a 4K CCD camera and a FEG or LaB₆ cathode working at 200 kV or 120 kV acceleration voltage, respectively. The HR-TEM was equipped with an EDAX EDX system and a STEM detector by FEI to facilitate dark field EDX line scans with the TIA software.

XRD measurements were carried out on a STOE STADI P in transmission geometry, Mo-K α radiation and a DECTRIS MYTHEN 1K detector. The sample was prepared on acetate foil with dried powder of particles. Rietveld refinements were performed with TOPAS Academic V6 applying the fundamental parameter approach.
[54]

UV-VIS-spectra were collected on a Varian Cary 5000 UV-VIS/NIR-spectrometer equipped with a temperature-controlled stage for measurements at 25°C. A standard quartz glass cuvette with an optical window of 300 – 900 nm was used for UV-Vis spectroscopy.

All DLS experiments were performed on an instrument from ALV GmbH, Germany consisting of an electronically controlled goniometer and an ALV-5000 multiple tau full-digital correlator. A He-Ne laser with a wavelength of 632.8 nm and output power of 25 mW (JDS Uniphase, USA, Type 1145P) was used as the light source. The nanoparticle solutions were filtered through Millex-VV 100 nm filters into cylindrical quartz cuvettes (18 mm core diameter, Hellma, Germany).

3.1.2.3 Result & Discussion

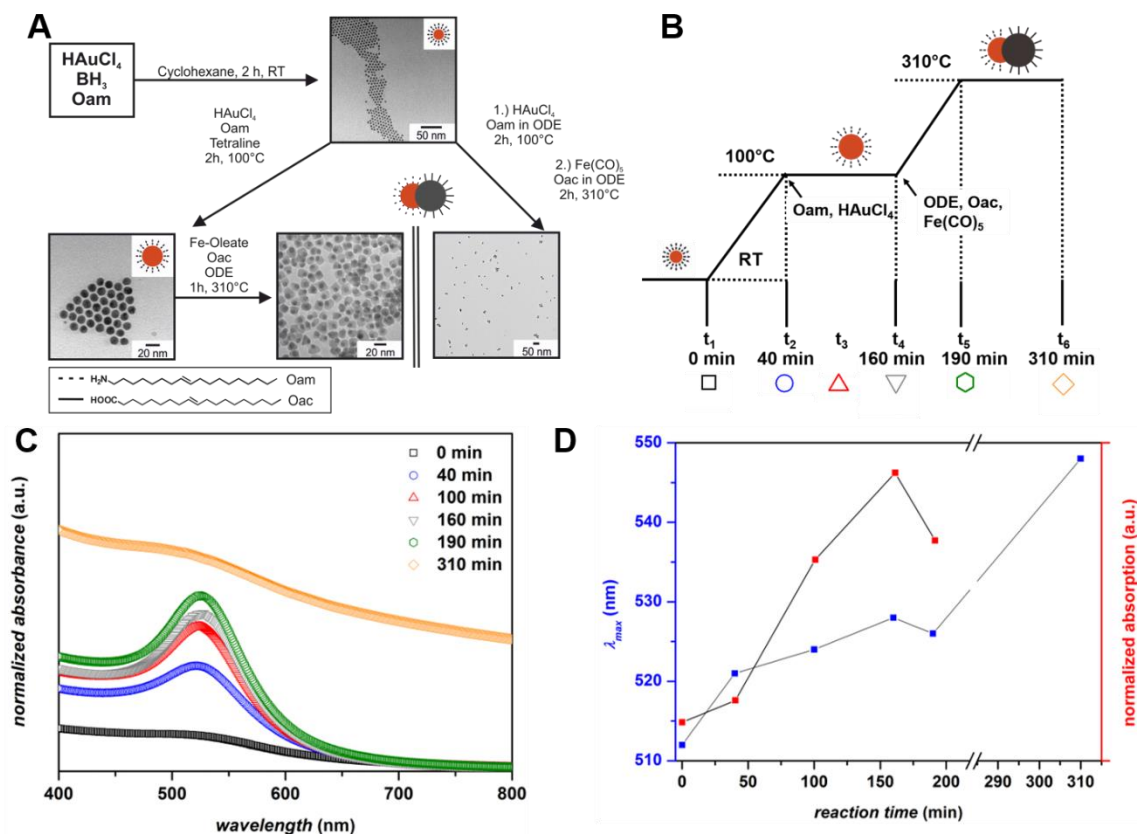


Figure 3.7: (A) Comparison of a conventional reaction and a one pot seed-mediated synthesis of Au@Fe₃O₄ JPs. (B) Heating program for the synthesis of large gold seeds in ODE and a subsequent heating step to 310°C for the formation of Fe₃O₄ domains. (C) UV-Vis spectra of aliquots from reaction mixture after different reaction times. The data was normalized to the Au concentration (except for the spectrum of the Au@Fe₃O₄ particles after 310 min). (D) Position of the maximum of the Au plasmon absorbance and the normalized absorption (proportional to the diameter of the NPs). The slight shift between 160 min and 190 min corresponds to matrix changes due to the addition of Oac and Fe(CO)₅ and heating of the solution.

The conventional route to Au@Fe₃O₄ Janus type particles was described by Yu *et al.* in 2005 [38] and later used by Schick *et al.* [18] The first step comprises the synthesis of seed particles. [49] The second step requires the growth of the gold domain for sensing of free oscillating charge carriers. [48] Tetraline, the solvent for this growth step, is harmful and malodorous. The high boiling point of ODE, which allows the thermal decomposition of Fe(CO)₅, avoids this drawback. The intermedi-

ate growth step for larger Au nanoparticles requires a proper Au seed concentration (23.6 mg of HAuCl_4 in 20 mL of ODE with 4 mL of Oam yields 1 mg of Oam capped gold seeds). The intensity of the plasmon band (Figure 3.7) shows the growth of gold seeds within 2 h at 100 °C. TEM images and particle diameters derived from DLS diameter of Au-NPs during the grow stage are shown in Figure 3.8.

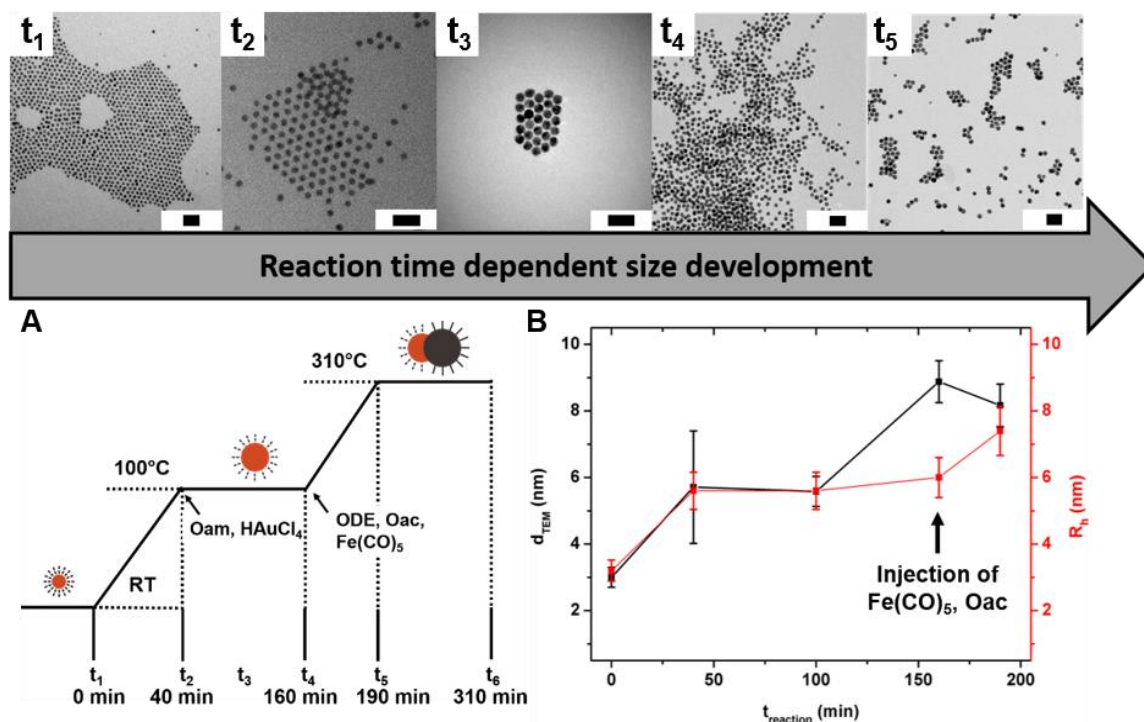


Figure 3.8: Size evolution of Au domains during the growth phase. Top: TEM images (scale bars: 20 nm) starting from seeds at 0 min (t_1) to 40 min (t_2), 100 min (t_3), 160 min (t_4), 190 min (t_5). (A) Temperature program with thermal decomposition of HAuCl_4 until t_4 and subsequent ODE, Oac and $\text{Fe}(\text{CO})_5$ addition at 160 min. (B) Diameter of nanoparticles from TEM (black) and hydrodynamic radii from DLS measurements (red, see Supporting Information Figure S 3.17 for details concerning DLS).

The addition of 0.05 mL (0.00018 mmol) of $\text{Fe}(\text{CO})_5$ with 4 mL of Oac at t_4 and heating to 310°C (within 30 min) followed by an annealing period of 120 min yielded monodisperse $\text{Au}@\text{Fe}_3\text{O}_4$ JPs with average sizes of 10.3 ± 0.3 nm for the Au and 15.1 ± 1.4 nm for the Fe_3O_4 domains. The nucleation of the Fe_3O_4 domains during phase t_4 (30 min) and their growth during phase t_5 (120 min) at 310 °C is associated with a damping of the plasmon and an increase of the overall particle size (Figure

3.9). Figure 3.9 shows (individual) JPs obtained from the one-pot (I) and the conventional two-step synthesis (II) to have the same morphologies and selected area electron diffraction (SAED, Ib, IIb) patterns. Figure 3.9 and the XRD diffractograms (average properties of a bulk sample) in Figure 3.10 demonstrate that the JPs contain indeed Au and Fe₃O₄ domains. The morphology in STEM mode (Figure 3.9 c) and gold to iron contribution derived from EDX line scans (Figure 3.9 d) are almost identical for JPs obtained from one step and two-step syntheses.

The structural (TEM, XRD, DLS) and spectroscopic (UV-vis) data demonstrate that highly monodisperse Au@Fe₃O₄ JPs can be synthesized in high yields (30 mg per single batch) from small amounts (1 mg per batch) of Au seed particles.

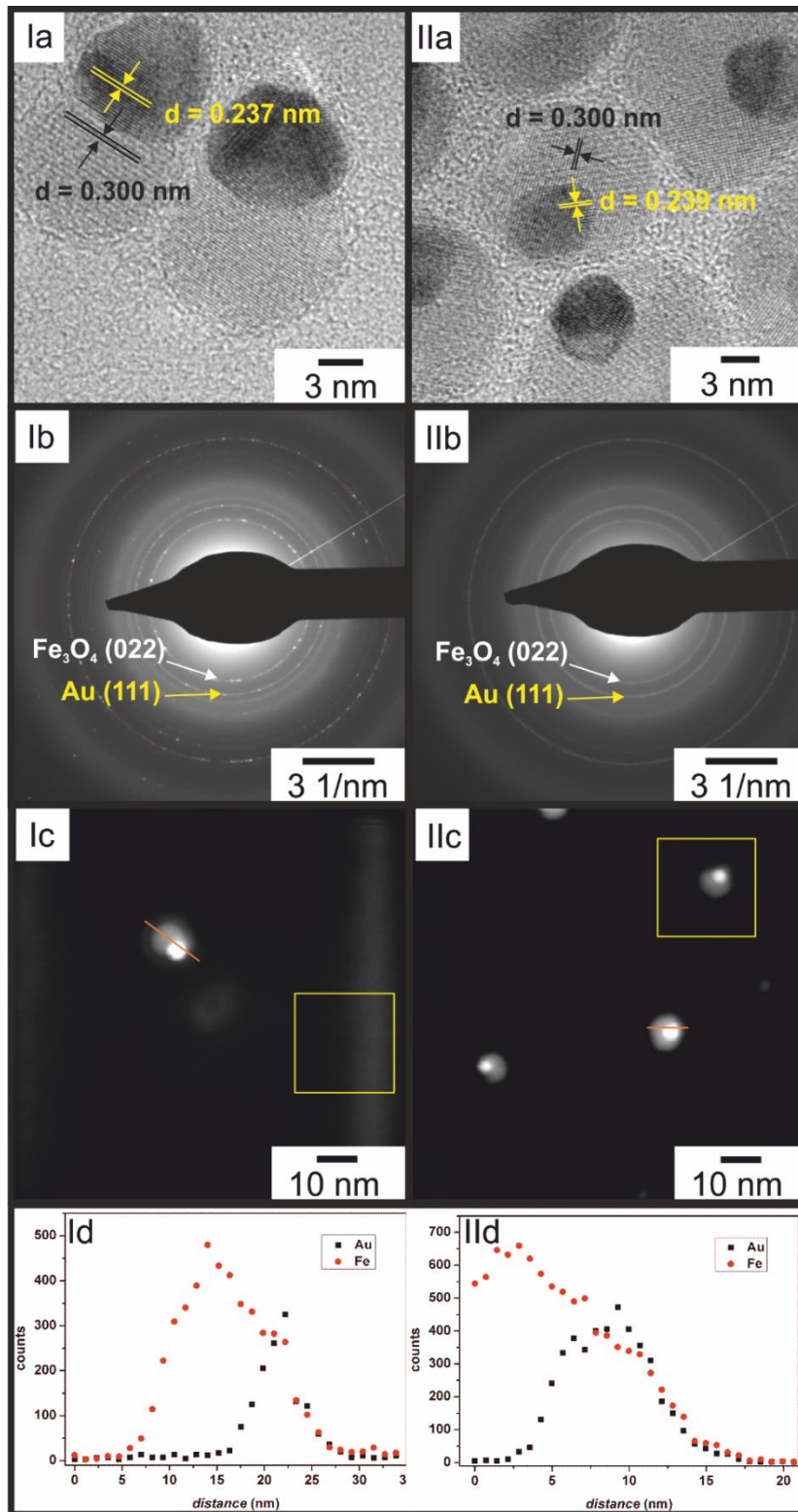


Figure 3.9: (a) HR-TEM images of Au@Fe₃O₄ JPs obtained from a one-pot reaction (I, left column) and a conventional two-step synthesis (II). (b) Single domains of Au and Fe₃O₄ appear in SAED, where the (220) facet of the Fe₃O₄ domain is associated with the (111) facet of the Au domain. (c) Corresponding STEM images. (d) EDX line-scans along the orange lines show identical Au : Fe contributions of the Au@Fe₃O₄ JPs obtained by one-pot and two-step synthesis.

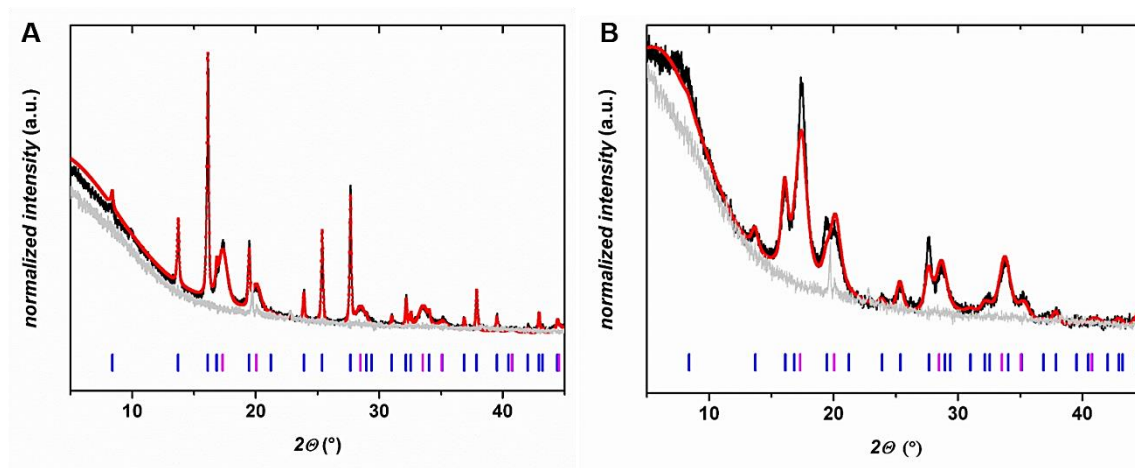


Figure 3.10: Powder X-ray diffraction patterns of Au@Fe₃O₄ JPs (black lines) synthesized via novel one-step synthesis (A) and the conventional two-step approach (B). The Rietveld refinements show good agreement to the HR-TEM evaluated relative phase distribution for both synthesis strategies. Grey lines show background signals from acetate foil, vertical bars show the positions of reflections from Au (magenta) and Fe₃O₄ (blue).

As conclusive statement on the analytics an easy way to use very small amounts (only 1 mg for each batch) of Au seed particles of small size to facilitate a reaction that yields about 30 mg of highly monodisperse Janus particles of same phase, shape and plasmon activity as shown by XRD, TEM, UV-Vis and DLS measurements per batch has been identified in this work.

3.1.2.4 Conclusion

Highly monodisperse Au@Fe₃O₄ JPs were prepared by a seed-mediated one-pot synthesis. The two-step process involving the pre-overgrowth of the Au seeds as precursor for the nucleation of Fe₃O₄ domains by thermolysis of an iron oleate precursor was circumvented by combining Au seed growth and Fe₃O₄ by a heating program that involves an annealing of Au domains and the formation of Fe₃O₄ domains. The Au@Fe₃O₄ JPs obtained by a one-pot approach have morphologies, phase compositions as well as physical and chemical properties that are virtually identical to those of Au@Fe₃O₄ particles obtained from conventional two-step re-

actions. The one-pot synthesis circumvents polydispersity and reproducibility issues of the two-step synthesis. It is a basic requirement for scale-up by microfluidics as shown for organics in double emulsion droplets. [55]

3.1.2.5 Supporting Information

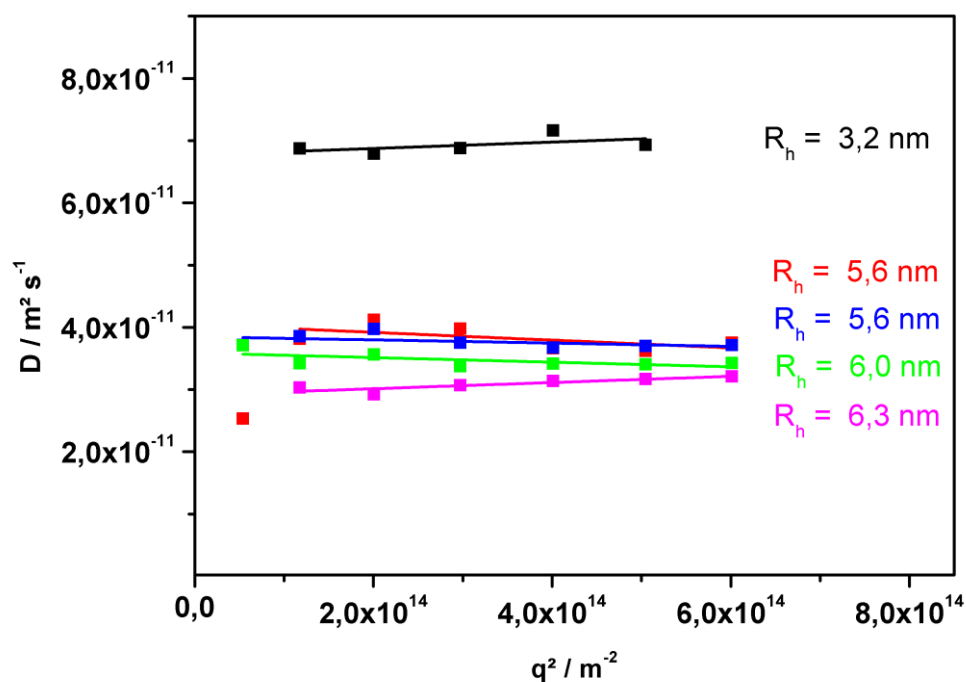


Figure S 3.17: DLS data plot of diffusion coefficient against q^2 for five different points (t_1 - t_5 from top to bottom) shown in Figure 3.8 of the main paragraph. Transformation of intensity correlation functions into amplitude correlation functions applying the Siegert relation, extended to include negative values after baseline subtraction by calculation $g_1(t) = \text{SIGN}(G_2(t)) \cdot \text{SQRT}(\text{ABS}((G_2(t)-A)/A))$. $g_1(t)$ was evaluated by fitting a bi-exponential function $g_1(t) = a \cdot \exp(-t/b) + c \cdot \exp(-t/d)$ to take polydispersity into account. Average apparent diffusion coefficients D_{app} were calculated according to $q^2 \cdot D_{app} = (a \cdot b - 1 + c \cdot d - 1) / (a + c)$. The obtained data was extrapolated to $D_{app}(q=0)$ and shown hydrodynamic radii were then calculated by using the Stokes-Einstein Equation.

3.1.2.6 References

- [1] J. H. Schröder, M. Doroshenko, D. Pirner, M. E. Mauer, B. Förster, V. Boyko, B. Reck, K. J. Roschmann, A. H. Müller, S. Förster, *Polymer* **2016**, *106*, 208–217.
- [2] A. Walther, K. Matussek, A. H. E. Müller, *ACS Nano* **2008**, *2*, 1167–1178.
- [3] A. Walther, A. H. E. Müller, *Chem. Rev.* **2013**, *113*, 5194–5261.
- [4] Y. Wei, R. Klajn, A. O. Pinchuk, B. A. Grzybowski, *Small* **2008**, *4*, 1635–1639.
- [5] H. Goesmann, C. Feldmann, *Angew. Chem.* **2010**, *122*, 1402–1437.
- [6] K. P. Yuet, D. K. Hwang, R. Haghgooeie, P. S. Doyle, *Langmuir* **2010**, *26*, 4281–4287.
- [7] J. Yuan, Y. Xu, A. H. E. Müller, *Chem. Soc. Rev.* **2011**, *40*, 640–655.
- [8] M. D. McConnell, M. J. Kraeutler, S. Yang, R. J. Composto, *Nano Lett.* **2010**, *10*, 603–610.
- [9] L. M. Liz-Marzán, C. J. Murphy, J. Wang, *Chem. Soc. Rev.* **2014**, *43*, 3820–3822.
- [10] S. Gangwal, O. J. Cayre, O. D. Velev, *Langmuir* **2008**, *24*, 13312–13320.
- [11] L. Nie, S. Liu, W. Shen, D. Chen, M. Jiang, *Angew. Chem. Int. Ed.* **2007**, *46*, 6321–6324.
- [12] R. Erhardt, A. Böker, H. Zettl, H. Kaya, W. Pyckhout-Hintzen, G. Krausch, V. Abetz, A. H. E. Müller, *Macromolecules* **2001**, *34*, 1069–1075.
- [13] J. Faria, M. P. Ruiz, D. E. Resasco, *Adv. Synth. Catal.* **2010**, *352*, 2359–2364.
- [14] F. Wang, G. M. Pauletti, J. Wang, J. Zhang, R. C. Ewing, Y. Wang, D. Shi, *Advanced materials* **2013**, *25*, 3485–3489.
- [15] N. Glaser, D. J. Adams, A. Böker, G. Krausch, *Langmuir* **2006**, *22*, 5227–5229.
- [16] Y.-M. Zhou, H.-B. Wang, M. Gong, Z.-Y. Sun, K. Cheng, X.-k. Kong, Z. Guo, Q.-W. Chen, *Dalton Trans.* **2013**, *42*, 9906–9913.
- [17] E. Umut, F. Pineider, P. Arosio, C. Sangregorio, M. Corti, F. Tabak, A. Lascialfari, P. Ghigna, *J. Magn. Magn. Mater.* **2012**, *324*, 2373–2379.

-
- [18] L. Landgraf, P. Ernst, I. Schick, O. Köhler, H. Oehring, W. Tremel, I. Hilger, *Biomaterials* **2014**, *35*, 6986–6997.
- [19] L. Landgraf, C. Christner, W. Storck, I. Schick, I. Krumbein, H. Dähring, K. Haedicke, K. Heinz-Herrmann, U. Teichgräber, J. R. Reichenbach, W. Tremel, S. Tenzer, I. Hilger, *Biomaterials* **2015**, *68*, 77–88.
- [20] K.-h. Roh, D. C. Martin, J. Lahann, *Nat Mater* **2005**, *4*, 759–763.
- [21] J. Reguera, D. Jiménez de Aberasturi, M. Henriksen-Lacey, J. Langer, A. Espinosa, B. Szczupak, C. Wilhelm, L. M. Liz-Marzán, *Nanoscale* **2017**, *9*, 9467–9480.
- [22] S. J. Ebbens, J. R. Howse, *Soft Matter* **2010**, *6*, 726–738.
- [23] B. J. Park, D. Lee, *ACS Nano* **2012**, *6*, 782–790.
- [24] C. Wang, J. Qian, K. Wang, X. Yang, Q. Liu, N. Hao, C. Wang, X. Dong, X. Huang, *Biosens. Bioelec.* **2016**, *77*, 1183–1191.
- [25] S. Polarz, *Adv. Funct. Mater.* **2011**, *21*, 3214–3230.
- [26] J. K. Sahoo, M. N. Tahir, F. Hoshyargar, B. Nakhjavan, R. Branscheid, U. Kolb, W. Tremel, *Angew. Chem. Int. Ed.* **2011**, *50*, 12271–12275.
- [27] J. Wei, S.-S. Li, Z. Guo, X. Chen, J.-H. Liu, X.-J. Huang, *Anal. Chem.* **2016**, *88*, 1154–1161.
- [28] C. J. Behrend, J. N. Anker, R. Kopelman, *Appl. Phys. Lett.* **2004**, *84*, 154–156.
- [29] C. J. Behrend, J. N. Anker, B. H. McNaughton, M. Brasuel, M. A. Philbert, R. Kopelman, *J. Phys. Chem. B* **2004**, *108*, 10408–10414.
- [30] J. H. Byeon, J. H. Park, *Sci. Rep.* **2016**, *6*, 35104.
- [31] G. Loget, J. Roche, A. Kuhn, *Adv. Mater.* **2012**, *24*, 5111–6, 5144.
- [32] M. Casavola, R. Buonsanti, G. Caputo, P. D. Cozzoli, *Eur. J. Inorg. Chem.* **2008**, *2008*, 837–854.
- [33] M. Lattuada, T. A. Hatton, *Nano Today* **2011**, *6*, 286–308.
- [34] X. Pang, C. Wan, M. Wang, Z. Lin, *Angew. Chem. Int. Ed.* **2014**, *53*, 5524–5538.
- [35] M. R. Buck, J. F. Bondi, R. E. Schaak, *Nature Chem.* **2011**, *4*, 37–44.

- [36] S. Gómez-Graña, B. Goris, T. Altantzis, C. Fernández-López, E. Carbó-Argibay, A. Guerrero-Martínez, N. Almora-Barrios, N. López, I. Pastoriza-Santos, J. Pérez-Juste, S. Bals, G. van Tendeloo, L. M. Liz-Marzán, *J. Phys. Chem. Lett.* **2013**, *4*, 2209–2216.
- [37] P. Quaresma, I. Osório, G. Dória, P. A. Carvalho, A. Pereira, J. Langer, J. P. Araújo, I. Pastoriza-Santos, L. M. Liz-Marzán, R. Franco, P. V. Baptista, E. Pereira, *RSC Adv* **2014**, *4*, 3690–3698.
- [38] H. Yu, M. Chen, P. M. Rice, S. X. Wang, R. L. White, S. Sun, *Nano Lett.* **2005**, *5*, 379–382.
- [39] M. Susewind, A.-M. Schilman, J. Heim, A. Henkel, T. Link, K. Fischer, D. Strand, U. Kolb, M. N. Tahir, J. Brieger, W. Tremel, *J. Mater. Chem. B* **2015**, *3*, 1813–1822.
- [40] M. Klueker, M. Nawaz Tahir, R. Ragg, K. Korschelt, P. Simon, T. E. Gorelik, B. Barton, S. I. Shylin, M. Panthöfer, J. Herzberger, H. Frey, V. Ksenofontov, A. Möller, U. Kolb, J. Grin, W. Tremel, *Chem. Mater.* **2017**, *29*, 1134–1146.
- [41] M. Nawaz Tahir, M. Klueker, F. Natalio, B. Barton, K. Korschelt, S. I. Shylin, M. Panthöfer, V. Ksenofontov, A. Möller, U. Kolb, W. Tremel, *ACS Appl. Nano Mater.* **2018**, *1*, 1050–1057.
- [42] T. Chen, G. Chen, S. Xing, T. Wu, H. Chen, *Chem. Mater.* **2010**, *22*, 3826–3828.
- [43] M. Klueker, M. N. Tahir, R. Dören, M. Deuker, P. Komforth, S. Planar Ruiz, B. Barton, S. I. Shylin, V. Ksenofontov, M. Panthöfer, N. Wiesmann, J. Herzberger, A. Möller, H. Frey, J. Brieger, U. Kolb, W. Tremel, *Chem. Mater.* **2018**, *30*, 4277–4288.
- [44] G. Backert, B. Oschmann, M. N. Tahir, F. Mueller, I. Lieberwirth, B. Balke, W. Tremel, S. Passerini, R. Zentel, *J Colloid Interface Sci* **2016**, *478*, 155–163.
- [45] B. Nakhjavan, M. N. Tahir, F. Natalio, H. Gao, K. Schneider, T. Schladt, I. Ament, R. Branscheid, S. Weber, U. Kolb, C. Sönnichsen, L. M. Schreiber, W. Tremel, *J. Mater. Chem.* **2011**, *21*, 8605–8611.
- [46] A. M. Percebom, J. J. Giner-Casares, N. Claes, S. Bals, W. Loh, L. M. Liz-Marzán, *Chem. Commun.* **2016**, *52*, 4278–4281.

- [47] T. D. Schladt, K. Schneider, H. Schild, W. Tremel, *Dalton Trans.* **2011**, *40*, 6315–6343.
- [48] I. Schick, D. Gehrig, M. Montigny, B. Balke, M. Panthöfer, A. Henkel, F. Laquai, W. Tremel, *Chem. Mater.* **2015**, *27*, 4877–4884.
- [49] S. Peng, Y. Lee, C. Wang, H. Yin, S. Dai, S. Sun, *Nano Res.* **2008**, *1*, 229–234.
- [50] Z. Xu, Y. Hou, S. Sun, *J. Am. Chem. Soc.* **2007**, *129*, 8698–8699.
- [51] L. Zhang, R. He, H.-C. Gu, *Appl. Surf. Sci.* **2006**, *253*, 2611–2617.
- [52] S. Mourdikoudis, L. M. Liz-Marzán, *Chem. Mater.* **2013**, *25*, 1465–1476.
- [53] D. Wilson, M. A. Langell, *Appl. Surf. Sci.* **2014**, *303*, 6–13.
- [54] A. Coelho, *TOPAS-Academic V5*.
- [55] C.-H. Chen, R. K. Shah, A. R. Abate, D. A. Weitz, *Langmuir* **2009**, *25*, 4320–4323.

3.1.3 Au@Fe₃O₄ Janus type nanoparticles as non-isotropic additives – CaCO₃ mesocrystal formation with nanoparticle inclusion

The manuscript “Au@Fe₃O₄ Janus type nanoparticles as non-isotropic additives – CaCO₃ mesocrystal formation with nanoparticle inclusion” is the underlying study for the following paragraph. The manuscript will be submitted to *Crystal Growth and Design* by the *American Chemical Society*. The following Chapter combines both the content of the main manuscript and the supporting information.

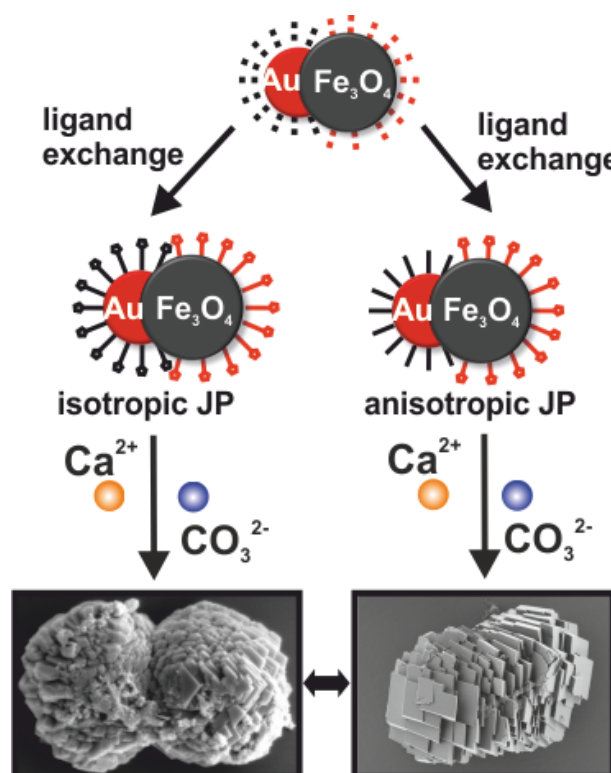


Figure 3.11: Scheme of functionalization patterns of Au@Fe₃O₄ Janus particles. Amphiphilic particles as well as isotropic anionic functionalized particles have been synthesized to study their effect on slow desiccator crystallizations of CaCO₃ by using the ammonia diffusion method.

Incorporation of gold and iron oxide nanoparticles has been demonstrated for polymer coated isotropic particles but direct surface interaction of CaCO₃ with the nanoparticle surface was impossible with polymer coatings. All particles used were of anionic functionalization and large isotropy. Hence the effect of anisotropy of

nanoparticles as well as the different materials surface interactions with CaCO_3 are central unstudied aspects on the way to new solid composite materials with advanced magnetic or optical properties. A crucial microscopy, spectroscopy and diffraction study of the intermediates and the final composite materials enlightens the requirements of good colloidal stability as well as anionic functional groups to trigger surface interaction of Janus particle domains with the CaCO_3 host-lattice material.

3.1.3.1 Introduction

The incorporation mechanism of additives within the calcite host mineral ^[1] is still an area of challenging and controversial discussions especially in the concern of the effect of materials and functional groups on CaCO_3 precipitation. ^[2-7] From nature bio-inspiration is already rolled out into the synthetic assembling of CaCO_3 composites, but still the assembly of nano-, micro- or even millimeter-sized crystals is challenging due to the manifold effects, that influence CaCO_3 crystal assembly. ^[8-10] Besides functional group assembly, ^[10] roughness, ^[11,12] material composition, ^[13] purity ^[14] also flexibility ^[15] or rigidity ^[16] of the additive influence the crystallization besides other external influences as purity of media, ^[17] temperature, ^[18] pressure, ^[19] concentrations ^[20] or even time of precipitation. ^[21] From biominerals the community learned that the alteration of carboxylic or hydroxyl functionalities together ^[22] with non-coordinating amino acids in proteins the so-called EF-Hand model ^[23] is an amino acid sequence with calcium complexing and thus CaCO_3 influencing properties. ^[24,25] Especially the ACC stabilization against spontaneous crystallization is a major role of protein in living CaCO_3 precipitating animals. ^[26,27] In such proteins often acidic functional groups ensure interaction with calcium ions. From this knowledge the polyacidic (co-)polymers for example PAA ^[28] and PAA-PAMPS ^[29] or even polyglycerol polyacids ^[30] have been studied for their effect on CaCO_3 precipitations due to their calcium ion complexation behavior. ^[31] As a result often anti-scalant properties have been observed. But occlusion of the polymers into calcite crystals in an oversaturated environment turned out to be observable. Recently De Yoreo *et al.* published their atomic force microscopy (AFM) studies on

the inclusion of soft polymer micelles of PAA and their shape changes during incorporation within the CaCO_3 host-lattice. [32] The key point of easy occlusion of PAA was its flexibility to ensure easy and fast overgrowth by continuously growing CaCO_3 mineral. Besides flexible materials that can influence the materials E-modulus or hardness the use as optical or magnetic properties carrying composite material motivated studies on the occlusion of nanoparticles (NPs). [33,34] Küther *et al.* have shown that Au-NPs functionalized with a self-assembled monolayer (SAM) [35,36] of 4-Mercaptophenol modify the morphologies of calcite from usual rhombohedra shape to spherical assemblies truncated with (104) several nanometer sized crystals of calcite. [37] The occlusion of NPs unlikely has not been demonstrated in this case. Recently Meldrum *et al.* also published two articles on the occlusion of functionalized NPs within CaCO_3 . [33,38] In their research they studied the occlusion of block-copolymer functionalized Au and Fe_3O_4 NPs. In both publications isotropic NPs with isotropic functionalization patterns have been studied. The total amount of particles occluded as well as the mechanism of occlusion was not resolved. To predict the morphology of CaCO_3 composites for the case of NP integration one needs to know how the influence of small molecules functionalization differs from polymer coated particles in CaCO_3 crystallization as shown for Au-NPs in chapter 3.1.1. Nonetheless the effect of the NP material on the composite formation is unknown in the case of close contact with the forming solid phase of CaCO_3 . [39,15,40] Thus we herein present the first study of non-isotropic NPs of the Janus particle class. Known approaches of $\text{Au}@Fe_3O_4$ functionalization are used to address anisotropy and surface effects on the formation of CaCO_3 composites. [41] Three different combinations of functionalization patterns were prepared by functionalizing oleylamine and oleic acid capped nanoparticles. [42–44] TGA, UV-Vis- and IR-spectroscopy was used to identify and quantify successful functionalization. The combinations can be distinguished via surface charge and degree of anisotropy. All functionalized particle fractions were added to a calcium chloride solution to precipitate CaCO_3 by an ammonia diffusion experiment in a desiccator. A detailed study of the morphology of the final CaCO_3 and the interaction of additives with the CaCO_3 is also conducted and presented. For the three different composites a comprehensive HR-TEM and XRD rocking study was conducted with the focus on the

degree of incorporation of particles as well as the interaction of the metal or metal oxide surface with the CaCO_3 .

3.1.3.2 Experimental

Chloroauric acid dihydrate (99.999% trace metals basis, abcr GmbH), borane tert-butylamine complex, (97%, Sigma Aldrich), iron(0)pentacarbonyl (99,98% trace metal free, Sigma Aldrich), 1-octadecene (ODE, >80% techn., Acros), Oleylamine (Oam, >50%, TCI), oleic acid (Oac, >90% techn., Sigma Aldrich), sodium hydroxide solution (98%, Sigma Aldrich), 11-mercaptoundecanoic acid (11-MUA, 95%, Sigma Aldrich), 1-dodecanethiol (1-DT, >99%, Fluka), 4-*tert*-butylcatechol (4-TBC, >99%, Acros), 4-sulfobenzoic acid potassium salt (4-SBA, 99%, Sigma Aldrich), tetramethylammonium hydroxide solution (TMAH, 25 vol% in water, Sigma Aldrich), calcium chloride solution (1 M, volumetric, Fluka), ammonia carbonate (>30%, NH_3 basis, Sigma Aldrich), cyclohexane (p.A., Fisher scientific), ethanol (p.A., Fisher scientific), isopropanol (p.A., Sigma Aldrich), chloroform (>99%, Sigma Aldrich) were used as received without further purification.

Quarz glass-slides for crystallization as well as transmission and scanning electron microscopy (TEM and SEM) equipment was received from Plano GmbH, Wetzlar, Germany. For water deionization a water purification setup from Millipore (Millipore GmbH) was used. The quartz glass slides were cleaned by subsequent washing with ethanol, NaOH, MQ water, HCl and threefold MQ water in an ultrasonic bath for 10 minutes each. To finalize cleaning the glass slides were dried under nitrogen flow.

Instrumentation

TGA data has been collected with a Perkin Elmer TGA sampler with the Pyris 8 software. For each measurement a temperature program with constant 50 °C for 10 min, slope with 5 °C / min to 650 °C that stays constant for another 10 min has been conducted. All measurements were facilitated with particle amounts between 2 and 10 mg.

Raman and IR-spectroscopy measurements for phase identification were carried out using a confocal HR800 μ -Raman by Horiba Scientific and a NicoletTM iSTM10 FT-IR spectrometer from Thermo scientific. Both instruments used $\lambda = 633$ nm He-Ne laser light without using any optical filters. Each spectrum was taken with resolution of 1 cm^{-1} at 16 iterations.

UV-VIS-spectra were collected by a Varian Cary 5000 UV VIS/NIR-spectrometer equipped with a tempered stage at constant $25\text{ }^{\circ}\text{C}$. Optical Imaging was performed with a confocal Keyence-8710 laser light microscope equipped with a 658 nm diode Laser to get height information of the precipitated samples.

For SEM the calcium carbonate crystals were analyzed using a JEOL-JSM 5610LV (JEOL Ltd., Tokyo, Japan) or FEI Phenom (Hillsboro, OR, USA). Images were acquired with an accelerating voltage of 20 kV or 10 kV respectively and at low vacuum. SEM samples have been sputtered with either Pt or Ag with layer thicknesses between 4 and 7.5 nm to prevent the electrostatic charging of samples.

For FIB cuts, a FEI 600 Nanolab focused ion beam (FIB)/SEM dual beam instrument (FEI, Hillboro, Oregon) equipped with an Omniprobe micromanipulator (Omniprobe Inc. Dallas, Texas) was used. The thin-cut was mounted on a copper mount for HR-TEM analysis.

TEM images were recorded using a FEI Technai F20, F30 or T12, all equipped with a 4K CCD camera and a LaB₆ cathode working at 200 kV or 120 kV acceleration voltage. The HR-TEM was furthermore equipped with EDX system by EDAX and a STEM detector by FEI.

Synthesis of Au@Fe₃O₄ heterodimers

The synthesis of Au@Fe₃O₄ Janus particles was conducted as described in chapter 3.1.2. The overall yield from each reaction was 30 mg of Oam/Oac capped Au@Fe₃O₄ Janus particles, which has been taken as a single batch for each surface functionalization combination reported.

Surface functionalization of Au@Fe₃O₄ nanoparticles

For all nanoparticle samples the Au domain of the Janus particles has been functionalized first to get best possible thiol ligand coverage on the Au domain. Either 11-MUA or 1-DT was used in an about tenfold molar excess to the surficial Au atoms available for the functionalization reaction. ^[15] Both substances were diluted in chloroform and a stock solution of 5 g/L Oam and Oac capped Janus particles was added for an over-night reaction to functionalize the Au domain. After the reaction the NPs were separated by adding ethanol for the 1-DT case or cyclohexane for the 11-MUA case as anti-solvent to precipitate the particles. The washing of the particles was performed by taking three turns of isopropanol washing and centrifugation steps.

The iron oxide domain has been functionalized by adding 1 mL of the TMAH solution to 1 mL of 2 g/L of Au domain functionalized Janus NPs either in water (11-MUA/Au@Fe₃O₄/Oac) or cyclohexane (1-DT/Au@Fe₃O₄/Oac) to remove Oac from the iron oxide domain and activate the surface for the new ligand. After excessive washing/precipitation procedure with ethanol as good solvent for Oac, cyclohexane was added to the gold domain functionalized 11-MUA/Au@Fe₃O₄ particles and water was added to 1-DT/Au@Fe₃O₄ particles to agglomerate the Janus particles at the polar/nonpolar boundary of the two-phase systems. 4-TBC or 4-SBA was added respectively to the NP dispersions in about tenfold molar excess in relation to the surface iron coordination centers for functionalization. The reaction mixture was stirred over-night and purified by dialysis through a 3000 kDa membrane for 72 h against ethanol to wash away unbound ligands such as Oac as well as the excess of 4-TBC and 4-SBA. Evaporation and dispersion in aqueous sodium hydroxide solution (pH 10) for a 1 g/L stock of (a) 1-DT/Au@Fe₃O₄/4-SBA, (b) 11-MUA/Au@Fe₃O₄/4-TBC and (c) 11-MUA/Au@Fe₃O₄/4-SBA for crystallization experiment finalized the synthesis.

Crystallization of CaCO₃ via ammonia diffusion method

Crystallization experiments were carried out using the standard ammonia diffusion method. ^[45,46,29,47,48] The reaction has a short induction time during which desicca-

tor atmosphere gets supersaturated with ammonia and carbon dioxide via subsequent thermal decomposition of the excess of ammonium carbonate placed on the bottom of a desiccator. From the atmosphere the solution starts to (super-)saturate with NH_3 and CO_2 and the hydrogencarbonate-carbonate equilibrium is generated. Crystallization was performed on quartz-glass slides with a diameter of 13 mm and a thickness of 1 mm placed on the bottom of 5 mL beakers. The beakers were filled with 2 mL of aqueous solutions of 5 mM CaCl_2 and distinct amounts of $\text{Au@Fe}_3\text{O}_4$ NPs of variable functionalities. The reaction room was covered with perforated Parafilm (Neenah, WI, USA) to prevent external impact by dust or other impurities. The pH of the solution subsequently increased from about 7 to 9.5 during crystallization. After 15 h crystallization time the glass-slides were removed from the solution, washed carefully with saturated CaCO_3 solution on both sides to ensure complete removal of ammonium carbonate crystals and unbound NPs without inducing dissolution/ recrystallization processes.

3.1.3.3 Results & Discussion

Form as described synthesis the following anisotropic additives were compared in CaCO_3 crystallizations. First a nonpolar/polar batch with (a) 1-DT/Au@Fe₃O₄/4-SBA, second a further non-isotropic polar/nonpolar Janus particle species (b) 11-MUA/Au@Fe₃O₄/4-TBC and third bi-anionic functionalization with (c) 11-MUA/Au@Fe₃O₄/4-SBA have been synthesized.

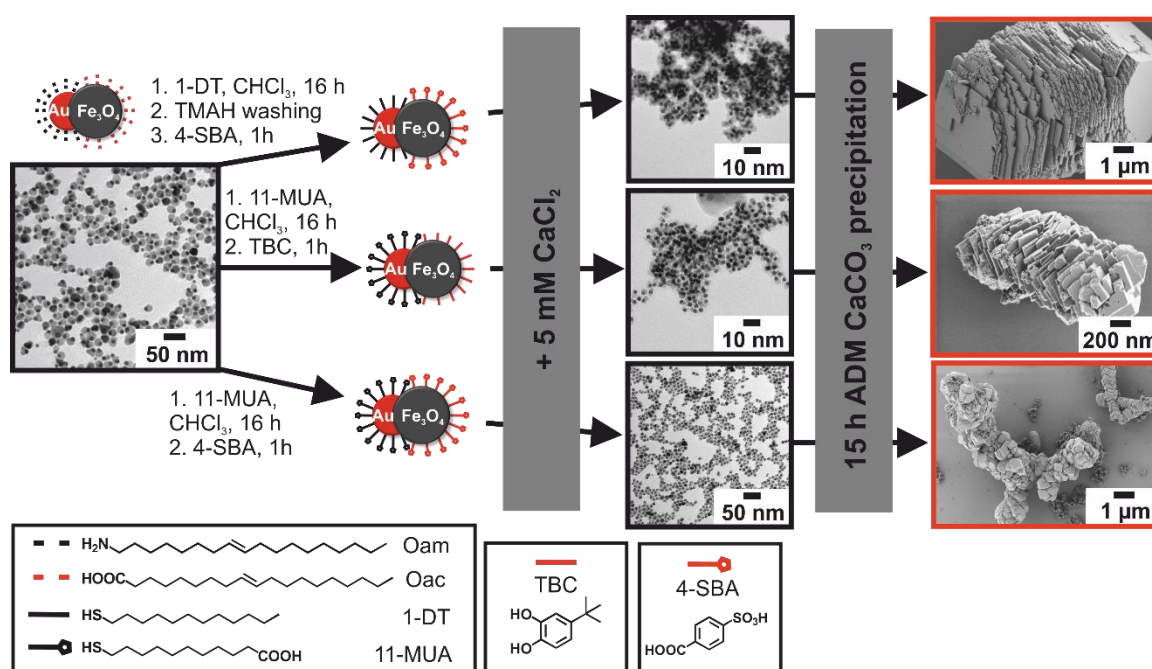


Figure 3.12: Sketch of Au@Fe₃O₄ functionalization and agglomeration of Janus Particles (black boxes) and the resulting CaCO_3 crystals if 0.2 g/L of the NPs (a) 1-DT/Au@Fe₃O₄/4-SBA (b) 11-MUA/Au@Fe₃O₄/4-TBC or (c) 11-MUA/Au@Fe₃O₄/4-SBA were added in an ammonia diffusion experiment for 15 h (red boxes). The size of the final CaCO_3 crystals indicate strongest inhibition taking place for both 11-MUA functionalized Janus particles (b) and (c) while the effects on the crystal morphology is weak in the case of functionalization pattern (a).

The successful functionalization of all types of NPs (a), (b) and (c) is verified by IR, UV-Vis and TGA studies (see Figure S 3.18, Figure S 3.19 and Figure S 3.20, Supporting Information) indicating various functionalization densities, which has a pronounced influence on the particles colloidal stability. Only weak stability in solution has been observed for Janus particles of type (a) due to close packing of non-polar 1-DT molecules on the Au surface. [49,50] 1-DT/Au@Fe₃O₄/4-SBA NPs carries 23 w% ligand on the NPs surface, while of that 70 % are 1-DT and only 30

% 4-SBA as determined from TGA. For type (b) Janus particles a total weight loss of bound ligand to be only 13 w% as calculated from TGA. Due to the close decomposition window of both ligands it is not possible to distinguish between them while IR-data (Figure S 3.18, Supporting Information) underlines binding of both ligand species. UV-Vis data shown in Figure S 3.19 of the Supporting Information also underlines successful functionalization of the Au-domain and plasmon coupling gives a hint for strong interactions of amphiphilic Janus particles of functionalization pattern (b) (compare Figure 3.12 middle row). The plasmon coupling is caused by the close contact of Au domains in agglomerates as shown in the TEM images in Figure 3.12. NPs of type (c) show the best colloidal stability at basic pH in aqueous solutions due to the all over polar anionic functionalization on both domains although only 8 w% ligand cover the NPs surface. Both functional molecules can be identified by the shift of both vibrational modes of the $-C-S-$ and $-C=O$ carbonyl bond of the carboxylic acid of 4-SBA in IR-spectra. UV-Vis also underlines successful functionalization by surface plasmon resonance red-shift due to the Au surface modification and the resulting particle interactions. The good colloidal stability of all particle samples in aqueous environment is shown in the inlays of Figure S 3.19 (see Supporting Information). The amphiphilic behavior of the particle fractions (a) and (b) are shown by the assembly from polar solvents to micellar assemblies on the TEM grid prepared from an ethanol solution of Janus particles type (a) (see Figure 3.12). Nonetheless also Janus particles functionalized the other way around agglomerate to micelles with iron oxide domains mainly pointing to the center of the micelle (compare Figure 3.12 (b)).

Due to the bad colloidal stability of amphiphilic Janus particles the crystallizations using Janus particles (a) and (b) the precipitation of most particles occurred very fast in $CaCl_2$ solution. For sure the increase of pH and formation of ACC in a solution of high ionic strength in the ammonia diffusion desiccator experiments disperses agglomerates to some extent as shown in Figure 3.13 (B, C) and Figure 3.14 (B, C). For the effects on $CaCO_3$ crystallization it is necessary to mention that the shape and phase modification of $CaCO_3$ crystals also occurs in analogous desiccator experiments with neat 4-SBA addition. In Figure S 3.21 of the Supporting Information the crystals from 15 h desiccator experiments with various amounts of

4-SBA are shown. Hence the added concentrations chosen in these experiments are higher than the amount of ligand in the NP samples. Thus the effects on shape of the final crystals might also be caused by the dissociation of 4-SBA from the Fe_3O_4 domain due to its weak coordination. For all other ligands no reference crystallization experiments were conducted due to bad miscibility within basic aqueous media. The TEM details of 1-DT/Au@ Fe_3O_4 /4-SBA particles (a) in CaCl_2 solution and after crystallization in the desiccator experiment for 15 h are shown in Figure 3.13. The particles agglomerate and absorb on CaCO_3 that is formed after 8 h of desiccator precipitation (see Figure 3.13 B). Amorphous calcium carbonate (ACC), which usually forms around this duration of crystallization is shown to agglomerate without close contact to the NPs surface. Rather the particles attach to the highly charged surfaces of growing crystalline CaCO_3 . The effect on the shape of the final crystals is mainly an elongation and inhibition of size compared to the reference rhombohedra (about 20 μm edge length, not shown). This might be caused by calcium ion binding of the charged ligand of the NPs (see Figure 3.13 C). The resulting crystal shapes for different particle concentrations (see Figure S 3.22, SI) also show terraces scattered over the crystal whereon Janus particles agglomerate and especially function as surface defects on the CaCO_3 surface. The Raman spectrum shown in Figure S 3.27 (B) shows nano-crystalline CaCO_3 (lattice band broadening) and small amounts of Fe_3O_4 and organic molecules on Au domain around 1500 cm^{-1} . This opens the question about occlusion of 1-DT/Au@ Fe_3O_4 /4-SBA particles (a) within the CaCO_3 crystals. Figure 3.13 D-F and the STEM-EDX in Figure S 3.25 of the Supporting Information answer this question with a positive statement. As shown by HR-TEM imaging the particles remain intact and incorporate as aggregates especially around the less crystalline center of the crystal. The CaCO_3 nanocrystals, which are formed (see rocking curve analysis Figure S 3.29 as evidence) do not interact with the surfaces of the Janus particles. But still their inclusion as rather large agglomerates forms defects in the crystal lattice of the CaCO_3 .

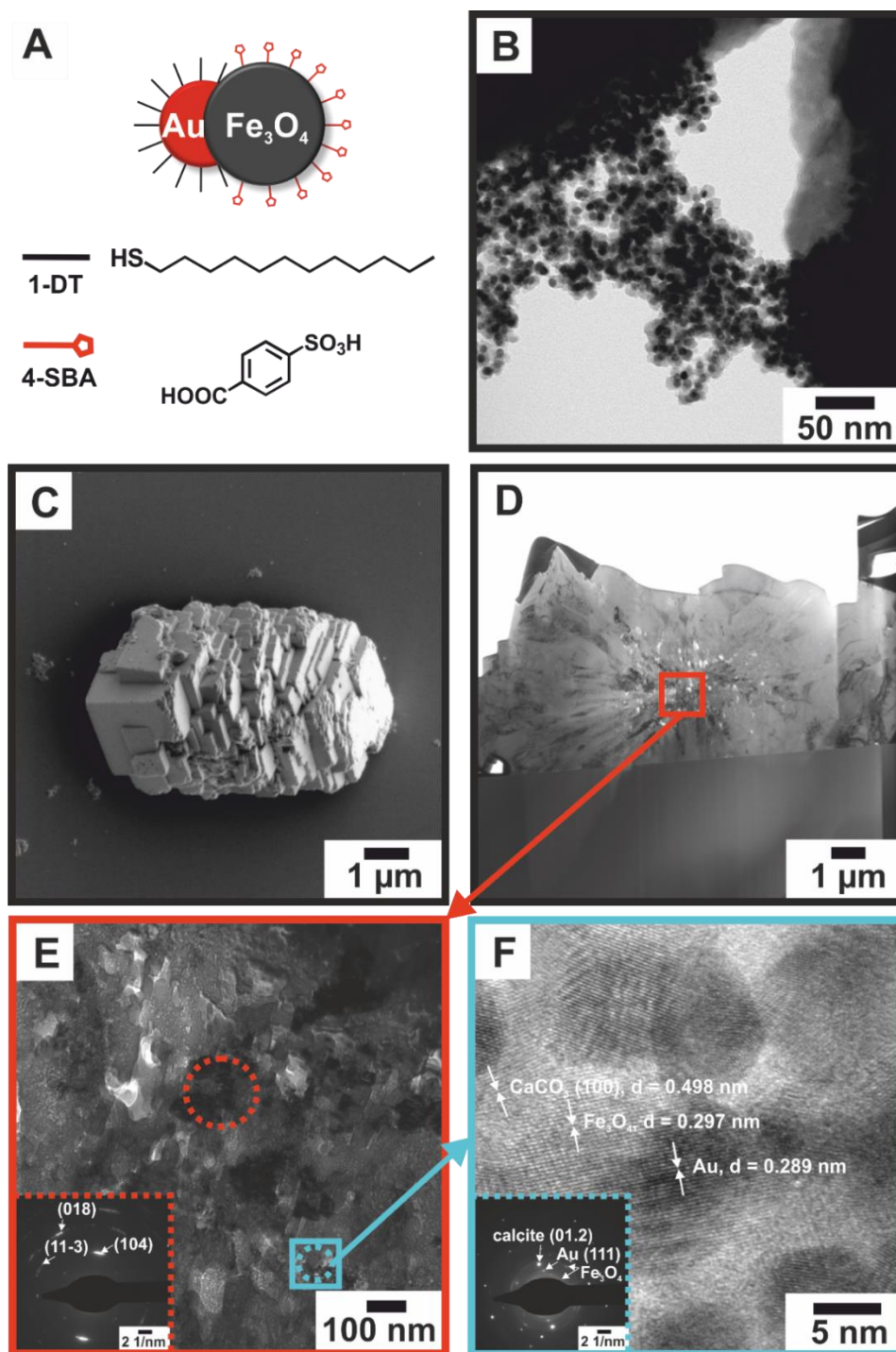


Figure 3.13: (A) Scheme of type (a) functionalized Au@Fe₃O₄ Janus particles (B) TEM image after 8 h desiccator CaCO₃ precipitation. Surface attachment of persistent Janus particle agglomerates on formed crystalline CaCO₃ can be observed. The SEM image of a calcite crystal (C) shows many terraces and elongated crystals. (D) Cross-section from FIB preparation and HR-TEM image (E) showing hollow nano-crystalline center of the crystal with multiple twinning (see inlay SAED). The zoom-in into a Janus particle bearing area (magenta square) and its related SAED pattern that indicates nano-crystallinity and successful occlusion of the Au@Fe₃O₄ particles within the meso-crystal.

If the Janus particles domain polarity is changed from non-polar Au and polar Fe_3O_4 for the functionalization pattern (a) to the polar/non-polar combination (b) 11-MUA/Au@ Fe_3O_4 /4-TBC (see Figure 3.14 (A)) still the particles form agglomerates on the TEM grid after 8 h of crystallization (see Figure 3.14 (B)). In contrast to type (a) particles a strong ACC stabilization on their NPs surface is visible for type (b) Janus particles. This fact might be dedicated to the already reported property of 11-MUA on Au-domains to stabilize CaCO_3 as ACC. (see Chapter 3.1.1 for analogous results). The effect on the shape of the final crystals is mainly an elongation of the calcite crystals to rod-like crystals truncated with multiple (104) terraces of calcite, which might be caused by additive absorption on polar step edges (see Figure 3.14 C). The resulting crystal shapes for lower particle concentrations (see Figure S 3.23, SI) also show these effects for all precipitated crystals. All over the CaCO_3 crystals Janus Particles agglomerate on the surface. These particles can be identified by the Raman spectrum shown in Figure S 3.27 (B). Again nano-crystalline CaCO_3 and a small amount of Fe_3O_4 and organic compounds on Au domain around 1500 cm^{-1} wavenumber can be observed. This once more entails the question: Are 11-MUA/Au@ Fe_3O_4 /4-TBC particles (b) incorporated into the CaCO_3 crystals? Figure 3.14 D-F answers this question. HR-TEM of the cross-section (Figure 3.14 (C and D)) underlines the nano-crystallinity of the precipitated CaCO_3 . Rocking curve analysis (compared Figure S 3.29 and Table S 3.4 of the Supporting Information) also shows the large mosaicity of the precipitated composite mesocrystals. HR-TEM shows that the NPs remain intact and occlude as aggregates especially around the less crystalline center of the crystal. The CaCO_3 nanocrystals interact with the functionalization layer of the Janus particles differently. The interaction of 11-MUA functionalized Au domains of the particles is stronger due to carbonate-carboxylate similarity compared to the weaker sulfonate-calcium carbonate interactions. As a result ACC can be stabilized on the Au domain surface (see Figure 3.14 and Figure 3.15). The subsequent transformation to crystalline calcite results in an interaction of the calcite (100) facet with the Au (111) facet of the Janus particles due to small lattice match of $\Delta \sim 0.2\%$ (as demonstrated for Au-NPs in chapter 3.1.1). From iron oxide domains, which remain attached to Au no

direct interaction is visible and the gold domain interaction with CaCO_3 is less organized due to the weaker ligand-calcium carbonate interaction and bad lattice match to CaCO_3 .

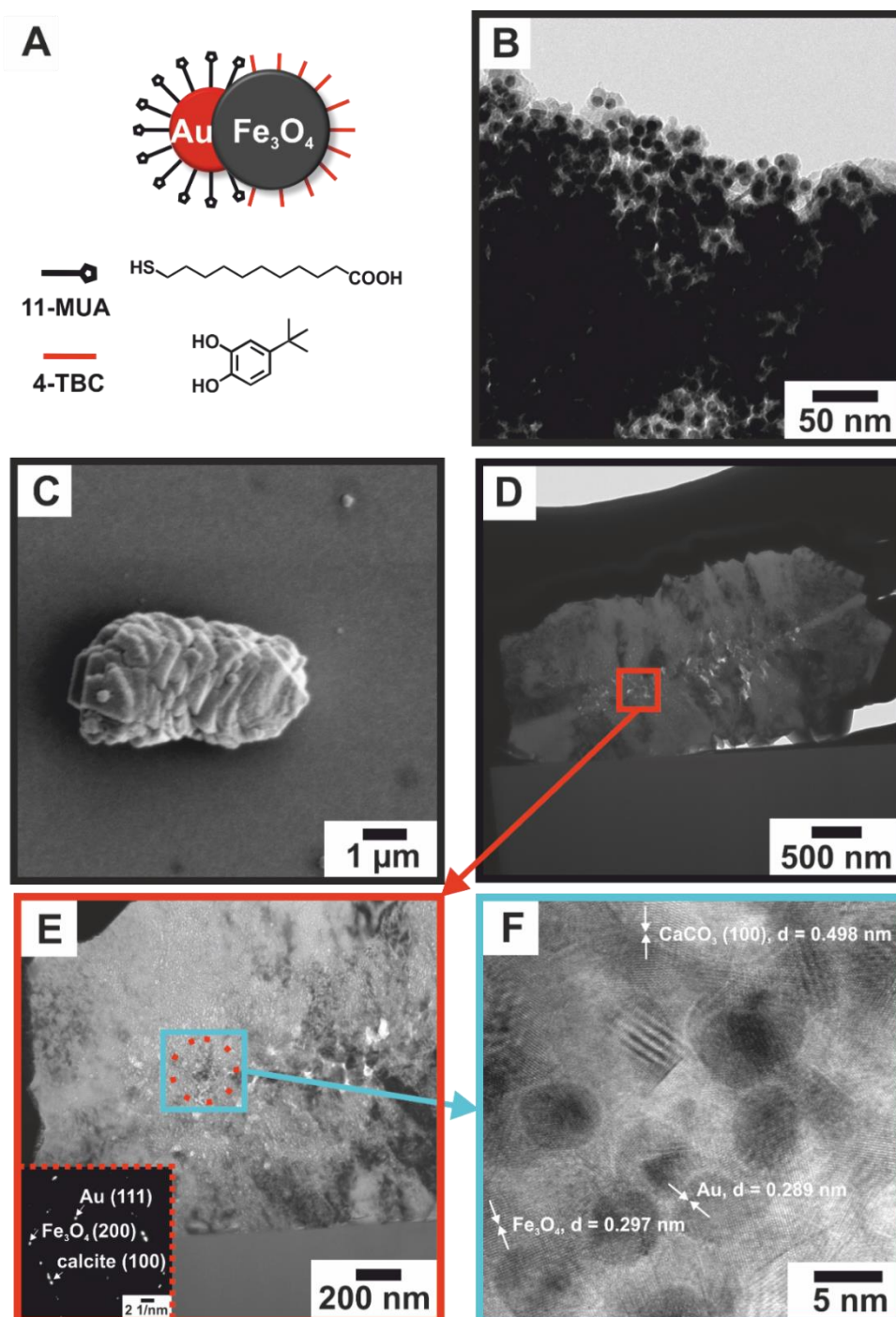


Figure 3.14: (A) Scheme of type (b) functionalized $\text{Au}@Fe_3O_4$ Janus particle (B) TEM image after 8 h desiccator CaCO_3 precipitation. The Janus particles agglomerate and CaCO_3 is precipitated on their surface. (C) SEM image of a calcite crystal after 15 h ADM experiment shows many terraces

on very small elongated calcite crystals. (D) Cross-section from FIB preparation and HR-TEM image (E) showing hollow nano-crystalline center of the crystal with multiple twinning (see inlay SAED of yellow circle). The zoom-in into a Janus particle containing area (magenta square) nano-crystallinity and successful occlusion of the Au@Fe₃O₄ particles within the mesocrystal.

For isotropic and all over anionic 11-MUA/Au@Fe₃O₄/4-SBA Janus particles (c) small scale inhibited dumbbell shaped CaCO₃ mesocrystals of grey color precipitate on the glass substrate within 15 h in the desiccator experiment (see Figure 3.15 B and Figure S 3.24, Supporting Information). Raman spectra of the CaCO₃ crystals have shown strong bands SERS bands for 11-MUA on Au and also Fe₃O₄ as well as shift and broadening of lattice modes of CaCO₃, which indicates integration of particles or fragments of particles and a less crystalline CaCO₃ host lattice (see Figure S 3.27 A of the Supporting Information). Also the shift of the rocking curve main reflex its large mosaicity as well as the reflection shift of the (104) reflex in XRD measurements (see Figure S 3.28 and Figure S 3.29 and associated Table S 3.3 and Table S 3.4 of the SI) underline the formation of a mesocrystal with integrated nanoparticles. Hence all these techniques provide no information on the material of the particles. For the addition of strong CaCO₃ interacting functionalized Au@Fe₃O₄ Janus particles one would expect the incorporation of the particle. Surprisingly this is only partially the case. FIB-cut cross-section analysis in Figure 3.15 C-F first shows existence of a lot of holes inside the mesocrystal and the presence of Janus particles on the surface of the mesocrystal. But HR-TEM of the core part around the holes shows small Au nanoparticles incorporated into the CaCO₃ mesocrystal (see Figure 3.15 F). Separation of Au and Fe₃O₄ domains can be caused by the good lattice match of Au and CaCO₃ but the worse interaction of the functionalization of the Fe₃O₄ domain and its worse lattice match to calcite of $\Delta = 1,5\%$. This match/mismatch relationship induced stress and strain into the mineralizing CaCO₃ and epitaxy of the Au (111) to the CaCO₃ (100) facet as shown by FFT in Figure 3.15 E can be observed.

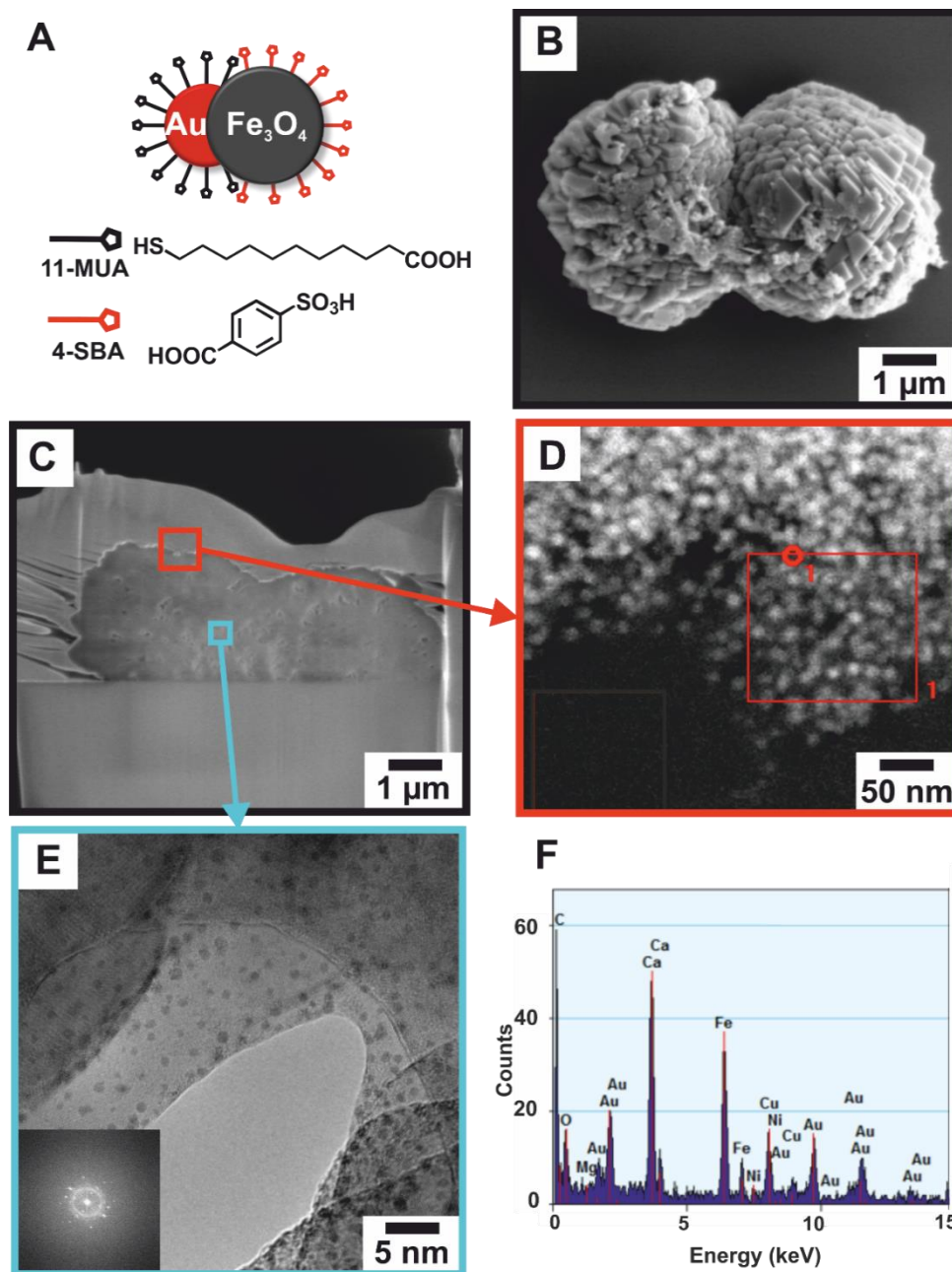


Figure 3.15: (A) Scheme of type (c) functionalized Au@Fe₃O₄ Janus particles (B) SEM image of an exemplary final dumbbell calcite crystal shows dumbbell shaped crystals with lot of terraces and elongation along *c*-axis of calcite. The cross-section from FIB preparation (C) shows small bulk crystal. (D) STEM image of surface bound particles with EDX (F) indicating Au@Fe₃O₄ and Fe₃O₄ agglomerated on the surface. The zoom-in (E) shows Au-NPs of variable sizes within the CaCO₃ lattice. Epitactic growth induces stress and strain into the nano-crystalline material which causes tilting and multiple twinning of the nanocrystals (see inlay FFT). Iron oxide is not found inside the CaCO₃ lattice due to large lattice mismatch to CaCO₃.

For isotropic and all over anionic 11-MUA/Au@Fe₃O₄/4-SBA Janus particles (c) small extremely scale inhibited dumbbell shaped CaCO₃ mesocrystals of grey color

precipitated within 15 h in the desiccator (see Figure 3.15 B and Figure S 3.24, Supporting Information). Besides the optical microscopy also Raman spectroscopy shows strong SERS bands for organics bound on Au domains and Fe_3O_4 assignable bands. Further broadening of the lattice mode of CaCO_3 which indicates successful integration of particles or fragments of particles and nano-crystallinity of the CaCO_3 host lattice has been observed (see Figure S 3.27).

3.1.3.4 Conclusion

Both anisotropic particle species (a) and (b) agglomerate and occlude in micellar assemblies into CaCO_3 . This is mainly caused by their amphiphilic character. The surface interaction with mineralizing CaCO_3 for case (a) is less specific than the interaction of Au/11-MUA domain in type (b) Janus particles. Both types (a) and (b) form elongated rhombohedral calcite crystals of overall low crystallinity due to particle occlusion. In all cases we were able to identify oriented, small crystallites within the crystal assemblies which is defined as a mesocrystal in literature. The small amount of incorporated particles for (a) and (b) can either be caused by bad colloidal stability or bad interaction of the particles with the forming CaCO_3 . In contrast to the anisotropic functionalized particle batches, the isotropic Janus particle functionalization pattern (c) shows surface agglomeration of both intact Janus particles as well as fragments of Fe_3O_4 on the mesocrystal surface and incorporation of Au nanocrystal fragments inside the mesocrystal. Incorporation of Au into CaCO_3 with nanocrystals with expressed (100) facets epitaxy to the Au (111) facet has also been shown for this particle functionalization. The integration of Janus particles has been demonstrated to correlate with the surface functionalization and total dispersion stability and thus resulting degree of interaction with CaCO_3 . To study for lattice anisotropy effects triggered by the functionalization pattern other stabilization strategies for example by polymers need to be used for better colloidal stability of the particles. Hence these results motivate further research on the formation of a cheap composite material with extraordinary magnetic as well as optic properties for diverse applications.

3.1.3.5 Supporting Information

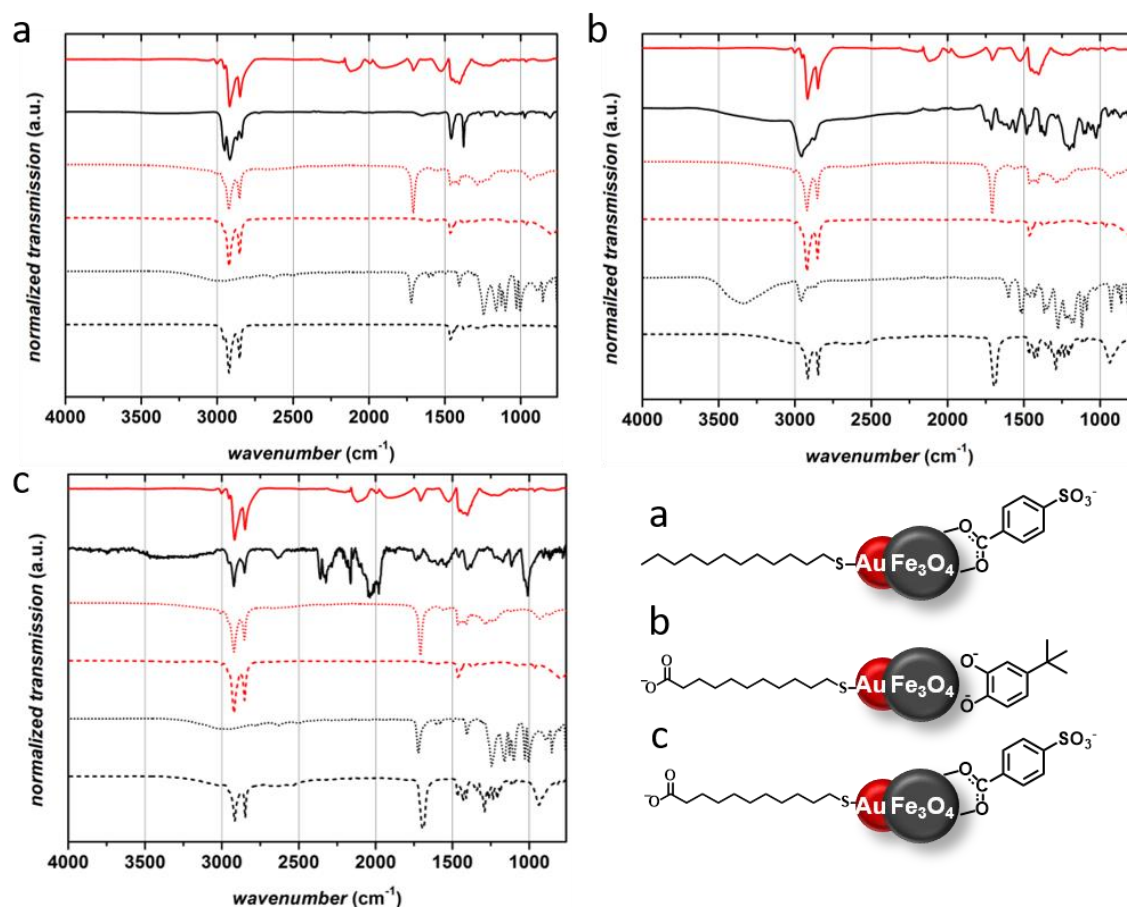


Figure S 3.18: IR-Spectra of Janus particles functionalized with (a) 1-DT/Au@Fe₃O₄/4-SBA, (b) 11-MUA/Au@Fe₃O₄/TBC and (c) 11-MUA/Au@Fe₃O₄/4-SBA. For all graphs the following order was plotted from top to bottom: Reference pattern Oam/Au@Fe₃O₄/Oac (red, solid line), finally functionalized particles (a,b or c pattern) as black solid line, Oac (red dotted line), Oam (red dashed line), ligand on Fe₃O₄ domain (either 4-SBA (a and c) or TBC (b)), ligand on Au domain (either 1-DT (a) or 11-MUA (b and c)). Successful functionalization was indicated for 1-DT and 11-MUA by shift of –C-S valence bending to higher wavenumbers caused by binding to Au-surface. For Fe₃O₄ domain bond TBC the shift of –C=O valence from hydroxyl groups to smaller wavenumbers was indicating binding on magnetite surface (see (b) 1100-1200 cm⁻¹). 4-SBA binding was confirmed by –C=O valence attenuation and shifting to smaller wavenumber (from 1720 cm⁻¹ to 1600 cm⁻¹)

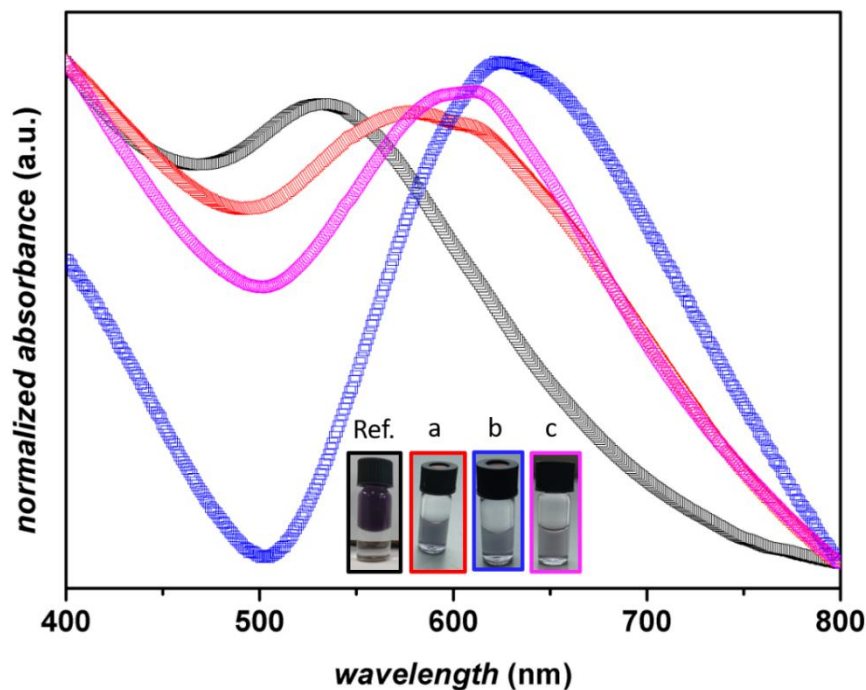


Figure S 3.19: UV-Vis spectra of aqueous Janus particle dispersions at basic pH value and of a hexane dispersion for reference sample. Reference particles are shown in black and functionalized with Oam/Au@Fe₃O₄/Oac. Such Janus particles have the plasmon absorbance maximum at $\lambda = 545$ nm. For (a) functionalized with 1-DT enhancing only weak agglomeration of the particles the band shifts to $\lambda = 580$ nm while for (b and c) functionalized with 11-MUA on the gold domain the shift is much larger. This is due to higher refractive index of the surface ligand and due to the strength of agglomeration induced by interactions of gold domains. For the amphiphilic particles of type (b) the plasmon band shifts to $\lambda = 630$ nm. For the totally negatively charged particle of type (c) the coulomb interactions are stronger thus the maximum of the band is $\lambda = 600$ nm due to weaker plasmon coupling.

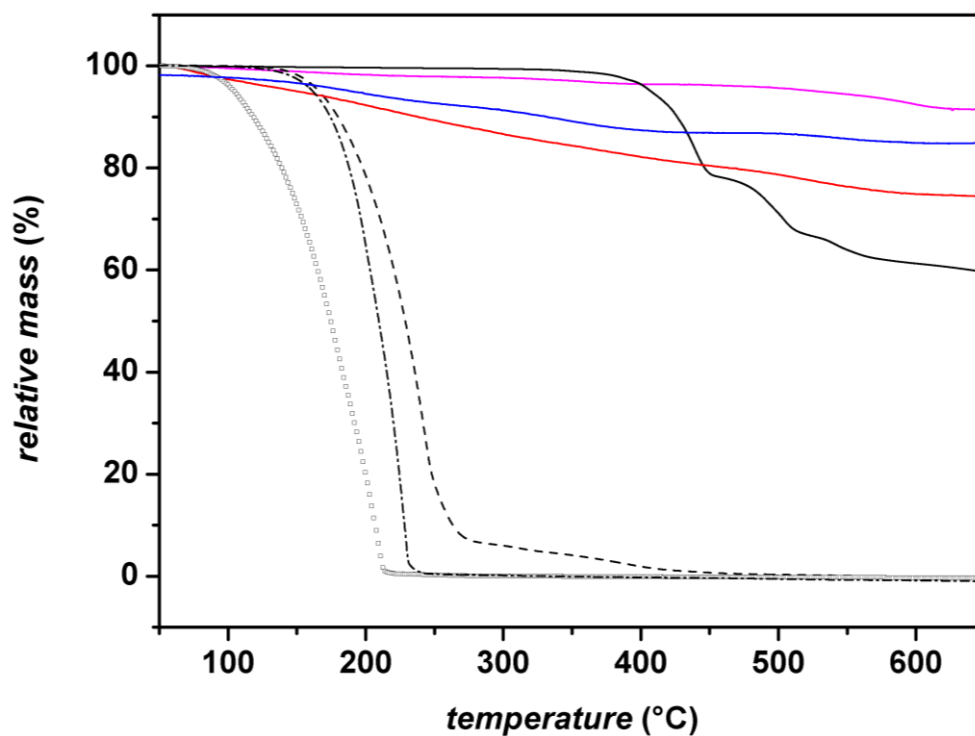


Figure S 3.20: TGA data of Janus particles of functionalization pattern shown in Figure S 3.18. The color code is similar as for Figure S 3.19. Reference TGA data for 1-DT (black box), TBC (dash dotted black line), 11-MUA (dashed black line) and 4-SBA (solid black line) is also added in the graph. Functionalization of Janus particles in general gives low density of packing, which is mainly due to interactions of sulfate and carboxylate head-groups during surface functionalization reaction and the persistent capping agents Oam and Oac on the Au and Fe_3O_4 surface.

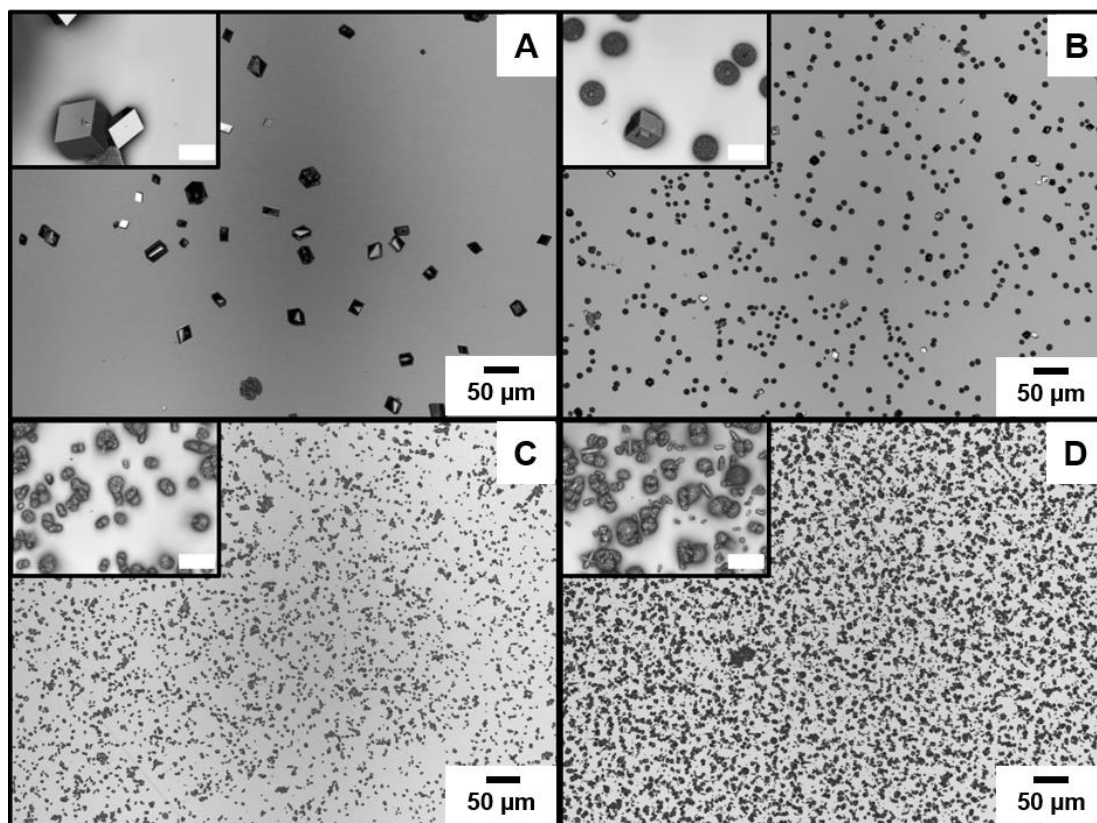


Figure S 3.21: Optical microscopy images of (A) reference without additive and with 4-SBA as additive in (B) 0.01 mM (C) 0.05 mM and (D) 0.1 mM concentration in the standard desiccator experiment as described (inlay scalebar: 20 μm). With increasing content of 4-SBA the average crystal size decreases while the overall amount of seeds increases. The shape and polymorph changes from calcite (A) without additive to vaterite in dumbbell to elongated cigar shape. Thus 4-SBA has an inhibition effect for classical crystallization because after 15 h usually the thermodynamically stable product calcite is formed.

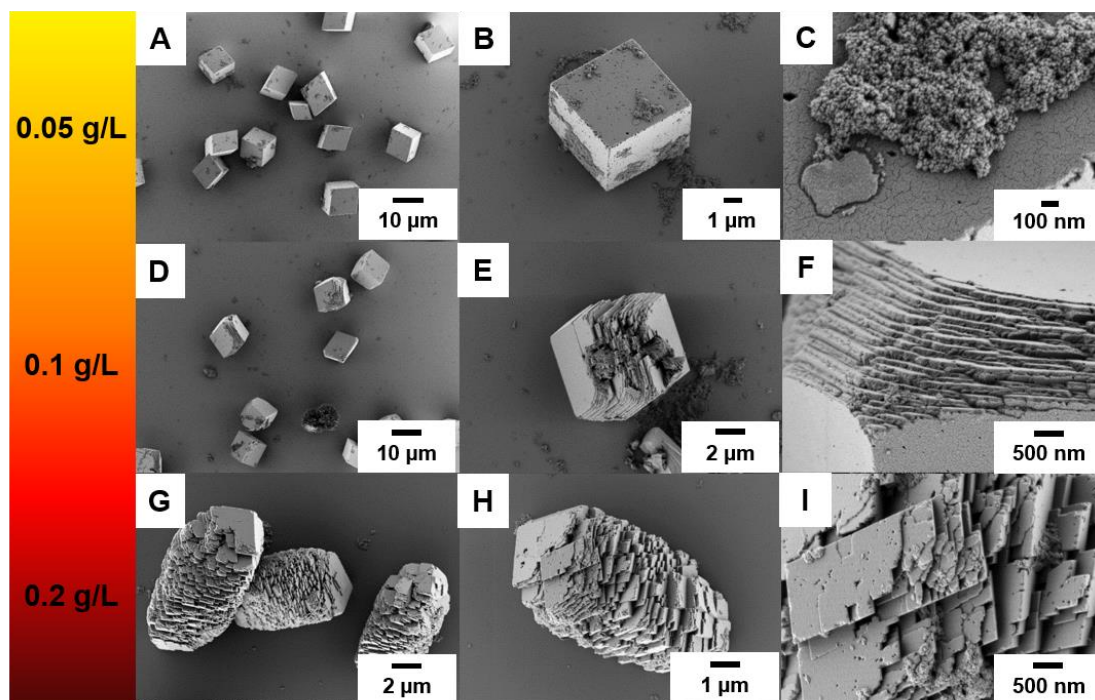


Figure S 3.22: SEM images of CaCO₃ crystals precipitated under presence of various concentrations of 1-DT/Au@Fe₃O₄/4-SBA NPs in a 5 mM CaCl₂ solution after 15 h in the standard desiccator ammonia diffusion experiment for CaCO₃ precipitation.

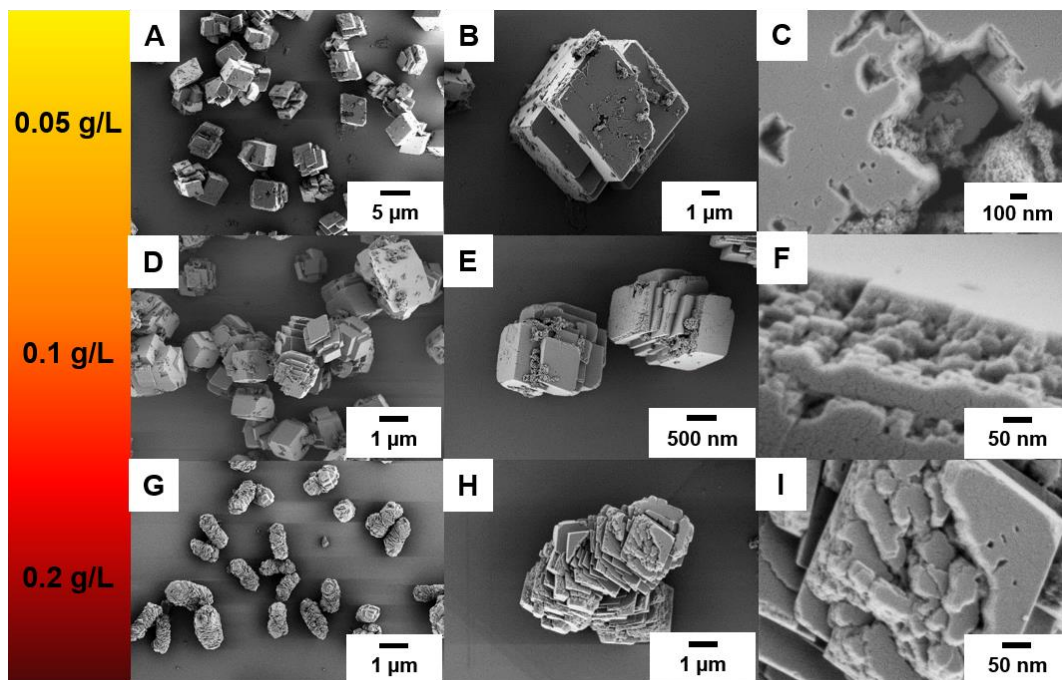


Figure S 3.23: SEM images of CaCO₃ crystals precipitated under presence of various concentrations of 11-MUA/Au@Fe₃O₄/4-TBC NPs in a 5 mM CaCl₂ solution after 15 h in the standard desiccator ammonia diffusion experiment for CaCO₃ precipitation.

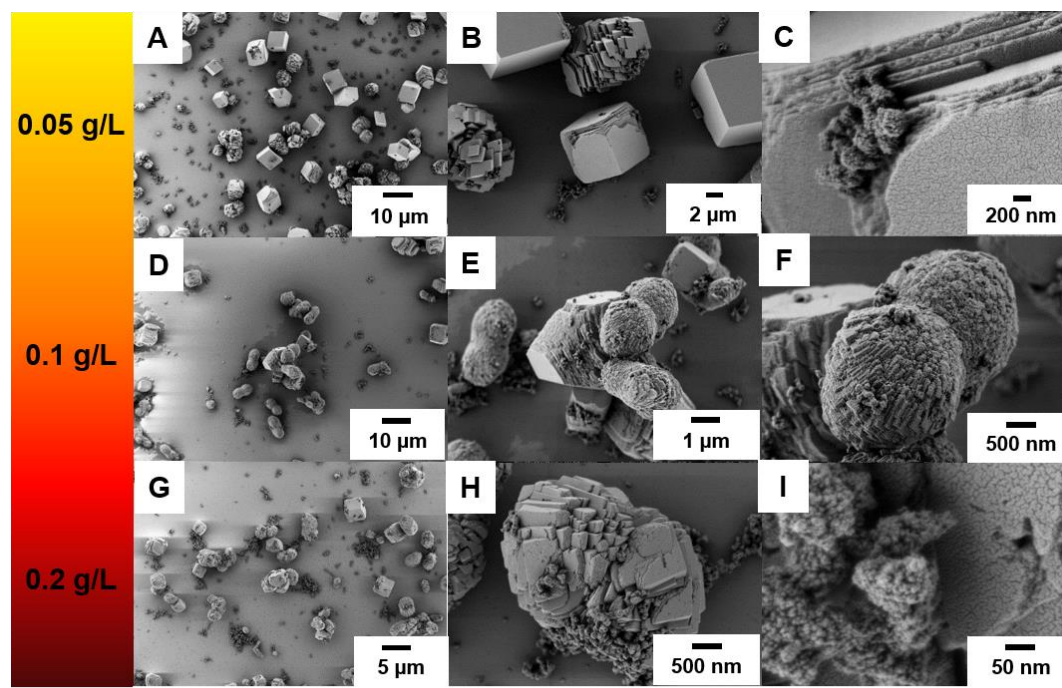


Figure S 3.24: SEM images of CaCO₃ crystals precipitated under presence of various concentrations of 11-MUA/Au@Fe₃O₄/4-SBA NPs in a 5 mM CaCl₂ solution after 15 h in the standard desiccator ammonia diffusion experiment for CaCO₃ precipitation.

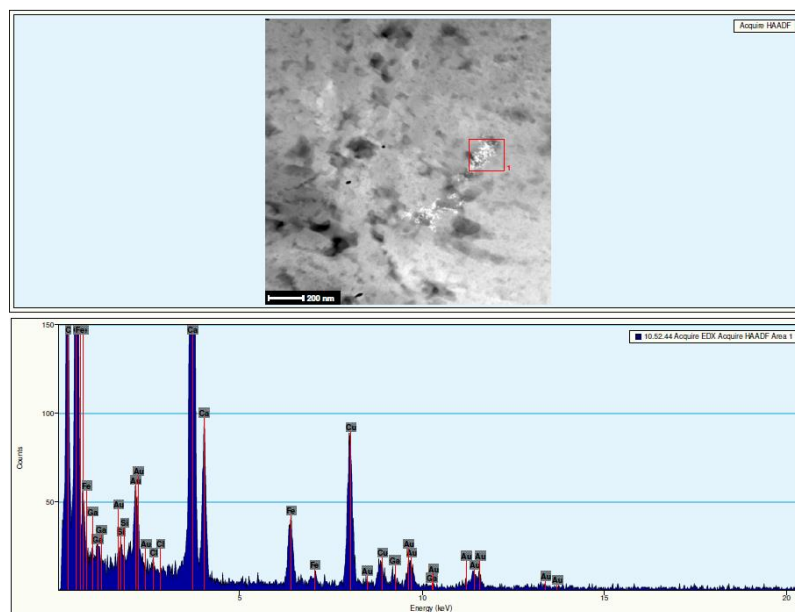


Figure S 3.25: STEM image of a cross-section of an exemplary CaCO₃ crystal precipitated after 15 h duration under presence of 0.2 g/L of (a) 1-DT/Au@Fe₃O₄/4-SBA NPs from a 5 mM CaCl₂ solution in the standard ammonia diffusion desiccator experiment. Light spots identify Au@Fe₃O₄ Janus particles included as particle clusters. The EDX shows Au and Fe to be present in the selected area of interest.

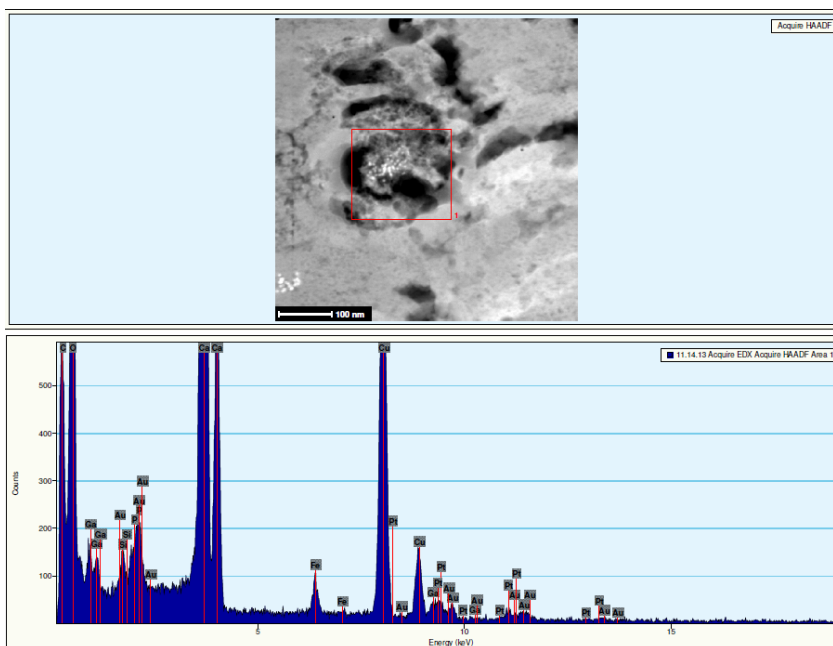


Figure S 3.26: STEM image of cross-section of an exemplary CaCO₃ crystal precipitated after 15 h duration under presence of 0.2 g/L of (b)11-MUA/Au@Fe₃O₄/4-TBC NPs from a 5 mM CaCl₂ solution in the standard ammonia diffusion desiccator experiment. Light spots identify Au@Fe₃O₄ Janus particles incorporated as particle clusters. The EDX identifies Au and Fe to be present in the selected area of interest.

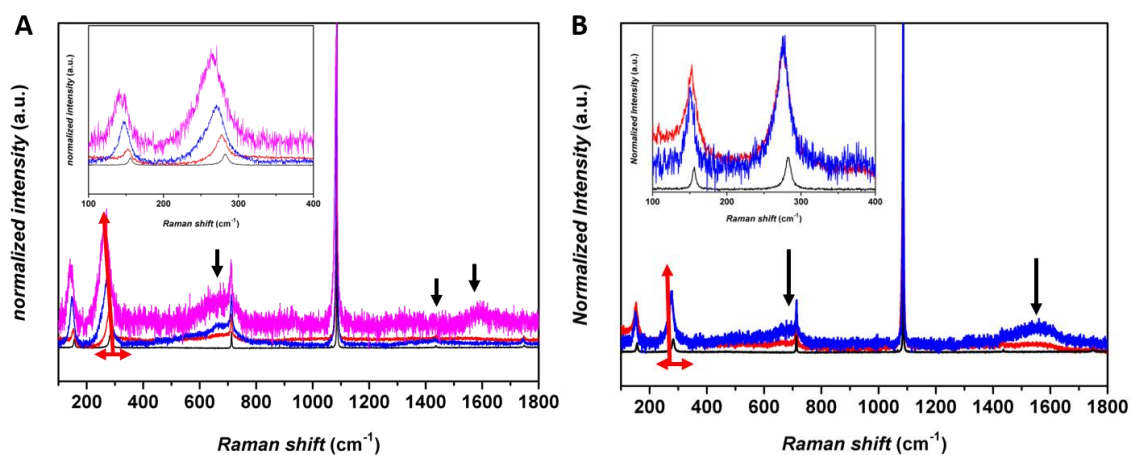


Figure S 3.27: Raman spectra of CaCO_3 precipitated under addition of (A) 11-MUA/Au@ Fe_3O_4 /4-SBA (black: reference, red: 0.05 g/L, blue: 0,1 g/L, magenta: 0,2 g/L). Black arrows show Fe_3O_4 bands between 500 cm^{-1} and 800 cm^{-1} and SERS signal of organic molecules on Au surface of particles between 1300 cm^{-1} and 1700 cm^{-1} . Continuous shift of lattice mode from 283 cm^{-1} to almost 260 cm^{-1} indicates inclusion of NPs. Nano-crystallinity results in a peak broadening of the lattice mode of CaCO_3 . In (B) Raman spectra of CaCO_3 crystals precipitated if 0.2 g/L of 11-MUA/Au@ Fe_3O_4 /TBC (blue) and of 1-DT/Au@ Fe_3O_4 /4-SBA (red) was present (black line = reference). For all cases a small peak shift and broadening of the lattice mode peak is observed, while the 11-MUA/Au@ Fe_3O_4 /TBC particles strongly bind to CaCO_3 as shown by better defined Fe_3O_4 and SERS bands.

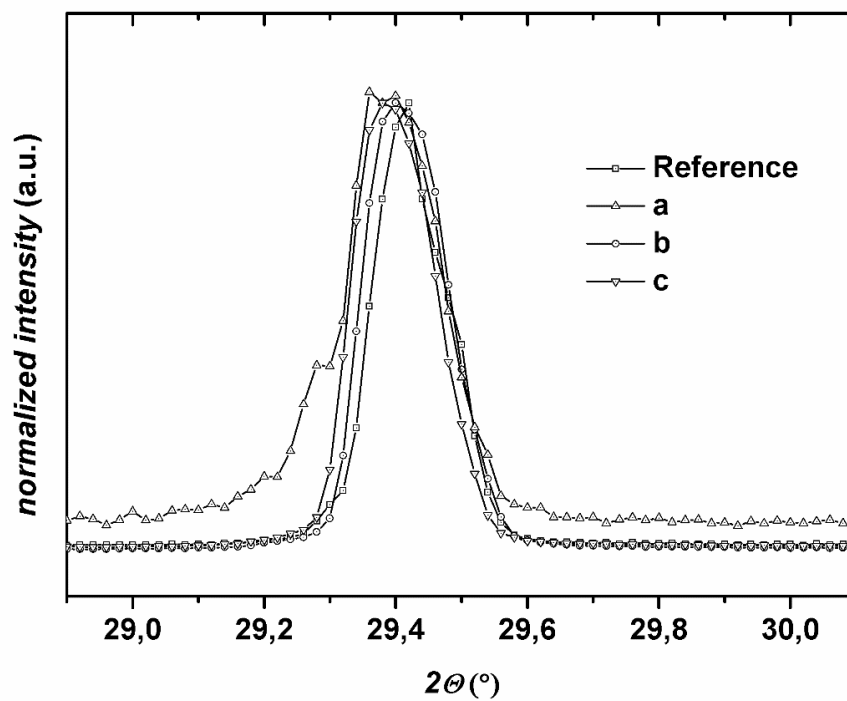


Figure S 3.28: XRD 2θ scan of calcites (104) reflex for different additives added to the crystallization. For all samples Gaussian or Lorentzian fits were used to find the reflex maximum and FWHM for average crystallite size determination via the Scherrer Equation shown in Table S 3.3.

Table S 3.3: Calculations for 2θ scans of reference sample and calcite precipitated if 0.2 g/L of different Au@Fe₃O₄ Janus particles of various functionalization patterns is added. Mass concentrations are constant for all particle fractions. FWHM in general is larger if particles are added, which results in smaller average crystal size within the mesocrystal assembly. Similar 2θ values for samples (a) and (b) compared to the reference measurement identifies the lattice plane distance to be not affected by addition of these particles. Only the integrated particle fraction (c) 11-MUA /Au@Fe₃O₄/4-SBA reflex shifts slightly to smaller 2θ value, which is due to the occlusion of Au particles and the resulting expanding of the average lattice plane distance by integration into grain boundaries.

Sample	<i>FWHM</i> (°)	<i>d</i> (nm)	2θ (°)
Reference	0.120	76.1	29.41
(a) 1-DT/Au@Fe ₃ O ₄ /4-SBA	0.168	54.3	29.40
(b) 11-MUA /Au@Fe ₃ O ₄ /4-TBC	0.149	61.0	29.41
(c) 11-MUA /Au@Fe ₃ O ₄ /4-SBA	0.149	61.0	29.38

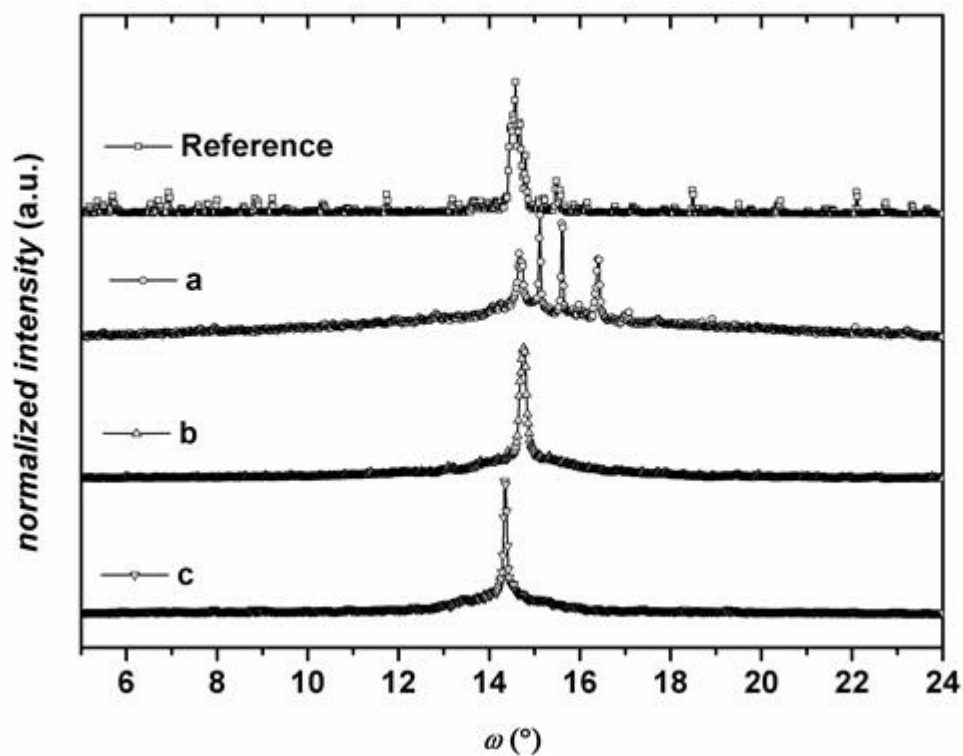


Figure S 3.29: Rocking curve analysis from 5° to 24° ω angle under constant 2Θ angle of 29.42° analyzing the (104) truncated CaCO_3 mesocrystals for their mosaicity as indicator for mesocrystals formed from nano-crystals. For all NP additions the same mass concentration of particles was used (0.2 g/L). For calculations and discussion see Table S 3.4.

Table S 3.4: Calculations from fits of rocking curve data. For the reference sample a sharp reflex of FWHM 0.251° and a maximum at $\omega = 14.63^\circ$ indicates highly oriented crystallites within the at times on the glass slide randomly oriented crystals (sharp reflexes at various angles). For addition of (a) 1-DT/Au@Fe₃O₄/4-SBA NPs the main reflex has a broad basis with two identified fractions with FWHM of 7.246° and 1.002° which indicates large mosaicity of the crystals. Additional sharp reflexes may have their origin in favored orientation of crystals on the substrate. If (b) 11-MUA /Au@Fe₃O₄/4-TBC nanoparticles are added the main reflex broadens and a broad background of large mosaicity can also be observed (FWHM 2.648°). NPs of type (c) 11-MUA /Au@Fe₃O₄/4-SBA shift the sharp reflex and its large mosaicity identifying basis to smaller ω angles. This is caused by the successful integration of Au nanocrystals within the CaCO₃ composite and systematic misorientation.

Sample	FWHM (°)	ω (°)	ω_{theo} (°)	$\Delta \omega$ (°)
Reference	0.251	14.63	14.7	0.07
(a) 1-DT/Au@Fe ₃ O ₄ /4-SBA	0.102	14.68	14.7	0.02
	1.002	14.89	14.7	0.19
	7.246	14.89	14.7	0.19
(b) 11-MUA /Au@Fe ₃ O ₄ /4-TBC	0.165	14.77	14.7	0.07
	2.684	14.77	14.7	0.07
(c) 11-MUA /Au@Fe ₃ O ₄ /4-SBA	0.071	14.35	14.7	0.35
	1.673	14.33	14.7	0.37

3.1.3.6 References

- [1] S. Borukhin, L. Bloch, T. Radlauer, A. H. Hill, A. N. Fitch, B. Pokroy, *Adv. Funct. Mater.* **2012**, *22*, 4216–4224.
- [2] Y. Ning, L. A. Fielding, K. E. B. Doncom, N. J. W. Penfold, A. N. Kulak, H. Matsuoka, S. P. Armes, *ACS Macro Lett.* **2016**, 311–315.
- [3] A. S. Schenk, I. Zlotnikov, B. Pokroy, N. Gierlinger, A. Masic, P. Zaslansky, A. N. Fitch, O. Paris, T. H. Metzger, H. Cölfen, P. Fratzl, B. Aichmayer, *Adv. Funct. Mater.* **2012**, *22*, 4668–4676.
- [4] Y. Ning, L. A. Fielding, L. P. D. Ratcliffe, Y.-W. Wang, F. C. Meldrum, S. P. Armes, *J. Am. Chem. Soc.* **2016**.
- [5] S. E. Wolf, N. Loges, B. Mathiasch, M. Panthöfer, I. Mey, A. Janshoff, W. Tremel, *Angew. Chem. Int. Ed.* **2007**, *46*, 5618–5623.
- [6] R. C. Kang, Y.-Y. Kim, P. Yang, W. Cai, H. Pan, A. N. Kulak, J. L. Jau, J. DeYoreo, *Nat. Commun.* **2016**, *7*, 10187–10194.
- [7] Q. Meng, D. Chen, L. Yue, J. Fang, H. Zhao, L. Wang, *Macromol. Chem. Phys.* **2007**, *208*, 474–484.
- [8] M. H. Nielsen, D. Li, H. Zhang, S. Aloni, T. Y.-J. Han, C. Frandsen, J. Seto, J. F. Banfield, H. Cölfen, J. J. de Yoreo, *Microsc. Microanal.* **2014**, *20*, 425–436.
- [9] X. Ma, H. Yang, H. Chen, L. Yang, Y. Guo, Y. Si, *J. Cryst. Growth* **2011**, *327*, 146–153.
- [10] D. Gebauer, *Angew. Chem. Int. Ed.* **2013**, *52*, 8208–8209.
- [11] A. Jabbarzadeh, X. Chen, *Faraday Discuss.* **2017**, *204*, 307–330.
- [12] H. Hou, B. Wang, S.-Y. Hu, M.-Y. Wang, J. Feng, P.-P. Xie, D.-C. Yin, *J. Cryst. Growth* **2017**, *468*, 290–294.
- [13] V. K. Marghussian, A. Sheikh-Mehdi Mesgar, *Ceram. Int.* **2000**, *26*, 415–420.
- [14] P. Supaphol, W. Harnsiri, J. Junkasem, *J. Appl. Polym. Sci.* **2004**, *92*, 201–212.
- [15] S.-S. Wang, A.-W. Xu, *Cryst. Growth Design* **2013**, *13*, 1937–1942.
- [16] T. Wang, H. Cölfen, M. Antonietti, *J. Am. Chem. Soc.* **2005**, *127*, 3246–3247.

-
- [17] D. J. Nelson, T. C. Rains, J. A. Norris, *Science* **1966**, *152*, 1368–1370.
- [18] J. Chen, L. Xiang, *Pow. Tech.* **2009**, *189*, 64–69.
- [19] M. Merlini, M. Hanfland, W. A. Crichton, *Earth Planet. Sci. Lett.* **2012**, *333-334*, 265–271.
- [20] M. Kitamura, H. Konno, A. Yasui, H. Masuoka, *J. Cryst. Growth* **2002**, *236*, 323–332.
- [21] T. Ogino, T. Suzuki, K. Sawada, *Geochimi. Cosmochimi. Acta* **1987**, *51*, 2757–2767.
- [22] M. Ikura, *Trends Biochem. Sci.* **1996**, *21*, 14–17.
- [23] S. Brunet, T. Scheuer, R. Klevit, W. A. Catterall, *J. Gen. Physio.* **2005**, *126*, 311–323.
- [24] H. Kawasaki, R. H. Kretsinger, *Protein Sci.* **2017**, *26*, 1898–1920.
- [25] A. Lewit-Bentley, S. Réty, *Curr. Op. Struct. Bio.* **2000**, *10*, 637–643.
- [26] F. F. Amos, M. Ndao, J. S. Evans, *Biomacromolecules* **2009**, *10*, 3298–3305.
- [27] J. Su, F. Zhu, G. Zhang, H. Wang, L. Xie, R. Zhang, *Cryst. Eng. Comm.* **2016**, *18*, 2125–2134.
- [28] Y. Tang, W. Yang, X. Yin, Y. Liu, P. Yin, J. Wang, *Desalination* **2008**, *228*, 55–60.
- [29] M. Dietzsch, M. Barz, T. Schüler, S. Klassen, M. Schreiber, M. Susewind, N. Loges, M. Lang, N. Hellmann, M. Fritz, K. Fischer, P. Theato, A. Kühnle, M. Schmidt, R. Zentel, W. Tremel, *Langmuir* **2013**, *29*, 3080–3088.
- [30] G. Wang, L. Li, J. Lan, L. Chen, J. You, *J. Mater. Chem.* **2008**, *18*, 2789–2797.
- [31] P. Agarwal, K. A. Berglund, *Cryst. Growth Design* **2003**, *3*, 941–946.
- [32] K. Rae Cho, Y.-Y. Kim, P. Yang, W. Cai, H. Pan, A. N. Kulak, J. L. Lau, P. Kulshreshtha, S. P. Armes, F. C. Meldrum, J. J. de Yoreo, *Nat. Commun.* **2016**, *7*, 10187.
- [33] A. N. Kulak, P. Yang, Y.-Y. Kim, S. P. Armes, F. C. Meldrum, F. C. Meldrum, *Chem. Commun* **2014**, *2014*, 67–69.
- [34] A. N. Kulak, M. Semsarilar, Y.-Y. Kim, J. Ihli, L. A. Fielding, O. Cespedes, S. P. Armes, F. C. Meldrum, *Chem. Sci.* **2013**, *5*, 738–743.

-
- [35] J. Stettner, P. Frank, T. Griesser, G. Trimmel, R. Schennach, E. Gilli, A. Winkler, *Langmuir* **2009**, *25*, 1427–1433.
- [36] J. Hautman, J. P. Bareman, W. Mar, M. L. Klein, *J. Chem. Soc. Faraday Trans.* **1991**, *87*, 2031–2037.
- [37] J. Küther, R. Seshadri, W. Tremel, *Angew. Chem. Int. Ed.* **1998**, *37*, 3044–3047.
- [38] A. N. Kulak, M. Semsarilar, Y.-Y. Kim, J. Ihli, L. A. Fielding, O. Cespedes, S. P. Armes, F. C. Meldrum, *Chem. Sci.* **2013**, *5*, 738–743.
- [39] Y.-J. Han, J. Aizenberg, *Angew. Chem.* **2003**, *115*, 3796–3798.
- [40] H. Teghidet, M. C. Bernard, S. Borensztajn, L. Chaal, S. Joiret, B. Saidani, *J. Cryst. Growth* **2011**, *331*, 72–77.
- [41] T. D. Schladt, K. Schneider, H. Schild, W. Tremel, *Dalton Trans.* **2011**, *40*, 6315–6343.
- [42] S. Mourdikoudis, L. M. Liz-Marzán, *Chem. Mater.* **2013**, *25*, 1465–1476.
- [43] M. Bloemen, W. Brullot, T. T. Luong, N. Geukens, A. Gils, T. Verbiest, *J. Nanopart. Res.* **2012**, *14*, 1100–1109.
- [44] M. Kluenker, M. Mondeshki, M. Nawaz Tahir, W. Tremel, *Langmuir* **2018**, *34*, 1700–1710.
- [45] L. Addadi, S. Weiner, *PNAS* **1985**, *82*, 4110–4114.
- [46] L. Addadi, J. Moradian, E. Shay, N.G. Maroudas, S. Weiner, *PNAS* **1987**, *84*, 2732–2736.
- [47] C. Beato, M. S. Fernández, S. Fermani, M. Reggi, A. Neira-Carrillo, A. Rao, G. Falini, J. L. Arias, *Cryst. Eng. Comm.* **2015**, *17*, 5953–5961.
- [48] M. Schreiber, M. Eckardt, S. Klassen, H. Adam, M. Nalbach, L. Greifenstein, F. Kling, M. Kittelmann, R. Bechstein, A. Kühnle, *Soft Matter* **2013**, *9*, 7145–7149.
- [49] M. J. Esplandiú, H. Hagenström, D. M. Kolb, *Langmuir* **2001**, *17*, 828–838.
- [50] G. E. Poirier, E. D. Pylant, *Science* **1996**, *272*, 1145–1148.

3.2 Novel THF based (co-)polymers for mineralization

3.2.1 Polymer structure influence on calcium carbonate morphology

The manuscript “Novel THF Based Copolymers for Mineralization: Polymer Structure Influences Calcium Carbonate Morphology” is the underlying study for the following paragraph. The manuscript will be submitted to *Crystal Growth and Design* by the *American Chemical Society*. This chapter combines both the content of the main manuscript and the supporting information.

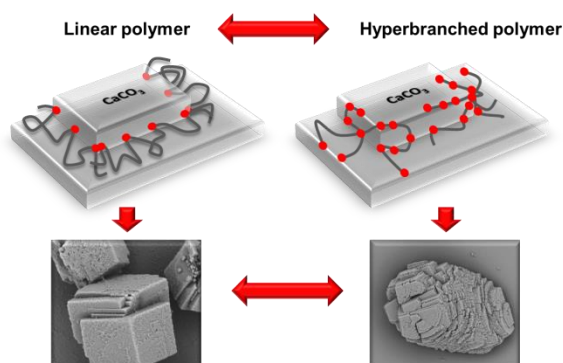


Figure 3.16: Relationships between linear and hyper-branched polymer and the related influences on CaCO₃ precipitates caused by the polymers structure.

Polyacid bearing (co-)polymers are used additives for scale inhibition of minerals such as CaCO₃, MgCO₃, and CaSO₄·2 H₂O in industrial facilities and household devices. Hyper-branched analogs were shown to induce less efficient scale inhibition due to face selective binding of agglomerates and more structure giving properties. We herein present a new class of polymers to distinguish between scale inhibition and shape modification for either linear or hyper-branched PolyTHF polyacids. For hyper-branched copolymer structures carrying carboxylic acid functions on the PolyTHF based (co-)polymers a comprehensive study on effects on CaCO₃ mineralization by using AFM, SEM, CLSM, FIB thin cuts, HR-TEM and titration techniques was carried out. As result hyper-branched PolyTHF copolymers have been found to elongate crystals by oriented attachment of polymer that also

covers the resulting polar nanostructured surfaces by formation of calcium carbonate/polymer composite nanopits. Strong inhibiting effects on CaCO_3 by linear PolyTHFs possess numerous carboxylic acid groups have already been shown to be based on lowering CaCO_3 supersaturation via complexation. These mechanism differences seem to be caused by structural differences in polymer structure as underlined by crystallographic study of both structures of PolyTHF polyacids by using advanced HR-TEM techniques of an exemplary FIB cut lamella of the final CaCO_3 composite crystals.

3.2.1.1 Introduction

CaCO_3 as well-established inorganic model system of mineralization from liquid phase has been studied with a plethora of additives, such as polar functionalized organic and inorganic nanoparticles, ^[1–3] surfactants, ^[4,5] polymers ^[6] and proteins ^[7] to investigate their effect on the CaCO_3 crystallization.

Mostly classical nucleation theory ^[8] and growth theories ^[9–11] aim to describe formation of crystalline CaCO_3 to end in the thermodynamically stable polymorph calcite by subsequent phase transitions over the reaction duration. ^[12–18] Within the recent two decades non-classical pathways of mineralization have exhaustively been studied especially under the scope of additive effects present in natural biomineral material such as exoskeletons of calcareous animals, ^[19–21] teeth, ^[22] and shells ^[23,24] or spines. ^[25–29] The key feature of many plants and animals is to control shape and polymorphism of their inorganic CaCO_3 skeleton and to hierarchically align small building subunits ^[30–32] under crystallographic alignment across long distances. ^[33] Such mesocrystalline biominerals encountered in spines, shells for example and exoskeletons. ^[34–38] have been evolutionary optimized for protection or as a load bearing skeleton. ^[39] This can only be encountered by non-classical pathways with a non-crystalline precursor ^[40,41] which is then assembled by genetically controlled pathways and transformed to build - often complex hierarchal - crystallographic commonly oriented so-called mesocrystals with extraordinary properties. ^[42–48] Upon discovery that many biominerals are superstructures of nanocrystals forming mesocrystals meanwhile the materials concept has emerged

various research fields. [49–51] It is assumed and partially proven that mesocrystalline hybrid materials exhibit an enhanced mechanical performance compared to single crystalline structures. [52,53] Their remarkable mechanical and optical properties, which are related to high leveled control mechanisms for structure, size, morphology, orientation, and assembly of the constituents, require an understanding of physicochemical effects of additive matrices. Often such matrices contain proteins rich in carboxylic acids [54] with specialized binding behavior and therefrom resulting effects on the growth and formation of biomineral hybrid crystals. [55–58]

The investigation of PolyTHF copolymers with carboxylic acid functions pushed the class to become an additive with its outstandingly non-polar backbone compared to the already studied and industrially used polymers (e.g. PAA) or copolymers (e.g. PAA-PAMPS) [83] which are used as scale inhibitors for urgent CaCO_3 crystallization. [84] As long as the effect of molecule structure on the CaCO_3 morphology has not been strategically investigated by the groups studying poly-acidic additives this chapter aims to do so for the presented PolyTHF polyacids.

Recently a new class of (co-)polymers based on tetrahydrofuran (THF) was presented in our previous work. [65] The class of PolyTHF copolymers is surprisingly uninvestigated although BASF SE had an annual production of 350,000 metric tons of non-polar PolyTHF polyol products in 2016 in its THF/PolyTHF plant in Shanghai, China. [66] Hence the usage of these non-polar products as additives in CaCO_3 crystallizations is impossible due to their insolubility in aqueous media. With the aim of fine-tuning and adjusting its properties, THF has been copolymerized with other cyclic monomers, [67–75] post-polymerized [76–78] or polymerized with various initiators to modify the end groups, [79–81] even to create bifunctional PolyTHF. [82]

To compare the nucleation and growth processes of the linear copolymer with the hyper-branched one we furthermore replenish the results reported elsewhere with a detailed HR-TEM study of linear copolymer. [65] For the hyper-branched system the hyper-branched polyol copolymers built of the AB_3 monomer 3,3-bis(hydroxymethyl)oxetane (BHMO) and tetrahydrofurane (THF), polymerized by CROP as reported elsewhere, [88] which has been post-functionalized with succinic anhydride to get a hyper-branched analog to the linear copolymer with a comparable amount of carboxylic acid groups its stability in basic pH moiety was proven by

NMR, IR, and DOSY to study the interaction of polymers with calcium ions by titrations followed by an analogue crystallization study in ammonia diffusion desiccator experiments and SEM/FIB preparation for a HR-TEM lamella for crystallographic work. For the surficial effects and the identification of attachment of the polymer to the mineral *in-situ* liquid cell AFM on CaCO₃ was conducted.

3.2.1.2 Experimental

Materials

All reagents were purchased from Acros Organics or Sigma Aldrich and were used as received, unless otherwise stated. The linear polymer was synthesized as reported elsewhere.^[65] Quarz glass-slides as well as TEM and SEM equipment were purchased from Plano GmbH, Wetzlar, Germany. Deionization was obtained with a purification setup from Millipore (Millipore GmbH). The quarz glass slides were cleaned by washing with ethanol, NaOH, MQ water, HCl and 3 times MQ water in an ultrasonic bath for 10 minutes each. The polymer was dissolved in NaOH (for AFM and crystallization) or KOH (for titrations) at pH 10. All titrations were performed with volumetric standard solutions purchased from Fluka.

Polymer Synthesis and Characterization

Hyper-branched PolyTHF copolymer was synthesized from AB₃ monomer 3,3-bis(hydroxymethyl)oxetane (BHMO) and tetrahydrofurane (THF) by cationic ring opening polymerization (CROP) with trifluoromethansulfonate as reported elsewhere.^[89] The procedure for the functionalization of hydroxyl groups follows the description of Zhu *et al.*^[90]

The stability of the polymer (cleavage of ester bonds) during crystallization at pH 10 was tested by NMR spectroscopy, DOSY, and IR spectroscopy. NMR spectra recorded after incubation overnight at pH values between 10 and 14 showed cleavage of the ester bonds starting at pH 12. The polymer was stable at pH 10 for at least 14 days (Figure S 3.30, Supporting Information). DOSY spectra recorded on a sample after 14 days of incubation time at pH 10 demonstrated the stability of

the polymer by the presence of a single component diffusing in d_5 -pyridine. The cleavage of the ester bonds in basic (pH 13-14) solutions was demonstrated by IR spectra, where the $-OH$ bending mode around 3250 cm^{-1} appeared at pH 12, while the bending modes of the carboxylate group around 1650 cm^{-1} vanished (Figure S 3.31 and Figure S 3.32, Supporting Information). Each experiment (crystallization, potentiometry titration, in situ atomic force microscopy (AFM)) was carried out with freshly prepared polymer solutions.

Precipitation and crystallization experiments.

Crystallization experiments were carried out using the ammonia diffusion method.^[83,91–94] The desiccator atmosphere was oversaturated permanently with ammonia and carbon dioxide by partial thermal decomposition of the excess of ammonium carbonate placed at the bottom of a desiccator. Crystallization was carried out on quartz-glass slides with a diameter of 13 mm and a thickness of 1 mm that were placed on the bottom of 5 mL beakers. The beakers were filled with 2 mL of aqueous solutions of 5 mM CaCl_2 and various μM concentrations of polymer. The polymer solutions were prepared as stock solutions by dissolving milligram amounts of the solid polymers in diluted KOH (pH 10) to obtain millimolar concentrations. The reaction vessels were covered with perforated Parafilm (Neenah, WI, USA) to prevent contamination by dust or other impurities. The pH of the solution increased from 8 to 9.5 during crystallization. After 15 h of crystallization duration the glass-slides were removed from the solution, washed carefully with saturated CaCO_3 solution on both sides to remove ammonium carbonate crystals as well as unbound polymer without inducing dissolution/recrystallization of the CaCO_3 crystals. Subsequently, the samples were dried under air flow.

Determination of calcium complexation.

Titration experiments were carried out using a Titrino system running with Tiamo software (Metrohm AG) equipped with pH, turbidity electrodes with a 532 nm laser and calcium ion selective electrode (Ca-ISE). External calibration of the Ca-ISE was done with a four-point calibration with various concentrations of a CaCl_2 solution in a 0,1 M KCl solution. The influence of carbonate species is not drawn attention in this way of calibration. External pH calibration was carried out with standard

solutions of pH 4, 7 and 9 purchased from Metrohm. The polymer solutions for uptake measurements were added to solutions containing Ca^{2+} cations with 0.1 M KCl as background conductivity electrolyte. For the nucleation experiments, 25 mL of a diluted 0.1 M KCl solution for better signal stability due to needed ionic strength for conductivity and a 0.01 M carbonate buffer solution were set to pH 9.75. Protons generated from the shift of the hydrogen carbonate/carbonate equilibrium due to CaCO_3 nucleation were neutralized by a continuous addition of 0.01 M KOH.

Scanning electron microscopy (SEM) was carried out using a JEOL-JSM 5610LV (JEOL Ltd., Tokyo, Japan) microscope. Calcium carbonate crystals were sputtered with 10 nm silver and analyzed. Images were acquired with an accelerating voltage of 20 kV at low vacuum. Focused ion beam (FIB) preparation of samples for analyzing the internal morphology were prepared by cross-sectioning with a FEI 600 Nanolab focused ion beam SEM dual beam instrument (FEI, Hillboro, Oregon) equipped with an Omniprobe micromanipulator (Omniprobe Inc. Dallas, Texas). Transmission electron microscopy (TEM) images were recorded on FEI Technai F30 or F20 instruments, both equipped with a 4K CCD camera and a LaB_6 cathode working at 200 kV acceleration voltage. Samples for TEM imaging of CaCO_3 precursors were prepared by drop-casting 20 μL of sample solution onto a carbon coated copper grid (Plano GmbH, Wetzlar, Germany).

Confocal laser scanning microscopy (CLSM) images were recorded using a confocal Leica SP5 system. All images shown were collected by exciting Rhodamin B bound to the polymer^[89] with a $\lambda = 532$ nm Laser beam and detecting at $\lambda = 565$ nm. Laser light microscopy images were collected with a Keyence-8710 microscope with 10, 20, 50 or 100-fold magnifying objectives from Carl Zeiss, Germany.

For AFM calcite crystals with a sample size of 4 x 4 mm² were purchased from Korth Kristalle GmbH. The crystals were freshly cleaved and cleaned under nitrogen flow prior to each experiment. All in-situ AFM measurements were conducted in the frequency modulation (FM) mode using a modified^[95,96] commercial atomic force microscope from Bruker Corporation (MultiMode V with Nanoscope V controller) for high-resolution imaging in liquid environment. All AFM images were taken at a constant temperature of 28 °C and with a liquid cell from Bruker Nano

Surfaces Division. The used cantilevers were gold-coated and *p*-doped silicon (PPP-NCHAuD, Nanosensors and Tap300GD-G, BudgetSensors) and exhibit in liquids a typical eigenfrequency of 100-150 kHz and a spring constant of ~40 N/m. For all measurements, the oscillation amplitude of the cantilever was kept constant at 1 nm. In all AFM images the slow and fast scan direction and the measured channel are shown in the schemes in the upper right corner.

Raman and IR-spectroscopy measurements for phase identification were carried out using a confocal HR800 μ -Raman by Horiba Scientific and a NicoletTM iSTM10 FT-IR spectrometer from Thermo Scientific. Both instruments used $\lambda = 633,318$ nm He/Ne laser light without any optical filters. Each spectrum was taken with at 16 iterations at a resolution of 1 cm^{-1} .

Intermolecular interaction of samples in solutions of hexafluoroisopropanol were analyzed by DLS using a multi-angular detection goniometer (ALV-CGS-8F SLS/DLS 5022F) equipped with a He/Ne Laser (Uniphase, 25 mW, $\lambda = 632.8$ nm), eight simultaneously working ALV7004 correlators connected to eight ALV high QE APD avalanche photodiode fiber optical detectors. The detectors were separated by 17° , two independent simultaneous sets of measurement separated by 9° resulting in 16 angular dependent values covering an angular range from 30 to 158° . This allowed an extrapolation to scattering angle zero with respect to polydispersity effects on the diffusion coefficient. All measurements were performed at $20 \pm 0.1^\circ\text{C}$ with the help of external ultra-thermostats (Lauda RKS6C).

In DLS the intensity-time correlation function $G_2(t) = \langle I(0) \cdot I(t) \rangle$ is measured with the scattering intensities $I(0)$ and $I(t)$ recorded at $t = 0$ and $t = t$, respectively. For practical reasons, $G_2(t)$ is converted into the correlation function $g_1(t) = \langle E(0)E^*(t) \rangle$ of the electrical field amplitudes by application of Siegerts relation^[97] as $g_1(t) = [(G_2(t) - A)/A] - 1$ with A as a value of $G_2(t)$ determined for very large times (called baseline) by a non-linear fitting (Simplex algorithm) of the field autocorrelation function by applying mono-or bi-exponential fit functions. Hydrodynamic radii were calculated from the Stokes-Einstein equation.

3.2.1.3 Result & Discussion

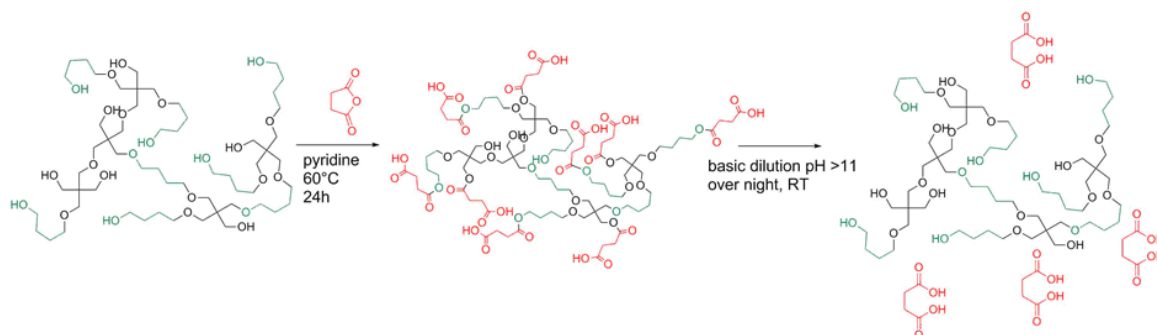


Figure 3.17: Functionalization of PolyTHF polyols to polyacids and degradation to polyols and succinic acid by hydrolysis at basic pH.

The solubility of the polymer in water at pH 10 and the presence of intermolecular interactions were demonstrated by dynamic light scattering (DLS). The PolyTHF polyacid (Figure 3.17 in the middle) has a hydrophobic backbone terminated by hydrophilic end groups. This may lead to the formation of nano-sized aggregates as shown DLS measurements for P(THF₈-co-BHMO₃₇-(C₄H₆O₄)₇₈) (herein C₄H₆O₄ stands for the bound succinic acid functional groups) in hexafluoroisopropanol (Figure 3.18). Polyions move faster in solution than the corresponding neutral polymers of similar molecular weight because of inter-chain repulsion. As a result, the apparent diffusion coefficient D_f detected by DLS is larger (“fast mode”).^[98] Inter-chain repulsion leads to a second diffusive mode (“slow mode”) with lower D_s values compared to the fast mode that originates from the formation of so-called “polyion domains” in solution, where the motion of polyion segments is correlated, i.e. affected by other segments. The “apparent size” of these metastable but long-lasting structures exceeds the size of individual segments reach values around 200 nm.^[98] DLS detects these “domains” as “particles” with their own D_s (and corresponding R_h value) through the Stoke-Einstein equation at high polyion concentrations for strongly charged chains and at high molecular weights.

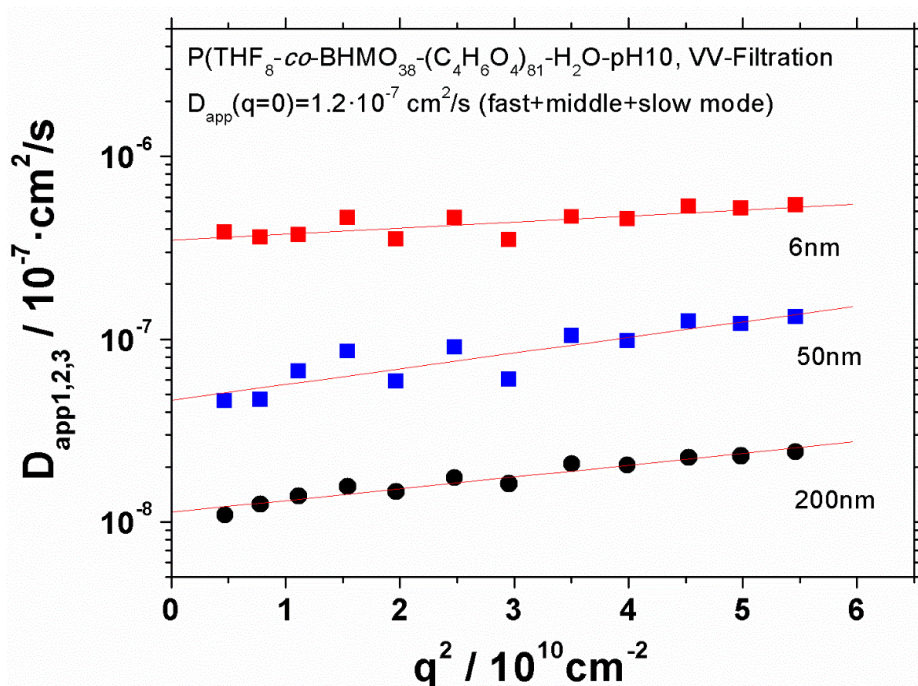


Figure 3.18: Apparent diffusion coefficient D_{app} plotted versus the squared scattering vector q^2 for P(THF₈-co-BHMO₃₈-(C₄H₆O₄)₈₁) dispersed in water at pH 10 after filtration (100 nm filter).

Complexation of Ca²⁺-cations by hyper-branched polymer in solution

Acidic polymers and proteins can strongly bind Ca²⁺ cations, which often leads to aggregation and even precipitation at higher calcium concentrations. A DLS and SLS study by Huber and coworkers [99,100] showed a Ca²⁺-induced collapse of PAA chains. This effect becomes more pronounced with increasing chain length. Similarly, proteins like ovalbumin were shown to self-aggregate in the presence of Ca²⁺ cations. [55,101] The precipitation process of the (bio)polymer is characterized by a coil contraction, most probably via conformational changes and Ca²⁺ cross-linking, followed by a distinct coil to branched chain transition. Although the polymer binds a fraction of the calcium ions from solution and thus reduce the effective supersaturation during precipitation, it cannot stabilize nucleating calcium carbonate clusters or growing particles. Ca²⁺ concentrations at constant pH values were measured to determine the complexation effect of the polymer at different stages of crystallization with increasing supersaturation. For the introduced hyper-branched PolyTHF polyacid (co-)polymers the interaction with calcium ions has been investigated by Ca-ISE measurements.

Ca-ISE titrations for different polymer concentrations (shown in Figure 3.19 (I)) lead to a linear relation of calcium ion uptake and polymer concentration. This allowed the calculation of the complexation constant of the polymer $K_a = [Polymer-Ca^{2+}]/([Polymer][Ca^{2+}]) = [Ca^{2+}_{bound}]/\{([Polymer]-[Ca^{2+}_{bound}]][Ca^{2+}_{free}]\} = 0.01925 \pm 0.0009$ mmol/L. The relationship between carboxylic groups and bound calcium ions shown in Figure 3.19 (II) is an almost fourfold complexation of each calcium ion with carboxyl groups.

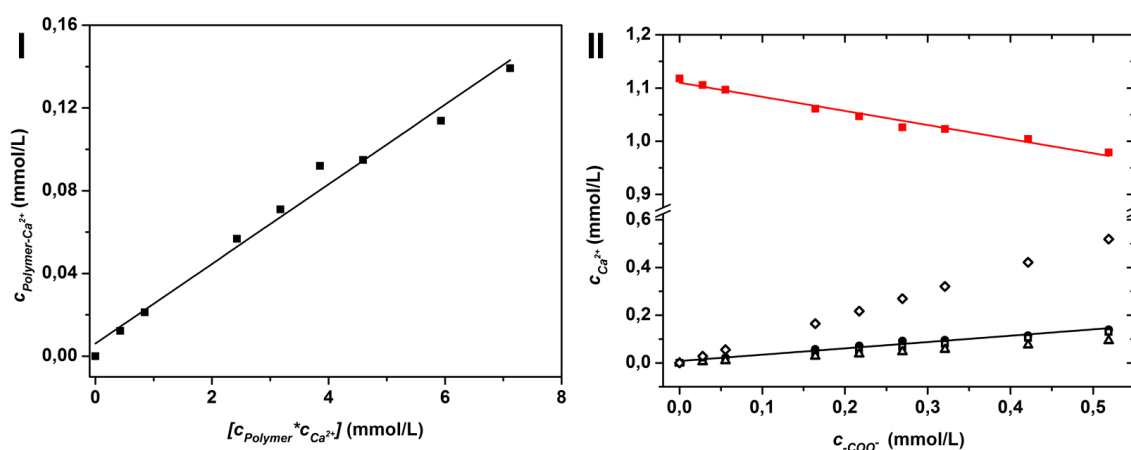


Figure 3.19: (I) Product of free polymer concentration and detected free $c(Ca^{2+})$ plotted against concentration of bound $c(Ca^{2+})$ what can be defined as Polymer- Ca^{2+} complex concentration. Linear regression line gives the association constant of the polymer. (II) Concentration of carboxylic groups of P(THF₈-*co*-BHMO₃₈-(C₄H₆O₄)₈₁) plotted against $c(Ca^{2+})$. The red squares and corresponding red line indicate data for unbound calcium. While similar black squares with linear regression line show bound calcium to fit best to unfilled squares of theoretical calculations of fourfold coordination geometry. The unfilled diamond indicates 1 by 1 coordination and the unfilled triangles belong to a sixfold coordination.

To determine the influence of calcium complexation on the crystallization of $CaCO_3$ by the presented polymer a dilute calcium chloride solution was added to a carbonate buffer solution. Subsequently the solutions supersaturation is reached and nucleation occurred followed by a precipitation of solid calcium carbonate (vaterite). The run of the calcium ion concentration over the reaction time is shown for an exemplary experiment at pH = 9.75 (Figure 3.20).

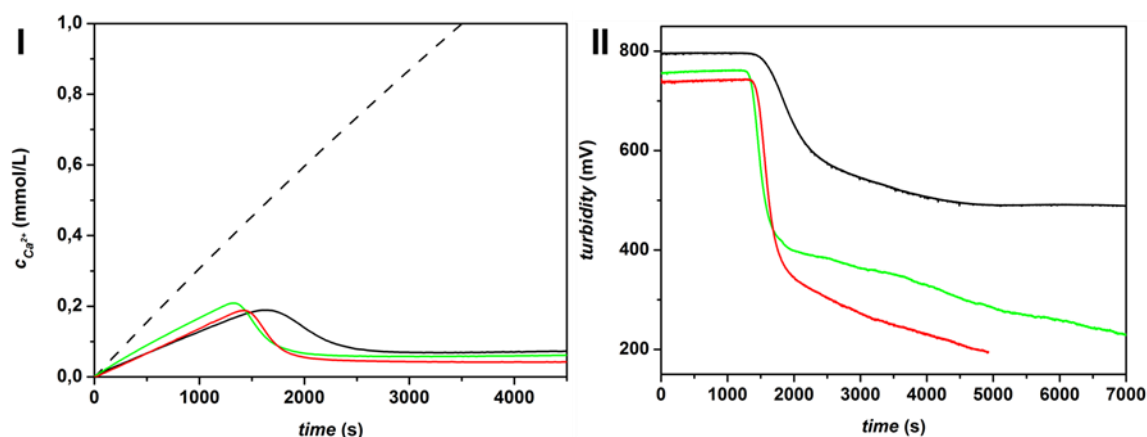


Figure 3.20: (I) Calcium ISE signal of CaCO_3 nucleation titrations in 10 mM carbonate buffer at pH 9,75 in a teflon vial with black no addition of polymer, green addition of 3 $\mu\text{mol/L}$ and red addition of 6 $\mu\text{mol/L}$ $\text{P}(\text{THF}_8\text{-co-BHMO}_{38}\text{-(C}_4\text{H}_6\text{O}_4)_{81})$. Dashed line shows theoretical signal that would be detected if only calcium ions are added to water. (II) Turbidity measurements of same titrations showing burst nucleation for both polymer concentrations (red, green) induced by polymer added (heterogeneous nucleation). The smooth time course of the blank measurement indicates slow homogeneous nucleation.

The black dotted line reflects the amount of calcium ions added. However, the amount of free calcium ions detected by the calcium ion selective electrode (black line) increases considerably slower straight from the beginning of the experiment; that is, a distinct part of free calcium ions disappears due to binding in carbonate clusters.^[41,101] The pre-nucleation-stage time development is linear, indicating that the calcium binding behavior in under- and supersaturated stages of the pre-nucleation stage is equal. Once a critical point is reached, nucleation occurs and the amount of free calcium ions drops to a value that corresponds to the particular solubility concentration of the precipitated phase according to a typical LaMer curve.^[8] The differences between the measured free amounts of calcium from polymer (red and green) to the non-polymer solution (black) might come from less amount of pre-nucleation activity due to the existence of a highly charged nucleation sites. The polymer can also be shown to serve as a site of nucleation by turbidity measurements shown in Figure 3.20 (II). To study the discussed seeding effect of the polymer for CaCO_3 crystallization the slower thermodynamically dominated precipitation via ammonia diffusion method (ADM) was carried out to ensure interactions of the polymers and the CaCO_3 substrate.

For a better comparability, the recently studied linear PolyTHF polyacid copolymer [65] and the hyper-branched P(THF₈-co-BHMO₃₇-(C₄H₆O₄)₇₈) have been added to the desiccator crystallization in comparable amounts of surficial carboxylic acid groups. The hyper-branched polymer P(THF₈-co-BHMO₃₇-(C₄H₆O₄)₇₈) with $M_n = 12800 \text{ g mol}^{-1}$ (obtained from ¹H NMR spectra, 300 MHz, pyridine-*d*₅) furthermore had a comparable molecular weight as the linear copolymer poly(THF-co-carboxylic acid ethylene oxide) (P(THF-co-CEO)) used in our recent publication with $M_n = 12100 \text{ g mol}^{-1}$ (calculated via ¹H NMR spectra, 300 MHz, THF-*d*₈). [65] Due to different solubility of the linear and hyper-branched (co-)polymers in water and organic solvents, results, obtained via Ca ISE and NMR, may vary from each other. Both methods show same trend and confirm that the hyper-branched polymer possesses more carboxyl groups per polymer chain than the linear one, with respect to similar molecular weights. Hence, the concentration of the linear polymers was doubled for further investigations, to obtain a comparable number of functional acid units in the linear and hyper-branched polymer solutions. Thus the solution of 20 μmol/L of hyper-branched polymer in 5 mM CaCl₂ in crystallization experiments contains a similar amount of carboxylic acid groups ($n = 1.2 \text{ mmol}$) as the linear polymer experiments in 40 μmol/L. Reference crystallizations without polymer gave calcite rhombohedra of about 20 μm edge length as usual for this supersaturation (see Figure S 3.33).

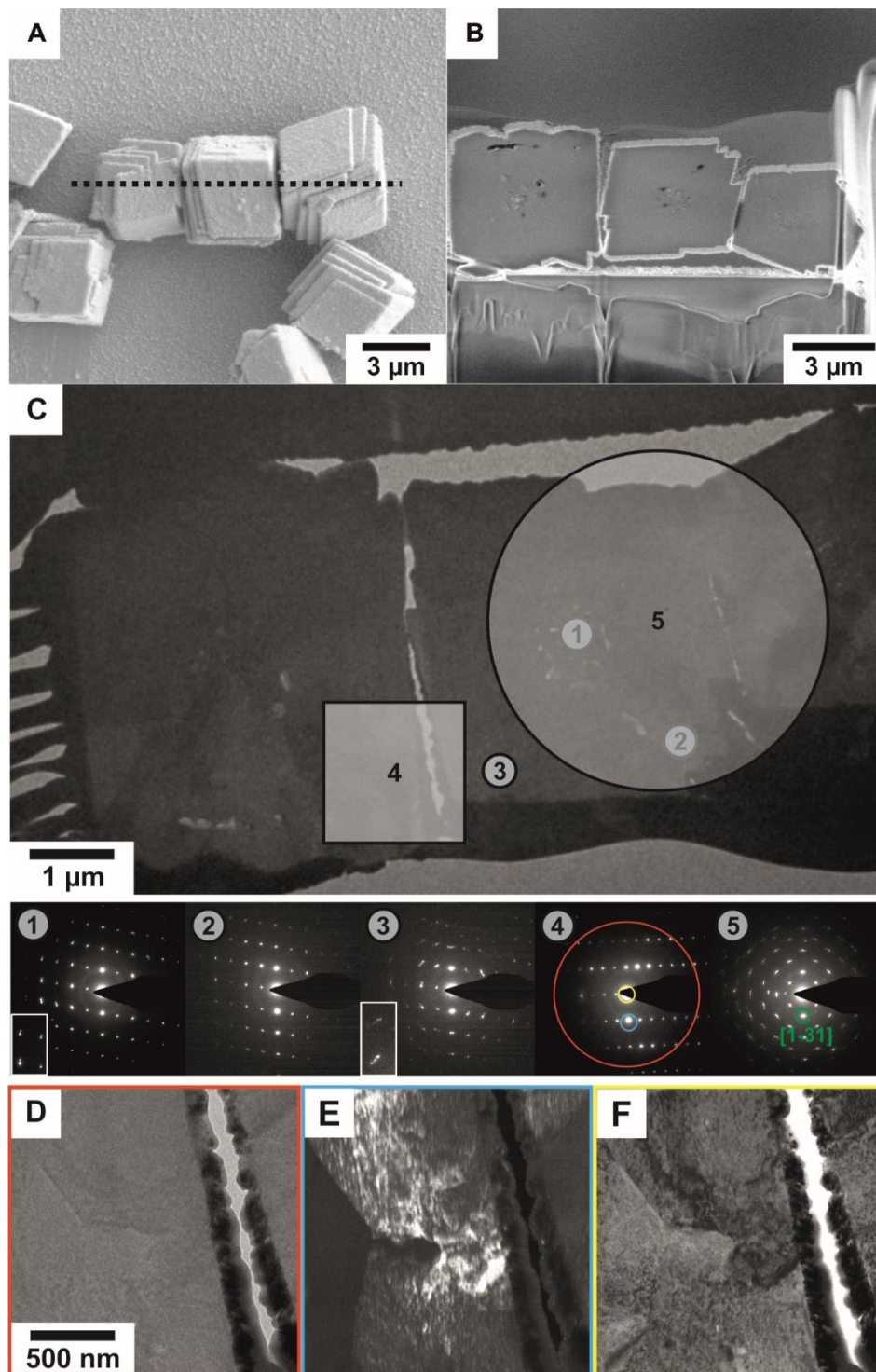


Figure 3.21: A: SEM of three calcite mesocrystals cut selected for the FIB cut preparation, B: FIB cut cross-section of these three mesocrystals showing almost complete massive material. C: HR-TEM image with chosen SAED spots (1-5) showing a pronounced $[1-31]$ plane of the crystal. D-F: diffraction reconstruction from diffraction area 4 and spots as indicated by the color code, red: brightfield image (all beams), blue: diffracted beam only (bright areas are highly crystalline), yellow: zero-beam.

For the addition of the linear PolyTHF polyacids copolymer ($M_n = 12100 \text{ g mol}^{-1}$, 8.4% acidic units) also rhombohedra were precipitated after 15 h duration of the experiment. In contrast to the reference the rhombohedra were smaller if the polymer was added (see Figure 3.21 A). FIB cut cross sections of the crystals show almost massive crystals with some defects close to the crystals center (Figure 3.21 B). HR-TEM imaging of representative areas gave an insight into the location of the polymer within the composites. Selective area electron diffraction (SAED) of areas 1-5 shows the crystals to be built of nano-crystals slightly tilted to one another. A closed look by reconstruction from diffraction (Figure 3.21 D-F) also shows crystalline areas which are oriented along the $[1-31]$ axis of the CaCO_3 mixed with amorphous areas that can be dedicated to either ACC, the polymer or a mixture thereof. The resulting mosaicity has also been detected by measuring Rocking curves with X-Ray diffraction, which show a pronounced broadened background caused by polymer addition (see Figure S 3.34 and Figure S 3.35 as well as Table S 3.5 and Table S 3.6 for calculated data). Especially on the surface of the small rhombohedra a drop-like structure can be observed. This is dominated by amorphous occlusions due to the polymer AFM imaging with the polymer solutions also gives a rounded surface after certain time with spherical occlusions all over the (104) surface of the CaCO_3 (see Figure 3.22 IV-VI).^[30] The absorbates are about 1 nm in height which corresponds to small aggregates of polymer (see Figure 3.22 Vp). The surface chemistry of the hyper-branched additive remained in focus after the uncertain complexation of calcium and the influence on CaCO_3 in nucleation titrations were identified. *In-situ* liquid cell AFM of polymer solutions of the hyper-branched polymer on freshly cleaved (104)- CaCO_3 showed no formation of etch pits due to surface reconstruction as usual. In contrast to the unspecific absorption on all orientations for the linear polymer the hyperbranched polymer shows occlusion of absorbates, surface roughening and crystallization defects. The addition of $0.166 \mu\text{M}$ hyper-branched PolyTHF aqueous solution at pH 10 shown in Figure 3.22 (I-III) shows the formation of surficial structuring along $[010]$ orientation. The formation of nano-pits that cause the by ADM crystallization observed surface roughness can be dedicated to dissolution of CaCO_3 around surface adsorbed-polymer. The absorbates on the tips of the nano-pits are between 0.2 and 1 nm in height as shown by profile in Figure 3.22 (IIp).

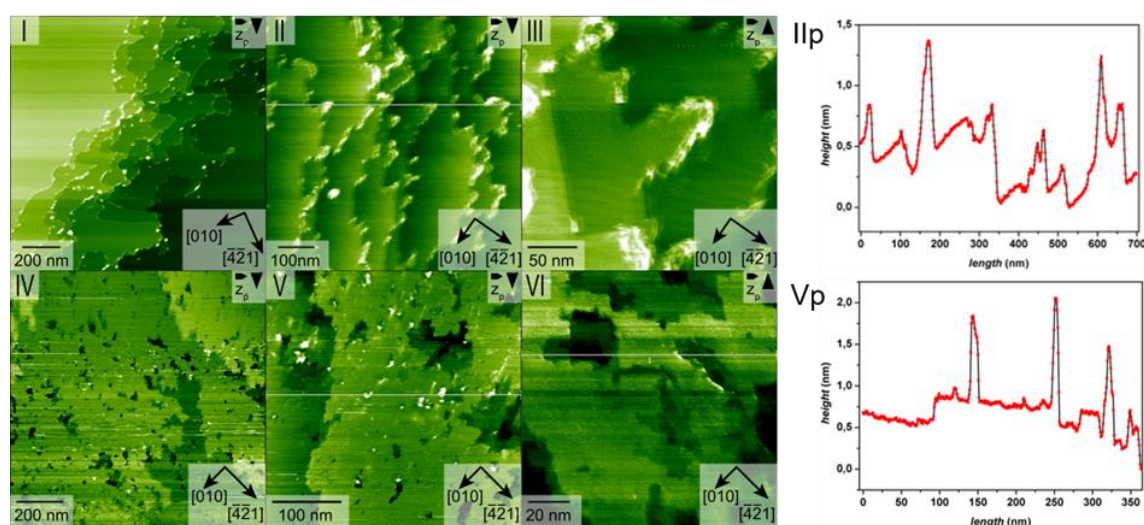


Figure 3.22: AFM on freshly cleaved (10.4)-calcite with pH 10 solutions of 0.166 μM hyper-branched PolyTHF (I, II, III, height profile of II plotted in IIp) and 0.3 mM linear PolyTHF (IV, V, VI, height profile of V plotted in Va) showing that the linear polymer attaches to all polar step edges without specific binding with distinct orientation and gets occluded over time. While agglomerates of hyper-branched PolyTHF in contrast are oriented along polar (010)-axis to form nano-structured surface. This surface termination is responsible for formation of as shown dumbbell shaped crystals elongated along c-axis the room diagonal in the rhombohedral calcite system that is a parallel axis of (010)-axis.

The oriented attachment found by AFM motivated a similar study in desiccator CaCO_3 crystallizations. In the case of hyper-branched PolyTHF polyacids compared to linear ones and the reference crystals without additive (Figure S 3.33, Supporting Information) elongated dumbbell shape mesocrystals terminated with (104) facets were found.

For the hyper-branched case the overall morphology of the calcite spherules changed only gradually with increasing polymer concentration (Figure S 3.36, Supporting Information). The time resolved TEM observations (see Figure S 3.37) from the solutions support the finding that the polymer underlies - in contrast to the linear polymer - a strong intermolecular interaction but also serves as nucleation site as it has strong interactions with calcium ions. After one hour in the desiccator ACC starts to form within the polymer network that is present close to the CaCO_3 precipitated all over the time course of 4 hours observation. Within the polymer matrix large particles agglomerated until 2 hours to about 200 nm sized ACC particles that

subsequently agglomerate to 500 nm sized crystalline CaCO_3 built of small particles by a non-classical growth observed for various additives before. ^[104]

The hyperbranched polymer is integrated as shown by an exemplary z-stack of a dumbbell crystal labeled with Rhodamine B bound covalently on the polymer (compare Figure S 3.38). The existence of surface-bound polymer gave rise of a strong and concentration dependent fluorescence in the Raman spectrum (Figure S 3.39, Supporting Information). ^[62] Integration of the additive lead to a characteristic shift of vibrational bands characteristic for calcite with signal due to the particle size. The calcite band at 283 cm^{-1} was shifted to 280 cm^{-1} , which is commonly referred to as symmetry breaking effect caused by occlusion of additives into the crystal. The small shift is due to the tiny influence of flexible soft material on the lattice crystallinity and orientation. The assembly of the mesocrystals built from nanocrystals and formation of nano-grains causes the observed broadening of the discussed signal.

The formation of mesocrystals is also proven by electron microscopy based imaging and diffraction of a FIB cut of an exemplary specimen formed under addition of $20\text{ }\mu\text{mol/L}$ hyperbranched polymer has been prepared and analyzed with HR-TEM techniques.

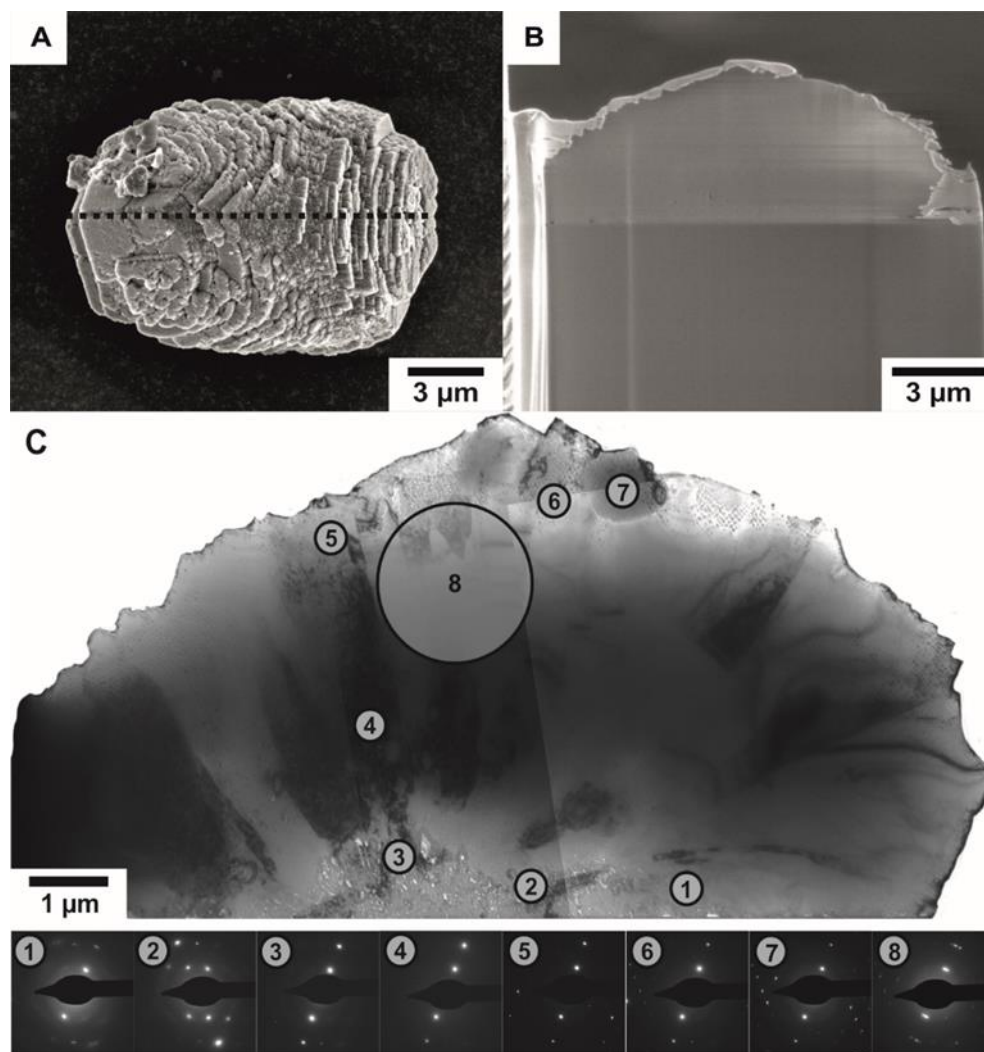


Figure 3.23: (A) SEM image of elongated calcite crystal precipitated from 5 mM CaCl_2 solution with 20 $\mu\text{mol/L}$ $\text{P}(\text{THF}_8\text{-co-BHMO}_{37}\text{-(C}_4\text{H}_6\text{O}_4)_{78})$ added. (B) FIB preparation of a TEM lamella along dotted line in (A). TEM reconstruction of cross-section of the cut crystal and areas of SAED (1-8) that show a high small area crystallite alignment while 8 indicated a slight twinning within a larger diffracted area that also proves the formation of mesocrystals.

The cross-section only has a few defects inside the mesocrystals. Figure 3.23 reveals that the characteristic crystal shown in (A) to be almost massive. By a closer look with the TEM (C) one can see few scattered holes on the surface that was close to the glass slide (best separated from the solution itself). SAED patterns 1 to 7 indicate small area crystalline and oriented CaCO_3 with weak twinning. Twinning turned out to exist if a larger area was scanned. The scanning of the lamella with the STEM and the brightfield mode shown in Figure 3.24 reveals inclusions

inside the crystals that support the findings from CLSM and Raman spectroscopy that polymer is included and surface attached in oriented fashion.

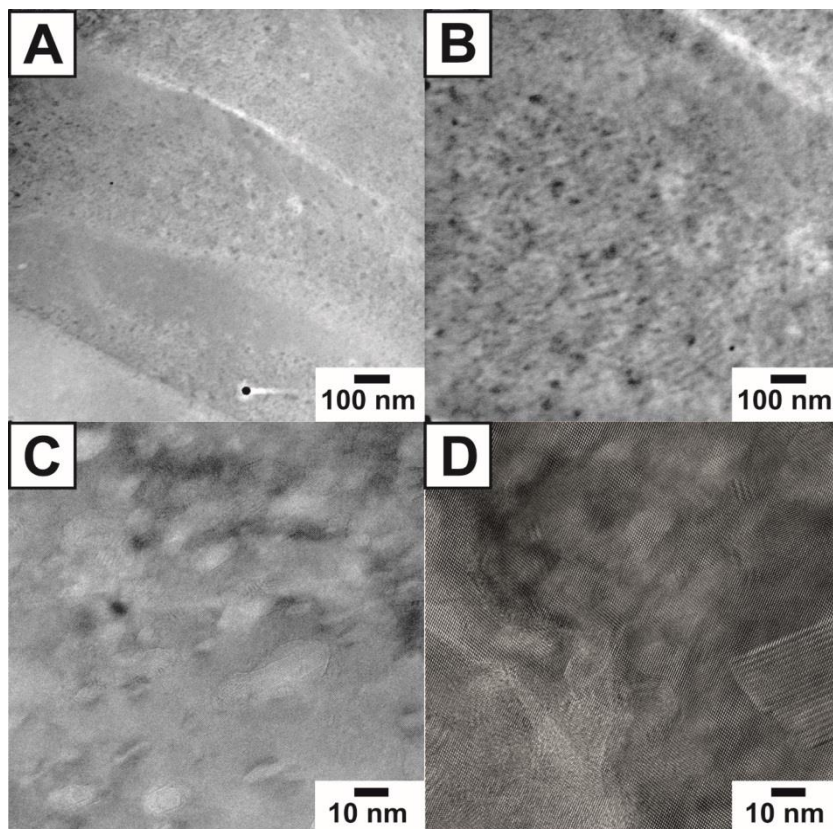


Figure 3.24: A, B: STEM images of two different sections of a TEM lamella showing a nano-structuring caused by occlusions that can be identified by HR-TEM images C and D.

3.2.1.4 Conclusion

Dumbbell-like calcite aggregates were reported to be formed under presence of polyglycerols as well as other polyacids by ammonia diffusion method. ^[105] The crucial difference between hyper-branched PolyTHF and hyper-branched polyglycerol is the higher polarity of the polyglycerol backbone. The crystal habitus was discussed to be changed by the polyacid functionality. The nature and polarity of the backbone plays a minor role for mesocrystal formation.

The presented results from electron microscopy show that polymer integration into CaCO_3 occurs via crystal grain boundary formation and increasing of nano-crystallinity. Surprisingly the crystal shape was shown to be different for a similar class of polymer if only the degree of freedom of the functional groups is decreased by synthesizing a hyper-branched analogue of a linear copolymer. While the linear polymer inhibits growth of CaCO_3 under formation of very small rhombohedral crystals ^[65] showing large amorphous areas, the hyper-branched polymer of similar molecular weight forms dumbbell shaped mesocrystals with surficial nano-pit structuring. Inhibition of polar facets caused by specific oriented binding leads to a strong elongation along a crystal axis, which results in dumbbell-type structures, as it has been reported for polar polycarboxylic acids as well. ^[105] Further studies of the surface behavior of this new class of polymers for example in oversaturated solutions on (104) calcite are planned to investigate the surface stabilization and the mechanism of incorporation of polymers, depending on their structure.

3.2.1.5 Supporting Information

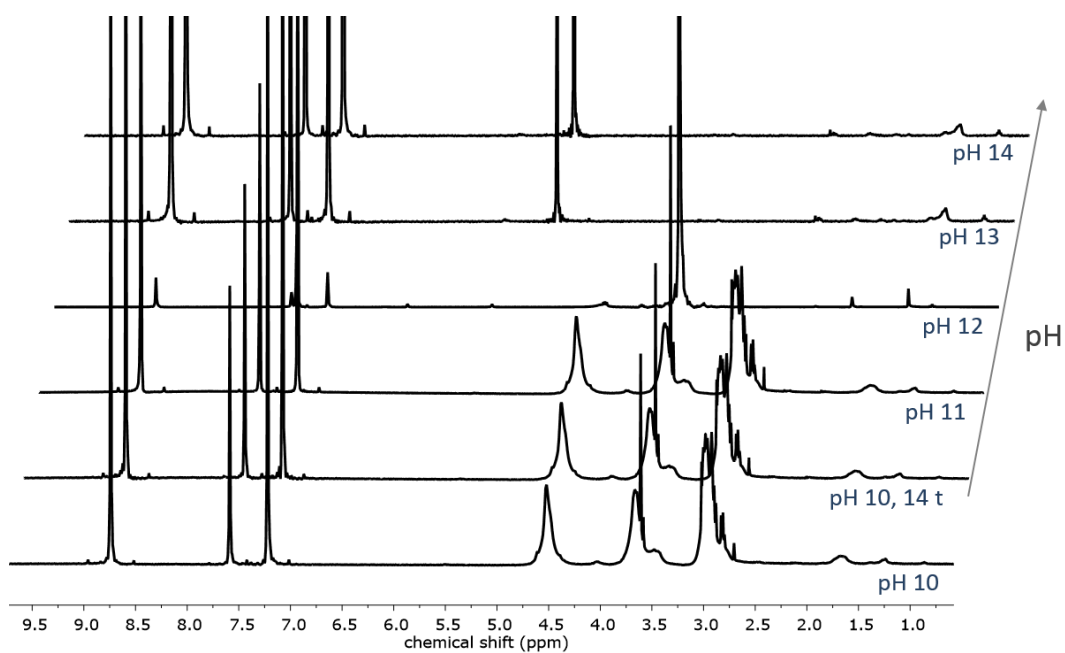


Figure S 3.30: A series of $^1\text{H-NMR}$ (300 MHz, pyridine-d_5) spectra of $\text{P}(\text{THF}_8\text{-co-BHMO}_{38}\text{-(C}_4\text{H}_6\text{O}_4)_{81})$ at varied pH values, from pH 10 to 14, as well as a spectrum at pH 10 with a delay of two weeks.

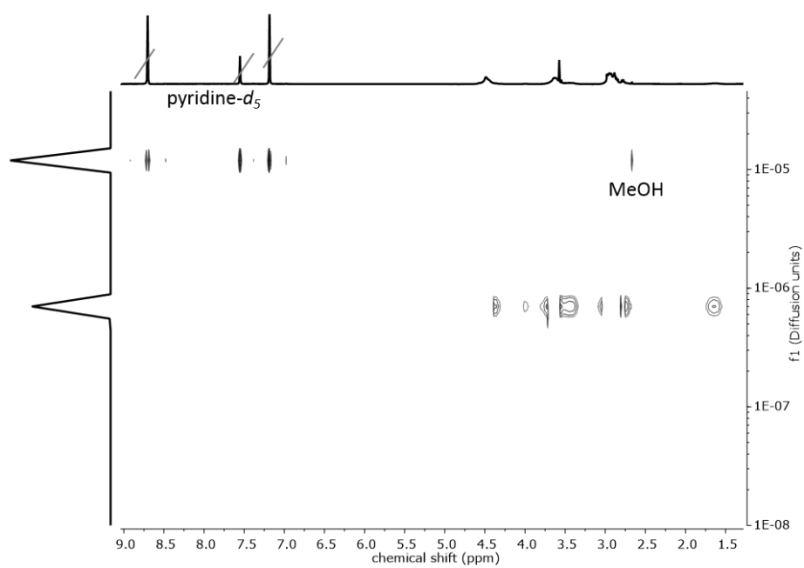


Figure S 3.31: Diffusion ordered spectroscopy (400 MHz, pyridine-d₅) of P(THF₈-co-BHMO₃₈-(C₄H₆O₄)₈₁) at pH 10 after a delay of two weeks.

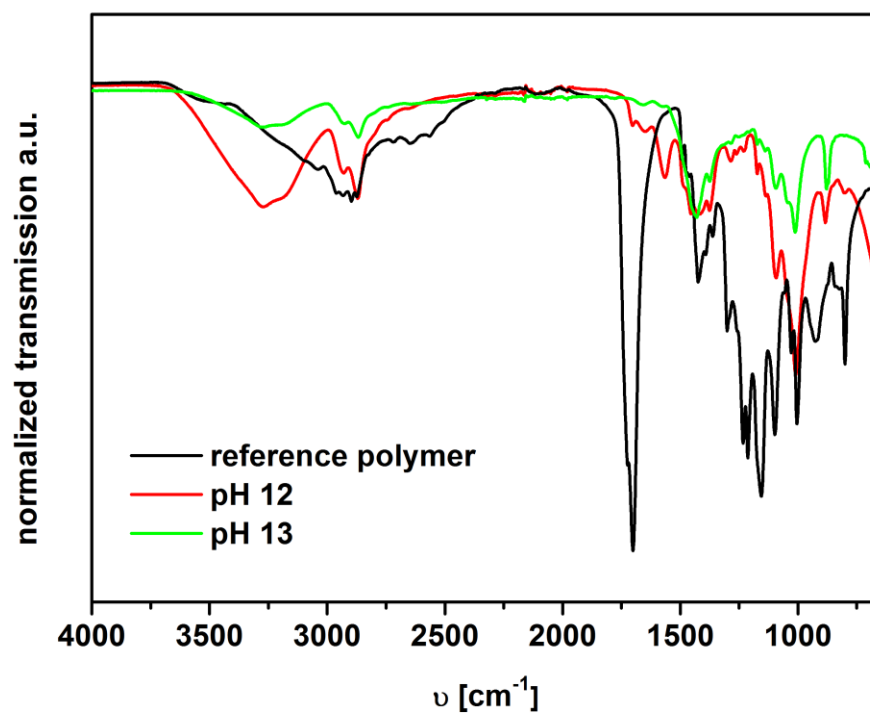


Figure S 3.32: FTIR spectra of P(THF₈-co-BHMO₃₈-(C₄H₆O₄)₈₁) in black and the same polymer after overnight incubation at pH 12 (red) and pH 13 (green). The formation of -OH stretching and bending modes and missing carboxylic acid as well as ester bond modes indicates degradation under these conditions as shown by NMR in Figure S 3.30 and Figure S 3.31.

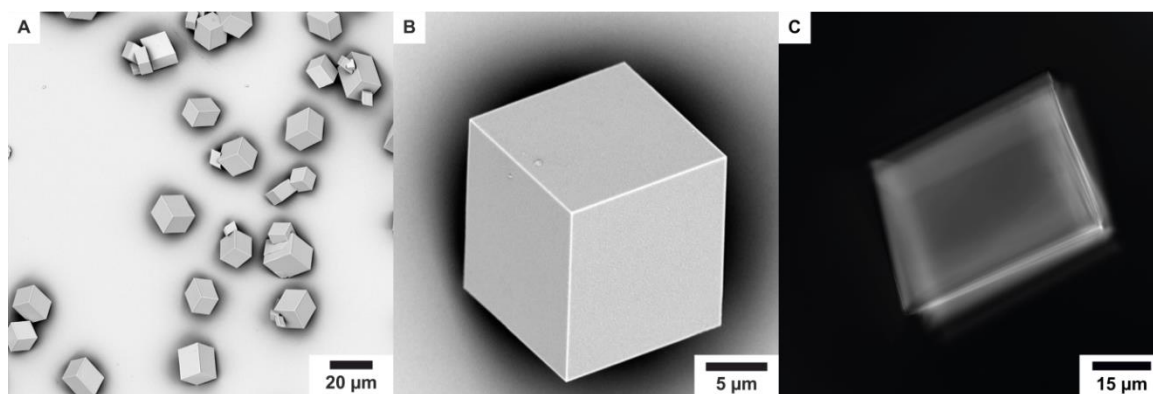


Figure S 3.33: A,B: SEM images of classically obtained calcite rhombohedra in reference crystallizations for 15 h without additives. C: CLSM image of calcite rhombohedra not showing any fluorescence activity.

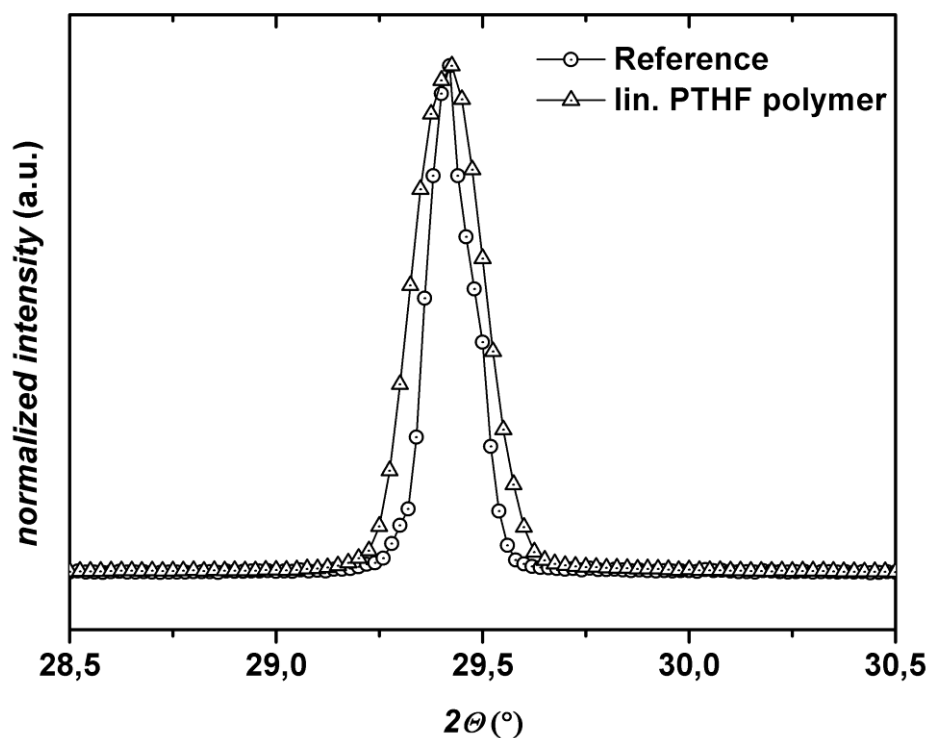


Figure S 3.34: XRD 2θ scan of characteristic (104) reflex of calcite. FWHM is determined by Gaussian fits of both curves. Data is presented in Table S 3.5.

Table S 3.5: Calculations for 2θ scans of Reference example and calcite precipitated with μM concentration of linear PTHF polymer added. FWHM tends to be large for added polymer which results in smaller average crystal size within the mesocrystal assembly under keeping the 2θ value and thus the lattice plane distance comparable to reference measurements.

Sample	FWHM (°)	d (nm)	2θ (°)
Reference	0.120	76.1	29.42
lin. PTHF Polymer	0.203	65.2	29.42

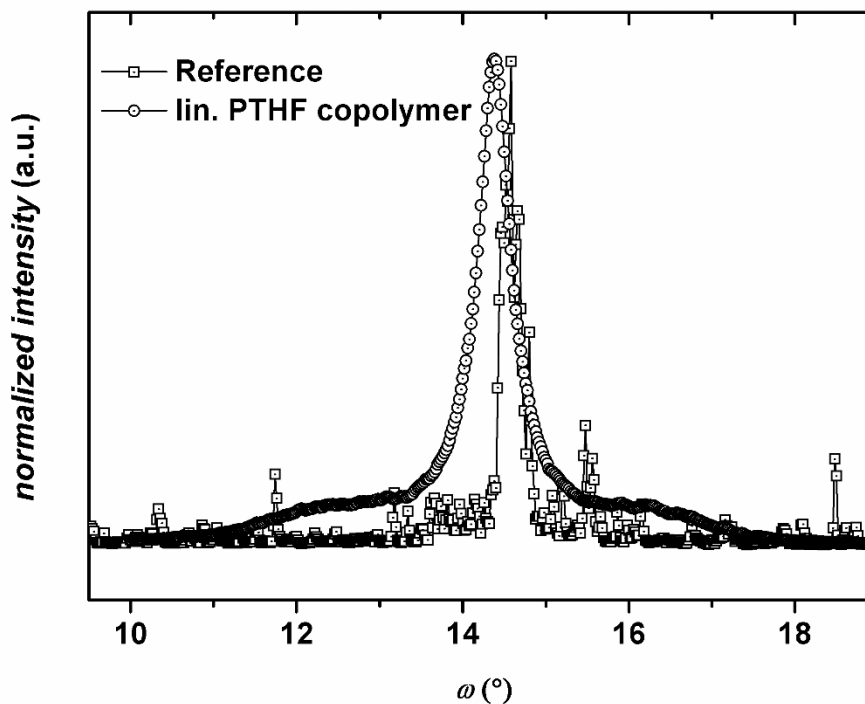


Figure S 3.35: Rocking curve analysis between $9,5^\circ$ and 19° ω angle under constant 2Θ angle of $29,42^\circ$ analyzing the (104) truncated nano-crystals of the mesocrystal. For the reference sample a very sharp reflex indicates highly oriented crystallites forming large crystals which are sometimes randomly oriented on the glass substrate (sharp reflexes at various angles). For addition of lin. PTHF polyacid copolymers the main reflex broadens and shows a second broad distributed crystal species. Together with 2Θ scan data the occlusion of PTHF that has been shown by STEM results in nano-crystalline mesocrystal assemblies of high mosaicity with oriented but also some mis-oriented crystallites.

Table S 3.6: Calculations from Gaussian fits for Rocking curve data. Reference shows a single mode of crystals only slightly tilted and of very small mosaicity. Addition of polymer even results in a little increase in tilting of crystallites and an increase in mosaicity of the sharp reflex part to FWHM $0,488^\circ$ and $5,535^\circ$ FWHM for the broad reflex part. For hyper-branched polymers the absolute signal from the samples was too small if 0.4 mm slits were used for an adequate comparison.

Sample	FWHM ($^\circ$)	ω ($^\circ$)	ω_{theo} ($^\circ$)	$\Delta\omega$ ($^\circ$)
Reference	0.261	14.6	14.7	0.1
lin. PTHF Polymer	0.488	14.4	14.7	0.3
	5.335			

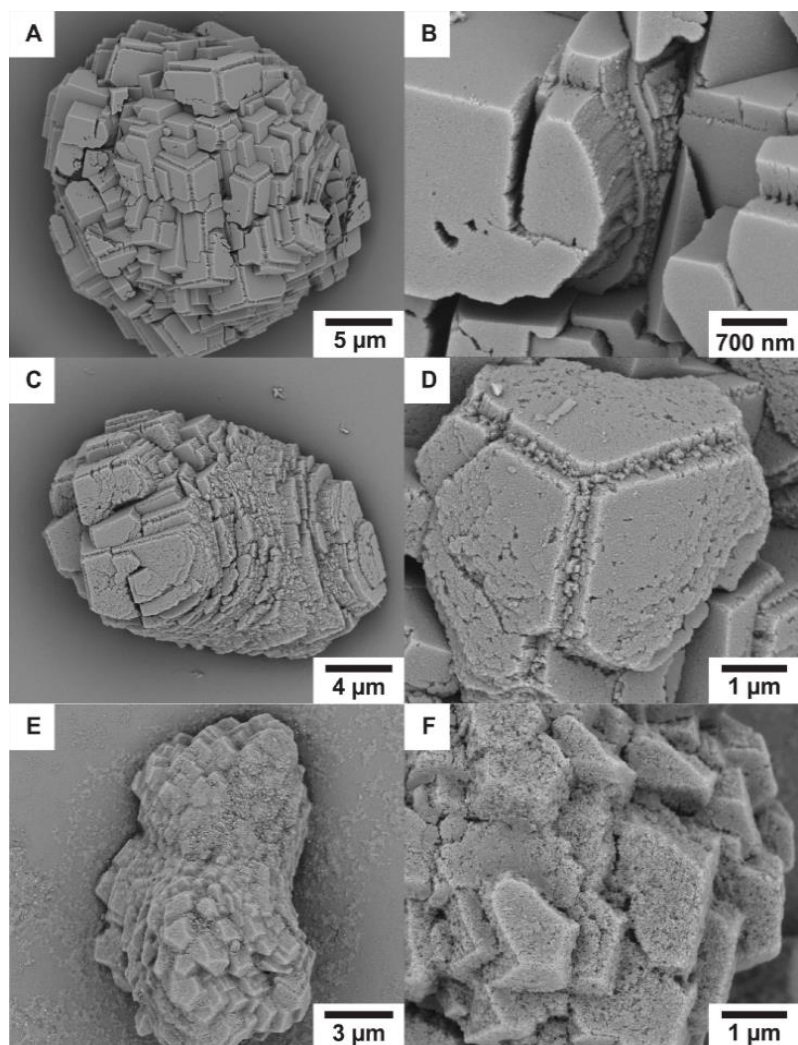


Figure S 3.36: SEM images of crystals in the presence of 10 μmol/L (A/B) , 20 μmol/L (C/D), and 40 μmol/L (E/F) of P(THF₈-co-BHMO₃₇-(C₄H₆O₄)₇₈) after 15 h crystallization time.

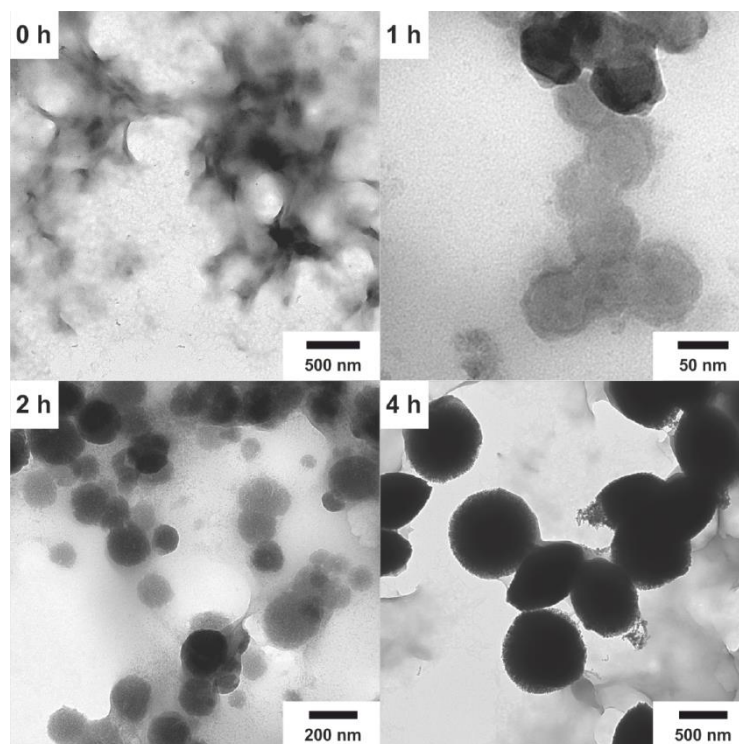


Figure S 3.37: TEM time course of the crystallization of calcium carbonate in the presence of P(THF₈-CO-BHMO₃₇-(C₄H₆O₄)₇₈) (40 μ mol/L). The initial stages of the crystallization showed the Ca²⁺-mediated formation of polymer aggregates of various sizes in agreement with the results from DLS (top left). After 1 h CaCO₃ seeds start to grow within the polymer matrix that form amorphous polydispers agglomerates (top right) after 2 h (bottom left) that grow to almost 200 nm large spherical aggregates of CaCO₃ nanoparticles with surface-bound polymer and oriented alignment of nanocrystals within 4h (bottom right).

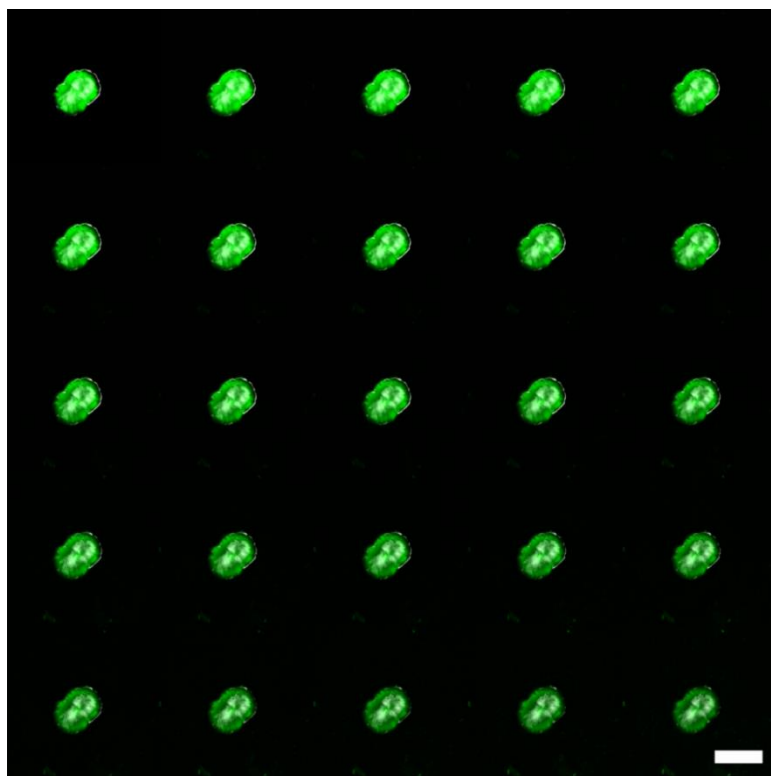


Figure S 3.38: CLSM z-stack of a mesocrystal formed by addition of 20 $\mu\text{mol/L}$ of Rhodamine B tagged $\text{P}(\text{THF}_8\text{-co-BHMO}_{38}\text{-(C}_4\text{H}_6\text{O}_4)_{81})$. To read row by row from top left (top of crystal) to bottom right (bottom of crystal). Scalebar: 15 μm .

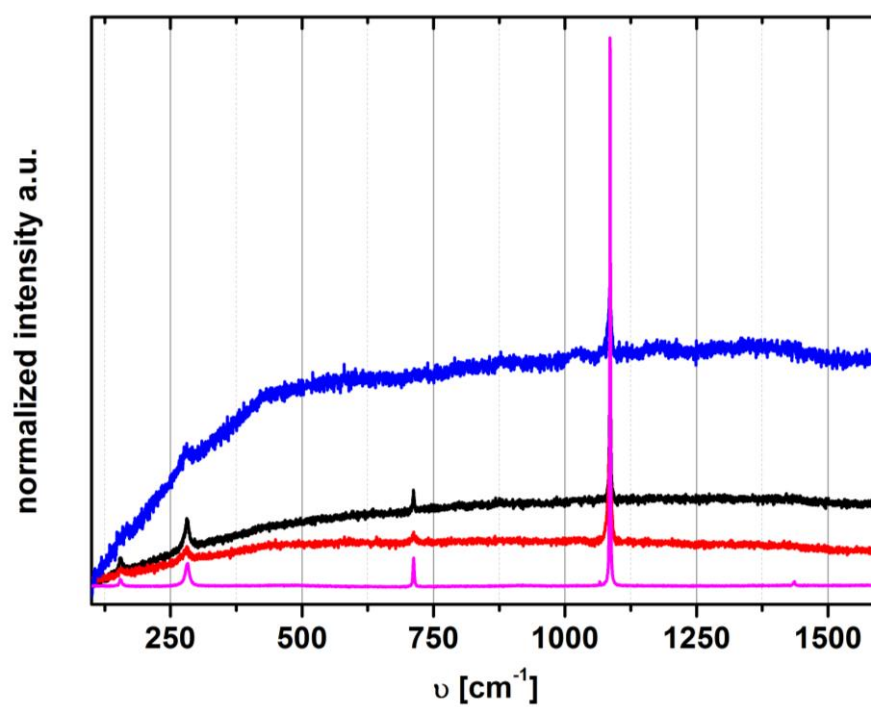


Figure S 3.39: Raman spectra of calcite reference (magenta), final calcite mesocrystals with 10 $\mu\text{mol/L}$ (red), 20 $\mu\text{mol/L}$ (black) and 40 $\mu\text{mol/L}$ (blue) polymer added. The high background level indicates coverage with fluorescent polymer on crystals surface.

3.2.1.6 References

- [1] Y. Ning, L. A. Fielding, K. E. B. Doncom, N. J. W. Penfold, A. N. Kulak, H. Matsuoka, S. P. Armes, *ACS Macro Lett.* **2016**, 311–315.
- [2] Y. Ning, L. A. Fielding, L. P. D. Ratcliffe, Y.-W. Wang, F. C. Meldrum, S. P. Armes, *J. Am. Chem. Soc.* **2016**.
- [3] A. N. Kulak, M. Semsarilar, Y.-Y. Kim, J. Ihli, L. A. Fielding, O. Cespedes, S. P. Armes, F. C. Meldrum, *Chem. Sci.* **2013**, 5, 738.
- [4] C. Rodriguez-Navarro, E. Doehne, E. Sebastian, *Langmuir* **2000**, 16, 947–954.
- [5] M. Maas, H. Rehage, H. Nebel, M. Epple, *Colloid Polym. Sci.* **2007**, 285, 1301–1311.
- [6] H. Cölfen, L. Qi, *Chem. Eur. J.* **2001**, 7, 106–116.
- [7] E. P. Chang, J. A. Russ, A. Verch, R. Kröger, L. A. Estroff, J. S. Evans, *Biochemistry* **2014**, 53, 4317–4319.
- [8] V. K. LaMer, R. H. Dinegar, *J. Am. Chem. Soc.* **1950**, 72, 4847–4854.
- [9] W. Kossel, *Die Naturwissenschaften* **1930**, 18, 901–910.
- [10] R. Becker, W. Döring, *Ann. Phys.* **1935**, 719–752.
- [11] J. Frenkel, *Zeitschr. Phys.* **1926**, 652–669.
- [12] M. Dietzsch, I. Andrusenko, R. Branscheid, F. Emmerling, U. Kolb, W. Tremel, *Zeitschr. Kristall.* **2017**, 232, 255–265.
- [13] H. Nebel, M. Epple, *Z. anorg. allg. Chem.* **2008**, 634, 1439–1443.
- [14] J. D. Rodriguez-Blanco, S. Shaw, L. G. Benning, *Nanoscale* **2011**, 3, 265–271.
- [15] R. Besselink, J. D. Rodriguez-Blanco, T. M. Stawski, L. G. Benning, D. J. Tobler, *Crystal Growth & Design* **2017**, 17, 6224–6230.
- [16] H. Henry Teng, Patricia M. Dove, Christine A. Orme, James J. De Yoreo, *Science* **1998**, 282, 724–727.
- [17] H. Teng, P. M. Dove, J. J. de Yoreo, *Geochim. Cosmochim. Acta* **2000**, 64, 2255–2266.
- [18] J. J. de Yoreo, P. G. Vekilov, *Rev. Mineral. Geochem.* **2003**, 57–93.

-
- [19] F. Neues, S. Hild, M. Epple, O. Marti, A. Ziegler, *J. Struct. Bio.* **2011**, *175*, 10–20.
- [20] A. Becker, W. Becker, J. C. Marxen, M. Epple, *Z. anorg. allg. Chem.* **2003**, *629*, 2305–2311.
- [21] A. Rao, M. S. Fernández, H. Cölfen, J. L. Arias, *Crystal Growth & Design* **2015**, *15*, 2052–2056.
- [22] H. Tlatlik, P. Simon, A. Kawska, D. Zahn, R. Kniep, *Angew. Chem.* **2006**, *118*, 1939–1944.
- [23] U. Bielefeld, W. Becker, *Int. J. Dev. Biol.* **1991**, 121–131.
- [24] U. Bielefeld, K. Zierold, K. H. Körtje, W. Becker, *Histochem. J.* **1992**, 927–938.
- [25] S. E. Wolf, C. F. Böhm, J. Harris, B. Demmert, D. E. Jacob, M. Mondeshki, E. Ruiz-Agudo, C. Rodríguez-Navarro, *J. Struct. Bio.* **2016**, *196*, 244–259.
- [26] R. van de Locht, T. J. A. Slater, A. Verch, J. R. Young, S. J. Haigh, R. Kröger, *Crystal Growth & Design* **2014**, *14*, 1710–1718.
- [27] R. van de Locht, A. Verch, M. Saunders, D. Dissard, T. Rixen, A. Moya, R. Kröger, *J. Struct. Bio.* **2013**, *183*, 57–65.
- [28] K. B. Chekroun, C. Rodríguez-Navarro, M. T. Gonzalez-Munoz, J. M. Arias, G. Cultrone, M. Rodríguez-Gallego, *J. Sedim. Res.* **2004**, *74*, 868–876.
- [29] R. Kröger, *Nat. Mater.* **2015**, *14*, 369–370.
- [30] R. C. Kang, Y.-Y. Kim, P. Yang, W. Cai, H. Pan, A. N. Kulak, J. L. Jau, J. DeYoreo, *Nat. Commun.* **2016**, *7*, 10187–10194.
- [31] C. Rodríguez-Navarro, E. Ruiz-Agudo, J. Harris, S. E. Wolf, *J. Struct. Bio.* **2016**, *196*, 260–287.
- [32] C. Rodríguez-Navarro, A. Burgos Cara, K. Elert, C. V. Putnis, E. Ruiz-Agudo, *Crystal Growth & Design* **2016**, 1850–1860.
- [33] M. Neumann, M. Epple, *J. Inorg. Chem.* **2007**, 1953–1957.
- [34] D. Gebauer, A. Volkel, H. Colfen, *Science* **2008**, *322*, 1819–1822.
- [35] D. Gebauer, *Angew. Chem. Int. Ed.* **2013**, *52*, 8208–8209.
- [36] A. Finomore, P. Cunha, T. Shean, S. Vignolini, S. Guldin, M. Oyen, U. Steiner, *Nat. Commun.* **2012**, *3*, 966.
- [37] J. C. Marxen, W. Becker, *Comp. Biochem. Physio. B:* **1997**, *118*, 23–33.

-
- [38] W. E. G. Müller, M. Neufurth, U. Schlossmacher, H. C. Schröder, D. Pisignano, X. Wang, *RSC Adv.* **2014**, *4*, 2577–2585.
- [39] Z. Huang, X. Li, *Sci. Rep.* **2013**, *3*, 1–6.
- [40] T. M. Stawski, T. Roncal-Herrero, A. Fernandez-Martinez, A. Matamoros-Veloza, R. Kröger, L. G. Benning, *Phys. Chem. Chem. Phys.* **2018**, *20*, 13825–13835.
- [41] D. Gebauer, M. Kellermeier, J. D. Gale, L. Bergström, H. Cölfen, *Chem. Soc. Rev.* **2014**, *43*, 2348.
- [42] C. Rodriguez-Navarro, K. Kudłacz, Ö. Cizer, E. Ruiz-Agudo, *Cryst. Eng. Comm.* **2015**, *17*, 58–72.
- [43] M. H. Nielsen, D. Li, H. Zhang, S. Aloni, T. Y.-J. Han, C. Frandsen, J. Seto, J. F. Banfield, H. Cölfen, J. J. de Yoreo, *Microsc. Microanal.* **2014**, *20*, 425–436.
- [44] H. Cölfen, A. Völkel *Coll. Poly. Sci.*, Springer-Verlag, Berlin/Heidelberg, **2006**, 126–128.
- [45] H. Cölfen, M. Antonietti, *Angew. Chem. Int. Ed.* **2005**, *44*, 5576–5591.
- [46] H. Cölfen, M. Antonietti, *Mesocrystals and Nonclassical Crystallization*, John Wiley & Sons, Ltd, West Sussex, **2008**.
- [47] Y.-Y. Kim, A. S. Schenk, J. Ihli, A. N. Kulak, N. B. J. Hetherington, C. C. Tang, W. W. Schmahl, E. Griesshaber, G. Hyett, F. C. Meldrum, *Nat. Commun.* **2014**, *5*, 1–14.
- [48] A. N. Kulak, P. Yang, Y.-Y. Kim, S. P. Armes, F. C. Meldrum, F. C. Meldrum, *Chem. Commun* **2014**, *2014*, 67–69.
- [49] H. Cölfen, M. Antonietti, *Mesocrystals and Nonclassical Crystallization*, John Wiley & Sons, Ltd, West Sussex, **2008**.
- [50] F. Natalio, T. P. Corrales, M. Panthfer, D. Schollmeyer, I. Lieberwirth, W. E. G. Müller, M. Kappl, H.-J. Butt, W. Tremel, *Science* **2013**, *339*, 1298–1302.
- [51] F. Natalio, T. P. Corrales, S. Wanka, P. Zaslansky, M. Kappl, H. P. Lima, H.-J. Butt, W. Tremel, *Sci. Rep.* **2015**, *5*, 13303.
- [52] K. Gries, R. Kröger, C. Kübel, M. Schowalter, M. Fritz, A. Rosenauer, *Ultramicroscopy* **2009**, *109*, 230–236.
- [53] E. Munch, M. E. Launey, D. H. Alsem, E. Saiz, A. P. Tomsia, R. O. Ritchie, *Science* **2008**, *322*, 1516–1520.

-
- [54] M. Suzuki, K. Saruwatari, T. Kogure, Y. Yamamoto, T. Nishimura, T. Kato, H. Nagasawa, *Science* **2009**, *325*, 1388–1390.
- [55] V. Pipich, M. Balz, S. E. Wolf, W. Tremel, D. Schwahn, *J. Am. Chem. Soc.* **2008**, *130*, 6879–6892.
- [56] C. Rodriguez-Navarro, L. G. Benning, *Elements* **2013**, *9*, 203–209.
- [57] L. Bergström, E. V. Sturm, G. Salazar-Alvarez, H. Cölfen, *Acc. Chem. Res.* **2015**, *48*, 1391–1402.
- [58] D. Gebauer, H. Cölfen, A. Verch, M. Antonietti, *Adv. Mater.* **2009**, *21*, 435–439.
- [59] T. Schüler, W. Tremel, *Chem. Commun.* **2011**, *47*, 5208–5210.
- [60] T. Schüler, J. Renkel, S. Hobe, M. Susewind, D. E. Jacob, M. Panthöfer, A. Hoffmann-Röder, H. Paulsen, W. Tremel, *J. Mater. Chem. B* **2014**, *2*, 3511–3518.
- [61] C. Li, G. D. Botsaris, D. L. Kaplan, *Cryst. Growth Design* **2002**, *2*, 387–393.
- [62] F. Marin, N. Le Roy, B. Marie, P. Ramos-Silva, S. Wolf, S. Benhamada, N. Guichard, F. Immel, *KEM* **2014**, *614*, 52–61.
- [63] I. Polowczyk, A. Bastrzyk, M. Fiedot, *Materials* **2016**, *9*, 1–16.
- [64] S. Elhadj, J. J. de Yoreo, J. R. Hoyer, P. M. Dove, *Proc. Natl. Acad. Sci.* **2006**, *103*, 19237–19242.
- [65] E.-M. Christ, J. Herzberger, M. Montigny, W. Tremel, H. Frey, *Macromolecules* **2016**, *49*, 3681–3695.
- [66] *Filtration Industry Analyst* **2003**, *4*.
- [67] H. Li, X. Fan, W. Tian, H. Zhang, W. Zhang, Z. Yang, *Chem. Commun.* **2014**, *50*, 14666–14669.
- [68] Y. M. Mohan, K. M. Raju, *Int. J. Poly. Mater.* **2006**, *55*, 203–217.
- [69] I. Penczek, S. Penczek, *J. Polym. Sci. B Polym. Lett.* **1967**, *5*, 367–373.
- [70] Jun won Kang, Yang-Kyoo Han **1997**, *18*, 433–438.
- [71] Q. Wu, L. Li, Y. Yu, X. Tang, *Colloid Polym Sci* **2008**, *286*, 761–767.
- [72] M. Bednarek, P. Kubisa, *J. Polym. Sci. A Polym. Chem.* **1999**, *37*, 3455–3463.
- [73] M. Basko, M. Bednarek, L. Billiet, P. Kubisa, E. Goethals, F. Du Prez, *J. Polym. Sci. A Polym. Chem.* **2011**, *49*, 1597–1604.

-
- [74] A. Aouissi, S. S. Al-Deyab, H. Al-Shahri, *Molecules* **2010**, *15*, 1398–1407.
- [75] I. Asenjo-Sanz, A. Veloso, J. I. Miranda, A. Alegría, J. A. Pomposo, F. Barroso-Bujans, *Macromolecules* **2015**, *48*, 1664–1672.
- [76] C. Fodor, B. Iván, *J. Polym. Sci. A Polym. Chem.* **2011**, *49*, 4729–4734.
- [77] Z. Tian, M. Wang, A.-y. Zhang, Z.-g. Feng, *Polymer* **2008**, *49*, 446–454.
- [78] C. Fodor, G. Kali, B. Iván, *Macromolecules* **2011**, *44*, 4496–4502.
- [79] F. D'Haese, E. J. Goethals, *Brit. Poly. J.* **1988**, *20*, 103–108.
- [80] S.-H. Lim, E.-J. Cha, J. Huh, C.-H. Ahn, *Macromol. Chem. Phys.* **2009**, *210*, 1734–1738.
- [81] M. F. Dubreuil, N. G. Farcy, E. J. Goethals, *Macromol. Rapid Commun.* **1999**, *20*, 383–386.
- [82] L. M. Tanghe, E. J. Goethals, F. Du Prez, *Polym. Int.* **2003**, *52*, 191–197.
- [83] M. Dietzsch, M. Barz, T. Schüler, S. Klassen, M. Schreiber, M. Susewind, N. Loges, M. Lang, N. Hellmann, M. Fritz, K. Fischer, P. Theato, A. Kühnle, M. Schmidt, R. Zentel, W. Tremel, *Langmuir* **2013**, *29*, 3080–3088.
- [84] Y.-Y. Kim, K. Ganesan, P. Yang, A. N. Kulak, S. Borukhin, S. Pechook, L. Ribeiro, R. Kröger, S. J. Eichhorn, S. P. Armes, B. Pokroy, F. C. Meldrum, *Nat. Mater.* **2011**, *10*, 890–896.
- [85] M. Balz, E. Barriau, V. Istratov, H. Frey, W. Tremel, *Langmuir* **2005**, *21*, 3987–3991.
- [86] H. Wei, Q. Shen, H. Wang, Y. Gao, Y. Zhao, D. Xu, D. Wang, *J. Cryst. Growth* **2007**, *303*, 537–545.
- [87] H. Yang, Y. Su, H. Zhu, H. Zhu, B. Xie, Y. Zhao, Y. Chen, D. Wang, *Polymer* **2007**, *48*, 4344–4351.
- [88] E.-M. Christ, D. Hobernik, M. Bros, M. Wagner, H. Frey, *Biomacromolecules* **2015**, *16*, 3297–3307.
- [89] Eva-Maria Christ, *Dissertation*, Joh. Gutenberg-Universität, Mainz, **2016**.
- [90] Y. Xia, Y. Wang, Y. Wang, C. Tu, F. Qiu, L. Zhu, Y. Su, D. Yan, B. Zhu, X. Zhu, *Coll. Surf. B* **2011**, *88*, 674–681.
- [91] L. Addadi, S. Weiner, *PNAS* **1985**, *82*, 4110–4114.
- [92] L. Addadi, J. Moradian, E. Shay, N.G. Maroudas, , S. Weiner, *PNAS* **1987**, *84*, 2732–2736.

-
- [93] C. Beato, M. S. Fernández, S. Fermani, M. Reggi, A. Neira-Carrillo, A. Rao, G. Falini, J. L. Arias, *Cryst. Eng. Comm.* **2015**, *17*, 5953–5961.
- [94] M. Schreiber, M. Eckardt, S. Klassen, H. Adam, M. Nalbach, L. Greifenstein, F. Kling, M. Kittelmann, R. Bechstein, A. Kühnle, *Soft Matter* **2013**, *9*, 7145–7149.
- [95] S. Rode, R. Stark, J. Lübbe, L. Tröger, J. Schütte, K. Umeda, K. Kobayashi, H. Yamada, A. Kühnle, *Rev. Sci. Instr.* **2011**, *82*, 73703.
- [96] H. Adam, S. Rode, M. Schreiber, K. Kobayashi, H. Yamada, A. Kühnle, *Rev. Sci. Instr.* **2014**, *85*, 23703.
- [97] B. Chu, *Laser Light Scattering*, Academic Press Academic Press, New York, **1974**.
- [98] M. Sedlák, *Langmuir* **1999**, *15*, 4045–4051.
- [99] K. Huber, *J. Phys. Chem.* **1993**, *97*, 9825–9830.
- [100] R. Schweins, K. Huber, *Eur. Phys. J. E* **2001**, *5*, 117–126.
- [101] S. L. P. Wolf, L. Caballero, F. Melo, H. Cölfen, *Langmuir* **2017**, *33*, 158–163.
- [102] J. Yu, M. Lei, B. Cheng, X. Zhao, *J. Solid State Chem.* **2004**, *177*, 681–689.
- [103] Y. Tang, W. Yang, X. Yin, Y. Liu, P. Yin, J. Wang, *Desalination* **2008**, *228*, 55–60.
- [104] M. Niederberger, H. Cölfen, *Phys. Chem. Chem. Phys.* **2006**, *8*, 3271–3287.
- [105] G. Wang, L. Li, J. Lan, L. Chen, J. You, *J. Mater. Chem.* **2008**, *18*, 2789–2797.

3.3 *Bg*-AChBP protein isoforms effect on CaCO_3

As it has already been discussed in Chapter 2.3.3 *Biomphalaria glabrata* Acetylcholine-binding proteins (short *Bg*-AChBP) have large sequential congruence to the ACCBP protein class that has been demonstrated to have effects on CaCO_3 stabilization in amorphous phase and an influence on the final polymorph if magnesium are present simultaneously as it is often the case in native environment of the snails. For the *Bg*-AChBP protein class which is expressed in two different isoforms within the snail a role in neural signal transduction and toxin-regulation or even the influence on CaCO_3 crystallization that is identified in this work. The work in Chapter 3.3.1 and Chapter 3.3.2 has been conducted using recombinant proteins instead of native ones to get usable concentrations of the protein. Note that the results still are all *in vitro* results that can only give important hints towards the *in vivo* role of the protein.

3.3.1 Effects of *Biomphalaria glabrata* Acetylcholine-Binding Proteins on CaCO_3 polymorph selective crystallization

This paragraph is based on corporation work with Dr. Daniela Treiber from the AG Markl and resulted in the manuscript "Effects of *Biomphalaria glabrata* Acetylcholine-Binding Proteins on CaCO_3 polymorph selective crystallization". The manuscript will be submitted to *Crystal Growth and Design* by the *American Chemical Society*. The following chapter combines the main manuscript and the supporting information.

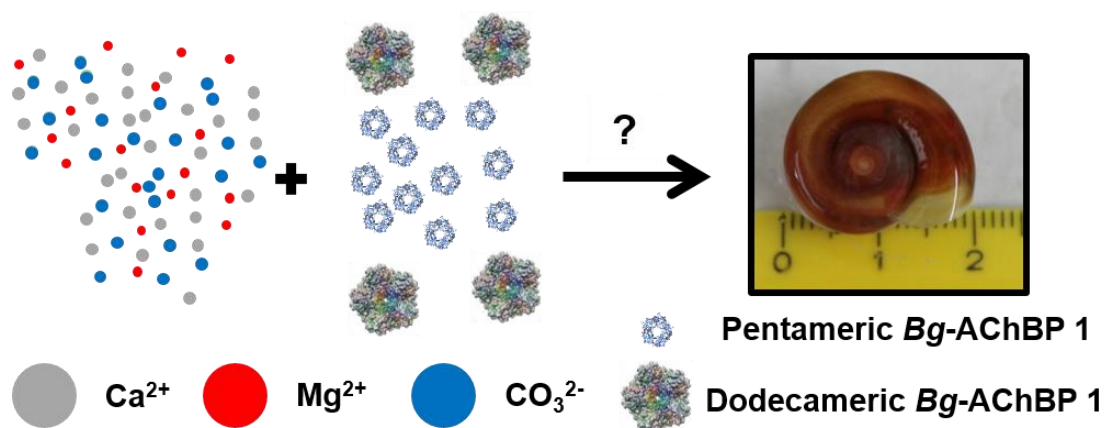


Figure 3.25: Scheme of central question how shell growth gets effected by both structures of Isoform 1 of *Bg*-AChBP protein class at distinct ratios of calcium and magnesium.

The snail *Biomphalaria glabrata* expresses two different acetylcholine binding proteins (AChBP) termed *Bg*-AChBP1 and *Bg*-AChBP2. Concerning biological functions of AChBP in snails, several possibilities have been discussed. The suppression of cholinergic transmission, the binding of algal toxins and the regulation of CaCO_3 crystallization because of its sequence- and structure similarity to amorphous calcium carbonate binding proteins (ACCBP). The details on the effects of CaCO_3 by published *in vitro* studies left manifold open questions. The following paragraph studies the proteins effects on CaCO_3 crystallization *in vitro* and discusses their possible role for *in vivo* shell development and shell growth. The presence of the protein isoforms during important stages of larval development is mapped by immunofluorescence microscopy and within the mantle epithelium, as well as the location during shell development of adult animals. According to the results from *in vitro* precipitation under simultaneous presence of magnesium ions and *Bg*-AChBP1 the assumption is made that *Bg*-AChBP1 influences the polymorph stabilization of the kinetically stable aragonite phase.

3.3.1.1 Introduction

Shells from bivalves and gastropods are highly specialized organic/inorganic composite materials evolved and improved in eons under the permanent selection pressure to mechanically support and vitally protect these animals. In the different

molluscan classes and subtaxa, the hierarchical assembly of these biominerals from nanometer-sized components to centimeter-sized objects, and the exact shaping of the latter, varies greatly. ^[1–5] As a prerequisite for biomineralization, various mechanisms have been identified to ensure selectivity in keeping the biomineral in an amorphous precursor phase and stabilizing it. ^[6] Frequently, extravagant structural details are formed by oriented attachment of nanometer-sized and often sub-structured building blocks which is called mesocrystal formation. ^[7] Mesocrystals are defined as micro- to macroscopic superstructures composed of small mineral building blocks and certain additives acting as stabilizers. ^[8] Stabilizers (also called fillers) may range from small molecules to proteins implemented in the domain boundaries of the crystalline building blocks to prevent fusion of inorganic material while maintaining the common mineral orientation. ^[9] This provides molluscs shells of extraordinary mechanical strength for protection against vital dangers such as predators, desiccation or breakwater. Moreover, in adaption to the habitat, a species-specific compromise of shell weight versus armored protection is maintained; for example, shells from intertidal periwinkle snails are very thick and robust, whereas shells from land snails living nearby at the beach are very thin and fragile.

The polymorphism of calcium carbonate complicates the role of additives to a certain extent. The classical nucleation and growth concept of CaCO_3 assumes a stepwise transition of an amorphous CaCO_3 (ACC) precursor to the crystalline CaCO_3 starting from vaterite, to aragonite and finally calcite. ^[10] Nevertheless, various recent studies revealed that this classical transition pathway is rarely followed in natural calcium carbonate systems. Face-selective binding of additives to distinct crystalline facets of the polymorph ^[11] might selectively inhibit certain transition steps as first predicted by theoretical calculations ^[12] and later experimentally found in oyster (*Pincta funcata*) shells. ^[13] The additives stabilize non-classical precursors such as dense liquid phases, ^[14] PILPs ^[15–17] or pre-nucleation clusters. ^[18] Such phases or clusters subsequently transform, in a controlled order, mostly by dissolution-recrystallization processes to a specific polymorph. ^[19]

The most detailed studied natural additives for bio-controlled CaCO_3 formation in mollusks and probably in the animal kingdom are the so-called amorphous-calcium-carbonate binding proteins (ACCBP). ^[20] They are ring-like homo-pentamers

of 25 kDa polypeptides and structurally closely related to the molluscan acetylcholine binding proteins (AChBP) that in turn are water-soluble homologs of the ligand binding domain of the nicotinic acetylcholine receptors. [21,22]

ACCBP has been detected, structurally analyzed and functionally studied in an oyster and an abalone. [23,13] In ammonia diffusion experiments with different calcium ion solutions, ACCBP did exclusively precipitate ACC. Apparently, ACCBP works as transformation and scale inhibitor for calcite mineralization *in vitro*, thereby stabilizing the crystalline aragonite phase, and this is assumed to be its major role also *in vivo*. Evans *et al.* [24] identified amino acid appositions in the protein that might strongly bind to the surface of aragonite, thereby stabilizing its crystalline aragonite phase.

In the previous studies on oyster and abalone ACCBP, the following remained unclear: (i) the kinetics of ACC transformation in the presence of ACCBP; (ii) details of this transformation process in the presence of ACCBP, and (iii) the possible role of other divalent cations in this process, notably of Mg^{2+} ions. The present study was designed to elucidate these points, using a variety of techniques.

As research organism we chose the planorbid freshwater snail *Biomphalaria glabrata*, because a detailed phase study of its shell, histological studies and analyzes of the hemolymph proteins are already available. [25–30] Moreover, the AChBP fraction of *Biomphalaria glabrata* hemolymph proteins showed, in preliminary experiments, ACC binding. [22] This fraction contains two distinct AChBP isoforms, termed *Bg*-AChBP1 and *Bg*-AChBP2 that are available as recombinant proteins. [22] As an additional intriguing feature, *Bg*-AChBP1 is assembled as a regular pentagonal dodecahedron of 60 monomers, 25 nm in diameter (as recombinant protein and also in the hemolymph). The hemolymph state of *Bg*-AChBP2 is unclear, but the recombinant protein forms solitary pentamers. [22]

3.3.1.2 Experimental

Materials and handling details

All reagents for crystallization and titration experiments were purchased from Sigma Aldrich and were used as received, unless otherwise stated. All protein solutions were continuously stored in a fridge at 7°C to prevent aggregation or denaturation.

Instrumentation

Optical imaging was performed with a confocal Keyence-8710 laser light microscope equipped with a 658 nm diode laser to get height information of the precipitated samples.

UV-Vis spectrophotometry for protein concentration determinations of the pull-down assay samples was performed with an Ultraspec 2100 Pro from Amersham Biosciences (Freiburg). The resulting concentration has been calculated from known cuvette thickness and extinction values by using Lambert-Beer law.

Immunofluorescence microscopy was performed on 7 µm cryo Chapters (Cryotome HM 500 OM, Microm, Waldorf, Germany) according to literature.^[31] Due to the water solubility of AChBP all tissue Chapters were prefixed for 20 min in chloroform / methanol (2:1) at 0°C.^[32] Rabbit polyclonal *anti-Bg-AChBP* antibodies were produced by Charles River Laboratories, Kisslegg. Two rabbits were immunized over two months by *Bg-AChBP1* (IF1) or *Bg-AChBP2* (IF2) injections. The isoform specificity was confirmed by Western blot. The *Bg-AChBP1* antiserum was applied at a solution of 1:250 and the *Bg-AChBP2* antiserum at a solution of 1:50. Both applied solutions were the result of a serial solution experiment. Images were recorded on a Leitz DM RBD fluorescence microscope (Leica, Wetzlar, Germany).

For scanning electron microscopy (SEM) the calcium carbonate crystals were sputtered with 4 nm platinum or gold respectively and analyzed using a JEOL-JSM 5610LV (JEOL Ltd., Tokyo, Japan) or FEI Phenom (Hillsboro, OR, USA). Images were acquired with an accelerating voltage of 20 kV or 10 kV respectively.

FIB cut sample preparation was used for investigation of internal morphology of the snail shell by transmission electron microscopy. For FIB cuts, a FEI 600 Nanolab focused ion beam (FIB)/SEM dual beam instrument (FEI, Hillboro, Oregon) equipped with an Omniprobe micromanipulator (Omniprobe Inc. Dallas, Texas) was used. The images were collected on an Ultrascan 1000 (Gatan) 2k CCD Camera, using the Digital Micrograph software (Gatan). The Tecnai F20 (FEI) was equipped with a 4K CCD camera, an EDX system by EDAX, a STEM detector by FEI and a LaB6 cathode working at 200 kV.

For transformation experiments of ACC was synthesized via Faatz-Wegner method [33] with and without addition of 40 μmol *Bg*-AChBP1 per mmol CaCl_2 . The transformation was studied at 40 °C at 40 % relative humidity in a ThermoTEC (ESPEC) climate chamber from ThermoTEC, Weilburg, Germany.

IR-spectroscopy measurements for phase identification were carried out using a NicoletTM iSTM10 FT-IR spectrometer from Thermo scientific. Each spectrum was taken with resolution of 1 cm^{-1} at 16 iterations.

XRD measurements were carried out with a Bruker Discover D8 with HiStar detector in Bragg-Brentano geometry using $\text{Cu-K}\alpha$ radiation. The resulting data has been refined by using a Rietveld refinement to determine the calcite to aragonite ratio.

X-ray Photoelectron Spectroscopy (XPS) was conducted using a Kratos Axis UltraDLD spectrometer (Kratos, Manchester, England) using an $\text{Al-K}\alpha$ excitation source with a photon energy of 1487 eV. The data were acquired in the hybrid mode using a 0° take-off angle, defined as the angle between the surface normal and the axis of the analyzer lens. Detailed region XP spectra were collected with setting analyzer pass energy at 80 eV. Neutralizer was always used during spectra collection and binding energy scales were further calibrated according to the dominant C 1s emission at 284.8 eV.

The ratio of Mg/Ca atomic composition was calculated according to Equation below, by calculating the emission peak areas (Intensity - I) after normalization with the supplied sensitivity factors (SF).

$$\frac{\%_{\text{Mg}}}{\%_{\text{Ca}}} = \frac{(I_{\text{Mg}}/SF_{\text{Mg}})}{(I_{\text{Ca}}/SF_{\text{Ca}})}$$

Linear background was always used for peak quantification.

Sample preparation for electron microscopy

1-3 mm³ tissue pieces of *Biomphalaria glabrata* mantle were fixed in a freshly prepared medium of 1 % glutaraldehyd in 0,02 M phosphate buffer (pH 7.2) for a minimum of 2 hours. The chemical fixation was implemented as described in literature. [29]

Synthesis of recombinant proteins

Bg-AChBP1 and *Bg-AChBP2* were individually expressed in eColi. Plasmids with the construct *Bg-AChBP1*-His-TEV and *Bg-AChBP2*-His-TEV were prepared due to Gateway™ cloning by Vanessa Möller. The Gateway™ pDEST™ 14 vector was used. Both *Bg-AChBP* isoforms were solubilized from inclusion bodies and purified on a nickel column and further processed according to reported procedures. [22]

Binding assay of *Bg-AChBP* on polymorphs of CaCO₃

To study binding affinity of recombinant proteins on ACC, vaterite, calcite and aragonite 5 mg of each polymorph of CaCO₃ was added to a glass vial and incubated for 72 h at 7 °C in the fridge with 1 mL TRIS buffer containing 21 µmol/L of Isoform 1 or 2 of *Bg-AChBP* respectively. After centrifugation the pellet has been washed three times with aliquots of 200 µL of MilliQ water and 1 M sodium chloride solution each to wash away unbound protein. Afterwards the pellet was diluted with 600 µL of 0.1 M acetic acid.

Direct precipitation of CaCO₃ with proteins under presence of Mg²⁺ ions

To study the influence of *Bg-AChBP* proteins on the CaCO₃ precipitation a direct precipitation procedure was used to mimic the snails natural CaCO₃ precipitation process. Recombinant proteins were added to a total 25 mL of 0.1 M solution of CaCl₂ and subsequently 25 mL 0.1 M sodium bicarbonate solution have been added to a PE vial. For research on the influence of simultaneous presence of magnesium and calcium ions and recombinant *Bg-AChBP* protein were performed by analogous direct precipitations in PE vials with various molar ratios of Mg and Ca ions at a total concentration of 0.1 mol/L. The concentration of protein in the mixtures was 0.4 µmol/L in total volume of 50 mL. The solutions were shaken for

72 h and washed with MilliQ water two times followed by a washing step with absolute ethanol with subsequent drying under vacuum to make further analysis possible. For AAS the precipitate was solved in 0.1 M acetic acid solution and further diluted with MilliQ water to be in a measurable concentration range.

Ethics statement

The freshwater pondsnail *Biomphalaria glabrata* was used for all experiments. The animals were obtained from a freshwater tank culture established more than ten years ago at the Institute for Molecular Physiology. The animals were held at a constant temperature of 20°C and feed two to three times a week. All animal work has been conducted according to the national guidelines. In case of these gastropods the approval of an ethics committee was not required. All efforts were made to minimize suffering.

3.3.1.3 Results & Discussion

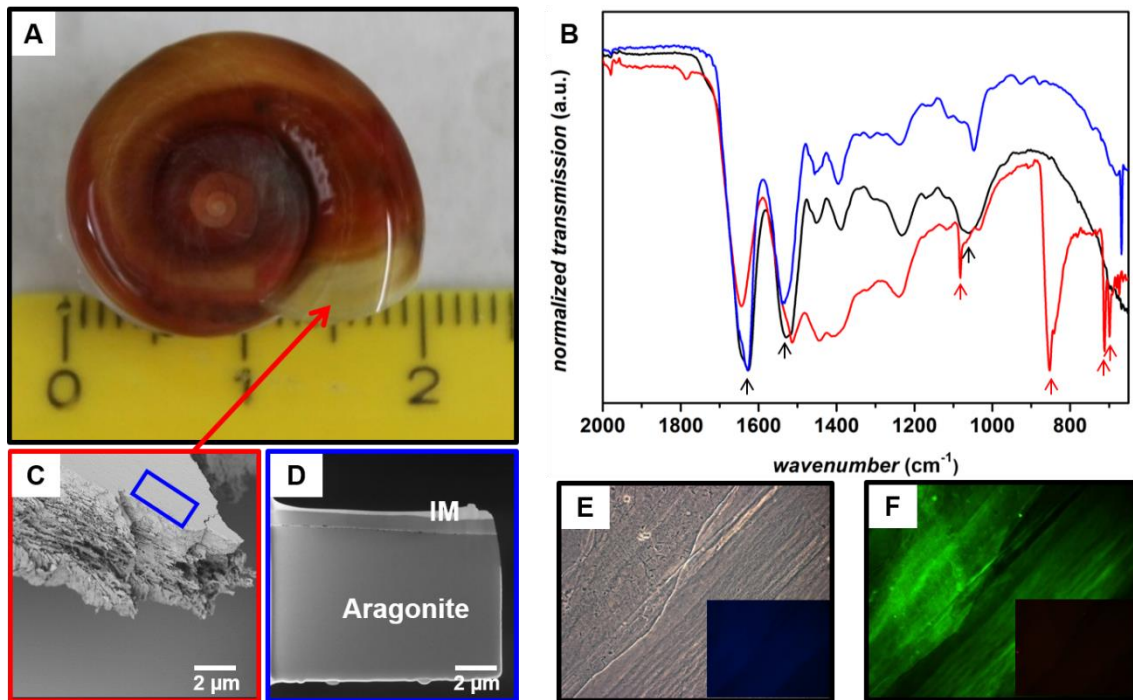


Figure 3.26: Shell structure and *Bg*-AChBP1 presence in the shell material. (A) Brownish/yellow shell of an adult *Biomphalaria glabrata* snail. (B) IR spectra of recombinant *Bg*-AChBP1 pentamers (black), enriched insoluble matrix material (IM, blue) and grinded shell material encompassing aragonite and insoluble matrix (red). Black arrows highlight putative amide bands typical for protein; note that they are also present in the matrix material. Red arrows highlight additional bands caused by aragonite. Changes in amide pattern would indicate conformational changes of the proteins induced by their environment. (C) SEM image of a cross-section of the shell close to the opening, showing the matrix to be covered by 90° stacked aragonite needles, from which a SEM grid was prepared (blue box). (D) FIB SEM cross-section from the shell which allows distinguishing the lighter matrix from the darker aragonite. (E) Light microscopy (phase contrast optics) of a matrix Chapter with the CaCO_3 removed by solving the inorganic material with acetic acid. The sample was treated with DAPI (insert) which was negative, indicating that no cells are present in the matrix. (F) Immunofluorescence microscopy using rabbit *Bg*-AChBP1-specific antibodies, showing a strong positive reaction, whereas *Bg*-AChBP2-specific antibodies reacted completely negative (insert); thus, the latter could be used as a negative control, and the presence of *Bg*-AChBP1 in the matrix is clearly indicated.

The shell is produced by the mantle epithelium that secretes the necessary components into the fluid of the extrapallial space. The extrapallial space is a narrow compartment between the existing shell and the mantle sealed at its rim from the environment by the leathery periostracum. The accumulation of ions in the extrapallial fluid occurs via ion pumps localized in the plasma membrane of the calcifying

cells distributed in the mantle epithelium. A scaffold of organic material directs the crystallization process that occurs mainly at the boundary of the growing aragonite layer and a covering organic insoluble matrix.

By FIB-SEM and immunofluorescence microscopy of adult *B. glabrata* shells, we collected evidence for the presence of *Bg*-AChBP1 and the absence of *Bg*-AChBP2 in the shell material (Figure 3.26). IR spectra of material from the insoluble matrix (further referred to as “matrix”) and of recombinant *Bg*-AChBP1 yielded comparable pattern, notably at 1650 cm^{-1} and 1520 cm^{-1} suggesting amide bonds, as well as very similar finger print pattern especially at 1100 cm^{-1} (Figure 3.26 B). The spectrum of whole shell material, including matrix material as well as the mineralized material revealed bands typical for aragonite. The missing symmetric stretching mode of carbonate is overlaid by the amide band around 1650 cm^{-1} . The inorganic shell material is composed of densely packed in 90° tilted bundles of aragonite needles (Figure 3.26 C), FIB-cut cross-sections visualize the thick layer of aragonite crystals and the covering amorphous matrix (Figure 3.26 D). According to the IR spectra, as expected the matrix contains proteins. However, is *Bg*-AChBP1 among them? This was confirmed by immunofluorescence microscopy, showing a strong positive reaction of the matrix with *Bg*-AChBP1-specific antibodies and a negative reaction with *Bg*-AChBP2-specific antibodies (Figure 3.26 E, F).

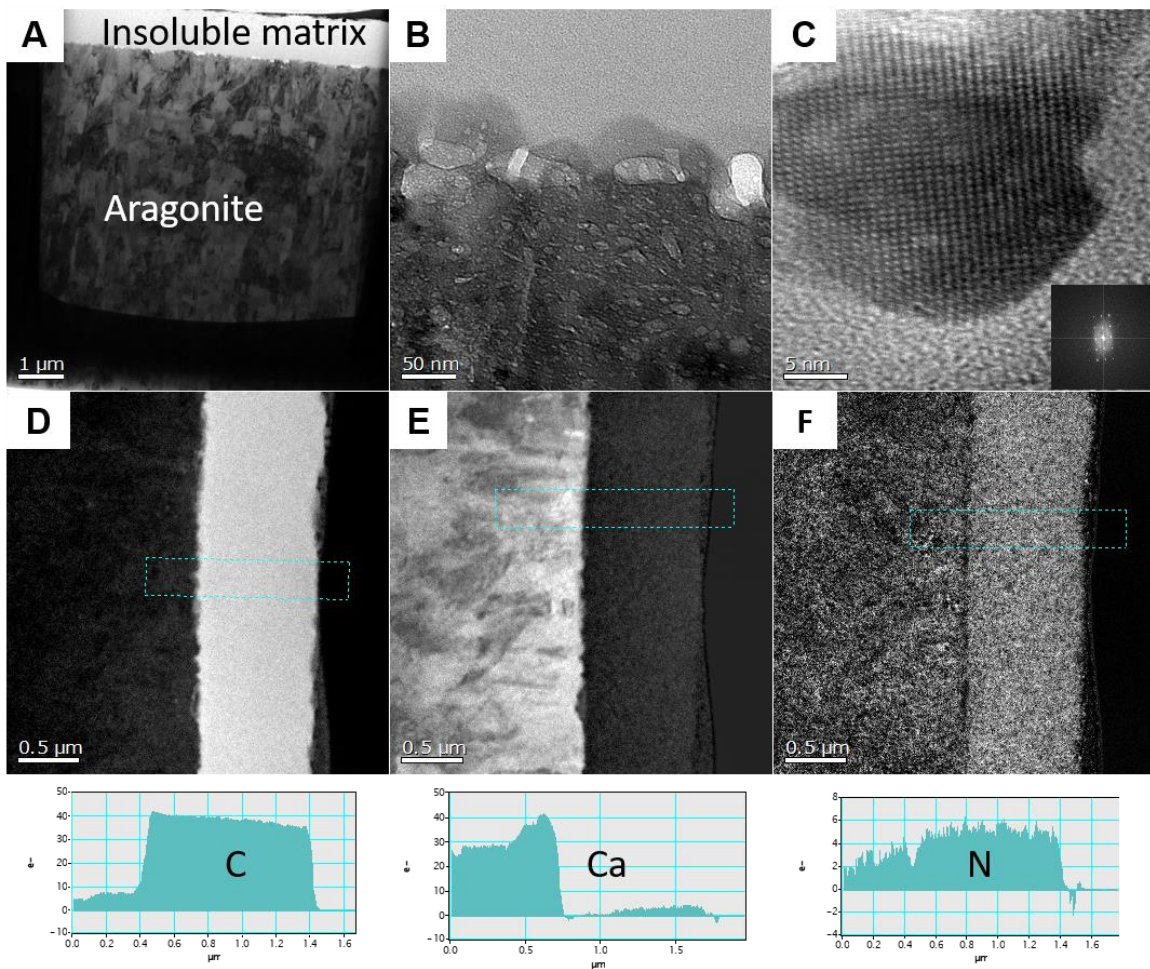


Figure 3.27: TEM and STEM-EDX analysis of the shell. (A) TEM overview of an ultrathin cross-section of the shell (light, less dense); note the matrix and variable contrasted aragonite needles. (B) Boundary between the amorphous matrix and partially crystalline CaCO_3 with organic inclusions which are present during aragonite particle formation within the amorphous/crystalline boundary (C). STEM-EDX cross-section of carbon (D) and calcium (E) show a sharp boundary of CaCO_3 to organics in insoluble matrix. Successive decrease of carbon and nitrogen signal (F) shows a successive transformation process wherein the more crystalline material is in farther distance to the matrix. Enrichment of Ca at the boundary indicates that the ACC/aragonite transformation happens at the boundary of matrix and solid needles.

Additional information about the shell structure was collected by TEM which revealed that the grain boundaries of altered shell parts lacked organic material (Figure 3.27 A-C). This is confirmed by the STEM EDX profiles that indicate a boundary-driven transformation process of ACC to aragonite which can be seen by the

stepwise decrease of organic occlusions from the outer to the core part of the shell (Figure 3.27 D-F).

In a thin layer in the matrix cross-section of the brownish colored part of the shell, we detected a significant amount of iron as shown by STEM-EDX in Figure S1 in the Supporting Information. Therefore, we suspected that the hemolymph protein hemoglobin of *Biomphalaria glabrata* (*Bg-Hb*) might also be a shell component. However, immunofluorescence microscopy of shell material with *Bg-Hb*-specific antibodies yielded completely negative results (not shown). We therefore assume that the iron is not transferred into the shell as a hemoglobin component, and that hemoglobin is not directly involved in shell growth. Accumulation of iron in the shell might occur either directly from the tank water, or indirectly via the hemolymph and mucus. Iron accumulation occurs gradually (see Figure S 3.40, Supporting Information) and its permanent enrichment might result in the sharp line visible in the matrix, yielding the brownish shell color after aging.

The boundary between inorganic aragonite and organic matrix showed small crystalline parts together with amorphous parts containing organic occlusions (see Figure 3.27 (A-C)). Thus, *Bg-AChBP1* might either play a functional role in the matrix, or more likely in the boundary between matrix and the inorganic crystalline layers (from which the protein seems to be excluded). We therefore assume that in the matrix respectively the boundary, *Bg-AChBP1* is either needed to prevent ACC from precipitating, or to transform it in a controlled manner into aragonite as it has already been observed for structurally related proteins. ^[34,24]

The presence of *Bg-AChBP1* in the matrix raises the question, in which developmental stages and cell types this protein is expressed. In adult snails it is present, in very low quantities, freely dissolved in the hemolymph, from which it has been purified previously. ^[35,36] It is also present in the extrapallial fluid (the thin fluid film between mantle epithelium and shell) of adult *Biomphalaria glabrata* ^[36] as it is the case with ACCBP from two other molluscan species. ^[13,37] Either, the protein is incorporated into the shell material after the actual transformation process of ACC to aragonite that starts within snail egg status between 72 h and 120 h after egg fertilization. ^[38] This would mean that *Bg-AChBP1* would not be involved in the

transformation process, at least in the juvenile stages. Alternatively, it could be already present in earlier developmental stages which would allow it to influence the transformation from the very beginning of shell growth. To clarify if *Bg-AChBP1* is expressed during all states of CaCO_3 biomineralization (enrichment, transportation and crystallization) we studied whole mounts from larvae 60 h and 70 h after egg fertilization, and from juveniles of about 120 h age (just finishing metamorphosis), as well as adult mantle tissues by immunofluorescence microscopy. Figure 3.28 shows the presence of *Bg-AChBP1* in both larval stages studied, and in juveniles, although it remained unclear which tissues express the protein. In Figure 3.28 C-C'', the periphery of the body, including the epidermis, seems to be excluded from the positive reaction. Nevertheless, *Bg-AChBP1* is present in the larvae at ACC status as well as during the earliest transformation to crystalline CaCO_3 . In contrast, negative reactions were obtained with *Bg-AChBP2* in the larval stages (see insert in Figure 3.28 A-A'') and in juveniles (not shown).

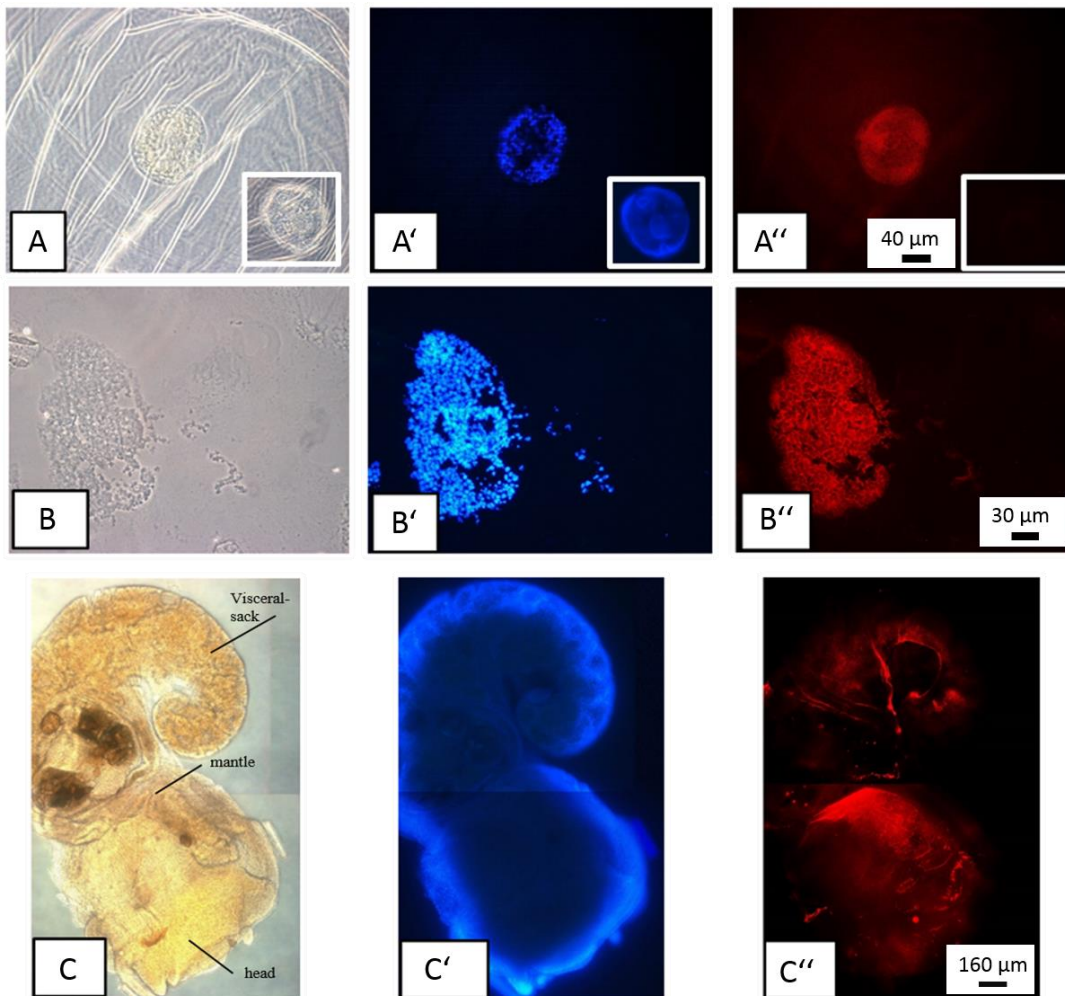


Figure 3.28: Whole mount immunofluorescence microscopy of *B. glabrata* larvae. (A-C) Phase contrast optics; (A'-C') epifluorescence optics after DAPI staining to visualize the cell nuclei; (A''-C'') epifluorescence optics showing immunofluorescence labelling with *Bg*-AChBP1 specific antibodies. (A-A'') 60 h old larva; (B-B'') 70 h old larva; (C-C'') juvenile snail in which aragonite formation from ACC is started. Note clear reaction with DAPI (blue fluorescence), and with the antibodies (red fluorescence). Also note very strong labelling of the collar part of the mantle in (C'). *Bg*-AChBP2-specific antibodies were found to be negative on all stages tested (an example shown in A-A'', insert).

Immunofluorescence microscopy of adult *Biomphalaria glabrata* tissue showed a strong signal in the mantle epithelium (Figure 3.28 A-A''), and a negative reaction of *Bg*-AChBP2-specific antibodies on this tissue (see insert in Figure 3.28 A-A''). Both antibodies yielded positive reactions in the brain (not shown) which, however, is not relevant in the present context.

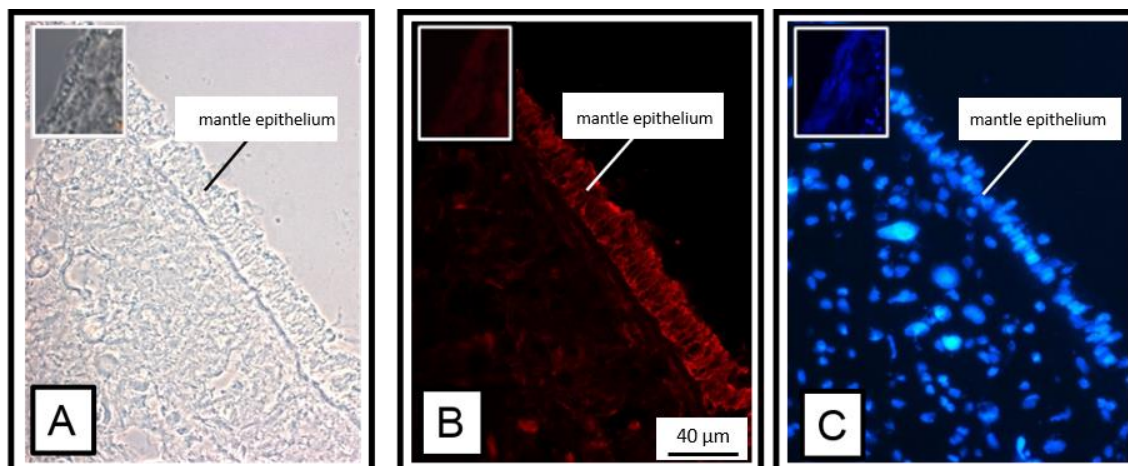


Figure 3.29: Immunofluorescence microscopy of a tissue section from *B. glabrata*, (A) phase contrast optics. (B) epifluorescence optics, showing strong reaction of *Bg*-AChBP1-specific antibodies with the mantle epithelium, and negative reaction of *Bg*-AChBP2-specific (insert). (C) The corresponding DAPI staining of cell nuclei.

From the results above it is worth to mention that *Bg*-AChBP1 (but not *Bg*-AChBP2) is expressed in larvae and juveniles. In adult snails it is specifically localized in the mantle epithelial cells. From there, it could be directly secreted into the extrapallial space together with ACC forming ions. We also collected evidence that *Bg*-AChBP1 is indeed incorporated in the shells IM and the outer part of the shells inorganic material that remained partially amorphous in this area (see Figure 3.26 and Figure 3.27). Thus a study of CaCO_3 stabilization properties of *Bg*-AChBP1 dodecahedra on ACC was conducted.

Possible stabilization of amorphous calcium carbonate by *Bg*-AChBP1 was tested by a climate chamber transformation of Faatz-Wegner ACC precipitated with and without protein at 40°C under 40% rel. humidity. Under these conditions, usually aragonite forms relatively fast within a few hours. By addition of $0.43 \mu\text{mol/L}$ *Bg*-AChBP1 dodecahedra to 50 mL a 0.1 M (CaCl_2 concentration) precipitation solution the transformation process is delayed by about 4 days (see Figure S 3.42, Supporting Information). The recombinant *Bg*-AChBP1 dodecahedra have been shown to stabilize the amorphous phase of CaCO_3 which is assumed to be an important

function of the protein *in vitro* as the snail is oversaturated with CaCO_3 by orders of magnitude.

Effects of *Bg*-AChBP1 and Mg^{2+} on CaCO_3 phases

X-ray photoelectron spectroscopy (XPS) measurements of the inner shell region showed only calcium, whereas the covering matrix of the outer shell region showed, besides calcium (95%), also the presence of magnesium (5%) and of nitrogen, the latter indicating bioorganic material (see Figure S 3.41, Supporting Information). In contrast to the Ca/Mg ratio of 95/5%, the bulk Ca/Mg ratio of the acetic acid soluble parts of the shell as measured by AAS was 84.5/15.5%. The penetration depth of the XPS measurement was only 10 nm which may also account for the discrepancy of the two measurements. Also following comparable findings of Su *et al.*,^[39] the presence of magnesium in certain regions of the shell prompted us to study not only effects of *Bg*-AChBP1 on the shell growth in *B. glabrata*, but also the possible influence of Mg^{2+} ions, and the combined influence of both components. It should be noted that the tank water of our *B. glabrata* culture showed a ratio of 90.2:9.8% for $\text{Ca}^{2+}/\text{Mg}^{2+}$ ions (1.57 and 0.17 mmol/L for Ca^{2+} and Mg^{2+} , respectively) as verified by AAS. Therefore, we performed precipitation experiments with both ions present in approximately this ratio. One has doubtless to note that the absolute concentrations in the precipitation experiments were two orders of magnitude higher than in the tank water due to the need of substance for analysis purposes. For comparison, the precipitation and binding experiments were also performed *Bg*-AChBP2.

For the conducted precipitation studies by direct mixing of sodium hydrogencarbonate and mixtures of the discussed bivalent ions with recombinant protein (pentamers for *Bg*-AChBP1 and *Bg*-AChBP2), similar ion proportions as in the snail tank water have been chosen. In case of a Ca:Mg ratio of 94:6 % at 0.1 M concentration of calcium, the formation of aragonite was completely suppressed if 0.43 $\mu\text{mol/L}$ *Bg*-AChBP1 was present, whereas in the control (omitting the protein) only 10 % of the material did not form aragonite (Figure 3.30). The reason is assumed to be under protein free conditions, formed aragonite is meta-stable compared to calcite the surficial concentration relation of Ca/Mg is almost 100 % Ca for all

cases. In contrast, for a Ca:Mg ratio of 89:11 %, in the protein-free precipitation an almost 50:50% mixture of both calcite and aragonite forms (for microscopy images of precipitates see Figure S 3.44, Supporting Information). But if protein is present during precipitation under 89:11 % ratio of calcium to magnesium ions the dissolution of formed aragonite in direct precipitation experiments over 72 h is inhibited by *Bg-AChBP1* compared to the control without protein. The polymorph of the precipitated crystals is almost pure aragonite in the case of the Ca:Mg ratio of 89:11 % with *Bg-AChBP1* and 85:15 % calcite to aragonite forms in the case of *Bg-AChBP2*, but as long as this protein is not present during *in vivo* precipitation it should not play a biological role in shell growth. For the final concentration of Ca^{2+} and Mg^{2+} ions of the bulk mineralized CaCO_3 , AAS measurements revealed that 2.5% of the bivalent cations integrated to be Mg^{2+} in case of *Bg-AChBP1* presence and 4.0 % in case of *Bg-AChBP2* presence. This indicates that from these closely related proteins, *Bg-AChBP1* is optimized for its role in shell growth. Furthermore, only in combination with *Bg-AChBP1* the surficial Mg^{2+} content is increased to 4.0 %. Apparently, this protein causes surface enrichment of magnesium ions which triggers effective stabilization by surficial attachment to aragonite crystallites.

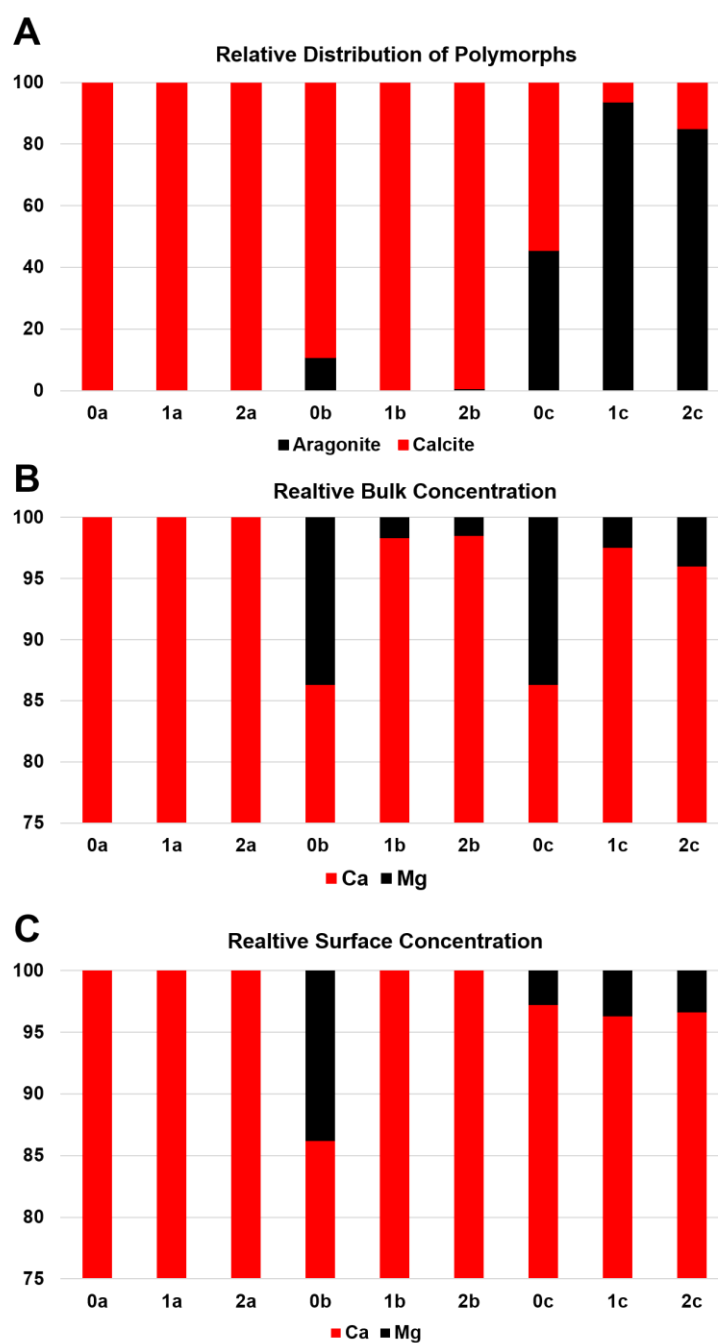


Figure 3.30: Calculations for relative polymorph contributions from (A) XRD and the bulk and surface concentrations from (B) AAS and (C) XPS. (A) Relative contribution of aragonite and calcite polymorph from Rietveld refinement of XRD data of precipitates from precipitation for 72 h at room temperature with (a) no addition of magnesium ions (b) ratio of 94.1% calcium to 5.9% magnesium (c) ratio of 88.9% calcium to 11.1% magnesium. Each of the samples have been precipitated either with no protein added (0), 0.4 $\mu\text{mol/L}$ of *Bg*-AChBP1 added (1) or 0.4 $\mu\text{mol/L}$ of *Bg*-AChBP2 (2) added. (B) Relative concentrations of calcium and magnesium ions of in 0.1 M acetic acid diluted precipitates from bulk AAS. (C) Relative concentrations of calcium and magnesium ions on the surface of precipitates from XPS analysis. For IR spectra see Figure S 3.42, XPS data see Figure S 3.43 and for light microscopy images see Figure S 3.44 of the Supporting Information.

To ensure that binding of *Bg*-AChBP1 to a specific polymorph is favored, a polymorph-selective pulldown assay has been conducted. This assay showed the strongest binding to ACC and vaterite as preliminary polymorphs on the pathway to aragonite which has in comparison to calcite as the thermodynamically stable polymorph a higher *Bg*-AChBP1 affinity (Table 3.1). This seems to be the central point why *Bg*-AChBP1 stabilizes aragonite as crystalline phase at this high ratio. Once a seed of aragonite is nucleated in the presence of *Bg*-AChBP1 plus enough Mg^{2+} , the formation of more aragonite is favored over the calcite formation. The present magnesium and *Bg*-AChBP1 is subsequently removed from the aging crystallized $CaCO_3$ material by a fusion process that extracts impurities to ensure phase transition because of good ACC stabilization by *Bg*-AChBP1. [40,41] The amount of magnesium in the bulk aragonite is also down-regulated by this process due to a magnesium solubility of extraneous ions in the mineral. Compared to *Bg*-AChBP1 which is present during the biomineralization process occurring in the snail, the closely related isoform *Bg*-AChBP2 showed an almost equal affinity to calcite and aragonite and has a very strong stabilization effect on $CaCO_3$ phases that tend to be unstable. This might be a general structural feature of AChBP which primarily play a role in regulating synaptic transmission. [21] It appears that some AChBPs, such as the ACCBP in oyster and abalone, [13,23] and *Bg*-AChBP1 in *B. glabrata*, have been optimized for their role in shell growth, and therefore are specifically expressed, in large quantities, in the mantle epithelial cells. From the present precipitation results, a possible protective role of *Bg*-AChBP2 against unwanted $CaCO_3$ crystallization in the brain might be considered in addition. At present, it remains open or not the dodecahedral quaternary structure of *Bg*-AChBP1 supports its role in the biomineralization process, for example by providing a multitude of Ca^{2+} and Mg^{2+} binding sites at nanometer range. This might indeed represent the crucial optimization step compared to *Bg*-AChBP2.

Table 3.1: Polymorph-selective protein pulldown assay. The relative amount in different fractions from the assay of *Bg*-AChBP1 (dodecahedra) and *Bg*-AChBP2 (pentamers) on CaCO₃ polymorphs was measured photometrically (1 OD at 280 nm ~ 1 mg/ml). The mother liquor residue containing the material which was extracted after overnight binding was measured after separation. Subsequent washing with MQ water and 1 M NaCl solution as described in the experimental section ensured the analysis of only strongly CaCO₃-bound protein which was extracted by resolving the pellet in 1 M acetic acid after the last washing step.

Polymorph <i>Bg</i> -AChBP isoform	ACC		vaterite		aragonite		calcite	
	1	2	1	2	1	2	1	2
Mother liquor	6.8%	18.2%	19.6%	9.4%	47.4%	67.6%	29.1%	55.2%
MQ water washing	0%	4.9%	9.3%	3.9%	27.8%	15.7%	58.3%	25.0%
NaCl washing	0%	0%	0%	0%	0%	3.7%	0%	0%
Diluted CaCO ₃	93.2%	77.8%	71.1%	86.7%	24.4%	13.0%	12.6%	19.8%

Bg-AChBP1 is synthesized in the mantle epithelial cells (see Figure 3.28 and Figure 3.29) and then released into the extrapallial fluid and from this oversaturated mixture of all required inorganic and organic components, shell formation is induced. *Bg*-AChBP1 with its binding to ACC might be needed to regulate, together with Mg²⁺ ions, the crystallization process. A specific role of the dodecahedral quaternary structure of *Bg*-AChBP1 might be to keep the formed amorphous precursor in its metastable amorphous state over a longer duration as shown for dodecahedra in Figure S 3.41 of the Supporting Information. Furthermore, the *in vitro* precipitation experiments under simultaneous presence of magnesium ions and *Bg*-AChBP1, and the presence of both components in the matrix, suggest that the protein might also play a role in stabilizing and controlling aragonite crystallization *in vivo*.

3.3.1.4 Conclusion

We have shown by advanced electron microscopy techniques that the snail *Biomphalaria glabrata* precipitates crystalline CaCO_3 in bundles of aragonite that are covered by an amorphous and mainly organic insoluble matrix. The dodecahedral acetylcholine-binding protein *Bg*-AChBP1 has been identified by IR spectroscopy as well as immunofluorescence microscopy as a component of the insoluble matrix. It was shown that recombinant *Bg*-AChBP1 binds to amorphous calcium carbonate (ACC) and stabilizes it in this phase. This has been substantiated in precipitation experiments with Faatz-Wegner ACC kept at 40°C in a climate chamber at 40% relative humidity with and without *Bg*-AChBP1 present during precipitation of ACC.

As we have demonstrated *Bg*-AChBP1 is synthesized in all the larval stages and, in adult animals, in the epithelial cells of the mantle, from which it is secreted into the extrapallial space. The simultaneous presence of magnesium ions within the insoluble matrix has been demonstrated by XPS, AAS, and EDX data. By *in vitro* precipitation experiments, almost 100% pure aragonite (calculated from Rietveld refinement of XRD data) has been formed under simultaneous presence of recombinant *Bg*-AChBP1 and magnesium ions at natural concentrations. In these experiments, CaCO_3 directly precipitated as ordered aragonite instead of forming unspecific mixtures of calcite and aragonite as in the controls omitting *Bg*-AChBP1. Our findings suggest a specific CaCO_3 polymorph stabilizing role of *Bg*-AChBP1 which reminds the role of the structurally related amorphous-calcium carbonate-binding proteins (ACCBP), with the difference that (i) *Bg*-AChBP1 is a pentagonal dodecahedron 25 nm in diameter, composed of 60 subunits, whereas ACCBPs are solitary pentamers, and (ii) *Bg*-AChBP1 is not a typical ACCBP but more closely related to other AChBPs. The binding motive present in the *Bg*-AChBP1 dodecahedron that stabilizes the aragonite phase is still unknown but might be unraveled by comparing it in structural detail to the closely related *Bg*-AChBP2 which turned out to be less efficient in polymorph stabilization. Site-directed mutagenesis of *Bg*-AChBP1 could be used to proof such hypotheses.

3.3.1.5 Supporting Information

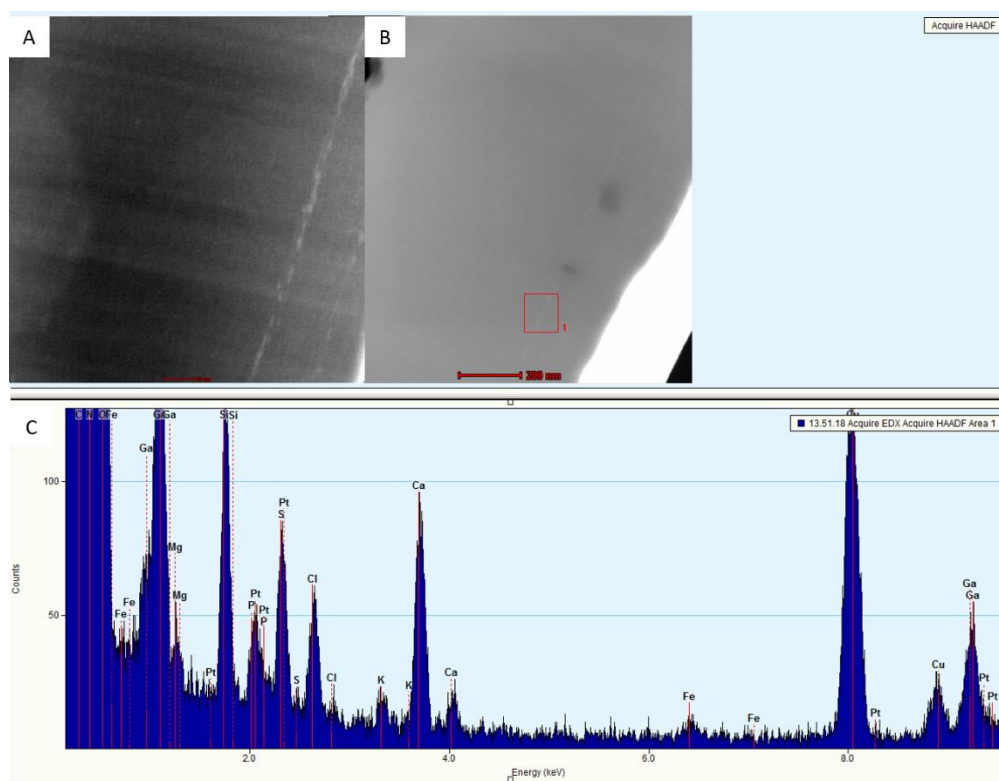


Figure S 3.40: (A) STEM HAADF image of IM of snail shell, light colored areas contain elements of high Z. (B) EDX scan area in amorphous IM. (C) EDX spectrum of area of interest. Presence of protein indicated by high nitrogen signal. Note the existence of Mg in the IM and presence of iron (probably from Hemoglobine) that most likely gives yellow/orange or brown color to the snail shell.

Table S 3.7: Summary of XPS determined elemental composition for the regions outside and inside snail shells.

	Mg	O	Ca	N	C
Out	0.1	24.9	1.9	4.9	68.2
	0.1	24.2	2.0	5	68.7
In	-	22.1	0.2	3	74.8
	-	23.2	0.4	5.1	71.4

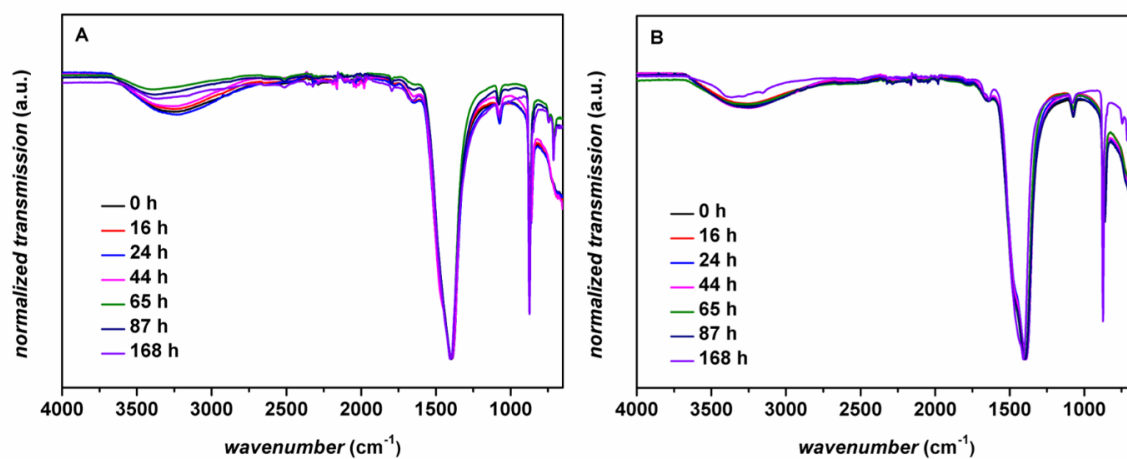


Figure S 3.41: (A) IR-spectra of ACC precipitated without addition and (B) with addition of dodecahedra of *Bg*-AChBP1 by Faatz-Wegner method. ACC sample was kept at 40°C in 40% relative humidity for noted times. ACC to aragonite transformation as usual under such conditions is hindered by absorption of protein on CaCO₃.

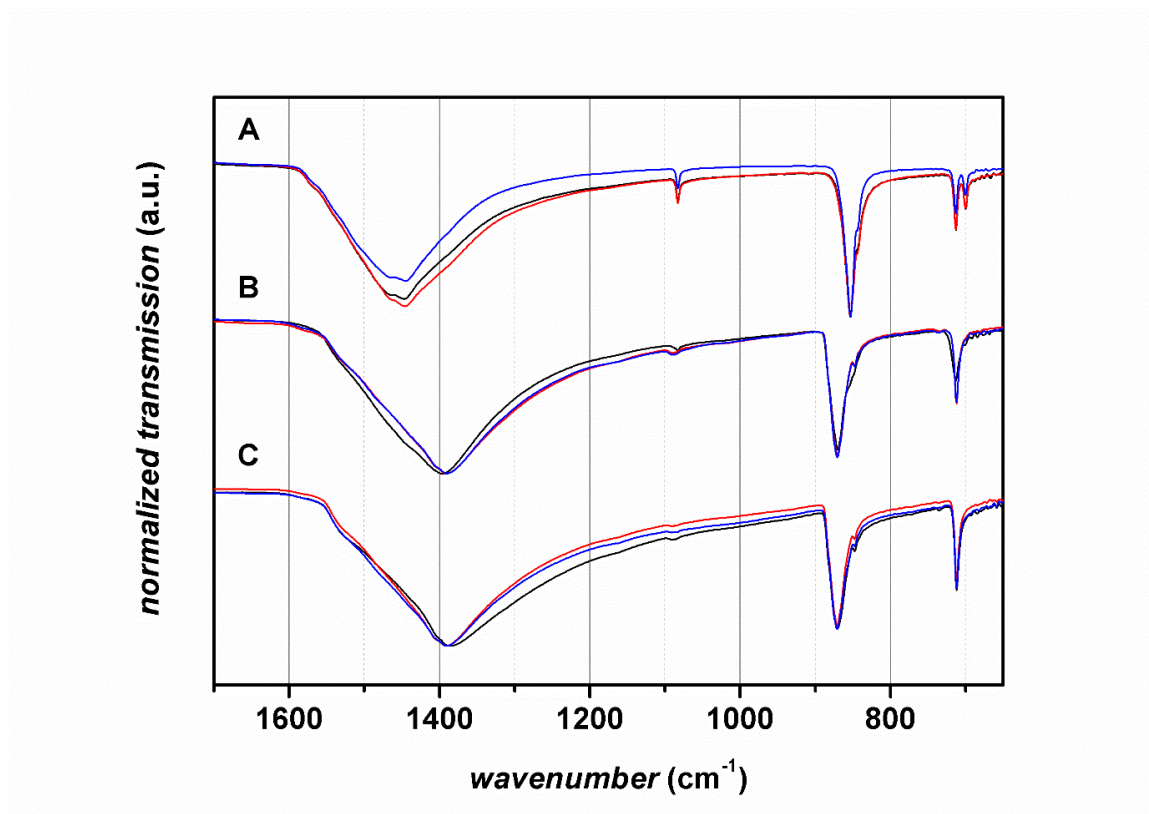


Figure S 3.42: IR Spectra of CaCO₃ precipitated for 72 h with (red) and without (black) pentamers of *Bg*-AChBP1 from a 89:11 % Ca/Mg solution (A), a 94:6 % Ca/Mg solution (B) and pure CaCl₂ solution (C). Addition of magnesium and protein gives pure aragonite while lowering of relative magnesium ion concentration fast changes polymorph to magnesium rich calcite.

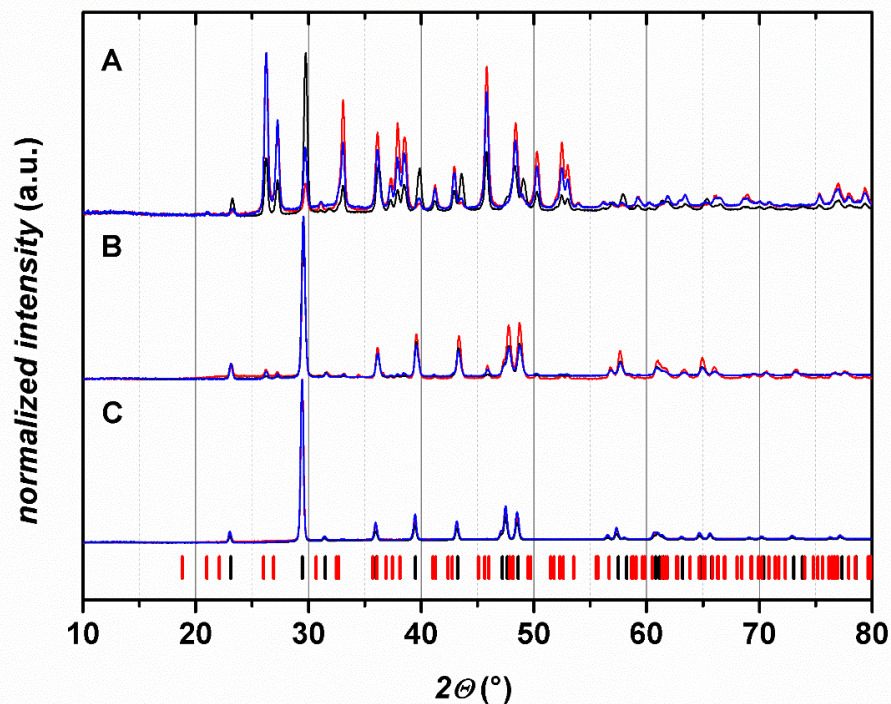


Figure S 3.43: XRD pattern of CaCO_3 precipitated for 72 h with (red, pentamers of *Bg*-AChBP1; blue *Bg*-AChBP2) and without protein (black) from 89:11 % Ca/Mg solution (A), a 94:6 % Ca/Mg solution (B) and pure CaCl_2 solution (C). Addition of magnesium and protein gives pure aragonite (yellow lines) while lowering of relative magnesium ion concentration fast changes polymorph to calcite (green lines). Other phases have been calculated to be lower than 0.01% of total CaCO_3 .

Table S 3.8: XPS elemental composition (%) of direct precipitation of CaCO₃ from Ca:Mg 94:6% with and without addition of no protein, *Bg*-AChBP1 or *Bg*-AChBP2 protein, respectively.

	Mg	Ca
94:6 % no protein	16.2	93.4
	12.5	87.5
	15.2	84.8
	11.3	88.7
94:6 % <i>Bg</i> -AChBP1	0	100
	0	100
	0	100
	0	100
94:6 % <i>Bg</i> -AChBP2	0	100
	0	100
	0	100
	0	100

Table S 3.9: XPS elemental composition (%) of direct precipitation of CaCO₃ from Ca/Mg 89:11 % with and without addition of no protein, *Bg*-AChBP1 or *Bg*-AChBP2 protein, respectively.

	Mg	Ca
89:11 % no protein	2.9	97.1
	2.6	97.4
	2.5	97.5
	3.2	96.8
89:11 % <i>Bg</i> -AChBP1	3.1	96.9
	3.7	96.3
	3.5	96.3
	4.6	95.4
89:11 % <i>Bg</i> -AChBP2	2.4	97.6
	3.5	96.5
	4.2	95.8
	43.4	96.6

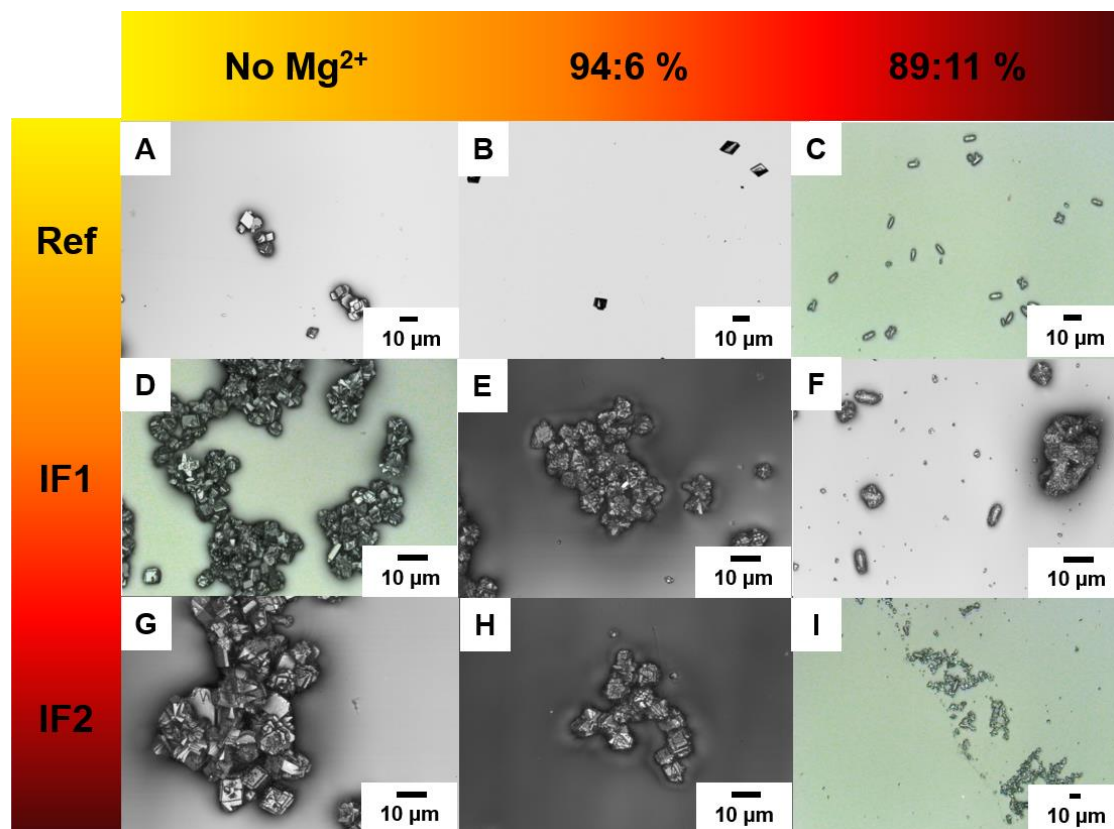


Figure S 3.44: Optical microscopy images from PE vial precipitations of CaCO₃ with and without Mg²⁺ in the absence and in the presence of *Bg*-AChBP1 pentamers (D-F) or *Bg*-AChBP2 pentamers (G-I). Note that polymorph to aragonite results in elongated cigar shaped crystals instead of agglomerated calcite.

3.3.1.6 References

- [1] S. Lin, M. Li, E. Dujardin, C. Girard, S. Mann, *Adv. Mater.* **2005**, *17*, 2553–2559.
- [2] S. P. Mulvaney, M. D. Musick, C. D. Keating, M. J. Natan, *Langmuir* **2003**, *19*, 4784–4790.
- [3] I. Matulaitienė, Z. Kuodis, O. Eicher-Lorka, G. Niaura, *J. Electroanal Chem.* **2013**, *700*, 77–85.
- [4] S. K. Ghosh, T. Pal, *Chem. Rev.* **2007**, *107*, 4797–4862.
- [5] L. J. Lucas, C. Tellez, M. L. Castilho, C. L. D. Lee, M. A. Hupman, L. S. Vieira, I. Ferreira, L. Raniero, K. C. Hewitt, *J. Raman Spectrosc.* **2015**, *46*, 434–446.
- [6] R. C. Kang, Y.-Y. Kim, P. Yang, W. Cai, H. Pan, A. N. Kulak, J. L. Jau, J. DeYoreo, *Nat. Commun.* **2016**, *7*, 10187–10194.
- [7] J. Ihli, P. Bots, A. Kulak, L. G. Benning, F. C. Meldrum, *Adv. Funct. Mater.* **2013**, *23*, 1965–1973.
- [8] D. Gebauer, *Angew. Chem. Int. Ed.* **2013**, *52*, 8208–8209.
- [9] J. Lahiri, L. Isaacs, J. Tien, G. M. Whitesides, *Anal. Chem.* **1999**, *71*, 777–790.
- [10] W. Ostwald, *Grundriss der allgemeinen Chemie*, Verlag von Wilhelm Engelmann, Leipzig, **1890**.
- [11] A. Schreiber, M. C. Huber, H. Cölfen, S. M. Schiller, *Nat. Commun.* **2015**, *6*, 6705.
- [12] T. A. Pham, A. Schreiber, E. V. Sturm, S. M. Schiller, H. Cölfen, *Beilstein J. Nanotechnol.* **2016**, 351–365.
- [13] Z. Ma, J. Huang, J. Sun, G. Wang, C. Li, L. Xie, R. Zhang, *J. Bio. Chem.* **2007**, *282*, 23253–23263.
- [14] A. Rai, C. C. Perry, *Langmuir* **2010**, *26*, 4152–4159.
- [15] S. V. Patwardhan, F. S. Emami, R. J. Berry, S. E. Jones, R. R. Naik, O. Deschaume, H. Heinz, C. C. Perry, *J. Am. Chem. Soc.* **2012**, *134*, 6244–6256.

-
- [16] S. L. P. Wolf, L. Caballero, F. Melo, H. Cölfen, *Langmuir* **2017**, *33*, 158–163.
- [17] H. Cölfen, M. Antonietti, *Mesocrystals and Nonclassical Crystallization*, John Wiley & Sons, Ltd, West Sussex, **2008**.
- [18] M. Schleegeer, M. Grechko, M. Bonn, *J. Phys. Chem. Lett.* **2015**, *6*, 2114–2120.
- [19] M. Rooth, A. M. Shaw, *Phys. Chem. Chem. Phys.* **2006**, *8*, 4741.
- [20] A. Sugawara, T. Nishimura, Y. Yamamoto, H. Inoue, H. Nagasawa, T. Kato, *Angew. Chem. Int. Ed.* **2006**, *45*, 2876–2879.
- [21] M. Merlini, M. Hanfland, W. A. Crichton, *Earth Planet. Sci. Lett.* **2012**, *333–334*, 265–271.
- [22] J. Küther, R. Seshadri, G. Nelles, W. Assenmacher, H.-J. Butt, W. Mader, W. Tremel, *Chem. Mater.* **1999**, *11*, 1317–1325.
- [23] J. Huang, H. Wang, Y. Cui, G. Zhang, G. Zheng, S. Liu, L. Xie, R. Zhang, *Marine Biotech.* **2009**, *11*, 596–607.
- [24] J. Wang, C. Sun, X. Liu, L. Xin, Y. Fang, *Coll. Surf. A* **2014**, *455*, 104–110.
- [25] J. C. Marxen, O. Prymak, F. Beckmann, F. Neues, M. Epple, *J. Mollusc. Stud.* **2008**, *74*, 19–26.
- [26] J. C. Marxen, O. Prymak, F. Beckmann, F. Neues, M. Epple, *J. Mollusc. Stud.* **2007**, *74*, 19–26.
- [27] J. C. Marxen, *J. Mollusc. Stud.* **2003**, *69*, 113–121.
- [28] Y. Luo, L. Sonnenberg, *Cryst. Growth Design* **2008**, *8*, 2049–2051.
- [29] B. Kowalczyk, K. J. M. Bishop, I. Lagzi, D. Wang, Y. Wei, S. Han, B. A. Grzybowski, *Nat. Mater.* **2012**, *11*, 227–232.
- [30] Y. Li, Q. Guo, J. A. Kalb, C. V. Thompson, *Science* **2008**, *322*, 1816–1819.
- [31] A. S. Schenk, B. Cantaert, Y.-Y. Kim, Y. Li, E. S. Read, M. Semsarilar, S. P. Armes, F. C. Meldrum, *Chem. Mater.* **2014**, *26*, 2703–2711.
- [32] J. Ihli, Y.-Y. Kim, E. H. Noel, F. C. Meldrum, *Adv. Funct. Mater.* **2013**, *23*, 1575–1585.
- [33] M. Faatz, F. Gröhn, G. Wegner, *Adv. Mater.* **2004**, *16*, 996–1000.
- [34] J. Su, F. Zhu, G. Zhang, H. Wang, L. Xie, R. Zhang, *Cryst. Eng. Comm.* **2016**.
- [35] D. J. Nelson, T. C. Rains, J. A. Norris, *Science* **1966**, *152*, 1368–1370.

- [36] M. Saur, V. Moeller, K. Kapetanopoulos, S. Braukmann, W. Gebauer, S. Tenzer, J. Markl, E. A. Permyakov, *PLoS ONE* **2012**, *7*, e43685.
- [37] Z. Mao, J. Huang, *J. Sol. State Chem.* **2007**, *180*, 453–460.
- [38] B. Hasse, H. Ehrenberg, J. C. Marxen, W. Becker, M. Epple, *Chem. Eur. J.* **2000**, *6*, 3679–3685.
- [39] M. Bonn, Y. Nagata, E. H. G. Backus, *Angew. Chem. Int. Ed.* **2015**, *54*, 5560–5576.
- [40] T. Ogino, T. Suzuki, K. Sawada, *Geochimi. Cosmochimi. Acta* **1987**, *51*, 2757–2767.
- [41] J. Chen, L. Xiang, *Pow. Tech.* **2009**, *189*, 64–69.

3.3.2 *Bg*-AChBP proteins calcium ion complexation and their effects on CaCO₃ crystallization

This paragraph is also based on my corporation work with Dr. Daniela Treiber from the AG Markl and resulted in the manuscript “*Bg*-AChBP proteins calcium ion complexation and their effects on CaCO₃ crystallization”. The manuscript will be submitted to *Crystal Growth and Design* by the *American Chemical Society*. The following chapter combines the main manuscript and the supporting information.

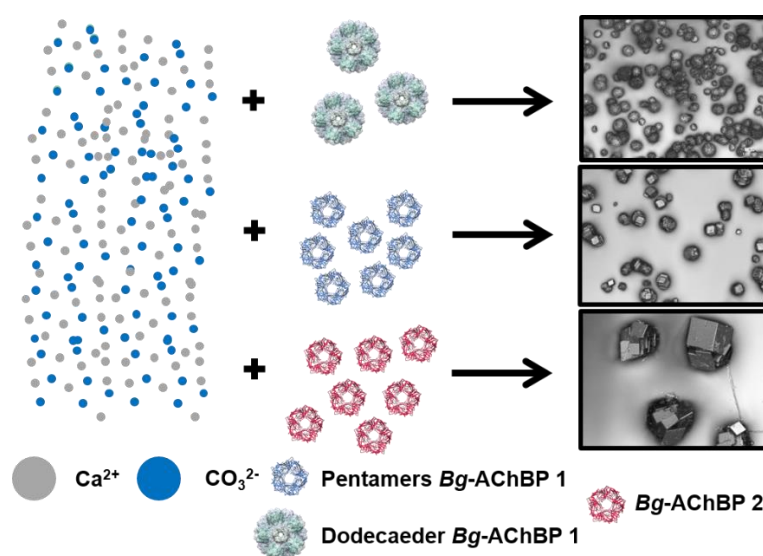


Figure 3.31: Scheme on CaCO₃ protein crystallizations in the desiccator presented in this paragraph.

AChBP proteins of the pondsnail *Biomphalaria glabrata* are relatives of ACCBP, a protein which is known to stabilize amorphous CaCO₃ against crystallization. Hence the origin of this effect has also been observed recently but the influence on the crystallization of CaCO₃ has not been studied to conclude influence on polymorphism of CaCO₃. We want to address this question by studying recombinant *Biomphalaria glabrata* AChBP proteins of two different isoforms, termed *Bg*-AChBP1 and *Bg*-AChBP2. The calcium ion complexation of the proteins is studied by ITC and calcium ion selective electrode measurements and their CaCO₃ crys-

tallization influence by desiccator ammonia diffusion method for CaCO₃ precipitation. The different interaction mechanisms of both isoforms with calcium ions and CaCO₃ mineral are monitored with microscopy and spectroscopy techniques as well as rocking curve measurements of the final precipitates.

3.3.2.1 Introduction

The concept of mesocrystal formation is known for almost twenty years for synthetic materials, but its first discovery in biomineralization was already made in the early 80s of the recent century. [1–6] The ways towards mesocrystal formation are numerous and reach from PILPS [7] over classical amorphous [8] and nano-crystalline precursor [9] stages towards an oriented attachment [10] driven formation of a quasi-single crystal [11] built of micro- or nano-crystalline building blocks. [9,12] For nature the concept of mesocrystal formation is advantageous for mechanical stability of biominerals. The brick-mortar structures of nacre for example have been shown to bear enormous stability in comparison to massive material. [13] Various protein motives seem to be identified to ensure stability of hydrated flexible precursor material and the resulting formation of extravagant structural details. [6,14–18] In contrast to studies on specialized proteins for CaCO₃ precipitation Natalio *et al.* [19] gave an imagination what may happen, if a non-specialized protein is added to the calcium carbonate precipitation. The beforehand introduced amorphous precursor is an intermediate precursor step in the formation of extremely bendable brick mortar structures. While the native spicule is shown to be built from Silicatein- α (a glass sponge protein of *Demospongia domuncula*) [18,20] and nano-crystalline SiO₂ in the synthetic case nano-crystalline CaCO₃ has been observed. [21] The spicule flexibility is caused by a rather weak coordination of CaCO₃ nanocrystals – that subsequently form out of the amorphous precursor – with the protein as mortar. The template of the spicule structure giving element within this system is the Silicatein- α , which agglomerates to fibrous structures, wherein CaCO₃ precipitates. A similar mechanism of aggregation has been observed for the agglomeration of the egg white protein Ovalbumin under presence of calcium ions during the process of egg shell formation. [22,23] Preliminary about three nanometer large proteins form small substructures of 50 proteins by unfolding and interlinking via covalent bonds (e.g.

cystin bridging) or even hydrostatic interactions. Subsequently the substructures agglomerate to about centimeter long fibrils. The crystallization of CaCO_3 has been shown to be inhibited by the additive complexation of calcium ions. A PILP-like precursor phase, ^[7] called liquid amorphous calcium carbonate (LACC), is formed in crystallizations in this publication. ^[24,25] A recent publication on a sea urchin matrix protein has shown the protein driven formation of a so-called bio-hydrogel to be another non-crystalline precursor of biomineralization. ^[26]

The unique fact for nature is that evolution triggered an extraordinary specialization of proteins. ^[27] The acetylcholine binding proteins we focus on in this publication, for example is strongly structurally related to amorphous calcium carbonate binding proteins ACCBP, which have been shown to stabilize calcium carbonate in its amorphous phase (ACC). ^[28,29] The well pronounced stabilization properties are mainly due to the strong binding to calcium ions by the carboxylic acid rich protein sequence that are covered by non-polar regions. ^[21,30] Hence the AChBP class of proteins was postulated to have similar effects besides the property to bind cytotoxins and ensuring neuronal signal transduction. ^[31,32] In Chapter 3.3.1 it was shown that the dodecahedral *Bg*-AChBP1 of the *Biomphalaria glabrata* AChBP has shown a very good ACC stabilization performance and the polymorph aragonite is stabilized with high selectivity during the crystallization. In contrast to that *Bg*-AChBP2, which has an amino acid sequence of almost 52% similar amino acid sequence compared to *Bg*-AChBP1, according to the identity matrix published by Saur *et al.* ^[28] But the proteins seem to have a totally different function within the snail. Histological results (unpublished data) show *Bg*-AChBP2 absence in CaCO_3 enriching or precipitating environment, while the cerebral ganglion is full of *Bg*-AChBP2, which gives the hint that *Bg*-AChBP2 might be responsible for signal transduction and detoxification, but also for effective prevention of urgent tissue calcification. Nevertheless, the effects of *Bg*-AChBP2 on calcium ions and CaCO_3 is needed to be studied to understand the native function of this isoform to support the conclusions of chapter 3.3.1. While this question has already been addressed by the fast precipitating burst nucleation method of mixing calcium chloride and sodium bicarbonate solutions with presence of magnesium ions in chapter 3.3.1 the slow ammonia diffusion method (ADM) for CaCO_3 crystallization is used in this

work to study the affinity and effects of absorption during CaCO_3 precipitation. The binding affinity of pentameric *Bg*-AChBP1 and pentameric *Bg*-AChBP2 for calcium ions is studied by ion selective titrations as well as isothermal calorimetry titrations. Furthermore, analysis for nano-crystallinity of the CaCO_3 precipitates by SEM, HR-TEM and XRD Rocking curve analysis is conducted additionally to understand the influence of the proteins on the CaCO_3 . AFM on calcite (104) facets is used to study the influence of the protein isoform and structure on CaCO_3 reassembly.

3.3.2.2 Experimental

Materials and handling details

All reagents for crystallization and titration experiments were purchased from Sigma Aldrich and were used as received, unless otherwise stated. Quartz glass-slides for crystallization as well as TEM and SEM equipment were received from Plano GmbH, Wetzlar, Germany. For water deionization a water purification setup from Millipore (Millipore GmbH) was used. The quartz glass slides were cleaned by washing with Ethanol, NaOH, MilliQ (MQ) water, HCl and threefold water treatment in an ultrasonic bath for 10 minutes each and subsequent drying under nitrogen flow. All Ca-ISE and ITC titrations were done with volumetric standard solutions purchased from Fluka. For the atomic force microscope (AFM) experiments calcite crystals with a sample size of 4 x 4 mm² were purchased from Korth Kristalle GmbH. The crystals were freshly cleaved and cleaned with a nitrogen flow prior to each experiment. We conducted all in-situ AFM measurements in the frequency modulation (FM) mode using for high-resolution imaging in liquid environment, modified ^[33,34] commercial AFM from Bruker Corporation (MultiMode V with Nanoscope V controller). All AFM images shown were taken at a constant temperature of 28 °C and with a liquid cell from Bruker Nano Surfaces Division. The used cantilevers were gold-coated and p-doped silicon (PPP-NCHAuD, Nanosensors and Tap300GD-G, BudgetSensors) and exhibit a typical eigenfrequency in liquids of 100-150 kHz and a spring constant of ~40 N/m. For all measurements, we kept the oscillation amplitude of the cantilever constant at 1 nm. In all AFM images shown, we display the slow and fast scan direction and the measured channel in the schematics in the upper right corner.

All protein solutions were continuously stored in a 10 mM TRIS buffer at pH 7.5 in a fridge at 7°C to prevent random aggregation.

Instrumentation

Optical Imaging was performed with a confocal Keyence VK8710 laser light microscope equipped with a 658 nm diode laser to get height information of the precipitated samples. Immunofluorescence microscopy was performed on 7 µm cryo

Chapters (Cryotome HM 500 OM, Microm, Waldorf, Germany) according to Schafeld & Markl, 2004 [35]. Rabbit polyclonal anti-Bg-AChBP antibodies were produced by Charles River Laboratories, Kisslegg. Two rabbits were immunized over two months by *Bg*-AChBP1 or *Bg*-AChBP2 injections. The isoform specificity was confirmed by western blot. The *Bg*-AChBP1 antiserum was applied at a solution of 1:250 and the *Bg*-AChBP2 antiserum at a solution of 1:50. Both applied solutions were the result of a serial solution experiment. Images were recorded on a Leitz DM RBD fluorescence microscope (Leica, Wetzlar, Germany).

For scanning electron microscopy (SEM) the calcium carbonate crystals were sputtered with 7.7 nm Au and analyzed using a JEOL-JSM 5610LV (JEOL Ltd., Tokyo, Japan) or FEI Phenom (Hillsboro, OR, USA). Images were acquired with an accelerating voltage of 20 kV or 10 kV respectively.

Titration experiments were carried out using the Tiamo system (Metrohm AG) with pH and calcium ion selective electrode (Ca-ISE). External calibration of the Ca-ISE was done with a four-point calibration with various concentrations of a CaCl₂ solution in a 0,1 M KCl solution. The influence of carbonate species is not paid attention to in this way of calibration. External pH calibration was carried out with standard solutions of pH 4, 7 and 9 purchased from Metrohm. The nucleation titrations were done in a 100 mM carbonate buffer solution at pH 9.75 by subsequent addition of 50 µL/min of a 100mM CaCl₂ solution under continuous addition of 100 mM KOH to keep the pH value constant. Binding titrations with the Tiamo system were facilitated in a TRIS buffer at pH 9.75 with addition of 50 µL/min of a 100 mM CaCl₂ solution as well.

ITC measurements were performed using a NanoITC Low Volume (TA Instruments, Eschborn, Germany) with an effective cell volume of 170 µL. During each experiment 50 µL of salt solution (2 mM CaCl₂ or 2 mM MgCl₂ solution) were titrated into 300 µL of protein solution (0,6 g L⁻¹ for *Bg*-AChBP1 or 0,4 g L⁻¹ for *Bg*-AChBP2 respectively). Furthermore, the same amount of salt solution was titrated into 300 µL of the used buffer for the proteins (20 mM Tris) to determine the solution heat for reference. The number of injections was 25 for each measurement (25 x 2 µL) with 300 s breaks between every injection. Each measurement was carried

out at 25 °C. The integrated heats of solution were subtracted from the integrated heats of every adsorption measurement. The normalized heats were fitted according to an independent binding model to obtain the association constant (Ka), the reaction stoichiometry (n), the reaction enthalpy (ΔH), the entropy (ΔS) and the Gibbs energy (ΔG). Each measurement was repeated three times and the mean value as well as standard deviation for each parameter were calculated. Data evaluation of the ITC measurements was performed using the Nano Analyze Data Analysis Software (Software version 2.5.0) from TA Instruments.

Raman spectroscopy measurements for phase identification were carried out using a confocal HR800 μ -Raman spectrometer by Horiba Scientific with a He-Ne laser at $\lambda = 633,318$ nm and an APD detector. Each spectrum was taken with resolution of 1 cm^{-1} at 16 iterations.

XRD measurements were conducted with a Bruker D8 Discover equipped with a proportional counter and a vacuum stage on a Eulerian cradle. All measurements were facilitated with Cu-K α radiation and a 0.4 mm slit after the X-ray source and in front of the detector. Rocking curve measurements were conducted at the 2θ angle of maximum intensity of the calcite (104) reflex within the Omega angle area of 5° - 24° at 1s measurement time at increments of 0.02° . To ensure calcite is the measured CaCO_3 phase of all samples a 2θ scan around the characteristic 29.4° angle was conducted with 0.02° increments at 1s measuring time.

Synthesis of recombinant proteins

Bg-AChBP1 and *Bg*-AChBP2 were individually expressed in *E. coli*. Plasmids with the construct *Bg*-AChBP1-His-TEV and *Bg*-AChBP2-His-TEV were prepared due to Gateway™ cloning by Vanessa Möller. The Gateway™ pDEST™ 14 vector was used. Both *Bg*-AChBP isoforms were solubilized from inclusion bodies and purified on a nickel column and further processed according to published procedure. [28] For synthesis of dodecahedra of *Bg*-AChBP1 the His-Tag has been cut off using a TEV interface inside the plasmide and the TEV Protease (roboklon GmbH, Berlin). Further purification by size-exclusion chromatography yields much lower concentrated TRIS buffered solutions of pure *Bg*-AChBP1 dodecahedra as shown in Figure S 3.45 A in the Supporting Information, which are even stable in aqueous non-

buffered media (compare Figure S 3.45 B). For His-Tag carrying proteins of *Bg*-AChBP1 and *Bg*-AChBP2 only pentamer assemblies has been found by TEM analysis (see Figure S 3.45 C and D).

Crystallization of CaCO₃ via ammonia diffusion method

Crystallization experiments were carried out using the standard ammonia diffusion method. [36–39] After a short induction time in which the solution starts to (super-)saturate with NH₃ and CO₂ the desiccator atmosphere gets supersaturated with ammonia and carbon dioxide via subsequent thermal decomposition of the excess of ammonium carbonate placed on the bottom of a medium sized desiccator. Crystallization was performed on well-defined quartz-glass slides with a diameter of 13 mm and a thickness of 1 mm placed on the bottom of 5 mL beakers. The beakers were filled with 2 mL of aqueous solutions of 5 mM CaCl₂ and as mentioned amounts of protein additive taking from stock solutions in TRIS buffer from recombinant protein synthesis. The reaction room was covered with perforated Parafilm (Neehan, WI, USA) to prevent external impact by dust or other impurities. The pH of the solution subsequently increased from about 7 to 9.75 during crystallization. The protein pentamer assemblies were shown to be stable over this wide range of pH 7.5 to pH 9.75 in glycine buffer by TEM analysis (see Figure S 3.45 E and F). After 15 h crystallization time the glass-slides were removed from the solution, washed carefully with saturated CaCO₃ solution on both sides to ensure complete removal of ammonium carbonate crystals without inducing dissolution/ recrystallization processes and to remove any unbound protein and dried under air flow.

Binding of fluorescent antibodies on desiccator samples

The final glass slide with CaCO₃ precipitates were prefixed for 20 min in chloroform / methanol (2:1) at 0 °C [40] and then fixed for 10 min. in acetone at -20 °C. The blocking of non-specific binding sites occurred in a 1% BSA in PBST solution for 30 min. at room temperature. The slides were kept within a primary antibody solution for 90 min. and thoroughly washed with PBST. Afterwards they were incubated for 60 min. in a fluorescence secondary antibody solution and washed with PBS. Then rinsed in water to remove the remaining salt and washed in ethanol to evaporate it under nitrogen flow.

3.3.2.3 Results & Discussion

We identify *Bg*-AChBP2 as strong scale inhibiting protein for CaCO_3 crystallizations previously. This gives a hint for a decalcification role in the neuronal tissues of the snail to prevent random crystallization from oversaturated environment. In contrast to that *Bg*-AChBP1 has been identified to have a vaterite stabilization property which might be useful in the shell calcification process the protein is present in. All these findings do have one in common: The effect of binding to bivalent ions or even the influence on the CaCO_3 phase transfer should give a deeper insight into their specific function.

Figure 3.32 A demonstrates calcium ion binding titrations conducted with a pH 7.5 TRIS buffered solution of 0.7 μM concentration. The high binding capacity of *Bg*-AChBP2 pentamers in contrast to *Bg*-AChBP1 pentamers results in an about 43 mol bound calcium ions for each mol of protein and *Bg*-AChBP1 pentamers only 3 mol calcium ions are bound to each mol protein (see Figure 3.32 B for calculated data). ITC measurements of the pentamer *Bg*-AChBP1 with addition of calcium chloride give almost none-detectable heat transfer from binding. For *Bg*-AChBP2 for both experiments heat transfer detection was possible (see Figure 3.32 C for data plots). Besides the pentamers of *Bg*-AChBP1 also the dodecahedra assembly has no calcium ion binding affinity in ITC titrations (data not shown).

Calculations from ITC data revealed for calcium ions an enthalpy driven process is present, while entropy is lost. From ITC the total process is identified to be exothermic and about 30 mol of both cations are bound per mol of *Bg*-AChBP2. This gives the hint that addition of calcium ions caused structural changes for example an unfolding of the protein.

Nucleation titrations with addition of 0.7 μM of both pentamers of *Bg*-AChBP1 and *Bg*-AChBP2, to carbonate buffer at pH 9.75 by continuous addition of CaCl_2 solution give vaterite as first precipitating metastable CaCO_3 phase for all cases (see Figure 3.32 E inlay). The interesting result is the delay of nucleation by several seconds and higher supersaturation achieved for *Bg*-AChBP1 and *Bg*-AChBP2 compared to the reference experiment. This can be caused by complexation of

calcium ions by the proteins or by effective binding of both proteins on the surface of precipitated CaCO_3 . This is shown first by the size inhibition of the crystals (compare scalebars of inlay of Figure 3.32 E) and second by the protein coverage of the vaterite crystals analyzed by IR-spectroscopy (compare Figure 3.32 F).

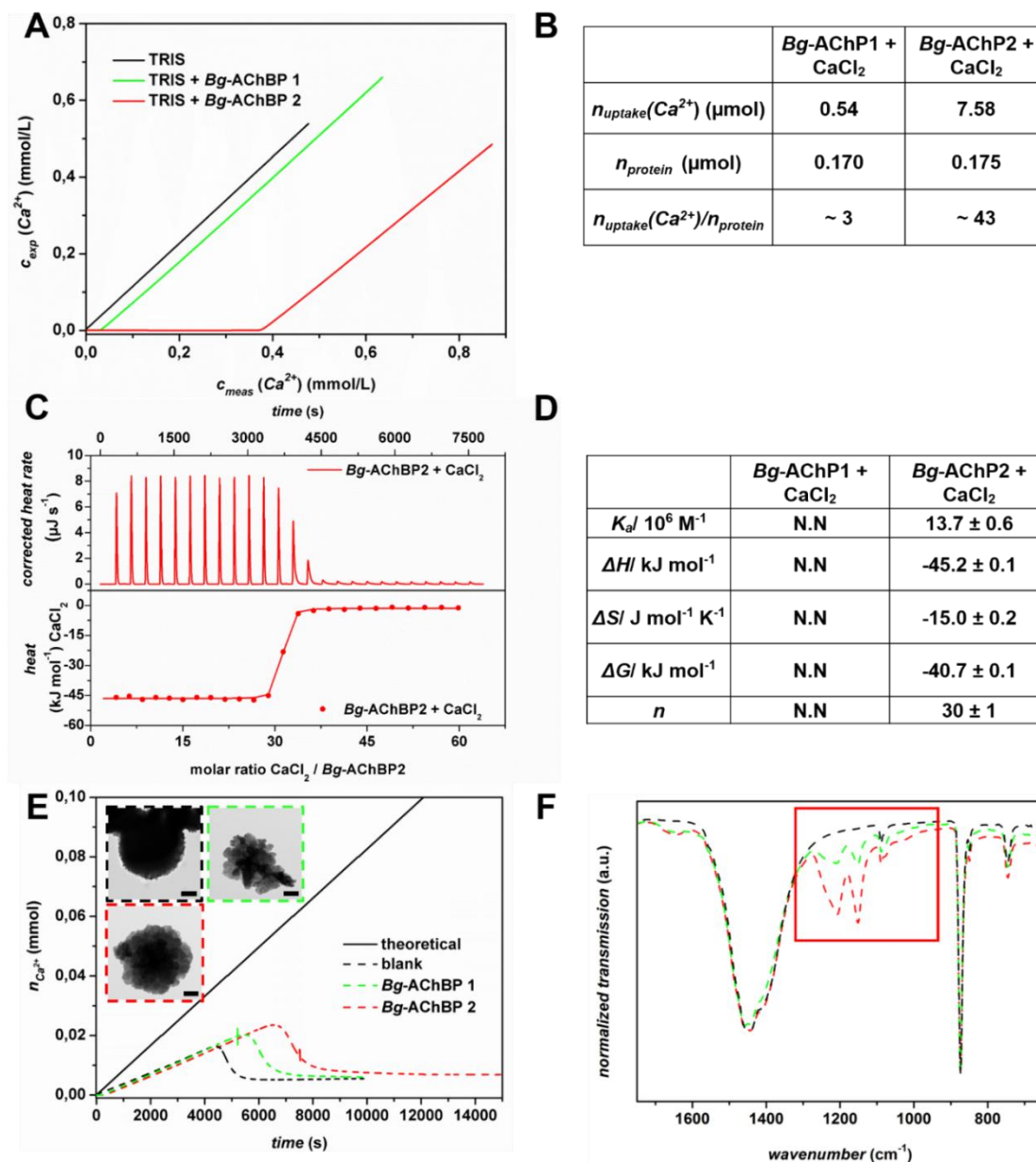


Figure 3.32: (A) Titrations of calcium chloride into a pH 7.5 TRIS buffered solution of pentamer proteins. *Bg*-AChBP1 shows weak complexation of calcium ions while *Bg*-AChBP2 shows coordination properties for calcium ions. Calculated data is shown in table (B). The strong complexation of calcium ions of *Bg*-AChBP2 is underlined by ITC (C, D) to be a strong exotherm enthalpy driven process with a ratio of 30 mol calcium bound to each mole of protein which also points to a hydrogel type formation of protein and CaCl_2 . The discrepancy of Ca-ISE and ITC measurements is due to the different way of detection. (E) Nucleation titrations in carbonate buffer at pH 9.75 by successive

addition of CaCl_2 under absence of protein (black), presence of $0.7 \mu\text{M}$ *Bg*-AChBP1 (green) or *Bg*-AChBP2 (red). TEM images inlay (scalebar for blank 500 nm, *Bg*-AChBP1 200 nm and *Bg*-AChBP2 100 nm) show strong size inhibition of vaterite products, if protein is added. The inhibition of *Bg*-AChBP2 is two times more effective as for *Bg*-AChBP1. This might be caused by a strong absorption of protein on the solid material that is precipitating as shown in IR spectra (F). The binding of protein to the vaterite from nucleation titrations is in correspondence to the elsewhere published data of the binding assay on CaCO_3 polymorphs.

AFM measurements of TRIS buffered protein solutions of pentameric *Bg*-AChBP1 on freshly cleaved (104) calcite crystals at neutral pH show unspecific aggregation and absorption on the step edges and on the flat surface of the crystal (see Figure 3.33 (A-C)). The observed aggregates have variable sizes from about 1 nm to aggregates of 5 nm height and 120 nm diameter, which are aggregates of pentameric *Bg*-AChBP1 structures (compare sizes in TEM Figure S 3.45 C, Supporting Information). For the dodecahedral assembled *Bg*-AChBP1 proteins homogenous, about 50 nm diameter aggregates with an AFM analyzed height of 9 nm, can be identified (see Figure 3.33 D-F and Figure S 3.45 A and B, Supporting Information). For the pentamers of *Bg*-AChBP2, for which high binding capacity to bivalent earth alkali ions have been demonstrated, the kinks of the CaCO_3 crystal have found to be completely saturated with about 14 nm thick and 1 nm high protein layers of obviously unfolded non-assembled protein strands (compare TEM images for sizes of pentamers Figure S 3.45 D). This is another indicator for the occurring structural change to be an unfolding by binding of calcium ions, as it was measured in isothermal calorimetry titrations.

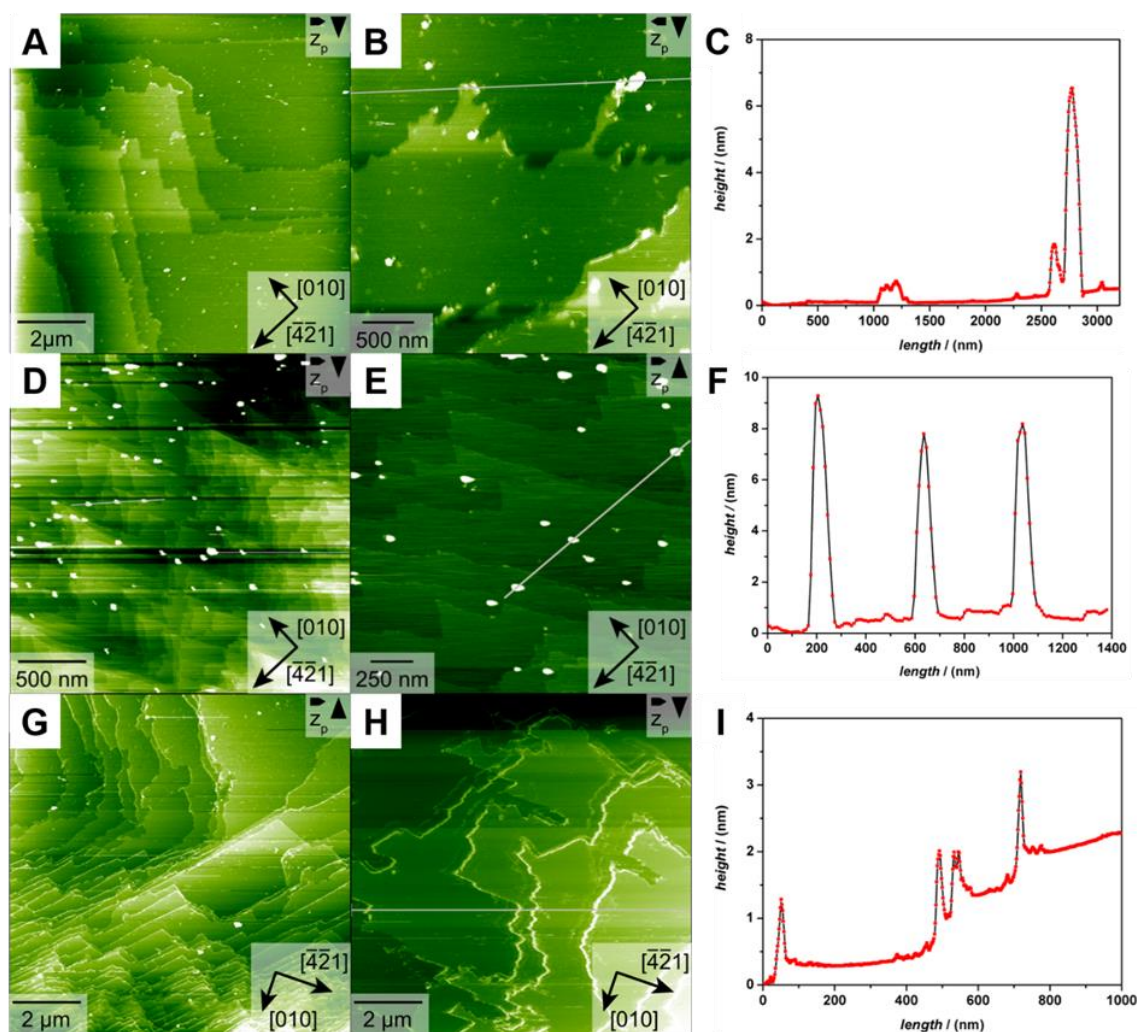


Figure 3.33: The nano-structure of a typical CaCO_3 crystal (104) surface after addition of 0.2 g/L pH 7.5 TRIS buffered pentameric *Bg*-AChBP1 protein solution is added (A) with a detailed view (B) and its height profile (C). Large and small agglomerates can be found. The large agglomerates are multiple pentamers clustered (5 nm in height and about 120 nm diameter). Attachment of agglomerates is non-specifically along various directions. Overview of dodecahedral assemblies of *Bg*-AChBP1 proteins assembled on a freshly cleaved (104) calcite (D). A closer look to very uniform clusters on the CaCO_3 surface after adding a 0.19 g/L pH 7.5 TRIS buffered solution is shown in (E). The scale of the clusters is about 9 nm in height and 50 nm in diameter as calculated from (F). Image (G) gives an overview on surface of a (104) calcite after addition of 0.2 g/L pH 7.5 TRIS buffered solution of pentameric *Bg*-AChBP2 protein showing absorbed protein on all polar kinks of calcite. This indicates a very strong interaction with the CaCO_3 substrate by obvious unfolding as shown by maximum 1 nm height and maximal 14 nm layer thickness on the kinks (I).

AFM measurements identified important differences of the *Bg*-AChBP1 whether its pentameric or dodecameric form is added to CaCO_3 . The introducing sketch reveals that different structural assemblies and *Bg*-AChBP protein sequences have different crystalline products in desiccator ammonia diffusion method precipitation

of CaCO_3 for 15 h. The thermodynamically stable product calcite is the normally observed CaCO_3 polymorph in this experiment after a 15 h precipitation (see Figure S 3.46 (A), Supporting Information).

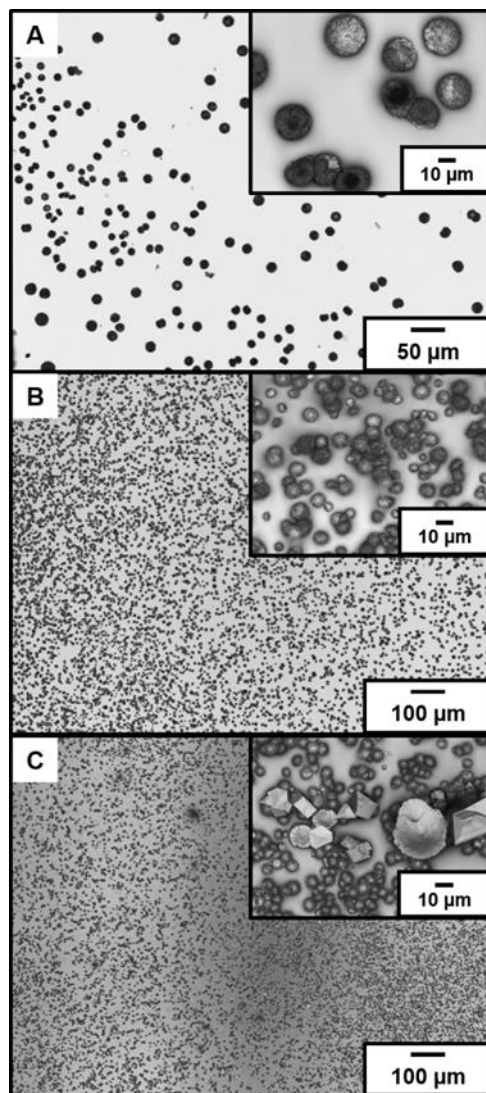


Figure 3.34: CaCO_3 crystals precipitated via desiccator ADM CaCO_3 precipitation experiment for 15 h with dodecahedral *Bg*-AChBP1. Large spherical crystals assemble when 0.2 μM protein is added (A). With increasing protein concentration 0.4 μM (B) to 0.8 μM (C), the size of the major product decreases while vaterite is the phase of the product, as proven by Raman data in Figure S 3.47, Supporting Information. Subsequent phase transformation to calcite occurs within a year as shown by XRD data in Figure S 3.53, Supporting information.

The optical microscopy images shown in Figure 3.34, present an increasing glass slide crystal coverage and simultaneous decreasing size of the crystals upon increasing concentrations of dodecahedral *Bg*-AChBP1. Raman spectroscopy of

crystals precipitated with 0.8 μM protein added (see Figure S 3.47, Supporting Information), identifies the polymorph to be vaterite and furthermore proves CaCO_3 surface to be covered with protein for the dodecahedral case by amide bound appearance. The XRD measurements conducted after half a year show the vaterite transformed to calcite phase. Vaterite undergoes a slow phase transition under keeping the crystals morphology (see Figure S 3.52 Supporting Information). In Figure 3.35 A, C and E the influence of 10 μM pentameric *Bg*-AChBP1 protein added in a similar precipitation of CaCO_3 . The thermodynamic stable phase calcite forms in in this case and a lot of the protein material is precipitated around the along c-axis elongated CaCO_3 crystals (see Figure 3.35 A, C, E). The effect is subsequently strengthened by increasing the amount of protein added (see Figure S 3.48). Besides the formation of multiple step edges a size termination in comparison to the reference crystals (compare Figure S 3.50, Supporting Information) is also occurring for the *Bg*-AChBP1 case.

In contrast *Bg*-AChBP2 addition triggers multi-domain crystals grown on precipitated protein/ACC composite without size termination (see Figure S 3.50, Supporting Information). On the crystals the precipitated protein can be identified by optical microscopy (see Figure 3.35 B) and immunofluorescence (see Figure 3.35 D, F). The number of crystals on the glass slide is much smaller for the *Bg*-AChBP2 case than for the pentamer *Bg*-AChBP1 case, which might be due to the good complexation properties for calcium ions. The unfolding of the protein induced by calcium ion interaction might result in a weaker solution stability that also entails a precipitation of protein molecules during formation of CaCO_3 . In both cases the first precipitated phase from crystallization is the calcite phase (see Figure S 3.49, Supporting Information for Raman Spectra) as thermodynamically stable phase (see Figure S 3.46, Supporting Information for references).

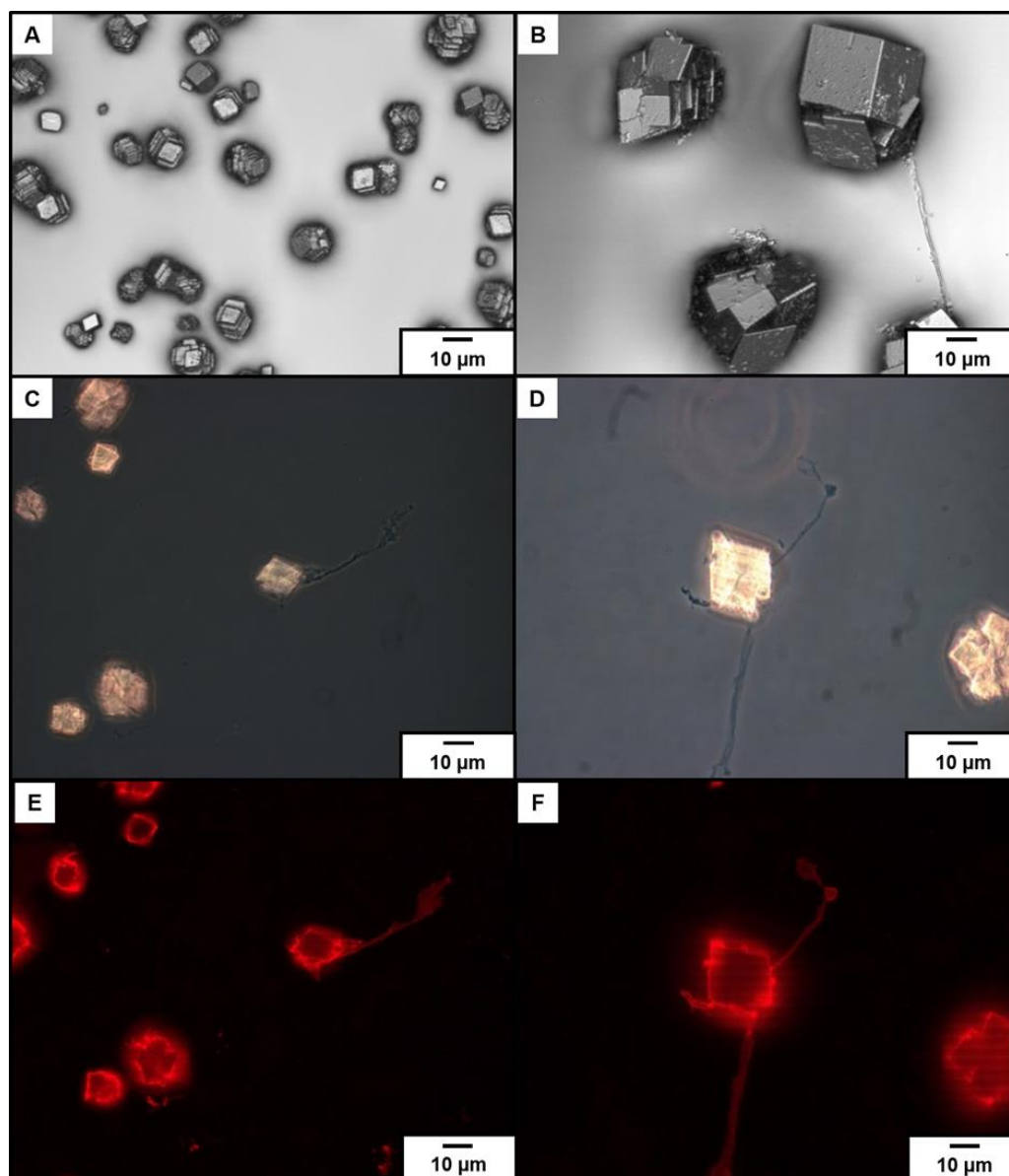


Figure 3.35: CaCO_3 crystals precipitated via desiccator experiment for 15 h with 10 μM pentameric *Bg*-AChBP1 (A, C) and 10 μM pentameric *Bg*-AChBP2 (B, D). Immunofluorescence imaging with selective antibodies for *Bg*-AChBP1 (E) and *Bg*-AChBP2 (F) is showing absorption of both proteins on polar calcite facets.

For *Bg*-AChBP1 pentamers the formation of nano-crystalline calcite crystals is identified by peak broadening in Raman spectroscopy signals (see Figure S 3.51 (A), Supporting Information) and large mosaicity background in rocking curve measurements (see Figure S 3.54 and Table S 3.11, Supporting Information). The smaller average crystallite size calculated by using the Scherrer-Equation for the (104) reflection of the 2θ scan (see Figure S 3.53 and Table S 3.10, Supporting

Information), is a hint for inclusion of protein. For *Bg*-AChBP2 pentamers addition a crystalline material with small mosaicity is formed (see Figure S 3.51(A), Supporting Information for Raman) as indicated by rocking curve measurements (see Figure S 3.54 and Table S 3.11, Supporting Information).

3.3.2.4 Conclusion

The function of both isoforms of *Bg*-AChBP proteins has been studied superficial in literature but only postulated assignments for protein tasks in the snail have been made so far. Until now no isoform specific function announcement has been tried so far. From the presented data first estimations on the proteins *in vivo* role are possible.

First, the influence of the proteins on the crystallization of CaCO_3 has its origin in the calcium complexing properties of both isoforms. While pentamers of *Bg*-AChBP2 inhibits growth of CaCO_3 very effectively, the *Bg*-AChBP1 protein works as a nucleation site for CaCO_3 crystallization, but only shows weak calcium complexation. While usually after 15 h calcite is formed from ADM precipitations *Bg*-AChBP1 presence leads to formation of vaterite. This might be due to a strong surface coverage of the calcium rich (010) facet of the crystals with protein. Doubtless the strong interaction of the surface of precipitated CaCO_3 with *Bg*-AChBP1 proteins might also have its origin in strong protein to carbonate interactions that need to be studied in future work. As mentioned beforehand in contrast to *Bg*-AChBP1, *Bg*-AChBP2 has been identified in our recent work to be absent in all mantle close tissues and the shell. The presence in non- CaCO_3 -forming tissues inside the snail neural tissue may have the reason to lower the risk of urgent CaCO_3 as precipitation is minimized very effectively by the presence of little amounts of *Bg*-AChBP2 protein in oversaturated moieties due to its demonstrated complexation properties.

3.3.2.5 Supporting Information

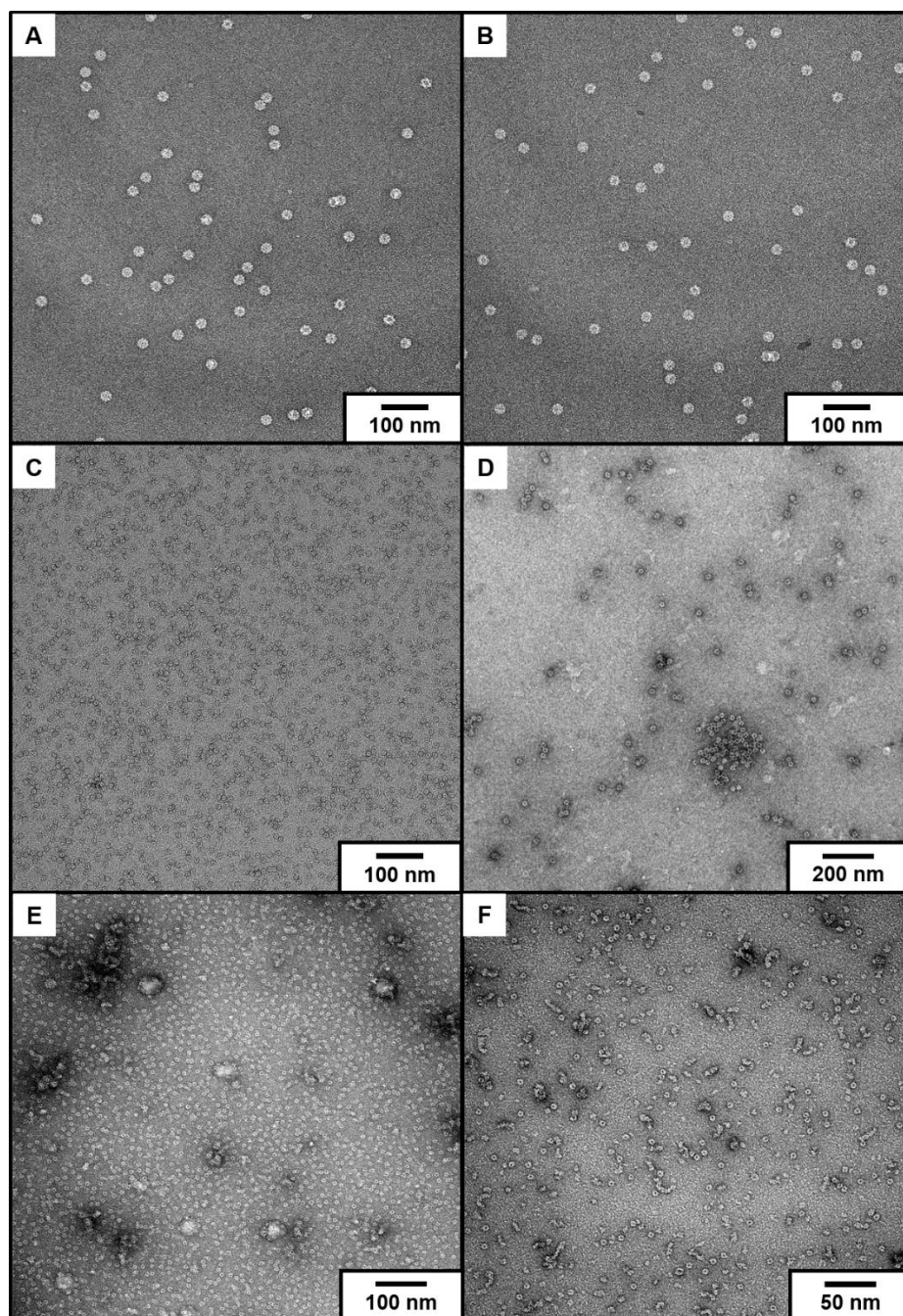


Figure S 3.45: TEM images of proteins prepared with negative staining with uranyl acetate. (A) recombinant *Bg*-AChBP1 dodecahedra after controlled cleavage of the His-Tag by using TEV protease in pH 7.5 TRIS buffer (B) *Bg*-AChBP1 dodecahedra in pure MQ water. (C) Recombinant *Bg*-AChBP1 pentamers with attached His-Tag and (D) recombinant pentameric *Bg*-AChBP2 without His-Tag. (E) and (F) both show pentameric *Bg*-AChBP1 from glycine buffer at pH 7.5 and 9.6 respectively indicating pentamer stability.

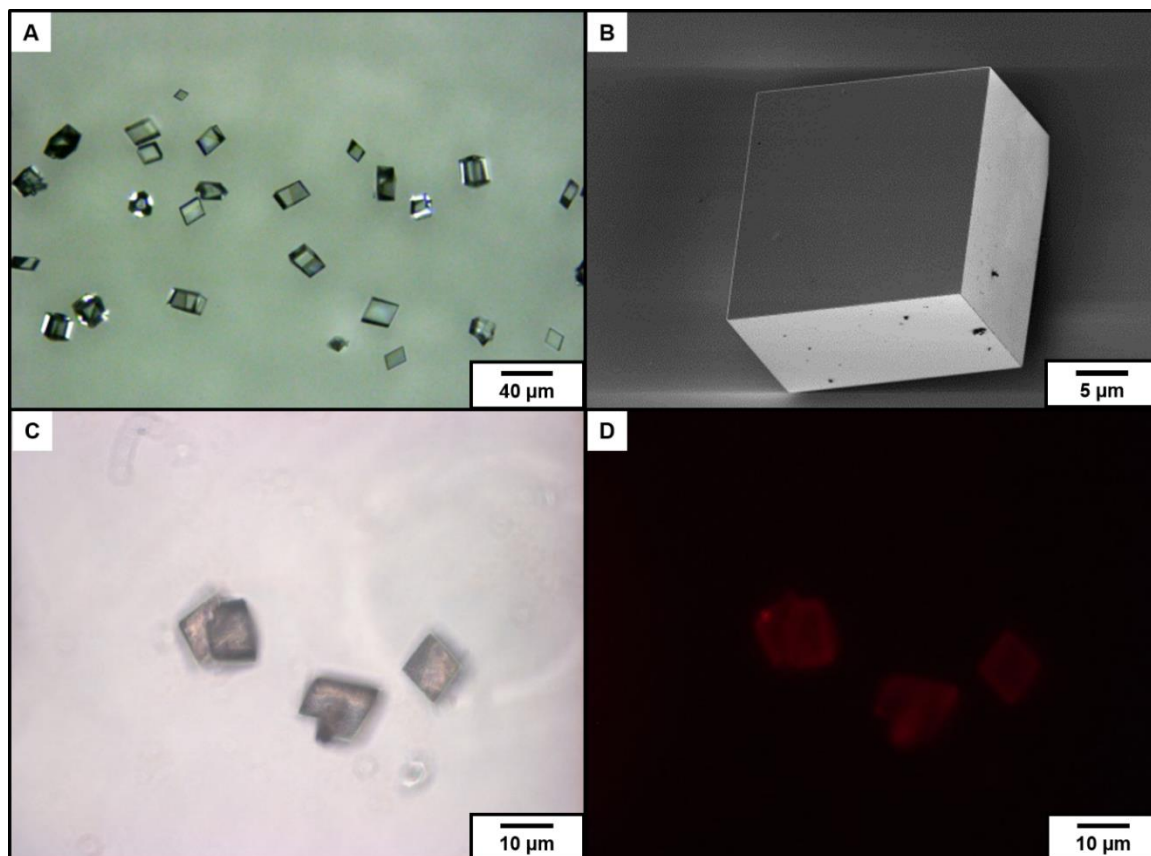


Figure S 3.46: CaCO_3 crystals precipitated without additive in a desiccator crystallization for 15 h (A) optical microscopy image, (B) SEM micrograph zoom-in to typical rhombohedral shape (C,D) contrast and fluorescence image of calcites after adding fluorescent antibodies for *Bg*-AChBP1 and *Bg*-AChBP2.

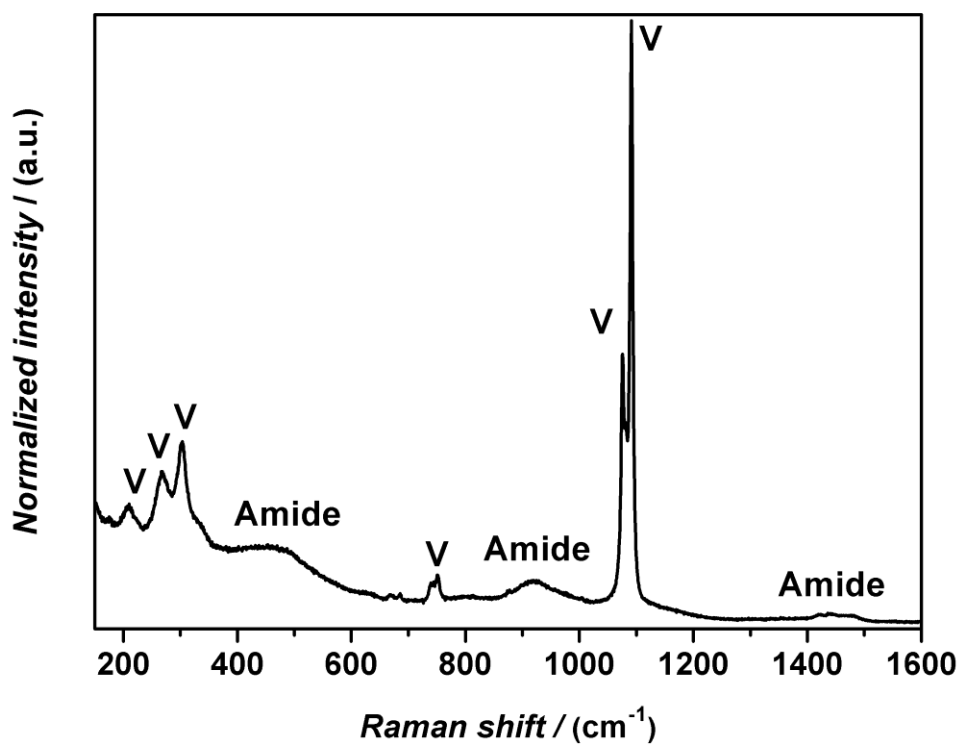


Figure S 3.47: Exemplary Raman spectrum of vaterite crystals precipitated if 0.8 μM of dodecahedral *Bg*-AChBP1 was added. Besides the characteristic vaterite Raman modes named (V) the amide Raman modes of the protein identify surface coverage with the protein.

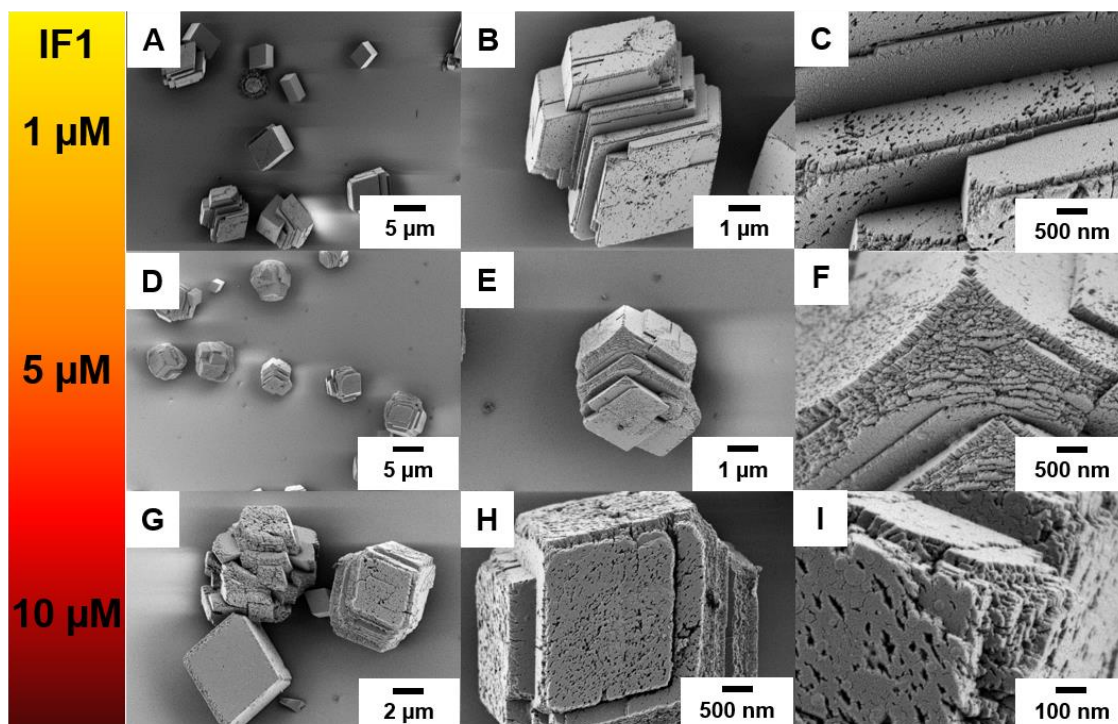


Figure S 3.48: A-I: SEM images of CaCO₃ crystals from desiccator experiment after 15 h. The total crystal size decreases with increasing amount of pentameric *Bg*-AChBP1 protein added from 1 μM (A-C) over 5 μM (D-F) to 10 μM (G-I). The crystals are in general much smaller than the reference sample crystals in Figure S 3.46. The nano-crystallinity and step edge formation is pronounced for *Bg*-AChBP1 samples.

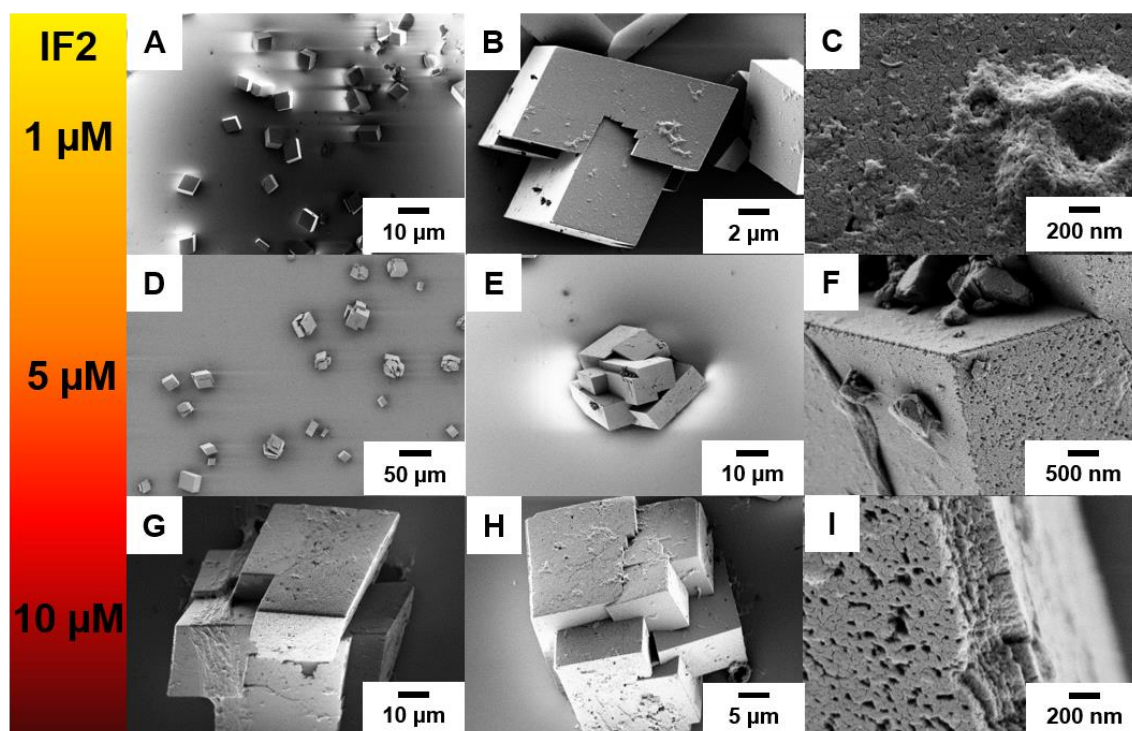


Figure S 3.49: A-I: SEM images of CaCO_3 crystals from desiccator experiment after 15 h. The total size decreases with increasing amount of pentameric *Bg*-AChBP2 protein added from $1 \mu\text{M}$ (A-C) over $5 \mu\text{M}$ (D-F) to $10 \mu\text{M}$ (G-I). The nano-crystallinity and step edge formation are less pronounced for these samples compared to *Bg*-AChBP1 samples. ACC/protein aggregates as shown in AFM are especially visible in C and G. The solubility of *Bg*-AChBP1/ACC that forms as early phase is higher in water than for the *Bg*-AChBP2/ACC. The size of the precipitated crystals is much larger than for *Bg*-AChBP1.

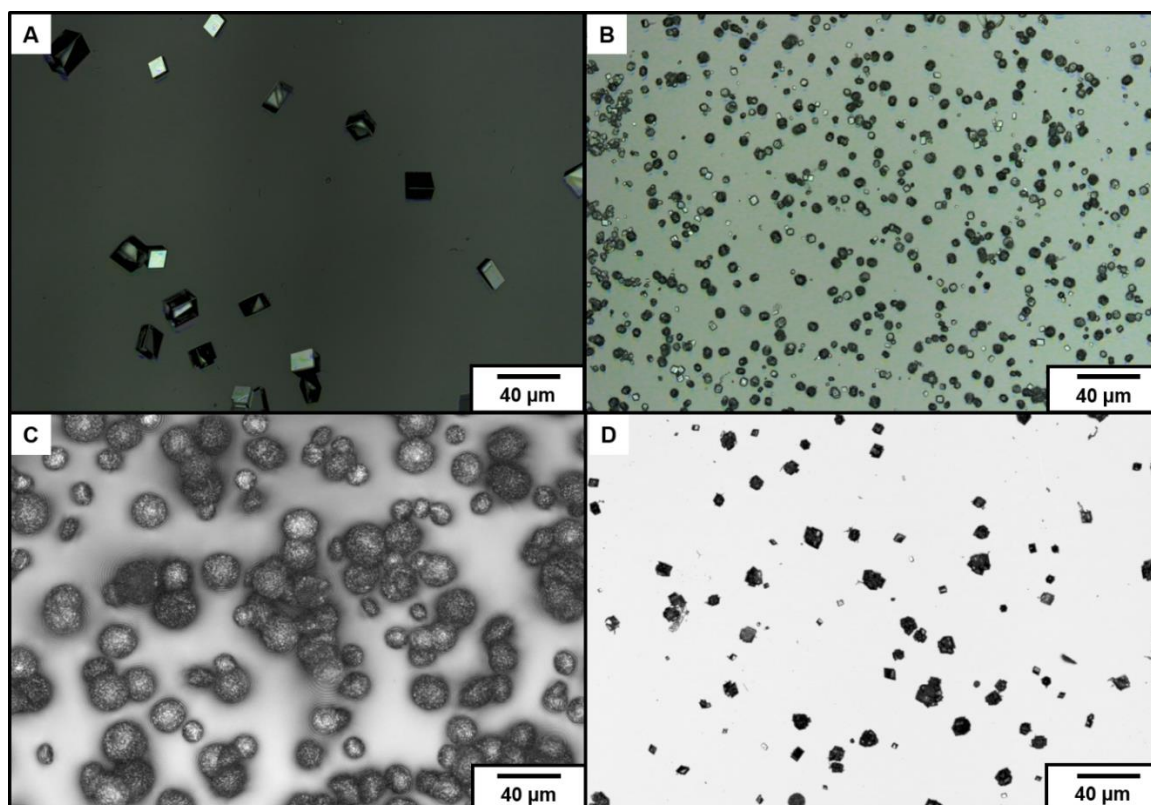


Figure S 3.50: Optical microscopy images of glass-slides covered with CaCO_3 crystals precipitated (A) without adding protein (B) with addition of 10 μM pentameric *Bg*-AChBP1 (C) addition of only 0.8 μM of dodecahedral *Bg*-AChBP1 and (D) with addition of 10 μM pentameric *Bg*-AChBP2. The average size of *Bg*-AChBP2 and reference crystals as well as the slide coverage is almost similar while for pentameric *Bg*-AChBP1 (B) the crystals is much smaller, but the total number is larger. For the dodecahedral *Bg*-AChBP1 (C) only vaterite as metastable preliminary phase with broad size distribution can be found.

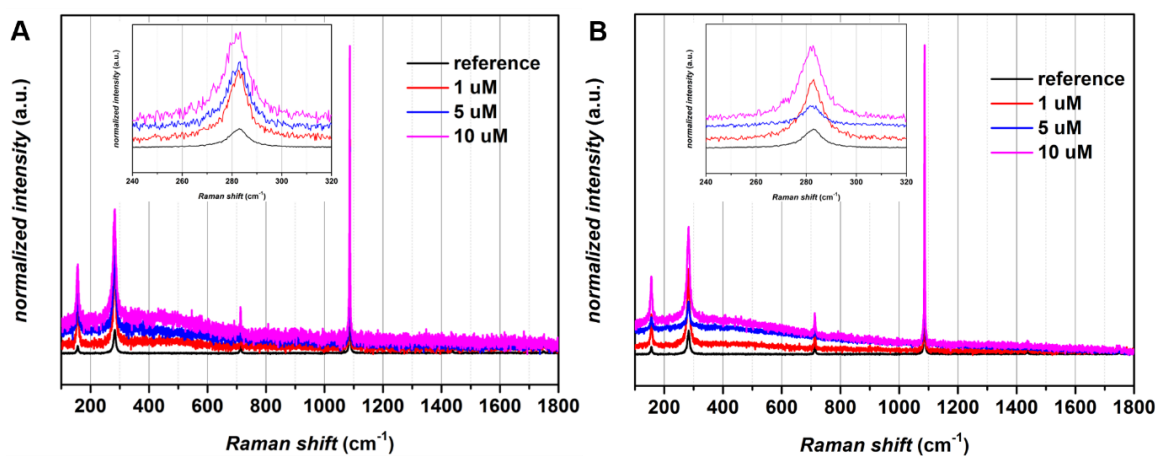


Figure S 3.51: Raman spectroscopy of CaCO₃ crystals on glass slides precipitated with presence of (A) pentamers of *Bg*-AChBP1 and (B) pentamers of *Bg*-AChBP2 protein showing CaCO₃ to be calcite phase and fluorescence indicating presence of surface bound protein. The inlay shows peak broadening and enhancing of the 283 cm⁻¹ band, which indicates nano-structuring of the crystals. For the pentamer *Bg*-AChBP1 case this is already visible for very small amounts of protein (1 μM), while for the pentamer *Bg*-AChBP2 case there is no clear trend.

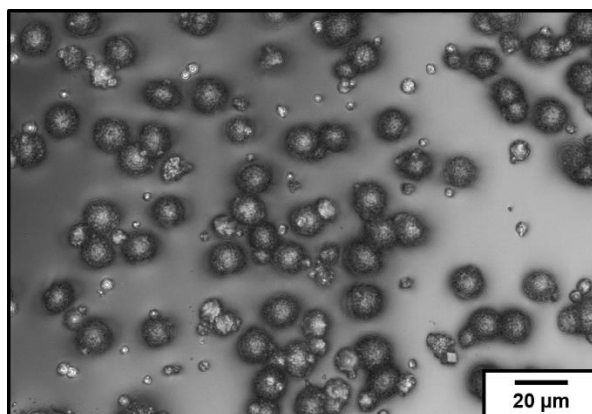


Figure S 3.52: Light microscopy image of CaCO₃ crystals after 1 year of aging (Rocking curve sample). Spherulite structure is still present as shown in Figure 3.35 of the main paper.

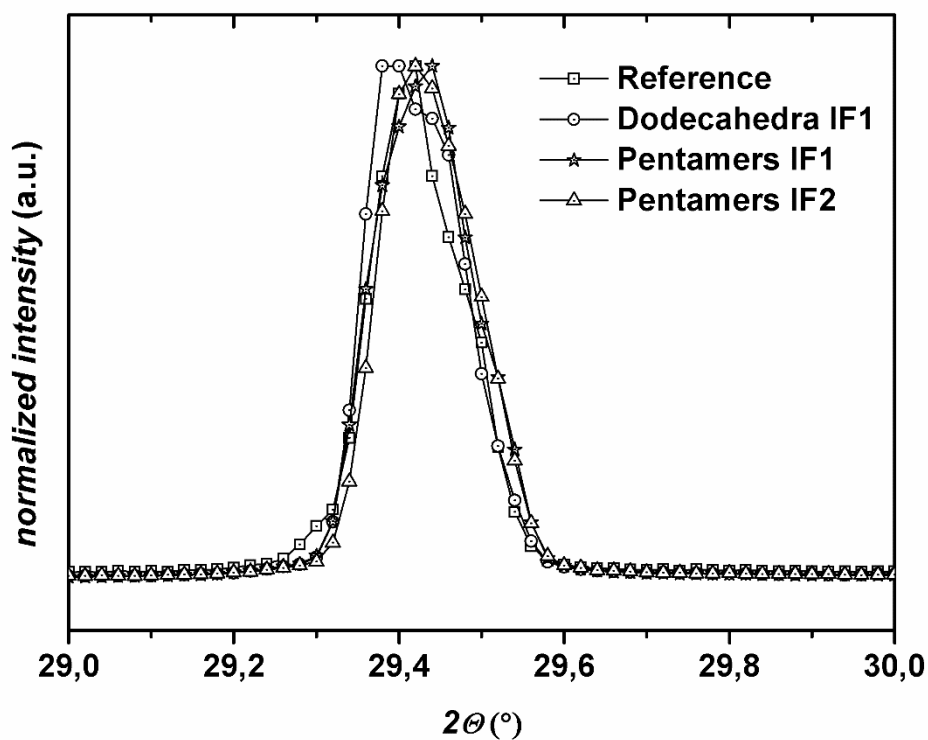


Figure S 3.53: XRD 2θ scan of calcites (104) reflex for different additives added to the crystallizations. For all samples Gaussian fits were used to find the reflex maximum and FWHM for average crystallite size determination shown in Table S 3.10.

Table S 3.10: Calculations for 2θ scans of Reference example and calcite precipitated with μM concentrations of different protein fractions and structures. FWHM tends to be large for added proteins, which results in smaller average crystal size within the mesocrystal assembly under keeping the 2θ value and thus the lattice plane distance fits to reference measurements.

Sample	<i>FWHM</i> (°)	<i>d</i> (nm)	2θ (°)
Reference	0.120	76.1	29.42
Dodecahedra <i>Bg</i> -AChBP1	0.142	65.2	29.41
Pentamers <i>Bg</i> -AChBP1	0.145	63.1	29.43
Pentamers <i>Bg</i> -AChBP2	0.140	64.3	29.42

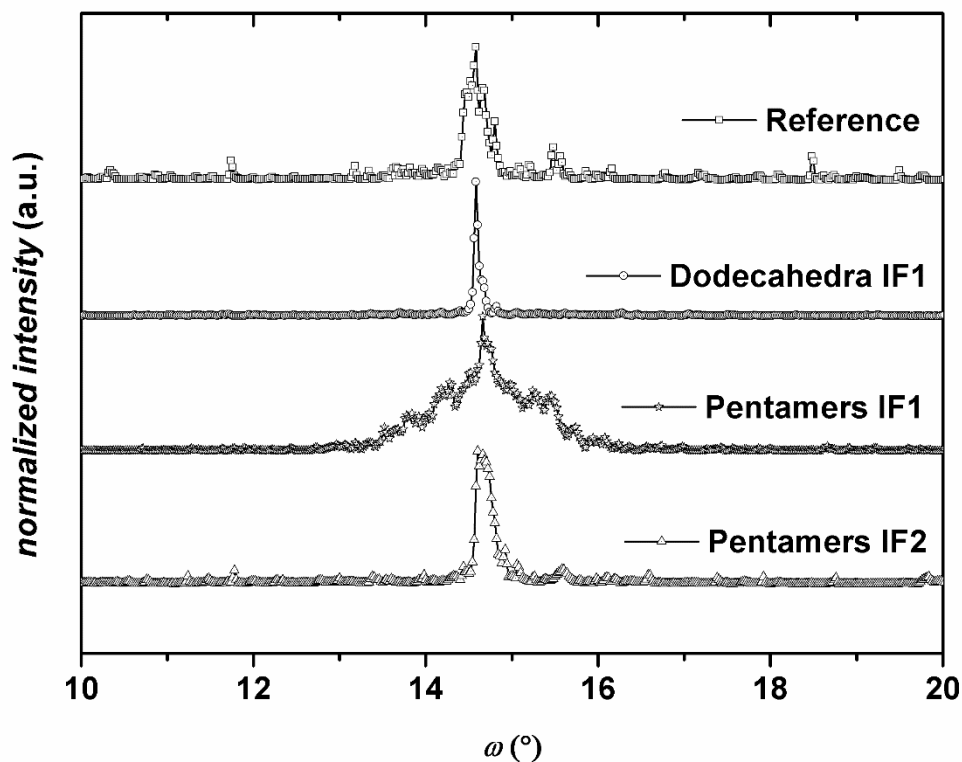


Figure S 3.54: Rocking curve analysis between 10° and 20° ω angle under constant 2Θ angle of 29.42° analyzing the (104) truncated nano-crystals of the mesocrystal. For the reference sample a sharp reflex indicates highly oriented crystallites forming large crystals which are sometimes randomly oriented on the glass substrate (sharp reflexes at various angles). For addition of dodecahedral *Bg*-AChBP1 protein the main reflex even is sharper than the reference sample which indicates low mosaicity of the found spherulite crystals after aging for one year. For the mesocrystal formation if pentamer *Bg*-AChBP1 is added the main reflex broadens and shows a second broad distributed nano-crystal species. If pentamers of *Bg*-AChBP2 are added to the crystallization experiment the rocking curve analysis agrees to some extent with the reference which reveals the protein to have no effect on nano-crystallinity in this case. Together with 2Θ scan data the occlusion of at least some protein is likely for the pentamer assemblies due to increased mosaicity, while the dodecahedral one shows almost no mosaicity.

Table S 3.11: Calculations from Gaussian fits for Rocking curve data. All samples show a single reflex of different FWHM. Addition of dodecahedra of *Bg*-AChBP1 even lowers mosaicity of the calcified vaterite crystals of spherulite structure. Although pentamers of *Bg*-AChBP1 increase mosaicity of the CaCO₃ crystals to polymer even results in a little increase in tilting of crystallites and an increase in mosaicity while *Bg*-AChBP2 pentamers are almost similar in crystallinity as the reference sample grown without additives. For all samples the Omega angle difference is almost zero for all samples.

Sample	<i>FWHM</i> (°)	ω (°)	ω_{theo} (°)	$\Delta\omega$ (°)
Reference	0.261	14.6	14.7	0.1
Dodecahedra <i>Bg</i> -AChBP1	0.145	14.7	14.7	0
Pentamers <i>Bg</i> -AChBP1	0.407	14.6	14.7	0.1
Pentamers <i>Bg</i> -AChBP2	0.226	14.6	14.7	0.1

3.3.2.6 References

- [1] J. Ihli, P. Bots, A. Kulak, L. G. Benning, F. C. Meldrum, *Adv. Funct. Mater.* **2013**, *23*, 1965–1973.
- [2] D. Gebauer, *Angew. Chem. Int. Ed.* **2013**, *52*, 8208–8209.
- [3] S. Patai (Ed.) *Amino, Nitroso and Nitro Compounds and Their Derivatives: Vol. 1 (1982)*, John Wiley & Sons, Ltd, Chichester, UK, **1982**.
- [4] J. Lahiri, L. Isaacs, J. Tien, G. M. Whitesides, *Anal. Chem.* **1999**, *71*, 777–790.
- [5] S. P. Mulvaney, M. D. Musick, C. D. Keating, M. J. Natan, *Langmuir* **2003**, *19*, 4784–4790.
- [6] Marcel L. de Vocht, Karin Scholtmeijer, Eric W. van der Vegte, Onno M.H. de Vries, Nathalie Sonveaux, Han A.B. Wösten, Jean-Marie Ruyschaert, Georges Hadziioannou, Joseph G.H. Wessels, George T. Robillard.
- [7] A. S. Schenk, H. Zope, Y.-Y. Kim, A. Kros, N. A. J. M. Sommerdijk, F. C. Meldrum, *Faraday Discuss.* **2012**, *159*, 327.
- [8] J. Aizenberg, S. Weiner, L. Addadi, *Connect. Tissue Res.* **2003**, *44 Suppl 1*, 20–25.
- [9] R. van de Locht, T. J. A. Slater, A. Verch, J. R. Young, S. J. Haigh, R. Kröger, *Crystal Growth & Design* **2014**, *14*, 1710–1718.
- [10] M. Niederberger, H. Cölfen, *Phys. Chem. Chem. Phys.* **2006**, *8*, 3271.
- [11] L. Bergström, E. V. Sturm, G. Salazar-Alvarez, H. Cölfen, *Acc. Chem. Res.* **2015**, *48*, 1391–1402.
- [12] R. van de Locht, A. Verch, M. Saunders, D. Dissard, T. Rixen, A. Moya, R. Kröger, *J. Struct. Bio.* **2013**, *183*, 57–65.
- [13] P. Fratzl, H. S. Gupta, E. P. Paschalis, P. Roschger, *J. Mater. Chem.* **2004**, *14*, 2115–2123.
- [14] S. Y. Bahn, B. H. Jo, B. H. Hwang, Y. S. Choi, H. J. Cha, *Cryst. Growth Design* **2015**, *15*, 3666–3673.
- [15] K. Gries, R. Kröger, C. Kübel, M. Schowalter, M. Fritz, A. Rosenauer, *Ultramicroscopy* **2009**, *109*, 230–236.
- [16] F. Nudelman, *Sem. Cell. Dev. Bio.* **2015**, *46*, 2–10.

-
- [17] S. Blank, M. Arnoldi, S. Khoshnavaz, L. Treccani, M. Kuntz, K. Mann, G. Grathwohl, M. Fritz, *J. Microsc.* **2003**, *212*, 280–291.
- [18] W. E. G. Müller, M. Neufurth, U. Schlossmacher, H. C. Schröder, D. Pisignano, X. Wang, *RSC Adv.* **2014**, *4*, 2577–2585.
- [19] F. Natalio, T. P. Corrales, M. Panthfer, D. Schollmeyer, I. Lieberwirth, W. E. G. Müller, M. Kappl, H.-J. Butt, W. Tremel, *Science* **2013**, *339*, 1298–1302.
- [20] W. E. G. Müller, U. Schloßmacher, X. Wang, A. Boreiko, D. Brandt, S. E. Wolf, W. Tremel, H. C. Schröder, *FEBS Journal* **2008**, *275*, 362–370.
- [21] M. N. Tahir, P. Theato, W. E. G. Müller, H. C. Schröder, A. Janshoff, J. Zhang, J. Huth, W. Tremel, *Chem. Commun.* **2004**, 2848.
- [22] S. Kim, H.-S. Ryu, H. Shin, H. S. Jung, K. S. Hong, *Mater. Chem. Phys.* **2005**, *91*, 500–506.
- [23] D. Schwahn, M. Balz, W. Tremel, *Physica B* **2004**, *350*, E947-E949.
- [24] K. Rae Cho, Y.-Y. Kim, P. Yang, W. Cai, H. Pan, A. N. Kulak, J. L. Lau, P. Kulshreshtha, S. P. Armes, F. C. Meldrum, J. J. de Yoreo, *Nat. Commun.* **2016**, *7*, 10187.
- [25] R. C. Kang, Y.-Y. Kim, P. Yang, W. Cai, H. Pan, A. N. Kulak, J. L. Jau, J. DeYoreo, *Nat. Commun.* **2016**, *7*, 10187–10194.
- [26] Y. Wang, A. E. Kaifer, *J. Phys. Chem. B* **1998**, *102*, 9922–9927.
- [27] O. L. Baron, E. Deleury, J.-M. Reichhart, C. Coustau, *Dev. Comp. Immu.* **2016**, *57*, 20–30.
- [28] J. Küther, R. Seshadri, G. Nelles, W. Assenmacher, H.-J. Butt, W. Mader, W. Tremel, *Chem. Mater.* **1999**, *11*, 1317–1325.
- [29] L. Landgraf, P. Ernst, I. Schick, O. Köhler, H. Oehring, W. Tremel, I. Hilger, *Biomaterials* **2014**, *35*, 6986–6997.
- [30] A. Verch, A. S. Côté, R. Darkins, Y.-Y. Kim, R. van de Locht, F. C. Meldrum, D. M. Duffy, R. Kröger, *Small* **2014**, *10*, 2697–2702.
- [31] X.-J. Wu, N. Dinguirard, G. Sabat, H.-d. Lui, L. Gonzalez, M. Gehring, U. Bickham-Wright, T. P. Yoshino, *PLoS pathogens* **2017**, *13*, e1006081.
- [32] S.-M. Zhang, Y. Zeng, E. S. Loker, *Innate immunity* **2008**, *14*, 175–189.
- [33] M. Kellermeier, A. Picker, A. Kempfer, H. Cölfen, D. Gebauer, *Adv. Mater.* **2014**, *26*, 752–757.

-
- [34] A. Rao, J. Seto, J. K. Berg, S. G. Kreft, M. Scheffner, H. Cölfen, *J. Struct. Bio.* **2013**, *183*, 205–215.
- [35] A. S. Schenk, B. Cantaert, Y.-Y. Kim, Y. Li, E. S. Read, M. Semsarilar, S. P. Armes, F. C. Meldrum, *Chem. Mater.* **2014**, *26*, 2703–2711.
- [36] S.-S. Wang, A. Picker, H. Cölfen, A.-W. Xu, *Angew. Chem. Int. Ed.* **2013**, *52*, 6317–6321.
- [37] M. A. Bewernitz, D. Gebauer, J. Long, H. Cölfen, L. B. Gower, *Faraday Discuss.* **2012**, *159*, 291.
- [38] H. Gong, M. Pluntke, O. Marti, P. Walther, L. Gower, H. Cölfen, D. Volkmer, *Coll. Surf. A* **2010**, *354*, 279–283.
- [39] A. Verch, D. Gebauer, M. Antonietti, H. Cölfen, *Phys. Chem. Chem. Phys.* **2011**, *13*, 16811.
- [40] J. Ihli, Y.-Y. Kim, E. H. Noel, F. C. Meldrum, *Adv. Funct. Mater.* **2013**, *23*, 1575–1585.

4 Conclusion and Outlook

Diverse influences on the precipitation of CaCO_3 has been demonstrated for a quite diverse collection of additives either flexible or rigid, polar or even non-polar. All systems have been studied in the slow precipitation of the ammonia diffusion method (ADM) in which the pH value subsequently equilibrates at 9.75 within about four hours and CaCO_3 precipitation rates do not diminish interaction properties of additives by simple encapsulation of surface-active additives. In Chapter 3.1 the synthesis and functionalization of Au and $\text{Au}@Fe_3O_4$ and their potential use as additives to influence CaCO_3 crystal morphology was demonstrated. It was shown that stabilization of ACC on the additive surface triggers epitactic growth of calcite on the Au (111) facets, which results in strong Kirkendall effect due to mechanical rigidity of the additive. In contrast to these findings non-specific interaction has been found due to close surface coverage for PEG2000/11-MUA ligand on gold particles. Unfortunately for the $\text{Au}@Fe_3O_4$ system the solubility in calcium ion rich moiety was non-handable due to the bad particle dispersion stability for amphiphilic functionalized particles. Thus, precipitation of micellar clusters and their non-specific inclusion within CaCO_3 has been shown. For the isotropic anionic functionalized $\text{Au}@Fe_3O_4$ Janus particles strong similarity to the observations with 11-MUA@Au particles influences on CaCO_3 has been shown with inclusion of Au particles by epitactic growth of CaCO_3 .

Besides polyanionic nanoparticles a new copolymer class of PolyTHF polyacids as flexible anionic materials have been studied. The morphology to structure relationship has been demonstrated in Chapter 3.2 with two solutions of hyper-branched and linear structured polymers with analogous concentration of calcium interacting carboxylic acid groups. The formation of elongated crystals caused by face selective binding of the hyper-branched polymer additive stands in contradiction to the strong scale inhibiting properties of the linear PolyTHF polyacid polymers, which is related to the amount of carboxylic acid groups in the copolymer structure. The effect might be caused by lowering of supersaturations and available material for crystallization of the CaCO_3 mineral. For both cases the interior of the crystals

looked almost perfectly massive, while the polymer has been identified to get incorporated within grain boundaries during crystallization. The comparison of the inclusion effect of both, the flexible polyacids of PolyTHF polymers and the rigid 11-MUA@Au functionalized polyacid nanoparticles is possible. The pattern of polyacids on gold particles seem to have a relationship to polyacid PolyTHF polymers as long as both additives precipitate dumbbell shaped CaCO_3 . While for the flexible polymer no Kirkendall effect has been observed a strong Kirkendall effect due to oriented epitactic growth has been noticed for the 11-MUA functionalized gold nanoparticles. Furthermore, the CaCO_3 crystals precipitated with isotropic anionic Janus particles also show analogy to this functionalization pattern of Au nanoparticles, which is also caused by epitaxy.

In contrast to the strong influence on CaCO_3 crystallization in desiccator experiments the addition of acetylcholine-binding proteins of the freshwater snail *Biomphalaria glabrata* has weaker influence on the precipitation of CaCO_3 . Surprisingly the His-Tag split off from recombinant *Bg*-AChBP1 gave an additive that has strong inhibiting properties as it stabilizes the intermediate vaterite during the duration of crystallization of CaCO_3 . This protein has furthermore been demonstrated to have ACC stabilizing properties over almost a week in humid warm conditions wherein phase transformation to aragonite occurred within 24 h without protein. Besides the ACC and vaterite stabilization the precipitation of the final crystalline polymorph as it is formed within the snail shell has been identified to be a cooperative effect of the protein *Bg*-AChBP1 and magnesium ions. The reason therefore lies in the better binding to aragonite in contrast to the calcite phase during the time course of dissolution/recrystallization within the CaCO_3 oversaturated environment of the snail and the lab tubes from direct precipitation methods.

The future perspectives of the shown projects can be manifold. The identification of key structural details in additives now might make final crystallization results more predictable. For industrial use a study in direct precipitation methods from basic calcium hydroxide solutions or precipitation from carbonic acid esters with additives needs to be conducted as the precipitation method used within this study is more basic scientific than industrial relevant. Nonetheless the formation of composite materials with additives of the studied type is of great interest for developing new composite materials. Besides this the formation of nano- and micro-particulary CaCO_3 crystals of different shapes might be of high interest for industrial production of polymer/ CaCO_3 blends. Hereby the presented work might flatten the way for future applications. The demonstration of flexibility to non-flexibility and epitaxy differences of additives hopes to enlarge general understanding in solid materials formation for applications that need massive or even non-massive composite materials.

Hence the effect of anisotropy we hoped to identify remained partially unclear and might be studied with better dispersable or functionalized Janus particles for example by introduction of a functionalized silica shell or coverage with a water-soluble polymer. The introduction of interesting properties into the cheap CaCO_3 crystalline material of either morphology (e.g. dumbbell, rhombohedra, speculi) might be a future goal in materials research to develop a blend filler material with interesting properties.

The insight into the properties of the *Bg*-AChBP protein might give another brick in the incomplete wall of structure to calcium binding property relationship for natural proteins. Hence the studies presented in this work were driven-out by using recombinant proteins for concentration reasons but if large amounts of native protein could be extracted in either way for both isoforms to study the additional effect of the protein glycosylation on the CaCO_3 precipitates. The conduction of knock-down assays for the snail protein production and their result on the CaCO_3 shell formation could complete the puzzle of protein influences in this specific species with an *in vivo* study.

5 Declaration for Scientific Contributions

The lab work in this thesis that have been conducted during the last three and a half years of research was only possible with successful collaborative work on a central area of interest I pushed forward. The following contributions have been made by colleagues:

AFM measurements were mainly done by Stefanie Klassen and Dr. Martin Nalbach in the group of Prof. Dr. Angelika Kühnle.

HR-TEM measurements were either conducted by Dr. Bastian Barton formerly AK Kolb or Kathrin Kirchhoff as part of Ingo Lieberwirths' group at the MPIP.

SEM and FIB-SEM preparations were done by Gunnar Glasser and Maren Müller from MPIP respectively.

XPS measurements were done by Hao Lu in the group of Prof. Dr. Mischa Bonn of the MPIP.

SAXS measurements of gold nanoparticles in titration setup have been conducted together with Dr. Ralf Bienert in the group of Dr. Franziska Emmerling on the Federal Institute for Material Testing in Berlin and analyzed by him autonomically.

Snail protein expressions, tissue coloring, and all biological histological preparations and analytics presented in Chapter 3.3 were conducted in a collaboration by Daniela Treiber from the group of Prof. Dr. Jürgen Markl in the FB 08 Biology. Materials have been provided to me for detailed biomineralization studies.

Polymer synthesis and analytics for the cooperation work with Dr. Eva-Maria Langhammer (born Christ) from the AK Frey presented in Chapter 3.2 have been conducted by her own and the material was provided to me for further studies.

Parts of the biomineralization lab work has been conducted under my supervision by Christian Ulrich, Marcel Maslyk, Jonas Junginger, Steven Nothhelfer, Rene Dören and/or my master student Melanie Viel.

5 Authorship Statements

5.1 Functionalized nanoparticles as additives in CaCO₃ crystallization

Manuscript:

The article “Inclusion mechanism of 11-MUA and PEG/11-MUA functionalized gold nanoparticles within CaCO₃” will be submitted to *Crystal Growth & Design* by the *American Chemical Society*.

All persons who have participated sufficiently in the work to take public responsibility for the content, its design, analysis, writing or the revision of the manuscript are listed as authors.

Authorship contributions:

Please note the specific contributions made by each author (list the authors initials followed by their surnames).

Category 1:

Conception and design of study: Mirko Montigny, Wolfgang Tremel

Acquisition of data: Mirko Montigny, Melanie Viel, Moritz Susewind, Steven Nothhelfer, Bastian Barton, Maren Müller, Katrin Kirchhoff, Ralf Bienert

Analysis and/or interpretation of data: Mirko Montigny, Moritz Susewind, Bastian Barton, Maren Müller, Katrin Kirchhoff, Ralf Bienert, Franziska Emmerling, Ingo Lieberwirth, Hans-Jürgen Butt, Wolfgang Tremel

Category 2:

Drafting the manuscript: Mirko Montigny

Revising the manuscript critically for important intellectual content: Mirko Montigny, Moritz Susewind, Ralf Bienert, Melanie Viel, Martin Panthöfer, Wolfgang Tremel

Category 3:

Approval of the version of the manuscript to be published: Wolfgang Tremel

Manuscript:

The article “Seed-Mediated One-Pot Synthesis of Au@Fe₃O₄ Janus Particles” will be submitted to *Crystal Engineering Communication* by the Royal Society of Chemistry.

All persons who have participated sufficiently in the work to take public responsibility for the content, its design, analysis, writing or the revision of the manuscript are listed as authors.

Autorship contributions:

Please note the specific contributions made by each author (list the authors` initials followed by their surnames).

Category 1:

Conception and design of study: Mirko Montigny

Acquisition of data: Mirko Montigny, Melanie Viel, Jonas Junginger, Domenik Prozeller, Katrin Kirchhoff

Analysis and/or interpretation of data: Mirko Montigny, Melanie Viel, Martin Panthöfer, Domenik Prozeller, Katrin Kichhoff, Ingo Lieberwirth, Svenja Morsbach

Category 2:

Drafting the manuscript: Mirko Montigny, Melanie Viel

Revising the manuscript critically for important intellectual content: Mirko Montigny, Melanie Viel, Domenik Prozeller, Martin Panthöfer, Wolfgang Tremel

Category 3:

Approval of the version of the manuscript to be published: Wolfgang Tremel

Manuscript:

The manuscript “Au@Fe₃O₄ Janus type nanoparticles as non-isotropic additives – CaCO₃ mesocrystal formation with nanoparticle inclusion” is the underlying study of paragraph 3.1.3. The manuscript will be submitted to *Crystal Growth and Design* by the *American Chemical Society*.

All persons who have participated sufficiently in the work to take public responsibility for the content, its design, analysis, writing or the revision of the manuscript are listed as authors.

Autorship contributions:

Please note the specific contributions made by each author (list the authors initials followed by their surnames).

Category 1:

Conception and design of study: Mirko Montigny

Acquisition of data: Mirko Montigny, Melanie Viel, Steven Nothhelfer, Bastian Barton, Katrin Kirchhoff, Maren Müller

Analysis and/or interpretation of data: Mirko Montigny, Melanie Viel, Martin Panthöfer, Steven Nothhelfer, Katrin Kichhoff, Ingo Lieberwirth

Category 2:

Drafting the manuscript: Mirko Montigny, Melanie Viel

Revising the manuscript critically for important intellectual content: Melanie Viel, Martin Panthöfer, Wolfgang Tremel

Category 3:

Approval of the version of the manuscript to be published: Wolfgang Tremel

5.2 Novel THF based (co-)polymers for mineralization

Manuscript:

The manuscript “Novel THF Based Copolymers for Mineralization: Polymer Structure Influences Calcium Carbonate Morphology” is the underlying study for paragraph 3.2.1. The manuscript will be submitted to *Crystal Growth and Design* by the *American Chemical Society*. The chapter combines both the content of the main manuscript and the supporting information.

All persons who have participated sufficiently in the work to take public responsibility for the content, its design, analysis, writing or the revision of the manuscript are listed as authors.

Authorship contributions:

Please note the specific contributions made by each author (list the authors initials followed by their surnames).

Category 1:

Conception and design of study: Mirko Montigny, Eva-Maria Langhammer (born Christ)

Acquisition of data: Mirko Montigny, Eva-Maria Langhammer (born Christ), Martin Nalbach, Stefanie Klassen, Katrin Kirchhoff, Maren Müller

Analysis and/or interpretation of data: Mirko Montigny, Eva-Maria Langhammer (born Christ), Martin Nalbach, Stefanie Klassen, Katrin Kirchhoff, Maren Müller, Ingo Lieberwirth, Martin Panthöfer

Category 2:

Drafting the manuscript: Mirko Montigny, Eva-Maria Langhammer (born Christ)

Revising the manuscript critically for important intellectual content: Mirko Montigny, Eva-Maria Langhammer (born Christ), Martin Panthöfer, Wolfgang Tremel

Category 3:

Approval of the version of the manuscript to be published: Wolfgang Tremel

5.3 Bg-AChBP protein effect on CaCO₃

Manuscript:

Paragraph 3.3 is based on my corporation work with Dr. Daniela Treiber from the AG Markl and resulted in two manuscripts “Effects of *Biomphalaria glabrata* Acetylcholine-Binding Proteins on CaCO₃ polymorph selective crystallization” and “Bg-AChBP proteins calcium ion complexation and their effects on CaCO₃ crystallization”. The manuscripts will be both submitted to *Crystal Growth and Design* by the *American Chemical Society*. The two subchapters both combine the main manuscript and the supporting information.

All persons who have participated sufficiently in the work to take public responsibility for the content, its design, analysis, writing or the revision of the manuscript are listed as authors.

Autorship contributions:

Please note the specific contributions made by each author (list the authors` initials followed by their surnames).

Category 1:

Conception and design of study: Mirko Montigny, Daniela Treiber

Acquisition of data: Mirko Montigny, Daniela Treiber, Steven Nothhelfer, Stefanie Klassen, Katrin Kirchhoff, Maren Müller

Analysis and/or interpretation of data: Mirko Montigny, Daniela Treiber, Stefanie Klassen, Katrin Kirchhoff, Maren Müller, Hao Lu, Ingo Lieberwirth, Martin Panthöfer

Category 2:

Drafting the manuscript: Mirko Montigny, Daniela Treiber

Revising the manuscript critically for important intellectual content: Mirko Montigny, Daniela Treiber, Martin Panthöfer, Jürgen Markl, Wolfgang Tremel

Category 3:

Approval of the version of the manuscript to be published: Wolfgang Tremel, Jürgen Markl

6 Curriculum Vitae

Mirko Montigny

Dipl.-Chem.

Born 01.08.1990 in Bad Kreuznach

Married, 2 children



Professional Career

Since 07/2018

Lab leader at BASF Construction Solutions GmbH

Development Construction Materials – Air Control

Selected Responsibilities:

- Project work and leadership of development projects
- Organization and leadership of two lab technicians
- Competencies on gypsum wallboards and surfactant formulations
- Development of new air management concepts for inorganic construction materials

02/2015 – 06/2018

Research Associate in the field of Research and Development

Johannes Gutenberg-University Mainz

Institute for Inorganic Chemistry and Analytical Chemistry

Group of Prof. Wolfgang Tremel

Academic Education

02/2015 – 06/2018 **PhD Thesis**

Johannes Gutenberg-University Mainz

Institute for Inorganic Chemistry and Analytical Chemistry

Group of Prof. Wolfgang Tremel – MPG Doctoral Program Fellow

Topic: Examination of the influences of additives on the crystallization of CaCO_3

10/2009 – 02/2015 **Study of Chemistry – Chemistry**

Johannes Gutenberg-University Mainz

Institute for Inorganic Chemistry and Analytical Chemistry

Group of Prof. Wolfgang Tremel

Thesis:

Die Kristallisation von Calciumcarbonat in Gegenwart von Nanopartikeln

Final grade: **sehr gut (1,5)**

Qualification: **Diplom-Chemiker**

08/2012 – 03/2013 **Semester abroad:** Rice University, Houston TX, USA, in the group of Dr. Christy Landes in the physical chemistry department

Additional Qualifications

11/2017 „Mitarbeiterführung für Nachwuchsführungskräfte der GDCh“, Frankfurt am Main

11/2017	„GMP/GLP“, Berlin
07/2017	„Projektmanagement mit Lean Six Sigma“ (GDCh), Frankfurt am Main
03/2017	„Klassische und nicht-klassische Kristallisation“ (GDCh), Konstanz
2015 & 2016	„BWL für Chemiker“ (GDCh, University), Idstein, Mainz
2015/2016	„Image Processing & Analysis Course“ (IMB), Mainz

Study Colleteral Activities

04/2013 – 04/2016	Tutor for the basic lab trainings on chemistry for doctors and dentists, biologists and the basic lab training in inorganic chemistry.
01/2014 – 07/2014	Teacher for Chemistry, Physics, Maths, English, Latin and Geography at the Schülerhilfe Bad Kreuznach
2017-2018	Student-Speaker of the MPGC Fellowship Programm for doctoral students at the MPI for Chemistry, the MPI for Polymer Science, the University Medical Center and the University Mainz

Publications and Conferences

Publications:

« **Effect of Charge Transfer in Magnetic-Plasmonic Au@MO_x (M = Mn, Fe) Heterodimers on the Kinetics of Nanocrystal Formation** »

I. Schick, D. Gehrig, M. Montigny, B. Balke, M. Panthöfer, A. Henkel, F. Laquai, W. Tremel, Chem. Mater. **2015**, 27, 13, 4877-4884.

« Methods of protein surface PEGylation under structure preservation for the emulsion-based formation of stable nanoparticles »

L. Radi, M. Fach, M. Montigny, E. Berger-Nicoletti, W. Tremel, P. R. Wich, *Med. Chem. Commun.* **2016**, *7*, 1738-1744.

« Poly(THF-co-cyano ethylene oxide): Cyano Ethylene Oxide (CEO) Copolymerization with THF Leading to Multifunctional and Water-Soluble PolyTHF Polyelectrolytes »

E.-M. Christ, J. Herzberger, M. Montigny, W. Tremel, H. Frey, *Macromolecules* **2016**, *49*, 10, 3681–3695.

« Novel THF based copolymers for Mineralization: Polymer structure influences calcium carbonate morphology »

M. Montigny, E.-M. Langhammer, M. Nalbach, M. Müller, K. Kirchhoff, I. Lieberwirth, A. Kühnle, H.-J. Butt, W. Tremel, H. Frey, to be submitted to *Cryst. Growth & Design*.

« Bg-AChBP proteins effect on CaCO₃ polymorph selective crystallization - an *in vivo* and *in vitro* study »

M. Montigny, D. Treiber, M. Panthöfer, I. Lieberwirth, M. Kokkinopoulou, B. Lieb, J. Markl, W. Tremel, in preparation.

« Isoforms of Bg-AChBP protein class effect calcite precipitation in different ways - classical vs. non-classical nucleation and growth »

M. Montigny, D. Treiber, S. Nothhelfer, D. Prozeller, M. Nalbach, S. Klassen, A. Kühnle, S. Winzen, J. Markl, W. Tremel, in preparation.

« Ligand effects on occlusion of gold nanoparticles into CaCO₃ »

M. Montigny, M. Viel, M. Susewind, S. Nothhelfer, M. Nalbach, S. Klassen, R. Bienert, M. Müller, K. Kirchhoff, F. Emmerling, M. Panthöfer, I. Lieberwirth, A. Kühnle, H.-J. Butt, W. Tremel, to be submitted to *Cryst. Growth & Design*.

« Seed-Mediated One-Pot Synthesis of Au@Fe₃O₄ Janus Particles »

Mirko Montigny, Melanie Viel, Domenik Prozeller, Katrin Kichhoff, Ingo Lieberwirth, Svenja Morsbach, Martin Panthöfer, Wolfgang Tremel, to be submitted to *Cryst. Eng. Comm.*

« **Au@Fe₃O₄ Janus type nanoparticles as non-isotropic additives – CaCO₃ meso-crystal formation with nanoparticle inclusion** »

M.Montigny, M. Viel, M. Panthöfer, S. Nothhelfer, K. Kichhoff, I. Lieberwirth, W. Tremel, to be submitted to Cryst. Growth & Design.

Conferences:

- | | |
|---------|---|
| 10/2015 | MRS Fall Meeting, Boston MA, USA |
| 03/2016 | Euro Bio-Inspired, Potsdam, Poster presentation |
| 03/2017 | 5 th International Conference on Multifunctional, Hybrid- and Nanomaterials, Lissabon, Portugal, Poster Presentation |
| 03/2017 | 4 th EuroBioMAT, Weimar, Talk |
| 04/2017 | 19. Frühjahrssymposium der GDCh, Mainz, Poster Presentation |

